2015

Deformation mechanisms in nanotwinned materials by molecular dynamics simulations

Xing Zhao
University of Wollongong

UNIVERSITY OF WOLLONGONG

School of Mechanical, Materials and Mechatronics Engineering

Faulty of Engineering and Information Sciences

Deformation mechanisms in nanotwinned materials by molecular dynamics simulations

Xing Zhao

"This thesis is presented as part of the requirements for the award of the Degree of

Doctor of Philosophy

of the University of Wollongong"

August 2015

ABSTRACT

Molecular dynamics simulations are performed to investigate the deformation mechanisms of nanotwinned materials. The simulations of <111> textured polycrystalline Cu under tensile loading parallel to the twin boundary (TB) reveal that the transmissions of dislocations dominate the plastic deformation. The majority of the TBs retain their initial coherency even after a considerable deformation. The tensile strength monotonically increases as the twin spacing decreases. The main strengthening effect in nanotwinned Cu results from TB restricting the dislocation transmission across TB. Dislocation processes involved in the slip-twin interactions are identified at atomic level, including the direct and indirect transmissions. The direct transmission involves either the successive transmission of the leading and trailing partials by the Fleischer cross-slip model or the absorption and desorption of the extended dislocation by the Friedel-Escaig cross-slip mechanism. In contrast, the indirect transmission involves the formation of special superjogs. The persistent slip transfer leaves zigzag slip traces on the cross-sectional view. The plastic anisotropy of individual grains leads to an inhomogeneous deformation, which results in the formation of intersected slip bands on the plane view.

The simulations of nanotwinned Cu with different orientations reveal a dynamic transition in deformation mechanisms as the TB orientation changes. The dislocation activities in nanotwinned Cu obey the Schmid's law. Three distinct dislocation processes are identified. When the TB is parallel or inclined by an angle less than 30° to the loading direction, the plastic deformation is dominated by the transmission of extended screw dislocations, which involves the successive transmissions of the leading and trailing dislocations and leaves the TB intact. As the angle of inclination increases, TB migration takes place in addition to slip transfer. When the TB is inclined by an angle between 30° and 60° with respect to the loading axis, TB migration governs the deformation. The nanotwinned samples can be fully twinned or detwinned to form single crystals depending on the TB orientations, which eliminates the TBs. When the TB is inclined by an angle between 60° and 90° to the loading axis, dislocation-TB interactions dominate the deformation, where deformation twins and shear bands are formed.

Deformation twinning occurs under specific crystallographic orientations. The formation of deformation twins involves the motion of Shockley partial dislocations on adjacent {111} slip planes. Two twinning mechanisms are identified based on the arrangement of these Shockley partials. The first type of twins involves the overlap of Shockley partials of different types, which occurs when the TB is inclined by an angle between 15° and 30° to the loading direction. Thin twin plates embedded in the original grains are formed, which are not sable and can be easily eliminated under further deformation. The second type of twins results from the passage of Shockley dislocations of the same type, which takes place when the TB is inclined by an angle between 75° and 90° to the loading axis. Deformation twins are well developed along one primary twinning system in samples with inclination angles close to 75°, while multiple twinning systems are activated in samples with inclination angles close to 90°. The twinning dependence on the crystallographic orientation agrees with available experimental results to some extent.

The simulations of nanotwinned Fe reveal a dynamic transition in the deformation mechanism as the TB orientation changes. The slip activities in nanotwinned Fe cannot be explained by the Schmid's law alone. The TB orientation determines three distinct dislocation processes. When the TBs are parallel or inclined less than 30° to the loading direction, the samples eventually fracture in an almost brittle manner. The initial yielding in samples with slanted TBs is due to TB migration. When the TBs are inclined with angles between 45° and 60° to the loading direction, TB migration dominates the plastic deformation. The nanotwinned samples can be fully detwinned or twinned to form single crystals depending on the TB orientations, which eliminates the original TBs. When the TBs are inclined by more than 74° to the loading axis, dislocation-TB interactions are the main deformation mechanism, which forms complicated dislocation networks. Under vertical orientations, extensive slip transmission takes place in samples with small twin spacing, while twinning occurs in addition to conventional dislocation slip in samples with large twin spacing.

ACKNOWLEDGEMENTS

First of all, I would like to thank to my PhD advisors, Professor Kiet Tieu and Associated Professor Cheng Lu for their guidance, support, patience and encouragement that contributed to the completion of this thesis. They are brilliant scholars and wonderful mentors. It is my honour to be one of their PhD students. My appreciation also goes to members of my research group, Mr. Linqing Pei, Dr. Kuiyu Cheng, Mr. Liang Zhang, Dr. Hongtao Zhu, Dr. Guillaume Michal, and Dr. Ajit Godbole for their helpful advice and suggestions on my PhD subject. I am really enjoying spending the research life with them.

I would like to express my gratitude to Professor Minghui Huang, Professor Lihua Zhan. They gave me many amazing suggestions which inspired my research work on deformation behaviour in nanotwinned metals. I am very grateful to them for this guidance as well as criticisms.

I would like to acknowledge financial supports from China Scholarship Council and University of Wollongong.

Thanks also go to the University of Wollongong and the National Facility of the National Computational Infrastructure of Australia for providing the powerful supercomputing resource.

My time was also made enjoyable over the past four years due to many friends who became a part of my life. I am grateful for time spent with my friends: Mr. Peitang Wei, Dr. Ning Kong, Dr. Guanyu Deng, Dr. Lihong Su, Dr. Yong Sun, Dr. Hailiang Yu, Mr. Hui Wang, Mr. Jie Zhang, Dr. Xuan Zheng, Dr. Qiang Zhu, Dr. Ming Xie, Mr. Weiqiang Wang. They gave me so many supports in my life and a lot of suggestions on my research. I will never forget them.

Finally, I would like to thank my family for all their love and encouragement. For my parents who raised me with their unwavering love, for my sister whose faithful supports during the final stages of this PhD, they are appreciated. I love all of them forever.

PUBLICATIONS

1. **Xing Zhao**, Cheng Lu, A.K. Tieu, Linqing Pei, Lihua Zhan, Minghui Huang, 2014. Heterogeneous dislocation process, slip transfer and shear band formation in the deformation of nanotwinned copper by molecular dynamics simulation. ***2014 TMS Annual Meeting & Exhibition***.

2. **Xing Zhao**, Cheng Lu, A.K. Tieu, Linqing Pei, Lihua Zhan, Minghui Huang, 2014. Grain size dependent mechanical behaviour and deformation mechanism in nanocrystalline copper. ***2014 TMS Annual Meeting & Exhibition***.

3. **Xing Zhao**, Cheng Lu, Kiet Tieu, Linqing Pei, Zhang Liang, Kuiyu Cheng, Minghui Huang, 2015. Strengthening mechanisms and dislocation processes in the deformation of nanotwinned copper. (In preparation)

4. Linqing Pei, Cheng Lu, **Xing Zhao**, Zhang Liang, Kuiyu Cheng, Guillaume Michal, Kiet Tieu, 2015. Brittle versus ductile behaviour of nanotwinned copper: A molecular dynamics study. ***Acta Materialia***, 89, 1-13.

5. Linqing Pei, Cheng Lu, Kiet Tieu, **Xing Zhao**, Liang Zhang, Kuiyu Cheng, 2015. Brittle versus ductile fracture behaviour in nanotwinned FCC crystals. ***Materials Letters***, 152, 65-67.

6. Linqing Pei, Cheng Lu, Kiet Tieu, **Xing Zhao**, Kuiyu Cheng, Liang Zhang, 2015. Ductile-to-brittle fracture transition in polycrystalline nickel under hydrostatic pressure. ***Computational Materials Science***, 109, 147-156.

7. Liang Zhang, Cheng Lu, Kiet Tieu, **Xing Zhao**, Linqing Pei, 2015. Shear response of copper bicrystal with $\sum 11$ symmetric and asymmetric tilt grain boundaries by molecular dynamics simulation. ***Nanoscale***, 7, 7224-7233.

8. Liang Zhang, Cheng Lu, Kiet Tieu, **Xing Zhao**, Linqing Pei, Guillaume Michal, 2015. Molecular dynamics simulation on generalized stacking fault energies of FCC metals under preloading stress. ***Chinese Physics B***. (accepted)

9. Liang Zhang, Cheng Lu, Kiet Tieu, Linqing Pei, **Xing Zhao**. 2015. Molecular dynamics study on the grain boundary dislocation source in nanocrystalline copper under tensile loading. ***Materials Research Express***, 2, 035009.

10. Liang Zhang, Cheng Lu, Kiet Tieu, Linqing Pei, **Xing Zhao**, 2014. Effect of stress state on deformation and fracture of nanocrystalline copper: molecular dynamics simulation. ***Chinese Physics B***, 9 (23), 098102.

11. Linqing Pei, Cheng Lu, Kiet Tieu, **Xing Zhao**, Kuiyu Cheng, Zhang Liang, 2014. Influence factors for brittle-to-ductile transition in twinned copper. ***TMS 2014 Annual Meeting***, 487-494.

12. Liang Zhang, Cheng Lu, Kiet Tieu, **Xing Zhao**, Linqing Pei, 2014. Atomistic simulation on the structure and mechanical response of Σ3, Σ5 tilt grain boundaries under tension. ***TMS 2014 Annual Meeting***, 817-823.

13. Linqing Pei, Cheng Lu, Kiet Tieu, Hongtao Zhu, **Xing Zhao**, Kuiyu Cheng, Zhang Liang, 2013. A molecular dynamics simulation of fracture in nanocrystalline copper. ***Journal of Nano Research***, 25, 188-194.

TABLE OF CONTENTS

LIST OF FIGURES

LIST OF TABLES

1 INTRODUCTION

1.1 Background

Nanocrystalline materials, with an average grain size of less than 100 nm, have undergone a considerable amount of researches over the last three decades, because of their superior properties, such as high strength and hardness compared to their coarse-grained counterparts (Gleiter, 1989, Gleiter, 2000, Kumar et al., 2003b, Meyers et al., 2006). But nanocrystalline materials are quite brittle and are inherently unstable (Kumar et al., 2003b, Meyers et al., 2006, Chookajorn et al., 2012). In recent years, the attention has turned to nanotwinned materials which contain parallel twins with twin spacing in the range of tens of nanometers (Beyerlein et al., 2014). It has been shown that nanotwinned materials exhibit simultaneous ultrahigh strength and increased ductility, as well as high electrical conductivity (Lu et al., 2004, Lu et al., 2009b), which make them attractive for numerous applications. The strength of nanotwinned Cu increases with decreasing twin spacing, reaching the maximum value at twin spacing of around 15 nm, followed by a softening as twin spacing is further reduced (Lu et al., 2009b). The ultrahigh strength is attributed to the effective blockage of dislocation movement by coherent twin boundaries (TBs) (Christian and Mahajan, 1995, Dao et al., 2007, Zhu et al., 2012). TBs restrict the movement of dislocations, resulting in dislocations piling up and cutting through TBs at large twin spacing, thus strengthening the nanotwinned materials (Li et al., 2010b). The softening mechanism is controlled by TB migration, which involves the nucleation and propagation of twinning dislocations along the twin plane (Li et al., 2010b, Wang et al., 2010).

1.2 Motivation

While conventional experiments can provide an insight into the deformation mechanism based on post-mortem transmission electron microscopy (TEM) observation (Morris Wang et al., 2013, Zheng et al., 2013), the microstructure evolution in real time cannot be recorded. Molecular dynamics (MD) simulations have been widely used to elucidate the deformation mechanisms of nanocrystalline and nanotwinned materials, i.e., interactions between dislocations and TBs at atomic

level that are not experimentally available (Yamakov et al., 2002c, Zhu and Gao, 2012).

The mechanical behaviour of nanotwinned metals is strongly dependent on three microstructural characteristics: twin spacing, grain size and TB orientation. The effect of twin spacing on the mechanical response of nanotwinned materials has been widely investigated. Recent synthesis of nanotwinned Cu with a preferred orientation (Hodge et al., 2012, You et al., 2013) has made the study of the influence of TB orientation possible. It has been found that the deformation of <111> textured nanotwinned Cu was heterogeneous. Moreover a considerable fraction of low angle grain boundaries (GBs) was identified in this type of nanotwinned Cu (Hsiao et al., 2012, Lagrange et al., 2013, Morris Wang et al., 2013). But previous simulations involved only two (Morris Wang et al., 2013) or four grains (You et al., 2013, Zhou et al., 2014), the mean field behaviour might not be fully captured and the effect of small angle GB was ignored. As a result, a statistically large number of grains and the small angle GBs need to be considered.

Most of the prepared nanotwinned samples (Morris Wang et al., 2013, Idrissi et al., 2011, Wei et al., 2014) were in polycrystalline forms which contained a large fraction of GBs, TBs with random orientations and other defects. Thus it is difficult to experimentally identify the origins of their supreme mechanical properties. Jang et al. (Jang et al., 2012) carried out in situ experiment to investigate the influence of TB orientation on the plastic deformation of nanotwinned Cu nanopillars. But only two orientations were tested. Experimental investigation of the deformation mechanism of nanotwinned materials has been limited because of the difficulty in synthesizing nanotwinned materials with specific orientations. The evolution of twin structure during plastic deformation of twinning-induced plasticity (TWIP) steels revealed that multiple twinning systems can be activated simultaneously (Karaman et al., 2000, Gutierrez-Urrutia et al., 2010, Gutierrez-Urrutia and Raabe, 2011, Idrissi et al., 2010). Until now no attempt has been made to explore the possibility for secondary twinning in nanotwinned materials, since it is not possible to distinguish deformation twins and growth twins which are identical from a crystallographic view (Mahajan, 2013).

The majority of experimental and theoretical studies have been conducted in nanotwinned face-centered cubic (fcc) materials (Beyerlein et al., 2014). The effect of nanotwins on the mechanical response of body-centered cubic (bcc) materials remains unexplored. As a result, it is necessary to study the influence of nanotwins on the mechanical behaviour of bcc materials and the corresponding deformation mechanisms.

In this thesis, MD simulations are used to systematically investigate the mechanical behaviour of nanotwinned fcc and bcc materials. The underlying deformation mechanisms at atomic level responsible for the mechanical properties are elucidated.

1.3 Outline of the thesis

This thesis consists of 7 chapters and is organised as follows:

In Chapter 2, the mechanical behaviour of nanocrystalline materials and the twinning mechanism are reviewed, followed by the fabrication methods, mechanical properties, deformation mechanisms and slip-twin interactions of nanotwinned materials.

In Chapter 3, the basic theory of MD simulations and visualisation techniques are introduced, followed by the slip systems in nanotwinned fcc and bcc materials.

In Chapter 4, the mechanical behaviour of <111> textured nanotwinned Cu is investigated. The full three-dimensional simulation cells contain a statistically large number of grains and the small angle GBs are retained. The dislocation structure evolution is traced and the dislocation-TB interactions are analysed at atomic level.

In this chapter 5, the effects of TB orientation and twin spacing on the mechanical behaviour of nanotwinned Cu are systematically investigated. The deformation mechanisms of nanotwinned Cu with different TB orientations are elucidated. Moreover, the atomistic mechanisms involved in the formation of secondary twins are identified.

In Chapter 6, the effects of TB orientation and twin spacing on the mechanical behaviour of nanotwinned Fe are investigated. The deformation mechanisms of

nanotwinned Fe with different TB orientations are elucidated and the plausible dislocation-twin reactions are systematically analysed.

In Chapter 7, the main conclusions and the recommendations for future work are given.

2 LITERATURE REVIEW

This chapter reviews the published researches considered essential to the understanding of deformation mechanism of nanotwinned materials.

2.1 Mechanical behaviour of nanocrystalline materials

Nanocrystalline materials with an average grain size of less than 100 nm have been the subject of considerable research over the past three decades (Gleiter, 1989, Gleiter, 2000). Advances in processing techniques and in computing materials science have improved the investigation on the mechanical response of nanocrystalline materials (Kumar et al., 2003b, Meyers et al., 2006). Owing to a very small grain size, nanocrystalline materials contain a large fraction of atoms occupied on the GBs, which may significantly alter their physical, mechanical and chemical properties. Nanocrystalline metals and alloys possess some appealing properties, including high strength/hardness, improved toughness, superior wear resistance and enhanced superplastic formability, compared with their coarse-grained counterparts.

Nanocrystalline materials can be synthesised by several laboratory-scale processing techniques. These approaches are classified into two groups: bottom-up by consolidating small clusters and top-down by breaking down the bulk polycrystalline material into a nanostructure. The principal synthesis methods are: inert gas condensation, mechanical alloying, electrodeposition, and severe plastic deformation including equal-channel angular processing and high-pressure torsion.

Interfaces play an important role in the deformation of crystals (Sutton and Balluffi, 1995). The strength or hardness of the material increase with decreasing grain size, which is known as Hall-Petch relation (Hall, 1951, Petch, 1953). This relation is explained in terms of dislocation pile-ups at the GBs (Yip, 1998). But when the grain is refined to nanoscale regime, a softening phenomenon occurs (an inverse Hall-Petch effect) (Schiøtz et al., 1998). There is a critical grain size at which the material is hardest to deform. The crossover from normal to inverse Hall-Petch effect is attributed to a transition in the dominant deformation mechanism, from dislocation-based plasticity to GB-mediated mechanism. Nowadays, with the advance in computational capability and the development of large massively parallel computing

architectures, MD simulations have become large enough to cover the whole range of grain sizes. The transition in deformation mechanism, from one based on dislocation activities to one mediated by GB processes was observed by MD simulations.

2.1.1 Inverse Hall-Petch effect and GB-mediated mechanisms

The yield strength increases with the inverse of the square root of the grain size following the Hall-Petch relation. But experimental results revealed this relation cannot be extrapolated to nanoscale regime. Chokshi et al. (Chokshi et al., 1989) first reported the inverse Hall-Petch effect in nanocrystalline Cu and Pd and attributed it to diffusion creep in nanostructured materials. Nieh and Wadsworth (Nieh and Wadsworth, 1991) revealed the existence of a critical grain size for dislocation pile-ups, below which weakening mechanisms led to a decrease in hardness with decreasing grain size. It was assumed there was a point at which the Hall-Petch relation broke down.

MD simulations by Schiotz et al. (Schiøtz et al., 1998, Schiøtz et al., 1999, Schioøtz and Jacobsen, 2003) revealed a softening phenomenon in the deformation of nanocrystalline Cu, which was explained in terms of GB sliding (Schiøtz et al., 1998). Van Swygenhoven and her colleagues have performed a large number of MD simulations in nanocrystalline materials. Their earliest studies (Van Swygenhoven and Caro, 1997, Van Swygenhoven and Caro, 1998, Van Swygenhoven et al., 1999a, Van Swygenhoven et al., 1999b, Van Swygenhoven et al., 2000, Van Swygenhoven and Derlet, 2001, Derlet et al., 2003a) on the plastic behaviour of nanocrystalline Ni and Cu, with a mean grain size ranging from 3.4 to 12 nm, revealed that GB sliding was responsible for the plastic deformation. No dislocation activity was detected, in contrast to the behaviour of coarse-grained materials (Van Swygenhoven and Caro, 1997).

The GBs in computer-generated nanocrystalline Cu and Ni samples exhibited order and structural units that are normally expected for high-angle boundaries(Van Swygenhoven et al., 2000). For low-angle boundaries, dislocation networks were observed to accommodate the misfit between the grains. For all other types of misfit, some degree of structural coherence was observed, and misfit accommodation

occurred in a regular pattern. The GBs in nanocrystalline metals were not highly disordered, amorphous, or liquid like interfaces. The results suggested that the GB structure in nanocrystalline materials is similar to that found in coarse-grained metals.

Further studies addressed the mechanism of GB sliding at atomic level in nanocrystalline materials (Van Swygenhoven and Derlet, 2001). Two atomic processes atomic shuffling and stress-assisted free-volume migration were identified in the interfaces during sliding. GB sliding comprises of massive discrete atomic activity, either through uncorrelated shuffling of individual atoms or in some cases correlated shuffling of several atoms. Moreover, hopping sequences involving several GB atoms were observed, which were regarded as stress-assisted free-volume migration. The two atomic processes constituted the rate controlling mechanism for the GB sliding. In addition GB sliding resulted in stress build-up across neighbouring grains. This local stress increase was relieved by the migration of GB and triple junction, and dislocation emission and propagation.

Yamakov et al. (Yamakov et al., 2001, Yamakov et al., 2002c, Yamakov et al., 2002a, Yamakov et al., 2004) simulated the behaviour of <110> textured nanocrystalline Al. They revealed that dislocations began to nucleate when the applied stress exceeded the threshold stress for the nucleation of extended dislocations from the GBs or grain junctions. Below this critical stress, the system slowly deformed through a GB-based mechanism (Yamakov et al., 2001). The network of straight and sharp GBs was almost unchanged during the deformation.

In addition to GB sliding, GB diffusion creep may contribute to the deformation of nanocrystalline materials with the smallest grain size at high temperature. Yamakov et al. (Yamakov et al., 2002b, Haslam et al., 2003) performed MD simulations at elevated temperatures and observed a homogeneous steady-state diffusion creep. The strain rate agreed well with that given by the Coble-creep formula. The GB diffusion creep was accommodated by GB sliding, which is known as Lifshitz sliding (Yamakov et al., 2002b, Wolf et al., 2005).

Grain rotation as a deformation mechanism was revealed by MD simulations (Yamakov et al., 2002a, Haslam et al., 2003) and was also reported in experiments (Ke et al., 1995, Jin et al., 2004, Shan et al., 2004, Wang et al., 2008). Grain rotation was confirmed under in situ TEM observation. Moreover, grain rotation was also found to induce grain growth during the deformation. The stress assisted grain growth was even reported at liquid nitrogen temperature (Zhang et al., 2004a, Zhang et al., 2005). These findings suggested that grain rotation is an important deformation mode in nanocrystalline materials and it can lead to stress-assisted grain growth.

2.1.2 Transition from inverse to normal Hall-Petch effect

Recent modelling works (Schioøtz and Jacobsen, 2003, Yamakov et al., 2003b, Wolf et al., 2005) have captured the mechanism transition from a dislocation-based plasticity to a GB-mediated process and elucidated the nature of the strongest grain size in full three-dimensional nanocrystalline metals. In the first study, Yamakov et al. (Yamakov et al., 2003b) carried out simulations in nanocrystalline Al consisting of four grains. The small grain number enabled to explore a relatively large grain size and so the deformation mechanism transition can be directly probed. These simulations demonstrated that the crossover in the mechanical behaviour resulted from a transition in the dominant deformation process.

The atomic configurations shown in Figure 2.1 reveal that a change in the deformation mechanism occurs as the grain size decreases from 32 nm to 7nm (Yamakov et al., 2003b). For the large grain sizes, the successive emission of leading and trailing Shockley partials from the GBs forms complete extended dislocations (labelled 1) inside the grain. These dislocation loops are extended 1/2[110] dislocations which split into two 1/6[112] Shockley partials. For samples with a grain size of 7 nm, as seen in Figure 2.1d, only stacking faults generated by the glide of the partial dislocation are observed (labelled 2). Stacking faults were also observed in large grains, as seen in Figure 2.1a, where the emission of the trailing partial was prevented by the local GB structure and the stress fields. The mechanical behaviour in the flow regime was probed by determining the strain rate as a function of the grain size. A pronounced change in the strain rate for the five grain sizes was observed. The average strain rate decreased as the grain size decreased from 32 nm

to 18 nm, and increased again as the grain size decreased further to 7 nm. The minimum strain rate was seen with a grain size of 18 nm. This strongest size in nanocrystalline Al was reached when the grains became too small to nucleate complete dislocations, but were still too large for extensive GB processes.

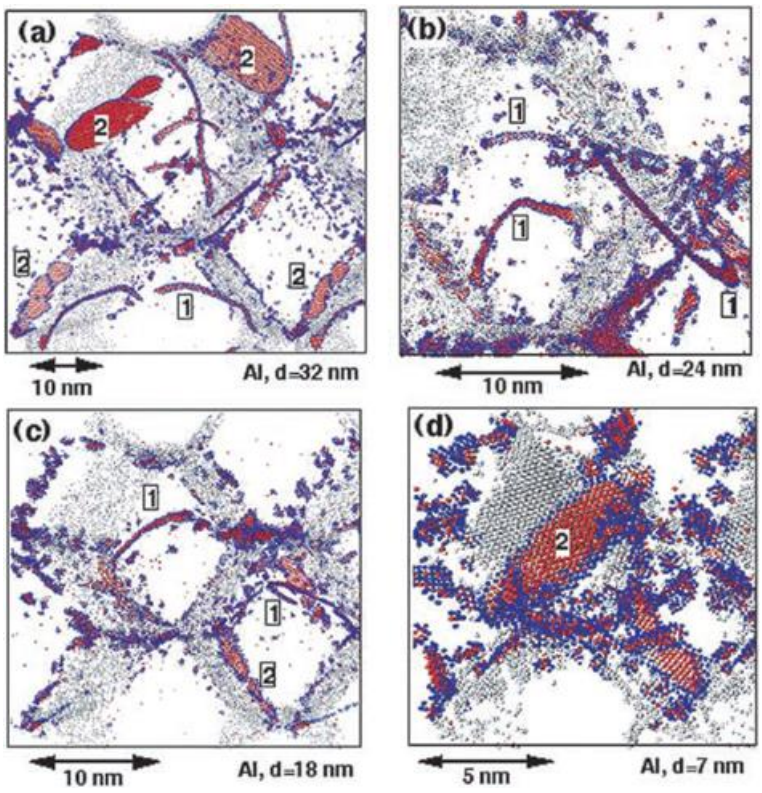

Figure 2.1 Snapshots of nanocrystalline Al at about 1.5% strain for four different grain sizes: (a) 32 nm; (b) 24 nm; (c) 10 nm and (d) 7 nm. Red atoms indicate hcp atoms. Grey atoms represent the GBs and blue atoms are other disordered atoms. Perfect fcc atoms are not shown. Label 1 indicate extended 1/2[110] dislocations; Label 2 represent stacking faults (Yamakov et al., 2003b).

In the study by Schiotz and Jacobsen (Schioøtz and Jacobsen, 2003), a large number of grains and a distribution in the grain size ranging between 5 and 50 nm were incorporated in the simulation cells. Figure 2.2 shows the stress-strain curves from 10 simulations with varying grain sizes. The strength exhibited a maximum at a grain size between 10 and 15 nm (Figure 2.2B). This maximum stress indicated a shift in the underlying deformation mechanism, from dislocation-mediated plasticity in samples with large grains to GB sliding in small grains.

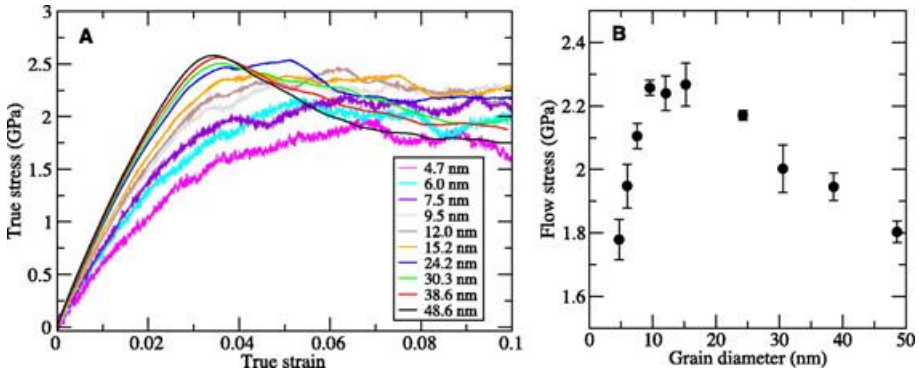

Figure 2.2. The grain-size dependence of the flow stress. (A) Stress-strain curves for 10 simulations with varying grain sizes. (B) The flow stress as a function of grain size (Schioøtz and Jacobsen, 2003).

Figure 2.3 shows atomic-scale structures after 10% deformation and the atomic strain from an additional 1% deformation. For the large grains (Figure 2.3A and B), dislocation slip in the grain interiors dominated the deformation. For the small grains (Figure 2.3C and D), GB sliding was the main deformation mechanism. The change in deformation mechanism is not a sharp transition, even for the largest grains some deformation occurs in the GBs. Throughout the simulation dislocations were generated at the GBs, glided through the grains and were absorbed at other GBs. With increasing grain size the dislocation activity increased significantly. Cu has a lower stacking fault energy than Al and thus favours partial dislocation slip over full dislocation slip. Most of the dislocations were partial dislocations, although several perfect extended dislocations were also observed. Remarkably, in some simulations deformation twins were observed (Schioøtz and Jacobsen, 2003, Schiøtz et al., 1999) as shown in Figure 2.3A. Bothe studies revealed that, the crossover in the mechanical response was accompanied by a change in the underlying mechanism, from dislocation dominant plasticity to GB-mediated processes.

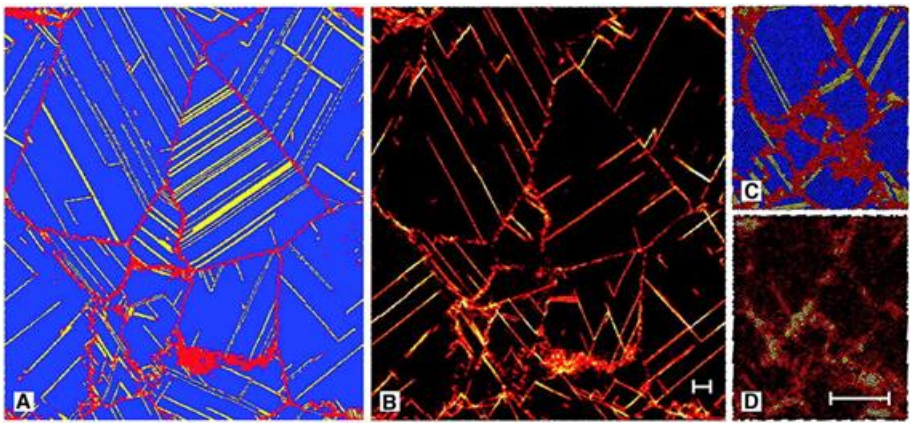

Figure 2.3 The deformation mechanism for different grain sizes. (A) The structure with a grain size of 49 nm. Blue atoms are in a perfect fcc structure; yellow atoms are at stacking faults and TBs; and red atoms are in GBs and dislocation cores. (B) The atomic strain from an additional 1% strain. The main deformation occurred on slip planes inside the grains. (C and D) The same configuration with a grain size of 7 nm. The main deformation occurred in the GBs (Schioøtz and Jacobsen, 2003).

Recently an analysis tool using localized slip vectors was developed to quantitatively describe the plastic deformation in nanocrystalline metals (Vo et al., 2008, Stukowski et al., 2010). Using this method, the contributions of dislocation activity can be separated from GB sliding. The dislocation activity was found to increase with grain size but decrease with increasing strain rate.

Yamakov et al. (Yamakov et al., 2004) proposed a deformation-mechanism map for the mechanical behaviour of nanocrystalline fcc metals at low temperature as shown in Figure 2.4. This map was based on the fundamental physical processes from MD simulations, different from the prevalent approach built on phenomenological constitutive equations. The underlying physics came from the length-scale competition between the grain size and the splitting distance, and from the grain-size dependence of the dislocation nucleation stress. In this way, the map connected the mechanical properties of nanocrystalline fcc metals with the structure and the dislocation process. The map was divided into three regions. In Region I, full dislocation slip prevailed in the deformation due to the large grain size and/or high stacking fault energy. In Region II, because of the small grain size and/or low stacking fault energy, only partial dislocations were nucleated, leaving stacking faults inside the grains. In Region III, the GB-mediated processes dominated the

deformation due to the small grain size or low stress. These processes resulted in the inverse Hall–Petch relation. The transition in the deformation mechanism and the related mechanical behaviour with decreasing grain size depended on the stacking fault energy, the elastic properties of the material, and the applied stress level. For metals with a high stacking fault energy, the change was governed mainly by the transition from perfect slip to GB-mediated process, the line between Region I and III. For metals with a low stacking fault energy or under high stress, the crossover involved partial slip in Region II as an intermediate stage. Stacking faults transected the small grains and GB processes increased with decreasing grain size. The strongest size was governed the line between Region I and II and increases with decreasing high stacking fault energy.

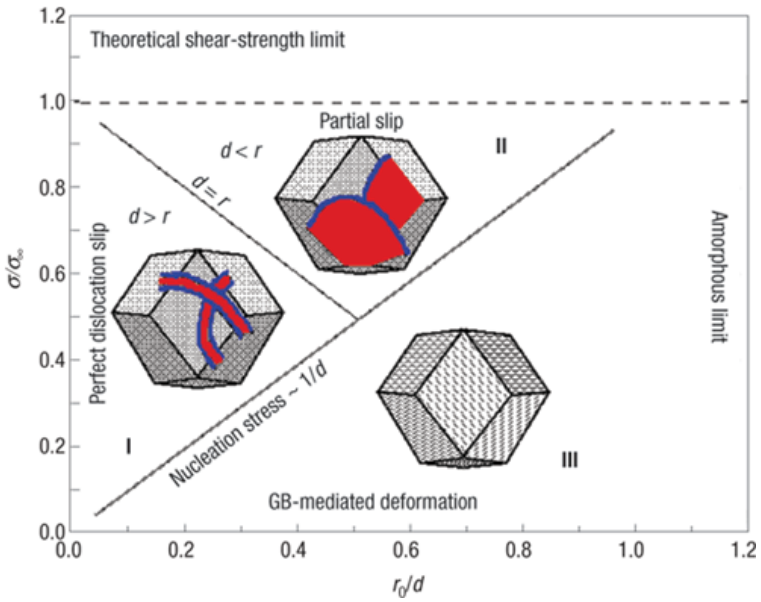

Figure 2.4 The deformation-mechanism map for nanocrystalline metals at low temperature (Yamakov et al., 2004).

2.1.3 Dislocation-based plasticity

The plastic deformation in coarse-grained fcc materials at low temperature involves the continuous nucleation of dislocations from Frank-Read sources and their glide on well-defined slip systems, where atomic diffusivity is minor. These dislocation sources cannot operate in nanocrystalline materials because the stress needed for their operation is inversely proportional to the size of the source. Thus GBs take over the role of sources and sinks for dislocations. Three possible intragranular

deformation mechanisms were observed from computer simulations: the first by means of partial dislocations which left stacking faults inside the grains; the second by means of full dislocations which consisted of leading and trailing partials on the same slip plane and left no dislocation debris; and the third by means of mechanical twinning which formed extensive deformation twins in the grain interiors.

To investigate the mechanism for dislocation nucleation from the GB simple bicrystal configurations were often used. Spearot et al. (Spearot et al., 2005, Spearot et al., 2007a, Spearot et al., 2007b, Tschopp and McDowell, 2008) systematically studied the dislocation nucleation process as a function of both loading and misorientation between the two crystals. They revealed that the stress required to nucleate dislocations were smaller than that for homogeneous dislocation nucleation in single crystals. Moreover, nucleation of partial dislocations from the interface could not be explained in terms of Schmid factors alone, and GB structure played an important role in the nucleation process (Spearot et al., 2007b).

The bicrystal set-ups have two-dimensional nature and only limited misorientation can be investigated. Three-dimensional nanocrystalline models were constructed using the Voronoi procedure. In these samples, the orientation of individual grains was randomly chosen, thus producing a wide variety of GBs. Van Swygenhoven and her colleagues (Derlet and Van Swygenhoven, 2002, Van Swygenhoven et al., 2002, Derlet et al., 2003b, Frøseth et al., 2004b, Van Swygenhoven et al., 2004, Van Swygenhoven et al., 2006, Derlet et al., 2003a, Van Swygenhoven and Weertman, 2006, Frøseth et al., 2004a) revealed the atomic mechanism responsible for dislocation emission from GBs in nanocrystalline materials. Their simulation results showed that local GB structures strongly affected dislocation nucleation. Ledge structures or triple junction lines with a high hydrostatic pressure concentration acted as nucleation sites for partial dislocations. The nucleation and subsequent emission of the dislocation were accompanied by atomic shuffling and stress-assisted free volume migration, which also relieved the stress concentration. Temporal analysis of atomic configurations indicated that nucleation and propagation are separate processes. Partial dislocations often nucleated but did not propagate. The leading and

trailing partial dislocations that constituted a full dislocation might not nucleate from the same GB region or from the same GB (Van Swygenhoven et al., 2006).

Atomistic simulations revealed that depending on the type of metal, either full dislocations or partial dislocations dominate the plastic deformation. Full dislocation activity was observed in simulations of Al, whereas in simulations of Cu and Ni no trailing dislocation occurred and stacking faults transecting the grain were observed as shown in Figure 2.5. The deformation-mechanism map based on the absolute value of the stable stacking fault energy (Yamakov et al., 2004) could not explain all simulation results, such as the partial slip activity in Ni with a high stacking fault energy.

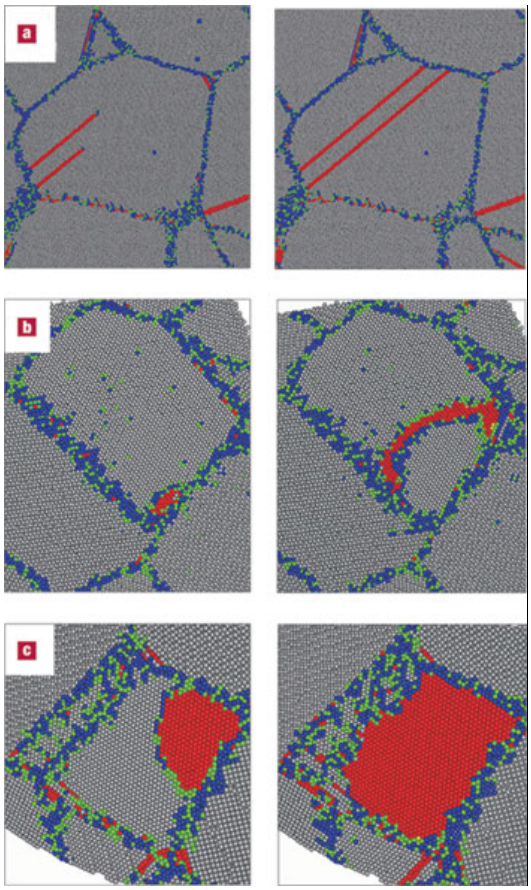

Figure 2.5 Typical deformation mechanisms in full three-dimensional samples. (a) Two partial dislocations in nanocrystalline Ni. (b) A full dislocation in nanocrystalline Al. (c) A partial dislocation in nanocrystalline Cu. The atoms are coloured according to the local crystallinity classification. Grey represents fcc atoms, red represents hcp atoms, green other 12-coordinated atoms, and blue non-12-coordinated atoms (Van Swygenhoven et al., 2004).

Van Swygenhoven et al. (Van Swygenhoven et al., 2004) suggested that the nature of the dislocation activity can be understood in terms of the generalized stacking fault energy curve, which involves both stable and unstable stacking fault energies. The generalized stacking fault energy curve represents the energy barrier of rigidly shifting a perfect crystal on a (111) plane along a [112] direction (Rice, 1992, Zimmerman et al., 2000). After the leading partial was nucleated, the energy barrier for the trailing partial was determined by the ratio between the stable and unstable stacking fault energies. When this ratio was close to unity, the energy barrier was low. Therefore a trailing partial was emitted to form a full dislocation within the time scale of MD simulations. But for the case of Ni and Cu, this ratio was low which means the energy barrier for nucleating the trailing partial was high. The presence of structural relaxations in the GB further delayed its nucleation. The observation of extended stacking faults in Ni and Cu might result from the timescale limitation of the MD simulations, since there was no experimental evidence of dislocation networks after deformation in nanocrystalline metals (Budrovic et al., 2004).

GB structure such as misfit regions or ledges can restrict the dislocation motion and the dislocation is pinned near these stress concentrations depending on the geometrical conditions and the Burgers vector (Van Swygenhoven et al., 2006). The de-pinning process was thermally activated and therefore not purely mechanically driven. In recent simulations of nanocrystalline Al (Bitzek et al., 2008b), the grain-averaged shear produced by dislocation slip and the grain-averaged resolved shear stress during deformation was determined. It was found that the slip activity was accompanied by rapid drops of resolved shear stress in that grain in that grain. The simulation results suggested that the dislocation-mediated plasticity in nanocrystalline metals was determined by dislocation propagation, which constituted the rate-limiting process rather than the nucleation of the dislocations. The dislocation avoided local pinning sites such as GB ledges and misfit regions by Fleischer cross-slip mechanism as they propagated through the grain (Bitzek et al., 2008a, Bitzek et al., 2008b). Figure 2.6a shows a dislocation has cross-slipped several times between slip planes during propagation.

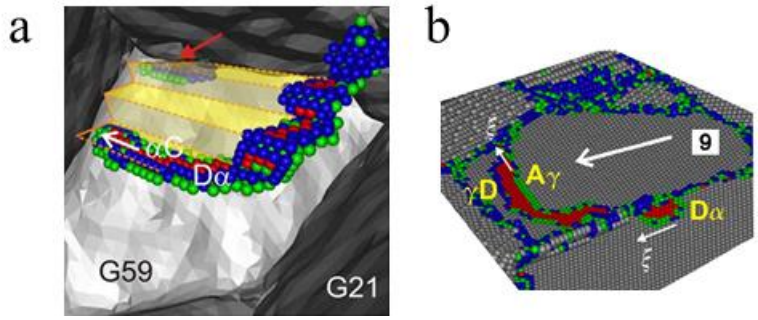

Figure 2.6 Motion of dislocations. (a) Cross-slip between slip planes (Bitzek et al., 2008a). (b) Transmission of dislocation (Brandl et al., 2007).

The interactions between dislocation and GB play an important role in the mechanical behaviour of nanocrystalline materials. Possible slip-GB interactions were outlined by Sutton and Balluffi (Sutton and Balluffi, 1995): (a) direct transmission, (b) direct transmission with the creation of residual dislocations, (c) indirect transmission including residual dislocations in the GB where the incident and outgoing slip systems do not intersect, and (d) no transmission where the dislocation is deposited or absorbed at the GB. Shen et al. (Shen et al., 1988, Shen et al., 1986) derived the criteria for slip transmission across the GBs and Lee et al. (Clark et al., 1992, Lee et al., 1990b, Lee et al., 1990a) further developed these criteria from TEM observations. The transmission of dislocation impinging on the GB is governed by the following three criteria: (a) the angle between the line of intersection between the slip planes of the incoming and outgoing slip systems and the GB plane should be minimized, (b) the magnitude of the Burgers vector of the residual dislocations left at the GB should be minimized, (c) the resolved shear stress acting on the outgoing slip system should be maximized. Figure 2.6b shows the transmission of a full dislocation across a general high angle GB to emit a partial dislocation (Brandl et al., 2007). Recently atomistic simulations (De Koning et al., 2002, De Koning et al., 2003a, De Koning et al., 2003b, Bachurin et al., 2010) and multiscale modelling (Dewald and Curtin, 2007b, Dewald and Curtin, 2007a, Dewald and Curtin, 2011) have been used to explore the slip transmission processes and some additional constrains have been developed. Sangid et al. (Sangid et al., 2011, Ezaz et al., 2011, Abuzaid et al., 2012) introduced a method to calculate the energy barriers during slip–GB interaction. The energy barriers for dislocation

transmission through the GB and dislocation nucleation from the GB were obtained. The coherent TB was found to provide the highest barrier to slip transmission.

Yamakov et al. (Yamakov et al., 2001, Yamakov et al., 2002c) carried out MD simulations in columnar nanocrystalline Al and revealed the length-scale effects in the nucleation of dislocations from GBs. If the grain size was not large enough, only partial dislocations nucleated, leaving behind stacking faults transecting the grain. Above a critical grain size, the deformation was dominated by the motion of extended dislocations. The nucleation of extended dislocations involved the successive emission of the leading and trailing dislocation from the GBs (Yamakov et al., 2001). As the plastic strain increased, the dislocation concentration inside the grains increased which led to various types of intragranular dislocation–dislocation interaction processes as shown in Figure 2.7 (Yamakov et al., 2002a, Yamakov et al., 2002c, Yamakov et al., 2003a, Wolf et al., 2005). Lomer–Cottrell locks were formed in each of the four grains in Figure 2.7. Moreover a variety of intergranular processes, involving the interaction of dislocations with GBs and deformation twins formed during the simulation took place (Wolf et al., 2005, Yamakov et al., 2002a, Yamakov et al., 2002c). The initially flat GBs became rough after deformation, which resulted from dislocation–GB interaction processes. Below the dislocation nucleation stress, the GBs remained straight during the deformation. A new grain grown from those GBs that were active during these dislocation processes (Yamakov et al., 2002c). In addition, extensive deformation twinning occurred under the very high GB and dislocation densities (Yamakov et al., 2002a, Yamakov et al., 2002b, Yamakov et al., 2002c).

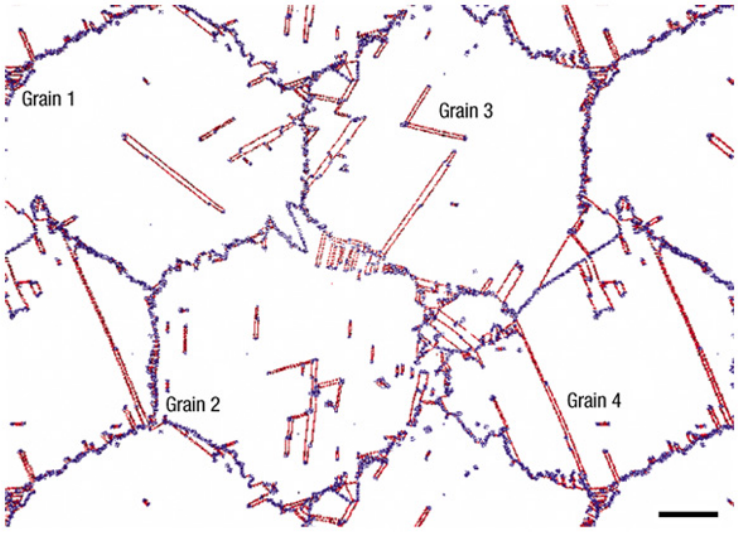

Figure 2.7 Snapshot of columnar nanocrystalline Al with a grain diameter of 45 nm. A variety of processes involving dislocation–dislocation and dislocation–GB interactions took place. Scale bar, 10 nm (Yamakov et al., 2002c).

2.2 Deformation twinning

2.2.1 Deformation twinning in coarse-grained materials

A TB is a special type of GB across which there is a mirror lattice symmetry (Callister Jr, 2007). Atoms on one side of the boundary are located in the mirror-image positions of the atoms on the other side. Twins are the regions between these boundaries. There are three types of twins: deformation or mechanical, annealing and growth twins. Twins are formed on definite crystallographic planes and in specific directions, depending on the crystal structure. Specifically, coherent TBs lie on the {111} planes along the <112> directions in fcc materials, and on the {112} planes in the <111> directions in bcc materials. These three types of twins are formed under dramatically different conditions (Mahajan, 2013). Deformation twins result from dislocations produced from applied mechanical shear forces, while annealing twins and growth twins are formed by growth accidents.

Dislocation slip and deformation twinning are two competitive deformation modes. Mechanical twinning has been widely observed in coarse-grained metals and alloys (Meyers et al., 2001). The propensity of the material to twin is largely determined by

its stacking fault energy. For example, deformation twinning occurs readily in fcc metals with low stacking fault energies such as TWIP steels and Ag. Deformation twining is promoted at high strain rates and/or low temperatures. The slip process is restricted under these conditions, because the number of operable slip systems is reduced.

A number of models have been proposed to rationalize the formation of deformation twins in fcc and bcc materials. It is usually assumed that the formation of deformation twins involves two separate processes: the nucleation of twin embryos and their subsequent growth to large twins (Christian and Mahajan, 1995). The twinning mechanisms in fcc materials often require a dislocation source in the grain interior to operate. The twinning source can be divided into two groups: prismatic and glide. In prismatic models, the primary slip does not lie on the twinning plane. Cottrell and Bilby (Cottrell and Bilby, 1951) proposed the first twin nucleation model which involved the dissociation of a full dislocation into a Shockley partial dislocation and a sessile Frank dislocation. But only monolayer stacking fault can be produced. Venables (Venables, 1961) extended the pole mechanism and explained how mechanical twins grown. Cohen and Weertman (Cohen and Weertman, 1963) suggested that the overlap of stacking faults led to the quick formation of imperfect deformation twins. These stacking faults resulted from glide of Shockley dislocations dissociated from piling-up dislocations near Lomer-Cottrel locks. A similar model involving the cross-slip of stair-rod dislocations was presented by Fujita and Mori (Fujita and Mori, 1975). A simple glide model was described by Mahajan and Chin (Mahajan and Chin, 1973a), in which the interaction between two coplanar perfect dislocation led to the nucleation of a three-layer twin. Recent experiments revealed the twin structure evolution and the orientation dependent twin formation in TWIP steels (Karaman et al., 2000, Gutierrez-Urrutia et al., 2010, Gutierrez-Urrutia and Raabe, 2011, Idrissi et al., 2010).

The nucleation of twin embryo in bcc materials is governed by dislocation reactions. Cottrell and Bilby (Cottrell and Bilby, 1951) proposed a pole model for twin nucleation which involvef the dissociation of a full dislocation into a glissile twinning dislocation and a sessile dislocation according to 1/2<111>→1/3<112>+

1/6<11-1>. In this model, the primary slip did not lie on the twinning plane. But experiments showed that the Burgers vector of the twinning partials was parallel to the dislocation. So the Cottrell-Bilby pole model was no longer acceptable. Other models were based on the dissociation of lattice dislocations. Sleeswyk (Sleeswyk, 1963) suggested that a three-layer twin formed from the dissociation of a screw dislocation into three twinning partials on adjacent {112} planes according to 1/2<111>→3×1/6<111>. Ogawa (Ogawa, 1965) made a similar proposal in which an edge dislocation spread the total Burgers vector on to three successive planes and created a three-layer fault. Mahajan (Mahajan, 1972) extended the Sleeswyk model and suggested the twins grow through the coalescence of multiple twin embryos. Lagerlöf (Lagerlöf, 1993) further proposed that the twin propagated by zonal dislocations and thickened via double cross-slip. Alternatively, Priestner and Leslie (Priestner and Leslie, 1965) proposed that a three-layer twin formed from the dissociation of a sessile <001> slip resulting from two dislocations on {110} and {112} planes. There is a lack of consensus for twin nucleation at the moment (Mahajan, 2013, Yu et al., 2012, Steinmetz et al., 2013).

Twinning also has a strong size effect (Meyers et al., 2001). According to the experimental results reported in the literature, smaller grain size impedes deformation twinning in coarse-grained metals and alloys, irrespective of their crystal structure. Meyers et al. (Meyers et al., 2001) summarized the Hall–Petch slopes for both perfect dislocation slip and twinning in a number of coarse-grained metals. The Hall–Petch slope for twinning was much higher than that for dislocation slip. So for coarse-grained metals, the stress required for twinning increased faster with decreasing grain size than the stress for dislocation slip. Therefore, smaller grain size reduced the possibility for twinning. But extensive deformation twinning was observed in nanocrystalline materials (Zhu et al., 2012).

2.2.2 Deformation twinning in nanocrystalline materials

2.2.2.1 Atomistic simulations

The deformation mechanisms in nanocrystalline materials are dramatically different from those in their coarse-grained counterparts due to the small grain size as Frank-

Read source ceases to operate. Yamakov and his colleagues (Yamakov et al., 2001, Yamakov et al., 2002c, Yamakov et al., 2002a, Yamakov et al., 2003a, Yamakov et al., 2003b, Yamakov et al., 2004, Wolf et al., 2005) revealed that extensive deformation twinning occurred in addition to dislocation slip during the plastic deformation of nanocrystalline Al. Both the heterogeneous and homogeneous mechanisms for the nucleation of deformation twinning were observed (Yamakov et al., 2002a). The heterogeneous mechanism involved the successive emission of partial dislocations from the same GB on adjacent slip planes (see process 1-5 in Figure 2.8). The stacking sequences in five regions of the twinned grain were indicated at the bottom of the figure. Letters in red indicated TB planes. The five regions were: (1) perfect fcc crystal; (2) intrinsic stacking fault; (3) extrinsic stacking fault; (4) two TBs separated by two (111) planes; and (5) more widely separated twins. Process 6 in Figure 2.8 revealed another mechanism for twin nucleation, which involved the splitting and subsequent migration of a GB segment. Process 7 revealed the nucleation of double-Shockley partials, leaving behind extrinsic stacking faults. This process required extremely large local stresses compared with the nucleation of single partial dislocations.

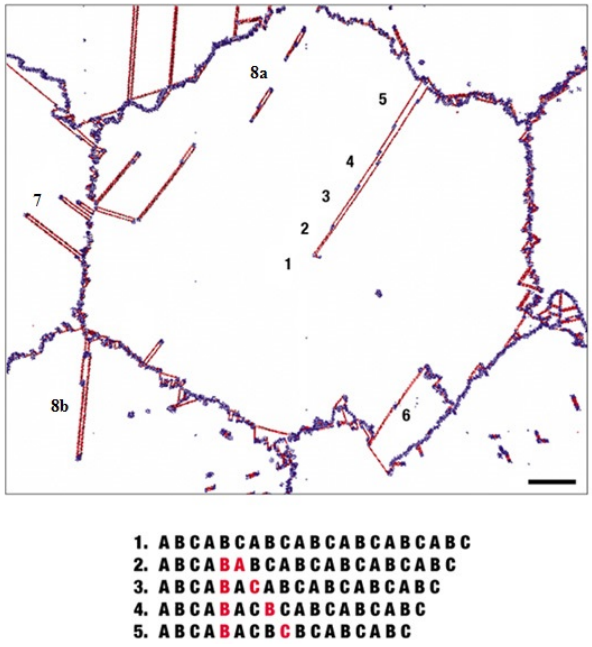

Figure 2.8 Snapshot for a grain with a diameter of 70 nm at 10.3% plastic strain, which reveal the heterogeneous (processes 1–7) and homogeneous (processes 8) mechanisms for the formation of deformation twins (Yamakov et al., 2002c).

In contrast, the homogeneous process involved the overlap of the stacking faults of intrinsically and/or extrinsically dissociated dislocations in the grain interiors. Process 8a in Figure 2.8 showed that when the Shockley partials of two extended dislocations on neighbouring planes glided past each other, the intrinsic stacking faults of the two dislocations overlapped to form an extrinsic stacking fault. Alternatively, when two extrinsically dissociated dislocations overlapped (8b in Figure 2.8), a three-layer microtwin was formed.

MD simulations also revealed deformation twinning in nanocrystalline bcc materials, including Mo (Frederiksen et al., 2004, Zhang et al., 2012a, Zhang et al., 2012b), Ta (Pan et al., 2008, Alcalá et al., 2012, Higginbotham et al., 2013) and Nb (Zhang et al., 2011). Marian et al. (Marian et al., 2004) reported dynamic transitions from smooth to rough to twinning in dislocation motion.

2.2.2.2 Experimental observations

Several experiments have confirmed deformation twinning in nanocrystalline materials via TEM observation (Chen et al., 2003, Liao et al., 2003b, Liao et al., 2003a, Liao et al., 2004). The presence of deformation twins was also related to the nanocrystalline microstructure, as twinning was not found in coarse-grained pure Al because of the high stacking fault energy. Moreover, the classic twinning mechanism cannot operate in nanocrystalline materials. Dislocation-based model was proposed to explain the observation of deformation twins and stacking faults in nanocrystalline materials. The basic models for deformation twinning should be extended to highlight the role of GB in the deformation of nanocrystalline materials.

The observation of deformation twins in nanocrystalline materials verified a transition of deformation mechanism from one based on normal slip activity to one controlled by partial dislocation activity when grains are refined to tens of nanometers, which can also be used to understand the unusual mechanical properties of nanocrystalline materials.

Deformation twinning has been widely observed in bcc metals (Wang et al., 2005, Chen et al., 2013, Chen et al., 2014, Wang et al., 2015). Wang et al. (Wang et al., 2005) observed deformation twinning during nanoindentation of nanocrystalline Ta.

Moreover, multiple twin intersections were observed which indicates the twinning mechanism in bcc nanocrystalline materials is different from that of fcc nanocrystalline metals. Deformation twins have a planar nature in fcc metals, while in bcc materials, the non-planar deformation twins are expectable (Duesbery and Vitek, 1998). The screw dislocation have non-planar cores and can glide on six slip planes which includes three <110>-type slip planes and three <112>-type twinning planes (Remington et al., 2014). Multiple twinning systems can be operative for each twinning dislocation.

2.3 Fabrication and microstructure of nanotwinned materials

Nanotwinned materials can be synthesised by several laboratory-scale processing techniques. The principal synthesis methods are electrodeposition (Lu et al., 2004, Lu et al., 2009b) and physical vapour deposition, such as magnetron sputtering (Zhang et al., 2004b, Zhang et al., 2006, Hodge et al., 2008, Morris Wang et al., 2013). Several major drivers have contributed to the synthesis of crystals containing nanotwinned structures. Lu et al. (Lu et al., 2004, Lu et al., 2009b) synthesised high purity Cu samples with nanoscale twins using a pulsed electrodeposition. Samples with different twin spacing were prepared by adjusting the deposition rate. TEM observations (Figure 2.9a) revealed that the as-deposited Cu consisted of equiaxed grains with random orientations. The grain size was about 500 nm on average. Twins were formed in all grains and the average twin thickness ranged from a few nanometers to about 100 nm. Detailed structural characterization showed that the presence of Shockley partial dislocations (as steps) on the coherent interfaces. These steps were intrinsic structural features of growth twin from electrodeposition and their density per unit area of TBs was found to be rather constant (Lu et al., 2009b). Columnar structured Cu with preferentially oriented parallel nanoscale twins was also synthesised by controlling the deposition parameters (You et al., 2011).

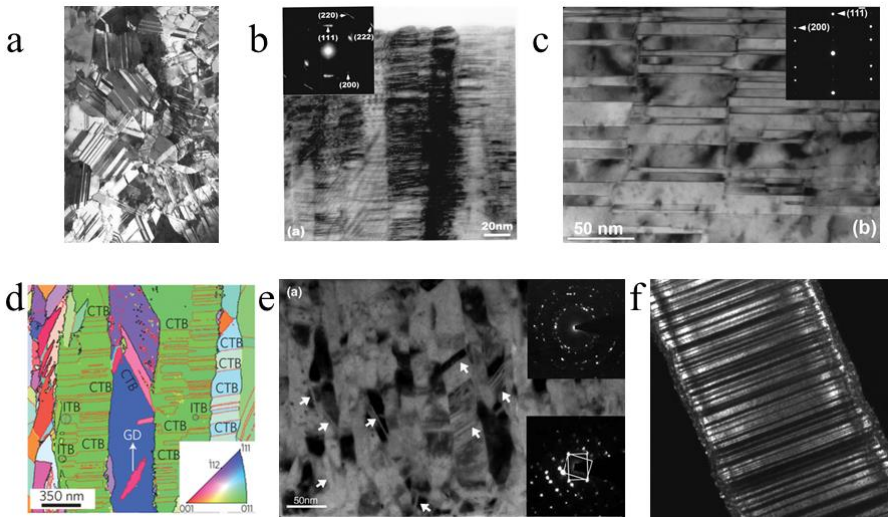

Figure 2.9 Nanotwinned materials synthesized by different methods. (a) Electrodeposited nanotwinned Cu (Lu et al., 2004). (b) Magnetron sputtered nanotwinned stainless steel (Zhang et al., 2004b). (c) Magnetron sputtered epitaxial nanotwinned Cu (Anderoglu et al., 2008a). (d) An inverse pole figure orientation mapping image of growth twins (Morris Wang et al., 2013) (e) Nanotwinned Pd (Idrissi et al., 2011) (f) Nanotwinned Cu nanopillars (Jang et al., 2012).

Zhang et al. (Zhang et al., 2004b, Zhang et al., 2004c, Zhang et al., 2006, Anderoglu et al., 2008a) deposited nanotwinned 330 stainless steels (Figure 2.9b) and Cu (Figure 2.9c) using magnetron sputtering. The twin thickness was controlled by the deposition rate. These samples had a strong <111> texture. TEM images indicated the average columnar grain size was around 50 nm with high density of twins. The average twin spacing was estimated to be around 5 nm. The epitaxial nanotwinned Cu films were indeed in a single crystalline form and not <111> textured (Anderoglu et al., 2008a). Nanotwinned structures were also successively prepared in high stacking fault energy materials (Bufford et al., 2012).

Hodge et al. (Hodge et al., 2006, Hodge et al., 2008, Shute et al., 2011, Morris Wang et al., 2013, Shute et al., 2009) also produced columnar nanotwinned Cu by magnetron sputtering. The thickness of the sputtered Cu was up to 178 μm. The columns were equiaxed with an average diameter of 500 nm. The TB spacing was highly variable with a median spacing of 35 nm (Shute et al., 2011). The atomic-level structural features of many TBs and GBs were examined using a recently developed inverse pole figure orientation mapping (IPFOM) in a field-emission TEM as shown in Figure 2.9d. The samples showed a strong <111> fiber texture. The

misorientation angle distribution maps indicated an appreciable fraction of low-angle GBs although the columnar boundaries were primarily random high angle boundaries (Morris Wang et al., 2013, Lagrange et al., 2013). Moreover the coherent TBs were found to be inherently defective with kink-like steps and curvature. These imperfections influenced the deformation mechanisms and mechanical behaviour of nanotwinned Cu.

Idrissi et al. (Idrissi et al., 2011, Wang et al., 2012a, Colla et al., 2012, Wang et al., 2012b) synthesised thin Pd films containing a significant density of growth twins. The orientations of the growth twins changed randomly from one grain to another, and were heterogeneously distributed within the grains as shown in Figure 2.9e. Randomly distributed growth twins were frequently observed in electrodeposited nanocrystalline Ni (Kumar et al., 2003a) and in vapour deposited nanocrystalline Al (Chen et al., 2003).

Another type of nanotwinned materials is metallic nanowires. A high density of nanoscale twins normal to the growth axis was introduced with TB spacing of less than 10 nm (Wang et al., 2013). Greer et al. (Burek and Greer, 2010, Jang et al., 2011, Jang et al., 2012) made a significant improvement in the fabrication of nanotwinned metallic nanopillars. They created nanotwinned Cu nanopillars using electroplating template fabrication. Samples with orthogonal (Figure 2.9f) and slanted TBs were synthesised by controlling the TB orientation. The diameters of these pillars range from 50 nm to 500 nm, with TB spacing of less than 5 nm.

2.4 Mechanical properties of nanotwinned materials

2.4.1 Strength and ductility

The mechanical properties of nanotwinned metals have been primarily derived from uniaxial tension/compression tests and nanoindentation (Lu et al., 2004, Lu et al., 2009b, Zhang et al., 2006, Lu et al., 2005, Morris Wang et al., 2013, Wang et al., 2013). Figure 2.10 summarises the yield stress of nanotwinned Cu as a function of inverse twin spacing ($1/\lambda$) from experiments and simulations. The strength of

equiaxed nanotwinned metals followed the conventional Hall-Petch effect as TBs were strong barriers for dislocation motion. Lu et al. (Lu et al., 2009b) reported a combination of ultrahigh strength and ductility in equiaxed nanotwinned Cu. The strength increased with decreasing twin thickness, reaching a maximum at 15 nm, followed by a softening at smaller values. Figure 2.11 shows the elongation to failure as a function of twin thickness (λ) and grain size (d). A pronounced increase in tensile elongation to failure was observed with decreasing twin spacing, while the ductility was reduced as grain size decreased (Lu et al., 2009a).

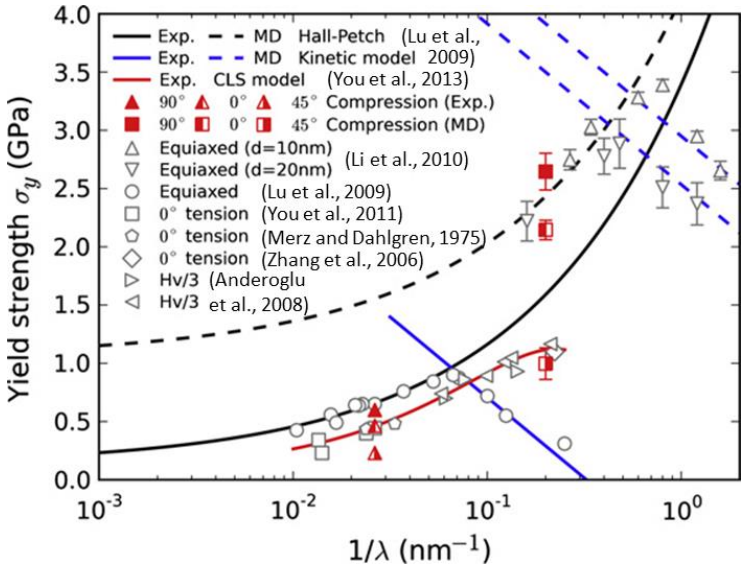

Figure 2.10 Yield stress of nanotwinned Cu (σ_y) as a function of inverse twin thickness (1/λ) (You et al., 2013).

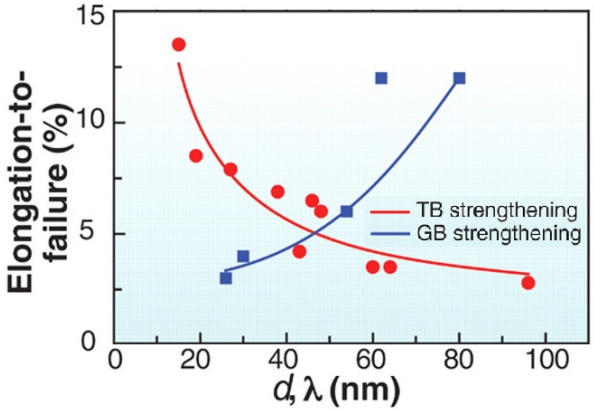

Figure 2.11 Elongation to failure as a function of twin thickness (λ) and grain size (d) (Lu et al., 2009a).

2.4.2 Strain hardening rate

The work-hardening behaviour of nanotwinned metals is strongly dependent on microstructural characteristics (twin spacing, grain size and TB orientation) and loading parameters (strain rate and temperature). Lu et al. (Lu et al., 2012) calculated the work-hardening coefficients from the uniform straining stages in the uniaxial tensile curves to analyse the twin thickness effect on work hardening. The strain hardening coefficient *n* was determined according to the Hollomon–Ludwik power law, $\sigma = K_1 + K_2\varepsilon^n$, where K_1 is the initial yielding stress σ_y, K_2 represents the strength increment due to work hardening at ε = 1.

The size effects on the strain hardening exponent *n* of nanotwinned Cu and its twin-free counterparts is shown in Figure 2.12. The value of *n* for twin-free Cu with a grain size of 500 nm was about 0.26, smaller than coarse-grained Cu. As the grain size decreased, the *n* value continuously decreased in ultrafine-grained and nanocrystalline materials until it became nearly undetectable when the grain size went down to tens of nanometers. Introducing nanoscale twins slightly affected *n*, as the *n* value increased from 0.22 to 0.30 as the twin spacing decreased from 90 nm to 20 nm. But when the twin thickness further decreased to less than 15 nm, n increased significantly and exceeded the value for coarse-grained Cu, and finally reached a maximum value of 0.66 at the twin thickness of 4 nm. The refinement in twin spacing led to a monotonic increase in strain hardening rate, which was opposite to the general observation where decreasing grain size reduced the work hardening rate.

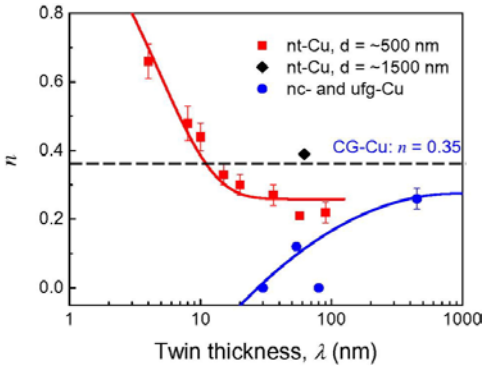

Figure 2.12 Effect of twin thickness λ on work-hardening coefficient *n* of the equiaxed nanotwinned Cu. For comparison, *n* values for nanocrystalline Cu and coarse-grained Cu are also plotted as a function of grain size (Lu et al., 2012).

2.4.3 Strain rate sensitivity

The strain rate sensitivity was used to explore the active deformation mechanism as the strain rate sensitivity and the associated activation volume varied by orders of magnitude for different rate-controlling processes. Experimental researches have shown that the mechanical response of nanotwinned materials under different loading conditions was highly strain rate sensitive. The strain rate sensitivity m was defined as $m = \frac{1}{\sigma_y}\frac{\partial ln\sigma}{\partial ln\dot{\varepsilon}}$, where σ is the flow stress and $\dot{\varepsilon}$ is the strain rate. By defining the activation volume, $v = \sqrt{3}k_B T\frac{\partial ln\dot{\varepsilon}}{\partial ln\sigma}$, where k_B is the Boltzmann constant and T is the absolute temperature, the strain rate sensitivity can be re-written as $m = \frac{\sqrt{3}k_B T}{\sigma_y v}$.

Lu et al. (Lu et al., 2009c, Lu et al., 2005, Chen et al., 2006) studied the twin spacing dependence of strain rate sensitivity in nanotwinned and nanocrystalline Cu as shown in Figure 2.13. The strain rate sensitivity increased with a decrease of grain size from micron to submicrometer, followed by a dramatic increase when the grain size was further reduced to below 100 nm. When the twin spacing was refined nanoscale regime, the strain rate sensitivity was much higher than that for coarse-grained Cu. Moreover, the dependence of rate sensitivity on twin spacing was close to the strain rate sensitivity as a function of grain size for nanocrystalline Cu. The increase in strain rate sensitivity with decreasing twin thickness indicated that TB-mediated dislocation activities played a dominant role in the deformation of nanotwinned Cu.

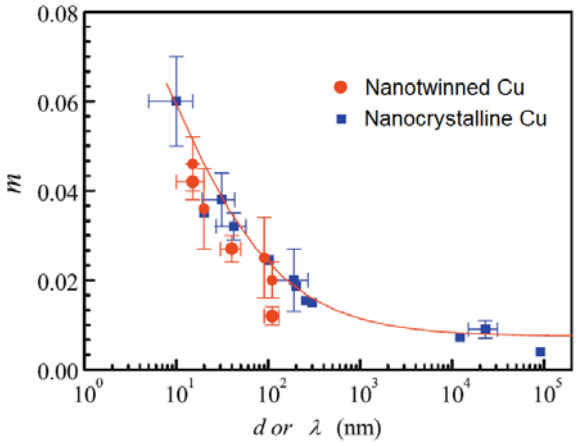

Figure 2.13 Effect of twin lamellar thickness λ on rate sensitivity for nanotwinned Cu (Lu et al., 2009c).

2.4.4 Fracture and fatigue response

The damage tolerance of nanotwinned metals is essential for evaluating their application as structural materials in engineering components. Qin et al. (Qin et al., 2009a, Qin et al., 2009b) prepared bulk nanostructured Cu samples with embedded nanoscale twin bundles by means of dynamic plastic deformation. They revealed that the tensile strength and fracture toughness of the samples increased simultaneously as a result of an increasing volume fraction of nanotwin bundles. The nanotwinned structures were effective in arresting crack propagation during fracture. The presence of the nanotwin bundles induced coarse and deep dimples in the fracture surfaces, which enhanced the fracture toughness. Singh et al. (Singh et al., 2011) showed that coherent nanoscale twins improved the damage tolerance under conditions of plane stress and an increase in twin density could enhance the damage tolerance. Kim et al. (Kim et al., 2012) carried out in situ TEM tensile experiments and observed crack arrest and bridging by nanoscale twins in Cu thin films.

Shute et al. (Shute et al., 2009, Shute et al., 2011) studied the fatigue response of nanotwinned Cu produced by magnetron sputtering. The S-N curves (Stress amplitude- Number of cycles to failure) for nanotwinned, ultrafine-grained and coarse-grained Cu are shown in Figure 2.14. The fatigue life for nanotwinned and ultrafine-grained Cu was greatly improved compared to coarse-grained counterparts. Moreover, nanotwinned Cu was much more stable than nanocrystalline Cu. The majority of the twins remained after the fatigue test, although some of the original nanotwinned structures were destroyed. Pan et al. (Pan et al., 2013, Pan and Lu, 2014) carried out fatigue tests on nanotwinned Cu synthesised by direct current electrodeposition. They found nanotwinned Cu had a better low cycle fatigue life and a higher endurance limit. The activation of a primary slip system dominated the deformation of nanotwinned sample, which led to the formation of zigzag slip bands.

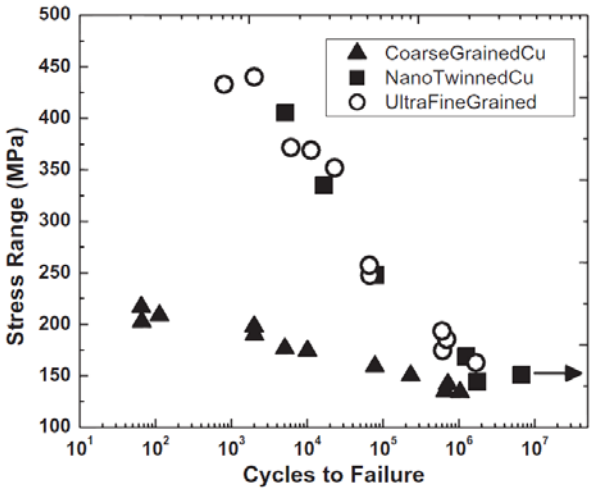

Figure 2.14 S–N curves for nanotwinned, ultrafine-grained and coarse-grained Cu (Shute et al., 2011).

2.4.5 Thermal stability

Zhang et al. (Anderoglu et al., 2008b, Zhang and Misra, 2012) compared the thermal stability of nanocrystalline and nanotwinned metals. Figure 2.15 shows the evolution of hardness with annealing temperature in nanotwinned stainless steel, and nanotwinned, nanocrystalline and ultrafine-grained Cu. The hardness of nanotwinned Cu decreased gradually with increasing annealing temperature. In contrast, the hardness of nanocrystalline and ultrafine-grained Cu decreased dramatically. The thermal stability of a coherent TB was superior to that of a general GB. On the other hand, Lagrange et al. (Lagrange et al., 2013) observed GB network evolution during thermal annealing o <111> textured nanotwinned Cu. They found that the nanotwinned microstructure coarsened through thermal-activated motion of incoherent twin segments followed by lateral motion of columnar boundaries (Lagrange et al., 2013).

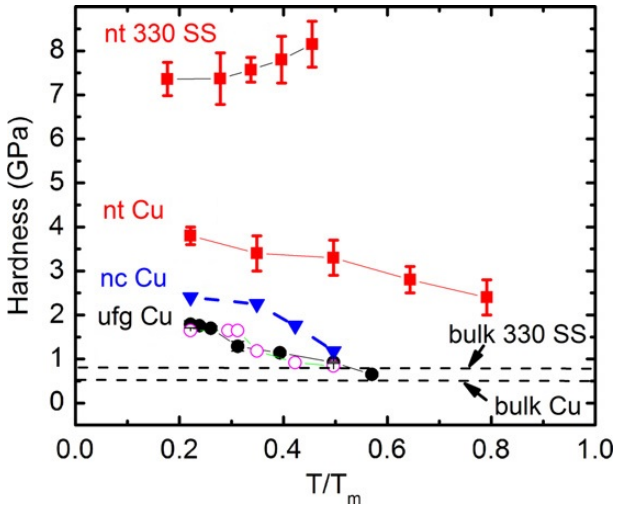

Figure 2.15 Evolution of hardness for nanotwinned 330 stainless steels, nanotwinned Cu, nanocrystalline Cu and ultrafine-grained Cu (Zhang and Misra, 2012).

2.5 Deformation mechanisms in nanotwinned materials

Nanotwinned materials exhibit a number of similarities in their deformation and fatigue processes as compared to nanocrystalline metals regardless of the apparent anomalies in strain hardening behaviour and thermal stability. In this section current understanding of deformation mechanisms of nanotwinned metals and alloys are reviewed, starting with experimental observations which are then supplemented by atomistic simulations.

2.5.1 Experimental observations

2.5.1.1 Three-dimensional nanotwinned materials

In nanocrystalline materials, GBs become the dislocation sources and sinks. Post-deformation TEM observations of nanocrystalline metals and alloys have failed to reveal the presence of dislocation debris (Kumar et al., 2003b), so alternate deformation mechanisms such as GB sliding (Schiøtz et al., 1999, Schioøtz and Jacobsen, 2003) and grain rotation (Shan et al., 2004) were suggested to be potential deformation mechanisms. The investigation on the microstructure of deformed nanotwinned Cu using TEM suggested that the interaction between dislocations and TBs played an important role in the plastic deformation of nanotwinned Cu (Lu et al.,

2004, Lu et al., 2009b, Lu et al., 2005, Dao et al., 2006, Dao et al., 2007, Shute et al., 2011, Jang et al., 2012, Morris Wang et al., 2013). Abundant dislocation debris was seen in the vicinity of TBs as shown in Figure 2.16.

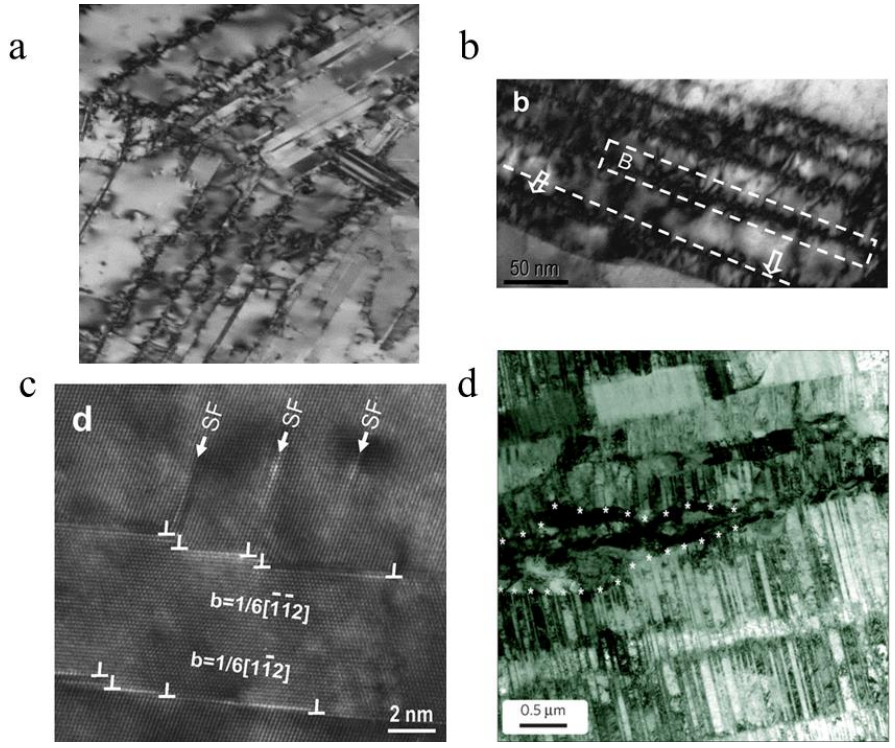

Figure 2.16 TEM observations of nanotwinned Cu after tensile deformation.(a) Plenty of dislocations at the TBs (Lu et al., 2004). (b) Dislocation pile-ups along TBs and curved TBs. (c) HRTEM image of Partial dislocations, dislocation pile-ups and TB bending (Dao et al., 2006). (d) Accumulations of dislocations between the TBs and inside the grains (Morris Wang et al., 2013).

Lu et al. (Lu et al., 2004) revealed the ultrahigh strength in nanotwinned Cu. The strengthening mechanism originated from the effective blockage of dislocation motion by coherent TBs (Ma et al., 2004). A large number of dislocations were identified from the TEM image of the sample after tensile tests as shown in Figure 2.16a. Their later investigation revealed the maximum strength of nanotwinned Cu samples with different twin thicknesses. The strongest twin thickness originated from a transition in the underlying deformation mechanism from the slip transfer across TBs to the motion of pre-existing easy dislocation sources (Lu et al., 2009b).

Wang et al. (Wang et al., 2010, Li et al., 2011) studied the stability of growth twins using in situ TEM, where rapid migration of incoherent TB was observed. The

detwinning process was explained in terms of the collective glide of multiple twinning dislocations that formed the incoherent TB. They also showed that detwinning took place easily for thin twins and the driving force resulted from the twin-twin interactions. These results explained the motion of incoherent TBs consisting of a set of Shockley partial dislocations. But the annihilation of twins with both ends at GBs involved the nucleation of multiple twinning dislocations, which was accompanied by a high kinetic barrier. So other mechanisms may contribute to the shrinkage or growth of thick twins.

Compared to the initial defect-free microstructure, the typical structure of the deformed sample is populated with a high density of dislocations (Figure 2.16b). TBs with numerous dislocations were not as clear and straight as the original coherent TBs, while stepped (indicated by the white arrows) or even curved TBs (see the white rectangle) were frequently seen. High resolution TEM (HRTEM) observation showed that a large number of Shockley partial dislocations were deposited along TBs as shown in Figure 2.16c. From the comparison of TEM observations before and after deformation it was proposed that most of the plastic strain was carried by the dislocations piling up along the TBs, which led to dislocations accumulation at the TBs (Figure 2.16d). The steps observed in the deformed TBs indicated that dislocations also transmitted across initially coherent TBs (Dao et al., 2006).

2.5.1.2 Columnar nanotwinned materials

Hodge et al. (Hodge et al., 2008, Hodge et al., 2011, Furnish et al., 2013) observed shear band formation during the tensile deformation of pure Cu samples containing aligned nanotwins. Samples tested at 77 K showed higher ductility and strength because deformation was much more localized at room temperature than at 77 K. More shear bands were observed at 77 K, so more deformation was carried compared to the room temperature tests. Parallel depressions were observed before fracture (Hodge et al., 2012), which were also indicated after tension-tension cycling tests (Hodge et al., 2012, Shute et al., 2011). The plastic deformation of columnar nanotwinned Cu was identified to be anisotropic (Ye et al., 2012, Zhu and Gao, 2012, You et al., 2013). Figure 2.17 shows by changing the loading orientation that the deformation mechanism can transmit among three dislocation processes,

threading dislocation slip between neighbouring TBs, dislocation transmission across the TBs, and TB migration induced detwinning (You et al., 2013).

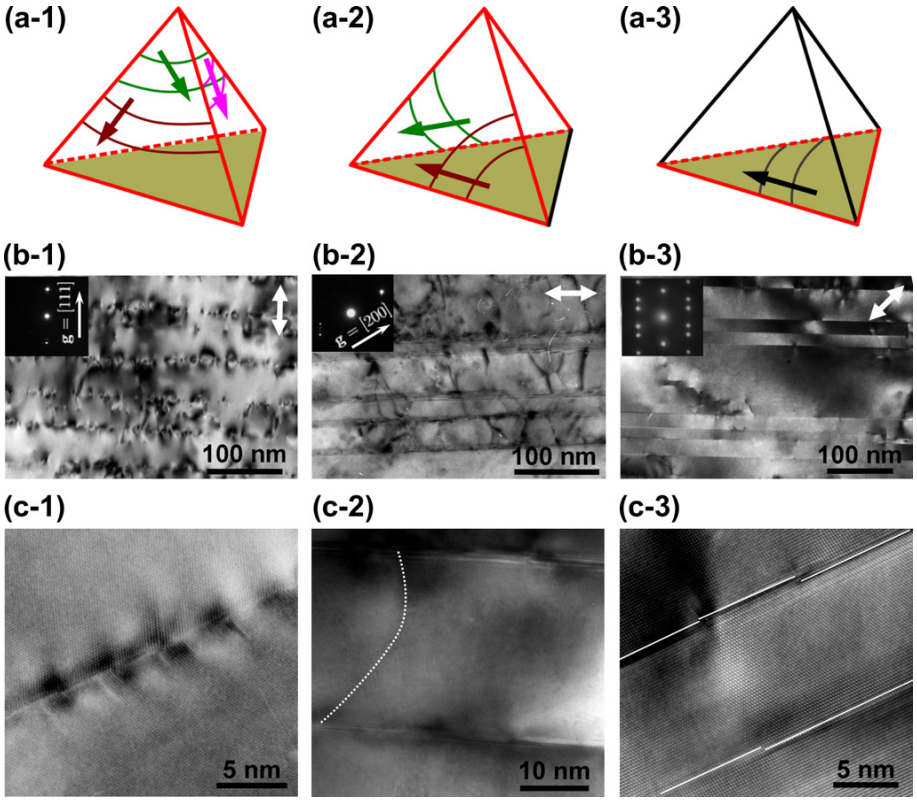

Figure 2.17 Deformation processes in columnar nanotwinned Cu with compression axis oriented at 90°, 0° and 45° with respect to TBs. (a) The active slip systems, (b) TEM (arrows indicate loading direction) and (c) HRTEM observations of the microstructure of samples in different loading directions: (a-1, b-1, c-1) 90° compression; (a-2, b-2, c-2) 0° compression; (a-3, b-3, c-3) 45° compression (You et al., 2013).

2.5.1.3 Nanotwinned nanopillars

Jang et al. (Jang et al., 2012) carried out in situ SEM tensile test to investigate the influence of TB spacing and twin orientation on the mechanical response of nanotwinned nanopillars. A brittle-to-ductile transition was observed in orthogonal samples as the twin spacing decreased to below 4 nm. The detailed deformation mechanism was revealed by TEM analysis. When the TB was perpendicular to the loading direction as shown in Figure 2.18a, necking was observed while all other regions were unaffected. Intense dislocation activities occured as indicated by arrows, but the twin thickness did not change even inside the neck regions. On the other hand, in samples with slanted TBs detwinning became the dominant

deformation mechanism. Significant growth of twin lamellae was observed as shown in Figure 2.18b.

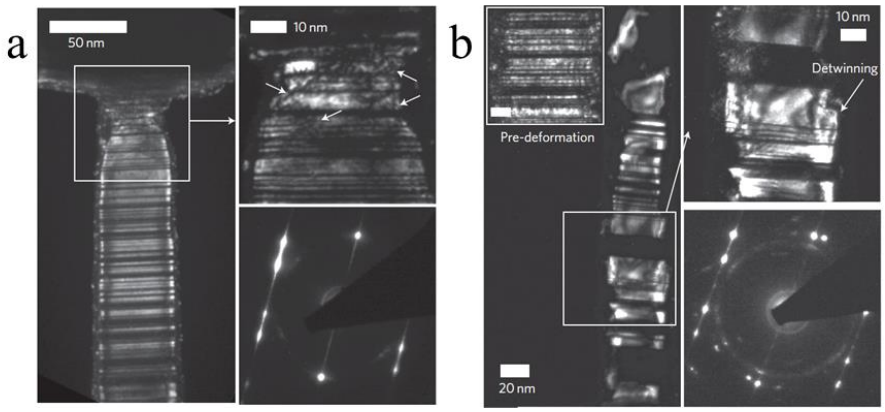

Figure 2.18 Deformation mechanism of nanotwinned nanopillars. (a) Neck formation and dislocation activities in orthogonal samples. (b) Detwinning in slanted samples (Jang et al., 2012).

2.5.2 Constitutive modelling

The mechanistic modelling of dislocation mechanics and crystal plasticity facilitates a direct connection between macroscopic deformation behaviour and the underlying dislocation mechanisms (Zhu et al., 2011a, Gu et al., 2011, Dao et al., 2006, Dao et al., 2007, Wei et al., 2014). These modelling studies have incorporated the unique role of coherent TBs in the deformation mechanisms of nanotwinned metals.

Motivated by the TEM and MD observations, Dao et al. (Dao et al., 2006, Dao et al., 2007) proposed a TB affected zone model. Each TB was considered as a special GB with a high aspect ratio in terms of the grain shape and mirrored slip geometries between adjacent twin lamellae. This model correctly predicted the experimentally observed trends on flow strength, rate sensitivity of plastic flow and ductility, and matched well with the quantitative details of plastic deformation. Zhu et al. (Zhu et al., 2011a) developed a dislocation density-based physical model generalizing the mechanism-based strain gradient plasticity for the constitutive description of nanotwinned metals. This model was capable of describing the variations in strength, ductility and work hardening rate of nanotwinned metals with different twin spacing.

2.5.3 Atomistic simulations

Among different modelling methods, MD simulations are able to obtain an atomic-level understanding of the dislocation-TB interactions (Jin et al., 2006, Zhu et al., 2007, Jin et al., 2008, Shabib and Miller, 2009, Wu et al., 2009, Chassagne et al., 2011). Recently, massively parallel MD simulations have been performed to investigate the strengthening and softening in polycrystalline nanotwinned metals with three-dimensional microstructures and size scales comparable to experiments (Li et al., 2010b, Stukowski et al., 2010, Wu et al., 2011, You et al., 2013, Morris Wang et al., 2013, Zhou et al., 2014, Tucker and Foiles, 2015).

2.5.3.1 Three-dimensional nanotwinned materials

Frøseth et al. (Frøseth et al., 2004a, Frøseth et al., 2004c, Frøseth et al., 2005) conducted the first simulation in nanocrystalline Al with and without growth TBs. They found that the presence of growth twins facilitated plastic deformation via TB migration. In twin-free samples, the motion of full dislocations was the dominant deformation mechanism. Generalised planar fault energy curves were used to discuss the results. Stukowski et al. (Stukowski et al., 2010) studied the effect of twins on the deformation behaviour of nanocrystalline Cu and Pd. While Cu showed hardening due to dislocation-TB interactions, the presence of twins softened nanocrystalline Pd. A statistical analysis of the dislocation evolution confirmed that TBs were effective sources for twinning dislocations. The low energy barrier for twin migration in Pd promoted the generation of twinning partials, which resulted in the observed softening.

Li et al. (Li et al., 2010b) performed MD simulations on full three-dimensional polycrystals containing nanoscale twins. The stress-strain behaviour showed that the average flow stress first increased with decreasing twin spacing, reaching a maximum, and then decreased with further refining the twin size, which agreed well with the maximum strength observed in experiments (Lu et al., 2009b). The dislocation nucleation was found to govern the softening phenomenon when the twin thickness fell below a critical value, at which a transition in deformation mechanism occurred. Above this critical spacing, dislocation pile-up and cutting through twin planes strengthened the materials following the classical Hall–Petch relation as

shown in Figure 2.19a. While below the critical twin thickness, TB migration resulting from nucleation and motion of partial dislocations parallel to the twin planes softened the materials as shown in Figure 2.19b. Moreover, a theory which incorporated the kinetics of dislocation nucleation and source density was proposed to explain the strength softening in nanotwinned metals.

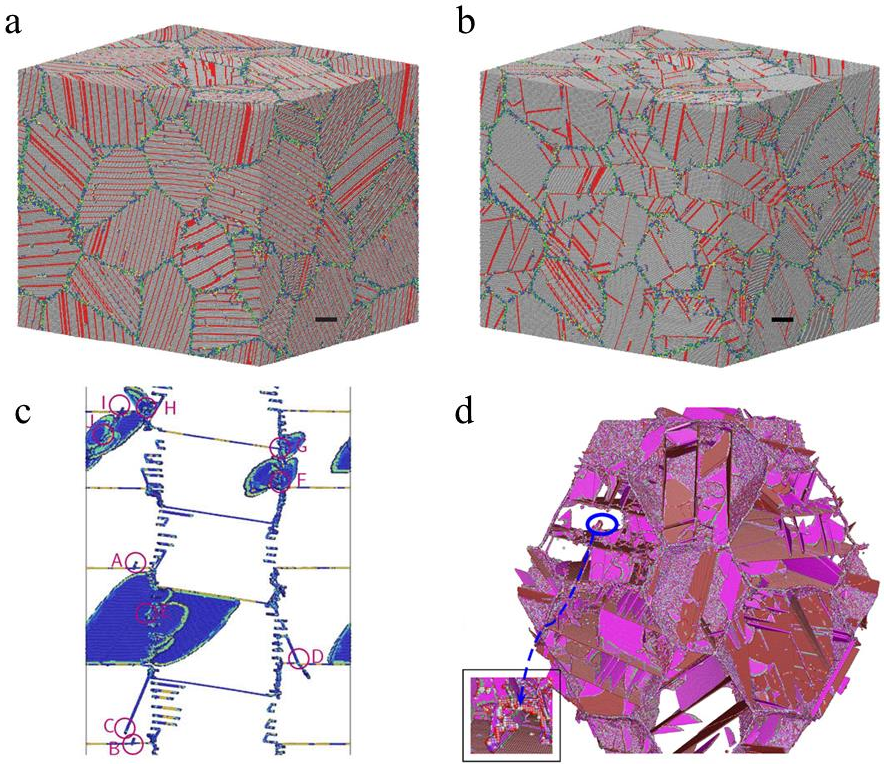

Figure 2.19 Atomic configurations of three-dimensional nanotwinned samples. (a-b) Deformation patterns in nanotwinned Cu with a grain size of 20nm and twin spacing of 1.25nm (a) and 6.25nm (b) (Li et al., 2010b). (c) Dislocation structure and their interactions with TBs (Wu et al., 2009). (d) Dislocation structure in nanotwinned polycrystalline Cu (Wu et al., 2011).

Wu et al. (Wu et al., 2009, Wu et al., 2011) observed two dislocation-twin interaction mechanisms to explain the ultrahigh strength and ductility by tracing the dislocation evolution (Figure 2.19c). First, the interaction of a 60° dislocation with a TB led to the formation of a Lomer dislocation which later dissociated into Shockley, stair-rod and Frank partial dislocations. Second, the interaction of a 30° Shockley partial dislocation with a TB generated three new Shockley partials during twin-mediated slip transfer. The high density of Shockley partial dislocations contributed to the ultrahigh ductility, while the sessile stair-rod and Frank partial dislocations resulted

in the ultrahigh strength. Furthermore, the simulations of polycrystalline nanotwinned Cu (Figure 2.19d) showed that the total plastic strain was carried mainly by three types of dislocations, namely pure screw dislocations, 60° dislocations and twinning dislocations. Both screw dislocations and 60° dislocations could cut across the TB. The transmission of screw dislocations left the TB intact, while 60° dislocation cutting through TBs resulted in the frequent formation of Lomer dislocations. TB migration contributed a minor part to the deformation, as the nucleation and propagation of twinning dislocations was not the dominant deformation mechanism for thick twins. The motion of various types of dislocations within individual grains satisfied the general plastic strain.

2.5.3.2 Columnar nanotwinned materials

Li et al. (You et al., 2013, Zhou et al., 2014) studied the plastic anisotropy in columnar structured Cu containing preferentially oriented nanoscale twins. The slip systems were no longer equivalent due to the presence of the TBs. Depending on the orientations of the slip plane and the slip direction relative to the twin plane, the slip systems was classified into three categories: hard mode I in which both the slip plane and the slip direction were inclined to TBs, represented by the dislocation in Figure 2.17a-1; hard mode II in which the slip plane was inclined to TBs, but the slip direction was parallel to TBs, represented by the dislocation in Figure 2.17a-2; and soft mode in which both the slip plane and Burgers vector were parallel to TBs, represented by the dislocation in Figure 2.17a-3. The dislocation motion was restricted by the TBs in both hard modes I and II so the mechanical strength was enhanced. The dislocation mean free path was determined by the twin spacing. But the dislocation motion was constricted by the GBs rather than the parallel TBs in the soft mode so the materials became weaker. The dislocation mean free path was determined by the relatively large grain size.

Each slip mode was activated by controlling the loading orientation (You et al., 2013, Zhu and Gao, 2012). When the loading direction was perpendicular to the TBs, hard mode I dominated the plastic deformation as shown in Figure 2.20a. The dislocations nucleated from the columnar boundaries and propagated on slip planes inclined with the growth twins until being blocked by the TBs. As the strain increased, these

dislocations cut through the TB. TBs were strong barriers to dislocation motion and the interactions between dislocations and TBs were the dominant deformation mechanism. When the compression was parallel to the TBs, dislocation motions on inclined slip planes confined by neighbouring TB became the dominant deformation mechanism as shown in Figure 2.20b. The threading dislocations moved through the twin lamellae and were stopped near GBs at the opposite side of the twin lamella. But other simulations (Morris Wang et al., 2013) revealed that the threading dislocations transmitted easily through the perfect TBs without blockage, as shown in Figure 2.20d. For 45° compression, when the maximum shear stress was oriented parallel to the twin plane, the soft mode dominated the deformation. Shockley partial dislocations nucleated predominantly from the intersections between TBs and GBs and glided on the twin planes as shown in Figure 2.20c. The motions of these partial dislocations led to TB migration, which changed the twin thickness. Moreover, Shockley partials also nucleated from the GBs and glided on slip planes parallel to the TB, leaving stacking faults behind.

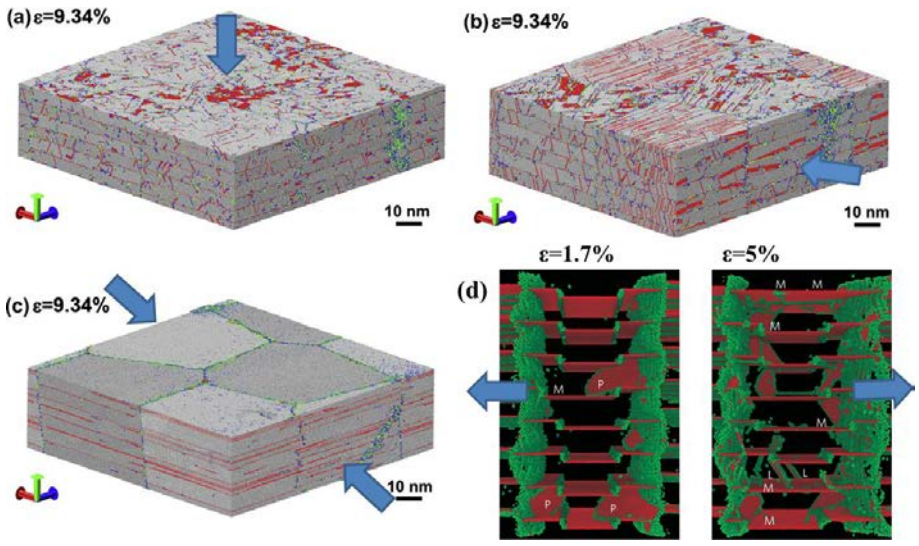

Figure 2.20 Deformation structure of nanotwinned Cu. (a-c) Atomic configurations of the samples under different loading modes: (a) 90° compression, (b) 0° compression, (c) 45° compression (You et al., 2013). (d) Deformation mechanisms in a columnar grain at different stages of deformation (Morris Wang et al., 2013).

2.5.3.3 Nanotwinned nanopillars

The role of nanoscale twins on the mechanical response of nanopillars has been widely investigated. Sansoz et al. (Afanasyev and Sansoz, 2007, Deng and Sansoz,

2009a, Deng and Sansoz, 2009c, Deng and Sansoz, 2009b) have shown that several factors, such as the twin spacing, the ratio of diameter over twin spacing, the stacking fault energy and the surface morphology were important to obtain the strengthening effect in nanotwinned metallic nanowires. Pronounced strain-hardening effects due to the blockage of dislocations by TBs was seen in Au nanowires as the twin spacing decreased (Afanasyev and Sansoz, 2007, Deng and Sansoz, 2009a). The surface morphology like {111} zigzag facets dramatically improved the strength of nanotwinned Au nanowires, where Lomer dislocations (001)[110] were nucleated instead of common partial dislocations in FCC metals (Deng and Sansoz, 2009c).

Li et al. (Jang et al., 2012) investigated the deformation mechanisms in nanotwinned Cu pillars. Figure 2.21a shows that in a nanopillar with orthogonal TBs, multiple dislocations nucleated at TB–surface intersections and glided on slip planes inclined to the TBs. These dislocations reacted with TBs, leaving multiple dislocations on the TBs. Necking and shear bands formation took place during later stages of deformation. The shear bands arisen from the penetration of dislocations through TBs and within the regions some of the original TBs were destroyed. The formation of shear bands indicated shear strain localization, a common deformation mode in ductile materials. The shear localization and specimen necking was also observed in nanotwinned Au (Wang et al., 2013), which were accommodated by twin migration as shown in Figure 2.21c.

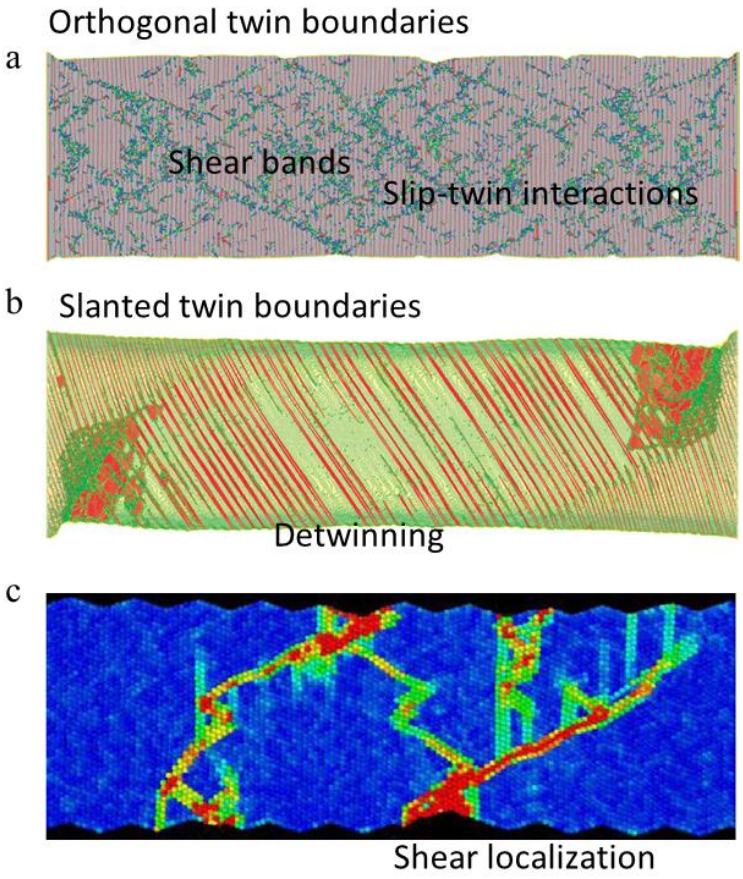

Figure 2.21 The atomic configurations of the nanotwinned samples after deformation. (a) Nanotwinned Cu with orthogonal TBs. (b) Nanotwinned Cu with slanted TBs (Jang et al., 2012). (c) Nanotwinned Au (Wang et al., 2013).

Figure 2.21b presents the atomic structures in a pillar with slanted TBs. Motion of twinning dislocations on TBs led to TB migration and some twin lamellae disappeared. Multiple surface steps were formed at the free surface where the dislocations escaped. These surface steps served as sources for new dislocations to facilitate further plastic deformation. Finally, the middle part of the sample became twin-free single crystal. The number of hexagonal closed packed (hcp) atoms decreased during the deformation, which provided another evidence for the detwinning process.

2.6 Interactions between dislocations and TBs

The slip-twin interactions play an important role in the deformation of nanotwinned materials. Such interactions become increasingly frequent and thus more important due to the high density of TBs. Mahajan and Chin (Mahajan and Chin, 1973b) examined the crystallographic characteristics of twin-slip, twin-twin and slip-twin interactions in single crystals by optical microscopy. The dislocation reactions were proposed to explain the evolution of the dislocation structures. Atomistic investigations of the interaction between dislocations and CTBs were first performed in simple bicrystal geometries and later in full three-dimensional nanotwinned models. In this section, recent investigation on the interactions between dislocations and TBs is reviewed.

2.6.1 Interactions between screw dislocations and TBs

The screw dislocation has a burgers vector parallel to the TB. The transmission of screw dislocation across the TBs is a special case of slip transfer, as it may cross slip to the twinned grain without leaving a step on the interface. Chen et al. (Chen et al., 2007) clarified the interaction force and energy to impinge a screw dislocation upon a TB based on an atomistic path approach. Jin et al. (Jin et al., 2006) studied the interaction between screw dislocations and coherent TBs by MD simulations for Al, Cu and Ni. Depending on the material and the applied strain, a screw dislocation approaching the coherent TB either penetrated across the TB into the twin or dissociated within the twin plane. Chassagne et al. (Chassagne et al., 2011) determined the influence of material and choice of interatomic potential on this interaction in a range of metals. The reaction mechanisms including absorption by the TB or transmission into the twinned region and reaction stress depended strongly on the potential. Moreover, there was a threshold shear stress for transmission of a crew dislocation, estimated to be between 300 and 400 MPa (Jin et al., 2006, Zhu et al., 2007, Chassagne et al., 2011), below which the dislocation was absorbed by the TB and above which the dislocation was transmitted into the twinned region.

To overcome the time scale limitation of MD, the atomistic reaction pathway was adopted to investigate the effects of temperature and strain rate on plastic

deformation on time scale available for real experiments (Zhu et al., 2007). Two competing pathways were identified when the applied shear stress was below the threshold stress as illustrated in Figure 2.22. The first path was a two-step process involving the absorption (Figure 2.22a) of the screw dislocation by the TB, followed by desorption (Figure 2.22b). Both absorption and desorption occurred through the Friedel-Escaig cross-slip mechanism (Püschl, 2002), where the two partials were first constricted to a full screw dislocation, and then spread into the twin plane (absorption) or to the twin (desorption). In contrast, the second pathway (Figure 2.22c) involved direct transmission of the screw dislocation by the Fleischer cross-slip model (Fleischer, 1959). The leading partial first penetrated into the twin, which temporarily left a sessile stair-rod dislocation on the TB. Then the trailing partial combined with the sessile dislocation to emit a dislocation in the twin. Due to the special geometry, there was no residual dislocation left on the TB after the transmission. Thus, the TB acted as a sink or source of dislocations, as well as a barrier against direct transmission. The minimum energy paths and associated activation energy barriers was determined for the absorption, desorption and transmission processes at the TB to understand the temperature effect on slip transfer. The calculated activation volume was 24 - 44 b^3 comparable with the values measured in experiments (Lu et al., 2009c), which revealed the slip transfer mediated by TB were the rate-controlling mechanisms in nanotwinned metals.

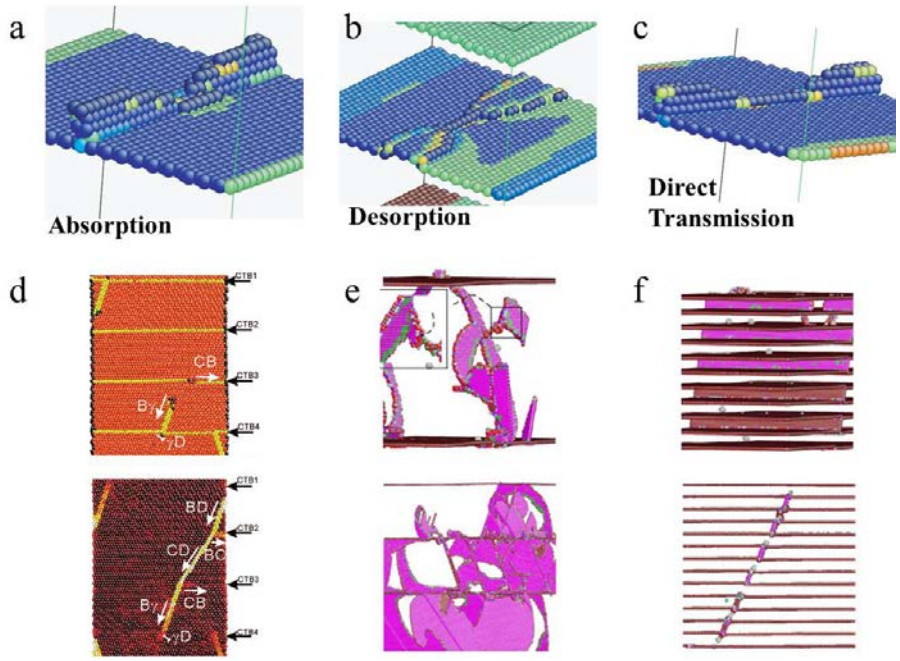

Figure 2.22 Atomistic simulations of interactions between dislocation and TB. (a-c) Atomic configurations of absorption (a), desorption (b) and direct transmission (c) of screw dislocations (Zhu et al., 2007) (d) The transmission of non-screw dislocations (Deng and Sansoz, 2009a). (e) Slip-twin interactions at large twin spacing. (f) Slip-twin interaction at small twin spacing (Wu et al., 2011).

Zhang et al. (Zheng et al., 2009) also observed the transmission of screw dislocation via the Fleischer cross-slip model and the absorption by Fridel-Escaig cross-slip mechanism in full three-dimensional nanotwinned Cu models. The transmission of dislocation dominated in the deformation of nanotwinned Cu when the loading direction was parallel to the TB (Wu et al., 2009). The consideration of defective GBs did not change the deformation mechanisms (Morris Wang et al., 2013).

2.6.2 Interactions between non-screw dislocation and TBs

The interaction between other slips and TBs is more complicated. The Burgers vector of the incoming dislocation has a component perpendicular to the twin plane, which means that a step is produced on the twin interface after the slip transfer. The TBs restrict dislocation motion and gradually lose their coherency during impingements with dislocations, which enhances the strength and ductility of nanotwinned metals (Lu et al., 2009a).

Wang and Huang (Wang and Huang, 2006) reported a novel deformation mechanism in bicrystal Cu nanowires. Under mechanical loading, a dissociated dislocation on a {111} plane penetrated across the TB, and a dislocation with Burgers vector of 1/2<110> nucleated and glided on a {100} plane, instead of conventional {111} planes. The dislocation glide was primarily facilitated by the matching of Burgers vector along the normal direction of the TB. Jin et al. (Jin et al., 2008) considered interactions between 60° dislocation and TB in Cu, Ni and Al. Depending on the material and the applied strain, dislocations interacted with the boundary in different ways. The incoming dislocation can dissociate into different partial dislocations cutting into the twin or propagating along the TB. A sessile dislocation lock may be generated on the twin plane if incomplete slip transfer occurred. The details of the interaction were controlled by the energy barriers from generalised stacking fault energy curves (Rice, 1992, Zimmerman et al., 2000, Van Swygenhoven et al., 2004).

Sansoz and his colleagues (Afanasyev and Sansoz, 2007, Deng and Sansoz, 2009a, Deng and Sansoz, 2009b) carried out a series of atomistic simulations of nanotwinned metallic nanowires, with TBs normal to the tensile direction. They observed that the slip-twin interactions led to the formation of Lomer dislocations (Figure 2.22d), which played a key role in the strengthening mechanism of twinned nanopillars. The dislocation reactions at the TB were given using Thompson's notation. Sangid et al. (Ezaz et al., 2011) explored the energetics of slip–coherent TB interactions under tensile deformation.

The Lomer dislocations were frequently observed to form after the cutting through of 60° dislocations. Wu et al. (Wu et al., 2011, Wu et al., 2009) examined the effect of twin spacing on this Lomer dislocation mechanism over a wide range of twin spacing. A transition in the deformation mechanism at a critical twin spacing was revealed. Figure 2.22e shows that at large twin spacing, cross-slip and dissociation of the Lomer dislocations created a complicated three-dimensional dislocation structure containing both mobile and sessile dislocations on various slip planes (Wu et al., 2011), which restricted dislocation motion and thus enhanced the strength. Figure 2.22f shows that at small twin spacing below the critical size, cross-slip did not occur. The dislocation propagated alternatively on {111} and $\{001\}^{T}$ planes in the matrix

and twin, leaving a Shockley partial dislocation on the TB and an extrinsic stacking fault in the matrix. Steps were formed on the TBs, which migrated and served as dislocation nucleation sites, thus softening the material (Wu et al., 2011).

2.6.3 Plausible dislocation-TB interactions

Dislocation reactions at TBs have been observed both in experiments and by MD simulations. Zhu et al. (Zhu et al., 2011b, Zhu et al., 2012) systematically described plausible dislocation reactions at TBs. Depending on the characteristics of the dislocations and the driving force, dislocations impinging on the TBs can cross-slip onto the twin plane to cause twin expansion or shrinkage, form sessile dislocations at the TB, or transmit across the TB. Table 2.1 summarised the plausible dislocation reactions and the energy barriers associated with the reactions. It was suggested that most of the dislocation–twin reactions may not occur in coarse-grained fcc metals and alloys because high applied stresses are required to overcome the energy barriers.

Table 2.1 Summary of dislocation-twin interactions and their energy barriers (Zhu et al., 2011b, Zhu et al., 2012).

Reaction description	**Equations in the double Thompson tetrahedron**	**Isotropic energy barriers**
30° partial, **Bα** Cross-slip onto the TB Stair-rod dislocation dissociation Transmit across the TB	 **Bα→Bδ+δα** **δα→δB+Bα** **Bα→Bα'+α'α**	 *E*+2.0*F* 3.5*E*+5.5*F* 2.7*E*+4.1*F*
90° partial, **Dα** Transmit across the TB	 **Dα→δα+δα'+α'D'** **Dα→δα+δβ'+β'D'** **Dα→δα+δγ'+γ'D'** **Dα→2/3Aδ+α'D'*** **Dα→1/3δB+β'D'*** **Dα→1/3δC+γ'D'***	 2.0*E*+4.0*F* 2.0*E*+4.0*F* 2.0*E*+4.0*F* 0.6*E*+1.4*F* 0.1*E*+0.2*F* 0.1*E*+0.2*F*
Cross-slip of perfect screw dislocation, **BC** absorption Cross-slip onto TB Transmit across TB 30° leading partial transmit across TB first and the trailing partial transmit cross TB second	 **Bα+αC→BC*** **BC→Bδ+δC*** **BC→Bα'+α'C*** **αC+α'α→α'C***	
Perfect 60° dislocation Cross-slip onto TB Transmit across TB	 **BD→BC+CD** **BD→2Bδ+D'B** **BD→δC+D'A** **BD→δA+D'C**	 6.0*E*+7.2*F* 4.5*E*+7.5*F* 3.0*E*+3.9*F* 3.0*E*+3.9*F*
30° leading partial cross-slip onto TB and trailing 90° partial transmit across TB	 **δα+αD→δD** **D'δ→D'α'+α'δ** **δα+αD→D'α'+α'δ**	 2.0*E*-0.3*F* 0
30° leading partial transmit across TB first and the 90° trailing partial transmit cross TB second	**αD+α'α→2α'δ+D'α'***	4.0*E*
90° leading partial and 30° trailing partial transmit across TB sequentially	**Bα+αδ+α'δ→Bα'+2α'δ** **Bα+αδ+β'δ→Bα'+α'δ+β'δ** **Bα+αδ+γ'δ→Bα'+α'δ+γ'δ**	3.4*E*+2.7*F* 2.8*E*+3.7*F* 2.8*E*+3.7*F*

$E = \frac{Ga^2}{72\pi(1-\nu)} ln\frac{\sqrt{2}d}{a}$, $F = \frac{Ga^2}{72\pi(1-\nu)}$, where G is the shear modulus, ν is the Poisson's ratio, d is the grain size, a is the lattice constant.

***** Equations are revised from Zhu's work.

3 METHODOLOGY

3.1 Molecular dynamics simulations

MD simulates the motion of atoms within a many-body system. The basic numerical technique of MD involves solving the Newton's equation of motion:

$$m_i \frac{d^2 r_i(t)}{dt^2} = f_i \tag{3.1}$$

where *m* and *r* are the mass and position of the atom *i*. The fore *f* through which the particles interact with each other derives from the interaction potentials:

$$f_i = -\frac{\partial}{\partial r_i} U(r_1, \ldots, r_N) \tag{3.2}$$

All the MD simulations in this thesis were performed using the parallel molecular dynamics package LAMMPS (Plimpton, 1995). To start the simulation, the initial positions and velocities of the atoms in the system should be assigned. The microstructure was built based on experimental observation and atoms were put on the lattice sites with a crystallographic orientation. The velocities were randomly chosen from a Gaussian distribution with a mean of 0.0 and a sigma scaled to produce the required temperature:

$$\frac{\dim}{2} N k_B T = \frac{1}{2} \sum_{i=1}^{N} m_i \dot{r}(t)_i^2 \tag{3.3}$$

Verlet algorithm was used to solve the equation of motion. Through Tayler expansion of the coordinate of an particle around time $t + \Delta t$ and $t - \Delta t$, the particle coordinate at time $t + \Delta t$ can be calculated by:

$$r_i(t + \Delta t) = 2r_i(t) - r_i(t - \Delta t) + \frac{f_i}{m_i} \Delta t^2 + o(\Delta t^4) \tag{3.4}$$

The velocity of the particle can be derived from

$$v_i(t) = \frac{r_i(t + \Delta t) - r_i(t - \Delta t)}{2\Delta t} + o(\Delta t^2) \tag{3.5}$$

Through the solution of Newton's equation of motion, the evolution of the system was obtained, which includes particle positions, velocities, kinetic and potential energies and so on for each time step. All further properties such as the stress, temperature can be determined from these information.

3.1.1 Interatomic potentials

The validity of MD simulations relies on the accuracy of the interatomic potential. In the early simulations, pair potentials were used for computational simplicity, the total energy is described as a sum of pairwise potentials *V*:

$$E = \frac{1}{2}\sum_{ij} V_{ij}(R_{ij}) \tag{3.6}$$

where *i* and *j* are indices referring to the atoms, R_{ij} is the distance between atom *i* and *j*. The pair potentials are simple and can be used to model relatively large systems. But they have limitations in quantitatively reproducing the properties of crystalline materials that are required to describe dislocation processes (Sinnott and Brenner, 2012). In pare potentials, the elastic constants are forced to obey the Cauchy relations and the generated surface and vacancy formation energies are inaccurate. The total energy cannot be expressed in terms of pair bonds alone, as in general the bonds are not independent of each other (Daw et al., 1993). Many-body potentials were introduced in 1980s, which do not have the limitations in the description of crystalline solids and the computational cost is slightly higher than pair potentials (Plimpton and Thompson, 2012). Several models were proposed almost simultaneously from different groups: embedded-atom method (EAM) potentials (Daw and Baskes, 1984), Finnis-Sinclair potentials (Finnis and Sinclair, 1984) and effective medium theory potentials (Jacobsen et al., 1987). These potentials have similar mathematical forms despite different physical deviations. In particular, the EAM potential combines the energy of embedding an atom into the electron density produced by its neighbouring atoms and the pairwise interaction (Daw and Baskes, 1983, Daw and Baskes, 1984). The energy can be expressed as:

$$E = \sum_i G\left(\sum_j \rho_{ij}(R_{ij})\right) + \frac{1}{2}\sum_{ij} V_{ij}(R_{ij}) \tag{3.7}$$

where G is the embedding energy, ρ is the electron density. The embedded energy is defined as the interaction of the atom with the electron gas.

In this thesis, the atomic interaction for Cu was modelled by the EAM potential by Mishin et al. (Mishin et al., 2001). This potential was constructed based on both experimental data and *ab initio* calculations and accurately reproduces many material properties, including lattice properties, point and extended defects, various structural energies and transformation paths. The intrinsic stacking fault and twinning energies were calculated to be 44.4 mJ/m^2 and 22.2 mJ/m^2, which agree well with experimental data. The stacking fault energy determines the width of dislocation dissociation in the fcc structured materials, the accuracy of this value is important for atomistic simulations of dislocation and fracture processes.

The atomic interaction for Fe was modelled by the EAM potential by Mendelev et al. (Mendelev et al., 2003). This potential was developed using perfect crystal data, crystal defect data and first principles forces to obtain the proper pairwise part behaviour at small atomic separations. It accurately reproduces many material properties, including lattice parameters, elastic constants, point defect energies, bcc–fcc transformation energy, liquid density, liquid structure factor, melting temperature and other properties. This potential has been widely used in simulations of defects in bcc Fe and for the solid–liquid interface properties.

3.1.2 Ensembles

An ensemble is a probability distribution of the state of the system. The ensemble is used to derive the properties of the thermodynamic systems from laws of classical mechanics. Three important thermodynamics ensembles are used in MD simulation. In conventional MD simulations, the energy and volume are fixed so the statistical ensemble is the microcanonical ensemble or NVE ensemble. In this ensemble, the number of the particles, volume and energy of the system are conserved. The system is thermally isolated. But in certain cases constant temperature or pressure are required so the equations of motion are modified to produce a particular statistical

ensemble. The canonical ensemble or NVT ensemble corresponds to the constant temperature experiment, where the number of the particles, volume and temperature are conserved. The temperature of the system is controlled by temperature rescaling, the Nose-Hoover thermostat, Berendsen thermostat and Langevin thermostat. If constant pressure is imposed as well, the isothermal-isobaric ensemble or NPT ensemble is the relevant one, where the number of the particles, pressure and temperature are conserved. In addition to a thermostat, a barostat is needed. The available techniques to control the pressure include Nose-Hoover barostat and Berendsen barostat. The NPT ensemble which includes a Nose-Hoover thermostat and barostat was used in the present simulations.

3.1.3 Loading methods

Two modes of deformation have been used in the simulation of plastic deformation: constant strain rate and constant stress simulations. In constant stress simulations (Yamakov et al., 2001, Yamakov et al., 2002c, Frøseth et al., 2004a), a constant stress was applied to the simulation cell and the structure evolution over time was followed. This approach produced strain versus time curve, like creep experiments. The plastic flow initiated when the applied stress exceeded a critical stress. When the simulation time was extended to nanoseconds, the strain rate can be greatly reduced (Van Swygenhoven and Derlet, 2008). Moreover, increasing the stress above the critical stress may lead to a significant increase in strain rate, which results in the destruction of the sample. The strain rate cannot be properly controlled under the constant stress approach. Constant strain rate simulations can produce stress–strain curves.

In the present study, the constant strain rate test was adopted. To equilibrate GBs in the polycrystalline samples, the samples were first minimized via the conjugate gradient method and then equilibrated at 300 K for 100 ps, using a Nose-Hoover thermostat and barostat (NPT ensemble). The system was then heated and annealed at 600K for another 100 ps before being cooled to room temperature (300K) to perform the simulation. Periodic boundary conditions were imposed in all three directions to model bulk materials. A uniaxial tensile strain was applied by continuously scaling the atomic coordinates and box size along the length direction

at a constant temperature of 300 K and a constant strain rate of 5×10^8 s^{-1}, while along the other two directions, NPT ensemble kept the stress around zero so the system can shrink or expand freely.

3.1.4 Virial stress

The instantaneous stress tensor of each atom can be calculated by the virial stress:

$$\sigma_i^{\mu\nu} = -\frac{1}{\Omega_i}\left(\frac{1}{2} m_i \dot{r}_i^{\mu} \dot{r}_i^{\nu} + \frac{1}{2}\sum_j F^{\mu}(r_{ij}) r_{ij}^{\nu}\right) \tag{3.8}$$

where Ω is the volume of the particle. The first term is the kinetic energy contribution, and the second term includes the pair, bond, angle, dihedral and other interactions. The volume of individual atom is not easy to compute in the deformed samples. A possible way to estimate the volume is to calculate the Voronoi tessellation of the atom. During the simulations, the computed stress per atom is in units of pressure×volume. The values of atomic stress are summed for all atoms in the system and the sum is divided by the volume of the system to obtain the total stress of the system.

3.1.5 Limitations of molecular dynamics simulations

The first limitation is the relatively small model systems consisting of typically millions of atoms. In order to reduce the number of atoms, periodic boundary conditions are imposed on the sample. The second limitation is the reliability of the interatomic potentials. The empirical interatomic force descriptions used in most MD simulations are computationally efficient, but they cannot fully capture the many-body nature of electronic bonding, particularly in the vicinity of defects. The third limitation is the relatively short time duration in the simulation of plastic deformation. As a result, such simulations always involve extremely high strain rates, i.e., many orders of magnitude higher than in experiments, which are accompanied by rather high stresses.

3.2 Visualization

The simulated configurations were visualized using the scientific software package Open Visualization Tool (OVITO) (Stukowski, 2010). This three-dimensional visualization software has been widely used to post-process atomistic data obtained from MD simulations. The input data is processed in a non-destructive way. The parameters, the order of the processing steps or the input data can be changed whenever needed and OVITO can immediately re-evaluate the procedure and update the visualization display in real time.

Several visualization methods have been developed which provide detailed characterisation of the atomic configurations. An arbitrary number of physical and structural properties can be calculated and assigned to individual atoms during the simulation. Using these quantities, a classification scheme can be developed to visualise each component of the atomic structure, including perfect atoms, dislocation cores, stacking faults, TBs, GBs, etc. The main visualization methods that are currently used in the study of mechanical behaviour of nanocrystalline materials are summarised in this section, followed by the visualization procedure used in the present study.

3.2.1 Common neighbour analysis

The common neighbour analysis (CNA) method is widely used to characterise the crystalline structure in atomistic simulation of fcc, hcp and bcc crystals. It can distinguish crystalline defects from perfect lattice. Five kinds of CNA patterns can be recognized in LAMMPS: fcc = 1, hcp = 2, bcc = 3, icosahedral = 4, unknown=5. The CNA pattern is sensitive to the cut-off radius. The cut-off distance should enclose the appropriate nearest neighbours: 12 atoms for perfect fcc crystals and 14 for bcc materials. The cut-off distance is given by:

$$r_c^{fcc} = \frac{1}{2}\left(\frac{\sqrt{2}}{2}+1\right)a \approx 0.8536a \tag{3.9}$$

$$r_c^{bcc} = \frac{1}{2}\left(\sqrt{2}+1\right)a \approx 1.207a \tag{3.10}$$

where a is the lattice constant.

3.2.2 Centro-symmetric parameter

The centro-symmetric parameter can be used to characterise whether the atom is part of perfect lattice, or a local defect (dislocations, twinning faults or stacking faults), or at a surface. The parameter is defined as

$$CS = \sum_{i=1}^{N/2} \left| \vec{R}_i + \vec{R}_{i+N/2} \right|^2 \tag{3.11}$$

where the N is the number of nearest neighbours, i indicates individual atom number, R_i and $R_{i+N/2}$ are vectors from the central atom to a particular pair of nearest neighbours. This parameter is only marginally affected by elastic distortions of the crystal, but is sensitive to random thermal displacements. A proper threshold should be chosen to distinguish defect atoms from perfect lattice atoms especially at elevated temperatures.

3.2.3 Coordination number

The coordination number is defined as the number of neighbour atoms that are within the specified cut-off distance from the central atom. The coordination number of atoms belonging to TBs and dislocation cores are the same with atoms with a perfect lattice in bcc materials.

3.2.4 Shear strain

The plastic deformation can be made visible by calculating the atomic strain of each atom. The atomic strain is the difference between the position of an atom after deformation and its initial position in the unstrained state. The *Atomic strain* operator in OVITO performs this calculation by taking the differences between two atomic data files. Since only the relative motion of neighbouring atoms are concerned, rather than the strains caused by the overall macroscopic strain, this macroscopic strain from homogeneous cell deformation were first eliminated before the calculation. The calculated atomic strains can be visualised by colouring each atom according to the shear strain component. If slip or twinning has occurred inside the grains, it will appear as a sharp contrast in the colouring of atoms.

3.2.5 Visualization of fcc structure

To visualize the fcc structure, three types of CNA patterns are used: fcc atoms, hcp atoms and all other atoms. The atoms are indicated by three different colour: grey represents perfect fcc atoms, red stands for hcp atoms (corresponding to stacking faults and TBs), and green indicates defected atoms (corresponding to GBs, dislocation cores, and other defects). When analysing the dislocation structures, perfect fcc atoms that are not involved in the plastic deformation were eliminated for the sake of clarity. This procedure was carried out by deleting atoms with shear strain, calculated by OVITO, of less than 0.15. In this way, the atoms that experience slips and still retain the fcc structure are coloured in grey. In addition, the relative shear strain and displacement of each atom with respect to its original position were used to trace the microstructure evolution during plastic deformation.

3.2.6 Visualization of bcc structure

To visualize the bcc structure, three types of CNA patterns are used: bcc atoms, fcc atoms and all other atoms. The atoms are indicated by four colours: grey represents perfect bcc atoms, dark grey indicates fcc atoms, red stands for atoms of non-bcc structure and with a coordination number of 14 (corresponding to TBs and dislocation cores in bcc materials), and green indicates defected atoms (corresponding to GBs and other defects). When analysing the dislocation structures, perfect bcc atoms that are not involved in the plastic deformation were eliminated. In this way, the atoms that experience slips and still retain the bcc structure are coloured in grey.

3.3 Dislocation analysis

The dislocation extraction algorithm Crystal Analysis (Stukowski and Albe, 2010) were employed to characterize dislocation while post-processing the simulation snapshots. This algorithm extracts the dislocation lines and identifies their Burgers vectors, which enabled a detailed analysis of dislocation reactions to be carried out. Although the shear displacements along three axes (*Burgers vector world* in Crystal

Analysis) were accurately calculated, some local Burgers vector determined from Crystal Analysis did not agree with the crystallographic orientation. These Burgers vectors were revised based on the orientation of individual grains, and occasionally the classical Burgers circuit construction was used to confirm the results. The conservation of Burgers vector was always fulfilled between reacted dislocations.

3.4 Slip systems in nanotwinned fcc materials

The slip systems in fcc materials can be represented with the help of Thompson tetrahedron. This tetrahedron can be formed by joining the atoms in a corner of a unit cell of an fcc lattice as shown in Figure 3.1

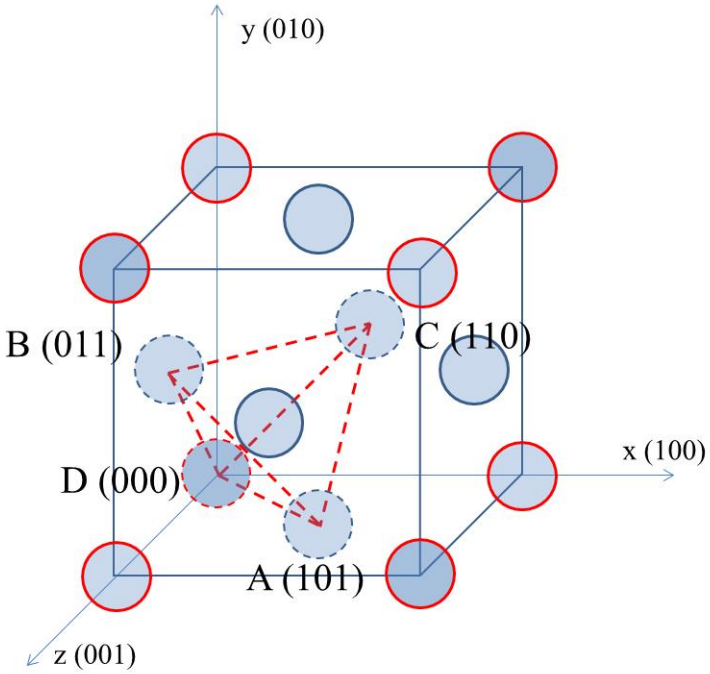

Figure 3.1 Thompson tetrahedron from a unit cell of an fcc lattice.

The slip system in nanotwinned fcc materials can be described by the double Thompson tetrahedron (Hirth and Lothe, 1982, Christian and Mahajan, 1995, Zhu et al., 2012) as shown in Figure 3.2. TB is the ABC(d) slip plane, shared by the twin above it and the matrix below it. The lower Thompson tetrahedron below the twin plane represents matrix slip systems, while the symmetric upper tetrahedron shows

slip systems in the twin. Slip systems in nanotwinned fcc materials are listed in Table 3.1.

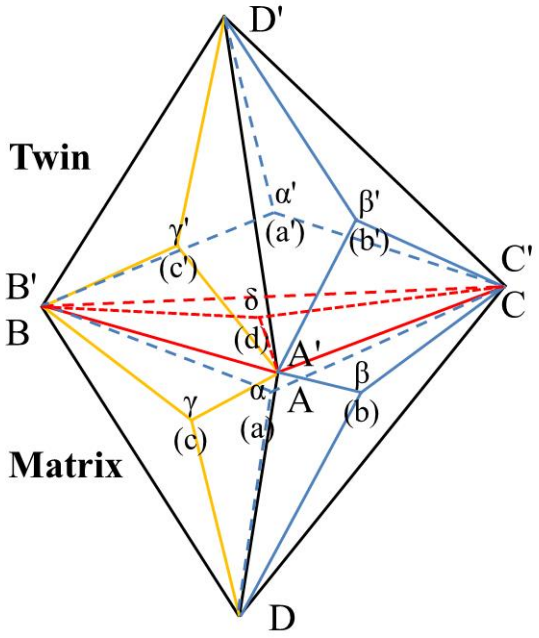

Figure 3.2. Double Thompson tetrahedron represents the slip systems in nanotwinned fcc materials. TB is the ABC(d) slip plane, shared by the twin above it and the matrix below it. Dislocation activities on symmetric slip planes are shown using the same colour.

In this thesis, the dislocation reactions are represented by Burgers vector equations expressed in terms of the double Thompson tetrahedron, and the same equation in vector form is also given (Christian and Mahajan, 1995). Indices relative to the twin lattice are given the superscript T. For simplicity, the energy of a dislocation is considered to be proportional to the square of the Burgers vector of the dislocation. The energy barrier is determined by the difference between the energy of the initial reacting dislocations and the resulting dislocations according to Frank rule (Hirth and Lothe, 1982, Weertman and Weertman, 1992).

Table 3.1 Slip systems in nanotwinned fcc materials.

Slip plane	Vector	Full dislocation	Vector	Partial dislocation	Vector
Matrix slip system					
ABC (d)	Dδ (111)	**AB**	1/2[-110]	**δC**	1/6[11-2]
		BC	1/2[10-1]	**δA**	1/6[1-21]
		AC	1/2[01-1]	**δB**	1/6[-211]
ABD (c)	Cγ (-1-11)	**AB**	1/2[-110]	**γD**	1/6[-1-1-2]
		DA	1/2[101]	**γB**	1/6[-121]
		DB	1/2[011]	**γA**	1/6[2-11]
BCD (a)	Aα (-11-1)	**DC**	1/2[110]	**αB**	1/6[-112]
		BC	1/2[10-1]	**αD**	1/6[-1-2-1]
		DB	1/2[011]	**αC**	1/6[21-1]
ACD (b)	Bβ (1-1-1)	**DC**	1/2[110]	**βA**	1/6[1-12]
		DA	1/2[101]	**βC**	1/6[12-1]
		AC	1/2[01-1]	**βD**	1/6[-2-1-1]
Twin slip system					
ABC (d')	D'δ (-1-1-1)	**AB**	1/2[-110]	**δC**	1/6[11-2]
		BC	1/2[10-1]	**δA**	1/6[1-21]
		AC	1/2[01-1]	**δB**	1/6[-211]
ABD' (c')	Cγ' (-1-15)	**AB**	1/2[-110]	**γ'D'**	1/18[552]
		D'A	1/6[-1-4-1]	**γ'B**	1/18[-72-1]
		D'B	1/6[-4-1-1]	**γ'A**	1/18[2-7-1]
BCD' (a')	Aα' (-15-1)	**D'C**	1/6[-1-1-4]	**α'B**	1/18[-7-12]
		BC	1/2[10-1]	**α'D'**	1/18[525]
		D'B	1/6[-4-1-1]	**α'C**	1/18[2-1-7]
ACD' (b')	Bβ' (5-1-1)	**D'C**	1/6[-1-1-4]	**β'A**	1/18[-1-72]
		D'A	1/6[-1-4-1]	**β'C**	1/18[-12-7]
		AC	1/2[01-1]	**β'D'**	1/18[255]

3.5 Slip systems in nanotwinned bcc materials

The bcc lattice can be indexed by its reciprocal lattice, which is fcc. So the slip systems can be presented by the fcc Thompson tetrahedron (Hirth and Lothe, 1982). The slip directions in the tetrahedron correspond to {110} and {112} slip planes in bcc lattice, while the slip planes in the tetrahedron correspond to <111> bcc slip directions.

The slip system in nanotwinned bcc materials can be described by the double Thompson tetrahedron as shown in Figure 3.3. TB is the (Dγ) slip plane, shared by the twin above it and the matrix below it. Slip systems in nanotwinned bcc materials are listed in Table 3.2.

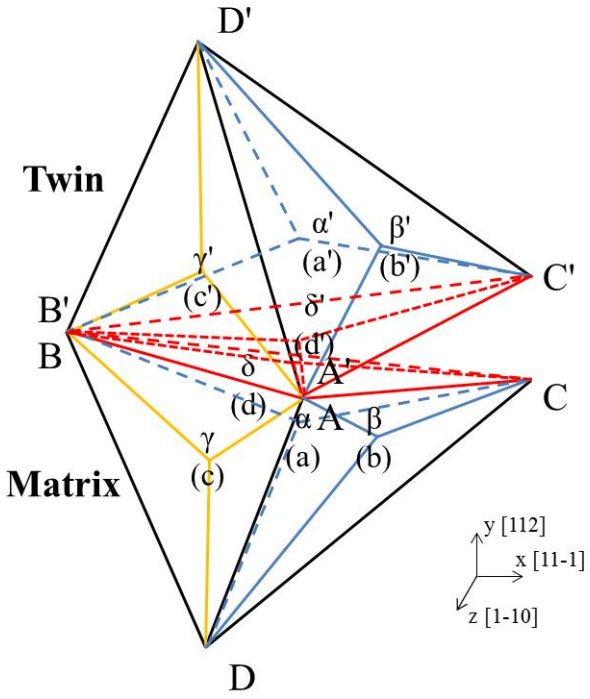

Figure 3.3 Double Thompson tetrahedron represents the slip systems in nanotwinned bcc materials. TB is the (Dγ) slip plane, shared by the twin above it and the matrix below it. Dislocation activities on symmetric slip planes are shown using the same colour.

Table 3.2 Slip systems in nanotwinned bcc materials.

Slip	**Vector**	**{110} Slip plane**	**Vector**	**{112} Slip plane**	**Vector**
Matrix slip system					
ABC **d**	Dδ 1/2[111]	(AB)	(-110)	(δC)	(11-2)
		(BC)	(10-1)	(δA)	(1-21)
		(AC)	(01-1)	(δB)	(-211)
ABD **c**	Cγ 1/2[-1-11]	(AB)	(-110)	(γD)	(-1-1-2)
		(DA)	(101)	(γB)	(-121)
		(DB)	(011)	(γA)	(2-11)
BCD **a**	Aα 1/2[-11-1]	(DC)	(110)	(αB)	(-112)
		(BC)	(10-1)	(αD)	(-1-2-1)
		(DB)	(011)	(αC)	(21-1)
ACD **b**	Bβ 1/2[1-1-1]	(DC)	(110)	(βA)	(1-12)
		(DA)	(101)	(βC)	(12-1)
		(AC)	(01-1)	(βD)	(-2-1-1)
Twin slip system					
ABC' **d'**	D'δ' 1/6[-1-1-5]	(AB)	(-110)	(δ'C')	(55-2)
		(BC')	(41-1)	(δ'A)	(2-71)
		(AC')	(14-1)	(δ'B)	(-721)
ABD' **c**	C'γ' 1/2[-1-11]	(AB)	(-110)	(γ'D')	(112)
		(D'A)	(0-1-1)	(γ'B)	(-21-1)
		(D'B)	(-10-1)	(γ'A)	(1-2-1)
BC'D' **a'**	Aα' 1/6[-151]	(D'C')	(11-4)	(α'B)	(-7-1-2)
		(BC')	(41-1)	(α'D')	(2-17)
		(D'B)	(-10-1)	(α'C')	(52-5)
AC'D' **b'**	Bβ' 1/6[5-11]	(D'C')	(11-4)	(β'A)	(-1-7-2)
		(D'A)	(0-1-1)	(β'C')	(25-5)
		(AC')	(14-1)	(β'D')	(-127)

4 STRENGTHENING MECHANISMS AND DISLOCATION PROCESSES IN <111> TEXTURED NANOTWINNED COPPER

4.1 Introduction

Recent experiments revealed a heterogeneous deformation in <111> textured nanotwinned Cu. Zhang et al. (Zhang et al., 2006, Anderoglu et al., 2008a) synthesized epitaxial nanotwinned Cu foils via magnetron sputtering deposition and reported a high tensile strength and limited uniform elongation of less than 2%. Hodge et al. (Hodge et al., 2008, Hodge et al., 2011) observed necking and shear band formation in Cu samples containing aligned nanotwins. Parallel depressions were observed before fracture (Hodge et al., 2012), which were also indicated after tension-tension fatigue tests (Hodge et al., 2012, Shute et al., 2011). Lu et al. (You et al., 2011, You et al., 2013) identified plastic anisotropy in the deformation of nanotwinned Cu and explained the hardening mechanism based on a confined layer slip model, while fatigue tests revealed distinct zigzag slip bands as a result of primary slip system activation (Pan et al., 2013).

While conventional experiments can provide an insight into the deformation mechanism based on post-mortem TEM observation, the microstructure evolution in real time cannot be recorded. MD simulations have been widely used to elucidate the interaction between dislocation and TB at atomic level that are not available experimentally (Yamakov et al., 2002c, Zhu and Gao, 2012). In <111> textured Cu, the glide of threading dislocations confined between neighbouring TBs was reported to be the main deformation mechanism, and jogged dislocations prevail when the twin spacing fell below a critical value (You et al., 2013, Zhou et al., 2014). All simulations proposed the slip-twin interaction to be the main strengthening mechanism in nanotwinned materials consistent with experimental results. Recent experiment and simulation (Morris Wang et al., 2013) indicated the defective characteristics of TBs, in contrast to conventional perfect interface assumption. The presence of imperfections on the TBs enriches the deformation processes via the migration of kinks and detwinning. Moreover a considerable fraction of low angle GBs was identified in nanotwinned Cu (Hsiao et al., 2012, Lagrange et al., 2013, Morris Wang et al., 2013). Traditional Voronoi construction procedure excluded the

low angle GBs, so the fabricated simulation cells cannot represent the <111> textured nanotwinned samples, and since only two (Morris Wang et al., 2013) or four grains (You et al., 2013, Zhou et al., 2014) were involved in these simulations, the mean field behaviour might not be fully captured.

In this chapter, MD simulations are used to investigate the effect of nanoscale twins on the mechanical behaviour of <111> textured polycrystalline Cu under tensile stress parallel to the TB. The full three-dimensional simulation cells contain a statistically large number of grains and the small angle GBs are retained. The dislocation evolution has been traced and the dislocation-TB interactions are analysed in details.

4.2 Methods

The Voronoi construction procedure was used to prepare [111] textured polycrystalline samples. A textured microstructure is ideal for this study because this columnar structure has been verified by experiments in nanotwinned Cu (Morris Wang et al., 2013, Lagrange et al., 2013) and relatively large grains can be simulated because only a few TBs need to be considered in the texture direction.

The as-annealed simulation cell shown in Figure 4.1 contains 18 columnar, almost regular hexagonal grains rotated by the angles between -90° and 90° about [111] texture axis. Each grain in nanotwinned samples contains 6 parallel TBs and there is no dislocation inside the grains. While conventional Voronoi method excludes low angle GBs by controlling crystallographic orientation of each grain, in the samples considered here the grains have random in-plane crystallographic orientation and [111] out-of-plane texture, thus the low angle GBs are retained. The discrete and continuous lines of GB atoms in the simulation cells indicate low angle and high angle GBs respectively. The Voronoi points are positioned on an elongated fcc plane, which result in regular hexagonal grains of the same size. The length in the texture direction is determined by the twin thickness, and since the simulation cell contains only 6 TBs, the initial thickness is 12.5 nm (twin spacing λ = 2 nm) and 23.8 nm (λ =

4 nm). The hexagonal shape of grains leads to an aspect ratio of $1:\sqrt{3}$ for the simulation cell. The grain size *d* is determined by the simulation cell length, *d* is 11 nm for the cell length of 54 nm with a total of 1,800,000 atoms (λ = 2 nm) or 3,420,000 atoms (λ = 4 nm); *d* is 16.4 nm for the cell length of 81 nm which results in a total of 4,050,000 atoms (λ = 2 nm) or 7,695,000 atoms (λ = 4 nm). There was no obvious coalescence of neighbouring grains during the annealing procedure despite of the abundance of small angle GBs and the slight GB migration.

Conventional [111] textured polycrystalline Cu with no growth twins (Figure 4.1c) was fabricated to act as references for the nanotwinned samples. All samples have the same topological microstructure, which enable a better comparison between nanotwinned and twin–free simulation cells. The twin-free sample is 12.5 nm thick, the same as the samples with twin spacing of 2 nm in order to save computation time.

The introduction of the TBs in nanotwinned samples complicates the columnar boundary structure compared to the twin-free samples. As well as the initial columnar GB between the matrix grains which are asymmetric [111] tilt boundaries; three more types of GBs are generated, including matrix-twin, twin-matrix and twin-twin boundaries. The columnar GBs can be divided into two groups. The first group consists of pure high angle GBs represented by continuous lines of GB atoms, this account for more than 70% of the total columnar GBs. The two adjacent grains have misorientation angles larger than 15°, so the intersection between matrices, twins, or matrix and twin of adjacent grains are all general GBs. The second group of columnar GBs is composed of alternative high angle and low angle GBs, which are indicated by a combination of discrete and continuous lines of GB atoms. The low angle GBs are formed between matrices or twins of neighbouring grains, because the misorientation angle about [111] direction is lower than 15°, unlike those that were formed by the rotation about $[1\bar{1}0]$ direction (Wu et al., 2009). And the high angle GBs are formed where the matrix in one columnar grain and the twin in adjacent grain meet. TEM observations have verified the existence of these two types of columnar boundaries (Morris Wang et al., 2013).

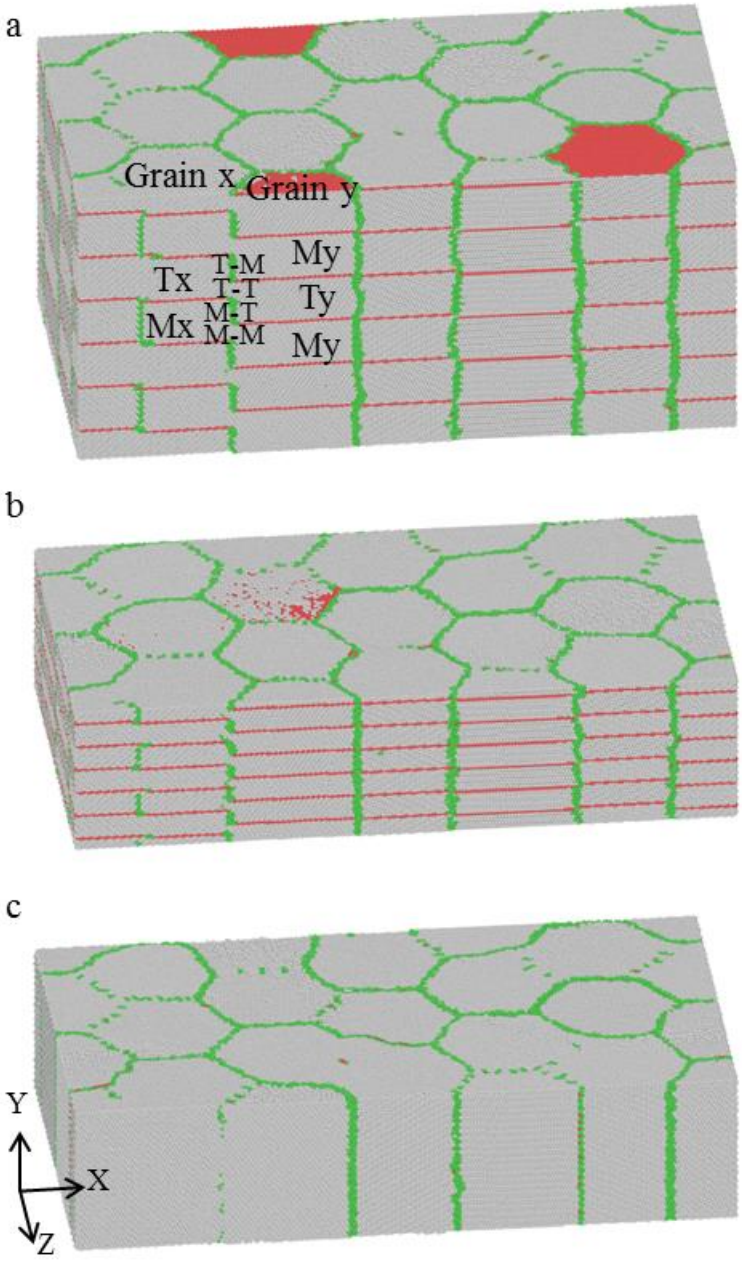

Figure 4.1 The initial structure of <111> textured polycrystalline Cu with a grain size of 11.0 nm. (a) Twin spacing is 4 nm. (b) Twin spacing is 2 nm. (c) Twin-free sample. Atoms are coloured according to the local crystalline order. Grey represents perfect fcc atoms, red stands for hcp atoms (corresponding TBs), and green indicates defected atoms (corresponding to GBs and other defects). The discrete and continuous lines of GB atoms indicate low angle and high angle GBs.

4.3 Results

4.3.1 Stress-strain behaviour

Figure 4.2 shows the stress-strain behaviour of [111] textured polycrystalline Cu with grain sizes of 11 nm and 16 nm. The stress-strain responses of all samples resemble each other. The stress first increases with the strain until it reaches the maximum stress, followed by a quick drop. After approximately 7% deformation, an equilibrium situation is obtained where the stress fluctuates around a mean value. This average stress in the strain interval from 7 to 20% deformation is defined as the flow stress.

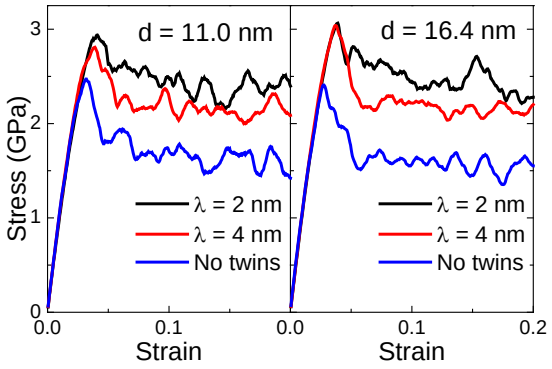

Figure 4.2 Stress-strain curves of polycrystalline Cu with different grain sizes.

The maximum stress and flow stress are extracted and plotted as functions of the twin spacing in Figure 4.3. A clear strengthening effect is observed in nanotwinned samples compared to the twin-free samples. The tensile stress monotonically increases as the twin spacing decreases. The maximum in the tensile stress is seen for nanotwinned Cu with a twin spacing of 2 nm. The improvement in the flow stress is more remarkable than the maximum stress. The flow stress for nanotwinned Cu shows a substantial enhancement by almost 40%, while the maximum stress increases by 20% on average. In addition, the grain size has a negligible influence on the mechanical response for the grain size range studied, as reflected by the slight variation in the maximum and flow stresses when the grain size changes. All of the results reported later are based on the small samples with grain size of 11 nm, since the large grain size provides similar results.

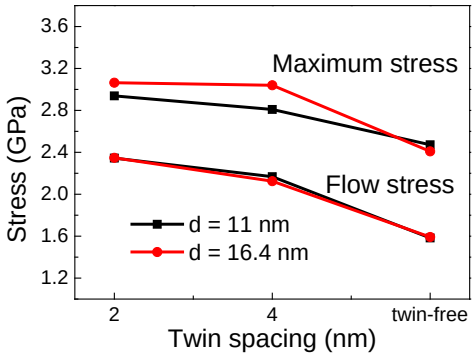

Figure 4.3 The maximum stress and flow stress as functions of twin spacing. A distinct strengthening effect can be seen in nanotwinned samples.

4.3.2 Deformation mechanism

Figure 4.4 shows the dislocation structures of the three samples with or without twins. Plastic deformation in all the models involves the continuous nucleation of dislocations from GBs and their propagations inside the grains until being absorbed by other GBs. The atomic configurations of the nanotwinned samples with twin spacing of 4 nm and 2 nm at 10% deformation are shown in Figure 4.4a and b, where plastic deformation is dominated by dislocation slip (examples indicated by black arrows) in the simulation cells and no deformation twinning occurs. These dislocations can transmit across the TB to the corresponding slip systems in the twinned grain. The transmission involves a change of slip planes across the TBs and leads to the formation of zigzag slip traces. However, in twin-free samples (Figure 4.4c), deformation twinning (examples shown by blue arrows) is widely observed, in addition to dislocation slip. The formation of deformation twins involves the successive glide of twinning partials on adjacent {111} slip planes, as previously reported in nanocrystalline Al (Yamakov et al., 2002a). Moreover, these dislocations, either full dislocations or twinning dislocations, can freely swipe over the whole grain, leaving straight slip traces. Therefore, the deformation mechanism changes from a combination of dislocation slip and deformation twinning in twin-free samples to pure dislocation activities in nanotwinned simulation cells.

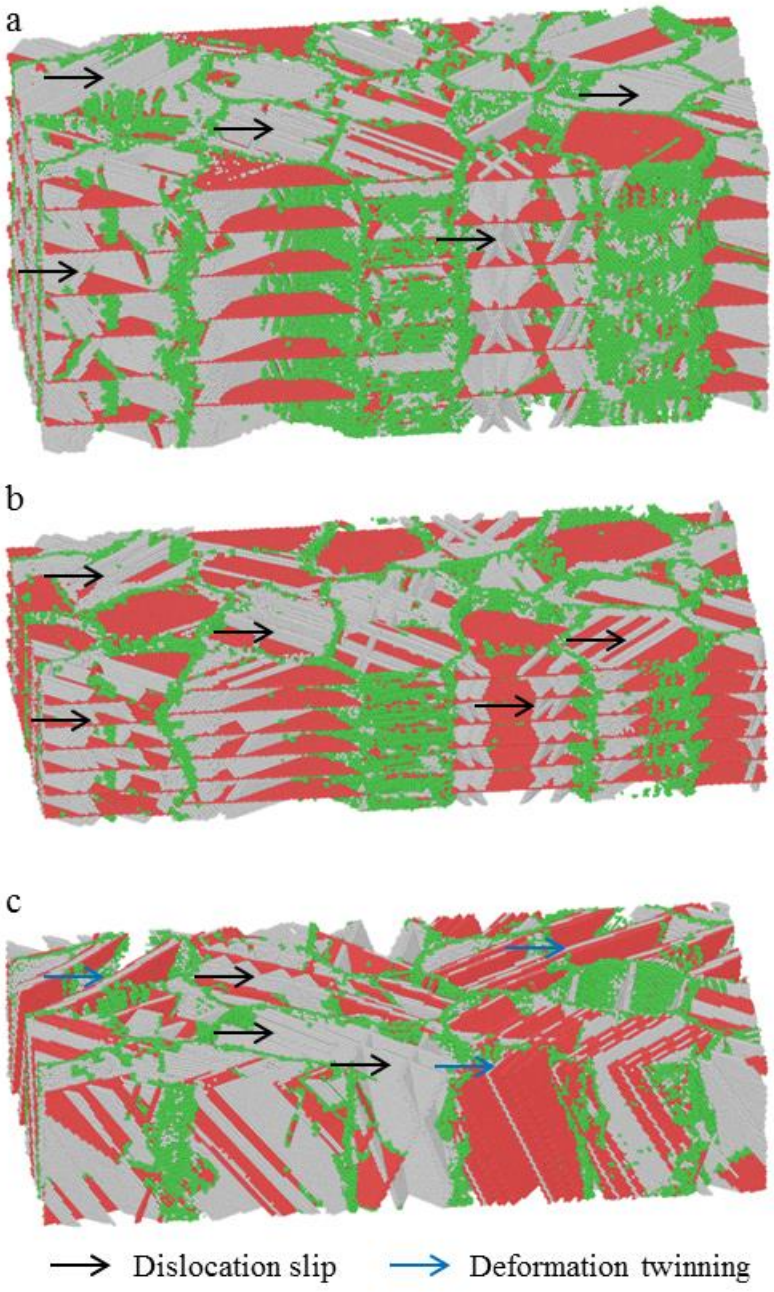

Figure 4.4. The atomic structure of <111> textured polycrystalline Cu with a grain size of 11.0 nm at 10% strain. (a) Twin spacing is 4 nm. (b) Twin spacing is 2 nm. (c) Twin-free sample. Plastic deformation is dominated by dislocation slips (indicated by the black arrows) in nanotwinned samples; while in addition to dislocation activities, deformation twinning (marked by the blue arrows) also plays a role in the deformation of twin-free samples. Perfect fcc atoms that are not involved in the dislocation slips are eliminated for clarity and the atoms that experience slips and retain the fcc structure are coloured in grey.

Typical dislocation structure evolutions of nanotwinned simulation cells are shown in Figure 4.5. Figure 4.5a-c shows the dislocation structures inside three grains at

different strains with a twin spacing of 4 nm. The initial yielding is accompanied by the nucleation and propagation of the Shockley partial dislocations which leave plenty of stacking faults transecting the sample (examples indicated by black arrows in Figure 4.5a). The motions of these partial dislocations are confined within neighbouring TBs, and the strain relived by their motions are lower than the applied strain so the total stress keeps on increasing as shown in the stress-strain curve. The stress peaks at a point where dislocations carry more strain than applied, and then drops to a lower state to sustain the dislocation activities. The plastic deformation is mainly accommodated by the continuous transmissions of the dislocations through the cross-slip of extended dislocations (examples indicated by black arrows in Figure 4.5b). Zigzag slip traces are observed from the cross-sectional view along the sample length as reflected by the dislocation debris in Figure 4.5b-c and the shear strain distribution in Figure 4.5d. Figure 4.5e shows the glide of partial dislocations in the interior of a grain in the nanotwinned sample with twin spacing of 2 nm. The dislocation structure from an additional 0.9% strain confirms the transmission of dislocations and the formation of zigzag slip traces as shown in Figure 4.5f.

Throughout the simulation, dislocations continuously nucleate from the GBs, swipe over the grain, transmit across the TB and are absorbed by other GBs. As the plastic strain increases, the dislocation density increases because the continuous nucleation of dislocations and dislocation multiplication involved in slip transfer exceed those that are absorbed by the GB until these two mechanisms reach a balance. The dislocations are not uniformly distributed among the grains, and a heterogeneous dislocation structure is formed. It can be seen from the dislocation debris in Figure 4.4 that one slip system dominates the plastic deformation for most of the grains, as indicated by one sets of parallel slip lines in the sample. In a few grains where two or more slip systems operate, the extended dislocations or stacking faults on different slip system sometimes intersect with each other. However, these interactions do not lead to the formation of dislocation tangles or sessile dislocations. This is in good agreement with the stress-strain behaviour reported above, where no strain hardening is observed.

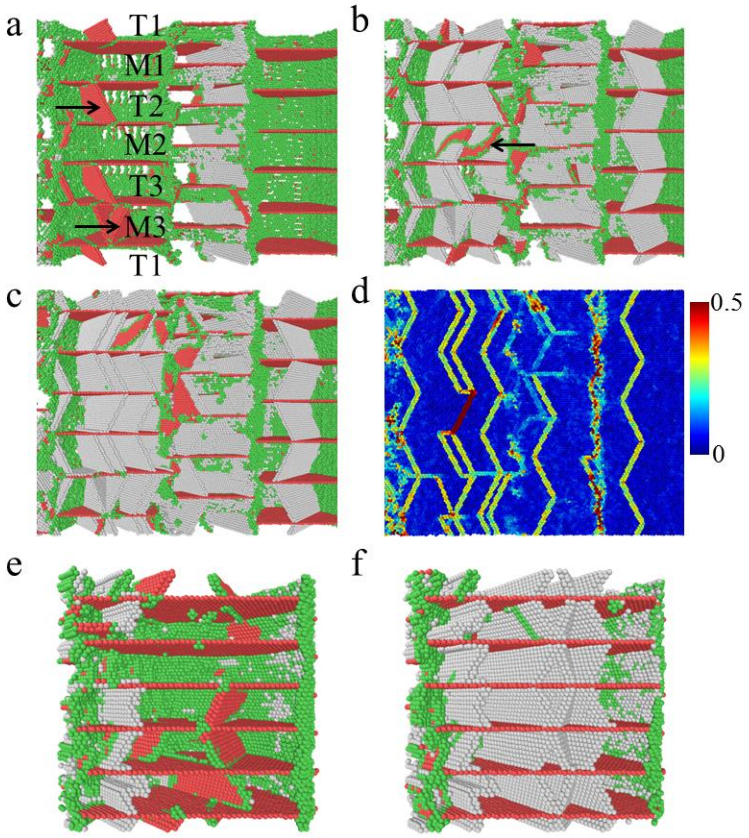

Figure 4.5. Dislocation processes in nanotwinned polycrystalline Cu with a grain size of 11 nm. (a-d) Cross sectional view of atomic structure with twin spacing of 4 nm at different strains. (a) The motions of partial dislocations (examples shown by arrows) are confined within neighbouring TB at 3.6% strain. (b) Extended dislocation (example shown by arrow) at 5.1% strain. (c) Atomic configuration at 6% strain. (d) Shear strain distribution at 6% strain. (e-f) Dislocation structures in a grain interior with twin spacing of 2 nm at different strains. (e) Nucleation of partial dislocations at 4.5% strain. (f) Dislocation structure at 5.4% strain. Dislocation slip is the dominant deformation mechanism.

4.3.3 Dislocation processes and slip-twin interactions

4.3.3.1 Direct transmission of the dislocation

To reveal the dislocation reactions involved in the slip transfer, a small part of the simulation cells is extracted for further analysis. Figure 4.6 illustrates the direct transmission of dislocation during the deformation of nanotwinned Cu. Under tensile strain, one leading Shockley partial dislocation nucleates from the right GB, and its glide leaves an intrinsic stacking fault inside the grain. The leading partial is blocked

from propagation by the TB and is deposited as a straight dislocation on the TB. Then this leading partial transmits across the TB and a curved dislocation is emitted on the other side of the TB, as shown in Figure 4.6a. This process leaves a sessile Frank partial dislocation on the TB and is widely observed in the simulations of nanotwinned models. The incoming dislocation is one of the 30° partial dislocations either in the matrix or in the twin depending on the crystallographic orientation. Partial dislocation **βC** is taken as an example so the above interaction can be expressed as:

$$\beta C_{(b)} \rightarrow \beta' C_{(b')} + \beta\beta' \tag{4.1}$$

or in vector form:

$$\frac{1}{6}[12\bar{1}]_{(1\bar{1}\bar{1})} \rightarrow \frac{1}{18}[\bar{1}2\bar{7}]_{(5\bar{1}\bar{1})} + \frac{2}{9}[111] \tag{4.1a}$$

with

$$\frac{1}{18}[\bar{1}2\bar{7}]_{(5\bar{1}\bar{1})} = \frac{1}{6}[12\bar{1}]^{T}_{(1\bar{1}\bar{1})^{T}} \tag{4.1b}$$

This interaction is energetically unfavourable according to the Frank rule because the elastic energy increases by 8/9 of the initial energy. The occurrence of this reaction is ascribed to the high stress state inherent in MD simulations, as reflected by the maximum stress of 3 GPa. Here, TB acts like a barrier against direct slip transfer.

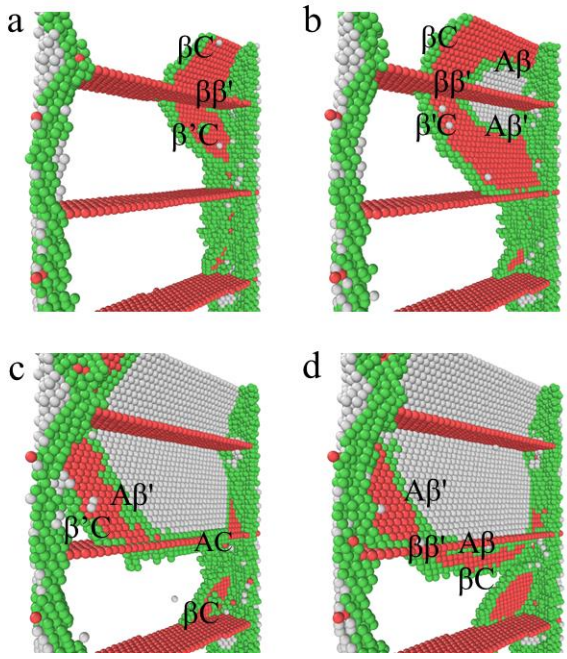

Figure 4.6. Transmission of dislocations across the TB in the deformation of nanotwinned polycrystalline Cu. (a) Transmission of a leading partial across TB leaves a Frank partial on the TB at 3.675% strain. (b) The emission of a trailing partial from GB-TB intersection and its transfer to the twinned grain at 3.75% strain. (c) The motion of extended dislocation is blocked by TB and is compressed to form a full dislocation at 3.85% strain. (d) Transmission of the extended dislocation and its dissociation at 3.875% strain.

The leading partials in the matrix and twin continue to expand and so are the corresponding stacking faults. If the energy of the stacking faults is considered, the total energy is almost doubled. The triple intersection of two stacking faults and the TB becomes energetically unstable and a trailing partial is emitted from the GB-TB intersection (Figure 4.6b) either in the matrix or in the twin. Once nucleated, the trailing partial interacts with the Frank partial left by the above interaction and form another trailing across the TB. In this case, the trailing partial **Aβ** is nucleated in the matrix, which will combine with the Frank partial to form a new trailing partial **Aβ'** in the twin. This reaction can be summarized as:

$$A\beta_{(b)} + \beta\beta' \rightarrow A\beta'_{(b')} \tag{4.2}$$

or in vector form:

$$\frac{1}{6}[\bar{1}1\bar{2}]_{(1\bar{1}\bar{1})} + \frac{2}{9}[111] \rightarrow \frac{1}{18}[17\bar{2}]_{(5\bar{1}\bar{1})} \tag{4.2a}$$

with

$$\frac{1}{18}[17\bar{2}]_{(5\bar{1}\bar{1})} = \frac{1}{6}[\bar{1}1\bar{2}]^{T}_{(1\bar{1}\bar{1})^{T}} \tag{4.2b}$$

This interaction is energetically favourable because the elastic energy of the resulting dislocation is almost half the reacting dislocations. Moreover, the glide of the trailing partials eliminates the corresponding intrinsic stacking faults left by the leading partials in the matrix and twin, releasing the energy of the intrinsic stacking faults. This further suggests that the penetration of the trailing partial across the TB is an energetically favourable mechanism.

The two Shockley partial dislocations connected by a stacking fault combine to form an extended dislocation, but its motion is hindered by the TB. The extended dislocation can either transmit across the TB through successive transmission of the leading and trailing partials as reported above or be absorbed by the TB plane. In the latter case, the two partial dislocations are constricted to form a full dislocation **AC** on the TB plane, shown in Figure 4.6c. This absorption process can be expressed as:

$$\beta' C_{(b')} + A\beta'_{(b')} \rightarrow AC_{(b')} \tag{4.3}$$

or in vector form:

$$\frac{1}{18}[\bar{1}2\bar{7}]_{(5\bar{1}\bar{1})} + \frac{1}{18}[17\bar{2}]_{(5\bar{1}\bar{1})} \rightarrow \frac{1}{2}[01\bar{1}]_{(5\bar{1}\bar{1})} \tag{4.3a}$$

with

$$\begin{aligned} \frac{1}{18}[\bar{1}2\bar{7}]_{(5\bar{1}\bar{1})} &= \frac{1}{6}[12\bar{1}]^{T}_{(1\bar{1}\bar{1})^{T}} \\ \frac{1}{18}[17\bar{2}]_{(5\bar{1}\bar{1})} &= \frac{1}{6}[\bar{1}1\bar{2}]^{T}_{(1\bar{1}\bar{1})^{T}} \\ \frac{1}{2}[01\bar{1}]_{(5\bar{1}\bar{1})} &= \frac{1}{2}[01\bar{1}]_{(1\bar{1}\bar{1})^{T}} \end{aligned} \tag{4.3b}$$

The Burgers vector of this constrained dislocation **AC** is parallel to the TB and it therefore has a pure screw nature when it is deposited on the TB, which can easily cross-slips to the corresponding slip plane in the twinned grain during later stages of deformation. This cross-slip mechanism can be summarized as follows:

$$AC_{(b')} \rightarrow AC_{(b)} \tag{4.4}$$

or in vector form:

$$\frac{1}{2}[01\bar{1}]_{(5\bar{1}\bar{1})} \rightarrow \frac{1}{2}[01\bar{1}]_{(1\bar{1}\bar{1})} \tag{4.4a}$$

with

$$\frac{1}{2}[01\bar{1}]_{(5\bar{1}\bar{1})} = \frac{1}{2}[01\bar{1}]_{(1\bar{1}\bar{1})^T} \tag{4.4b}$$

The cross-slipped dislocation then splits into two partial dislocations to reduce the elastic energy, as illustrated in Figure 4.6d. This dissociation mechanism can be summarized as follows:

$$AC_{(b)} \rightarrow \beta C_{(b)} + A\beta_{(b)} \tag{4.5}$$

or in vector form:

$$\frac{1}{2}[01\bar{1}]_{(1\bar{1}\bar{1})} \rightarrow \frac{1}{6}[12\bar{1}]_{(1\bar{1}\bar{1})} + \frac{1}{6}[\bar{1}1\bar{2}]_{(1\bar{1}\bar{1})} \tag{4.5a}$$

The leading partial may not directly transmit across the TB and slip transfer only occurs after the trailing partial catches up to form the full dislocation. This interaction resembles the transmission of extended screw dislocation. The dissociation of a perfect dislocation into two Shockley partials is energetically favourable according to the Frank energy criteria, as the magnitudes of the Burgers vectors of the partials are smaller than the full dislocation. However, the stacking fault complicates the problem. This split is widely observed throughout the simulations, and also confirmed in classic dislocation theory and experiment. It is acceptable that the decrease in elastic energy is greater than the increase in the misfit energy associated with the stacking fault. In contrast to this dissociation, the combination of two Shockley partials to form a full dislocation involves overcoming the repulsive interaction between the two partials. Therefore, the TBs act like a barrier to dislocation movement and the two partials are contracted on the TB, which is the main reason why TB can strengthen the materials.

Another slip-twin interaction is shown in Figure 4.7 where after the Shockley partials are compressed on the TB, this dislocation **AC** cross-slips to the TB plane, which then splits into two partials **Aδ** and **δC**. These interactions can be summarized as:

$$AC_{(b)} \rightarrow AC_{(d)} \tag{4.6}$$

or in vector form:

$$\frac{1}{2}[01\bar{1}]_{(1\bar{1}\bar{1})} \rightarrow \frac{1}{2}[01\bar{1}]_{(111)} \tag{4.6a}$$

$$AC_{(d)} \rightarrow \delta C_{(d)} + A\delta_{(d)} \tag{4.7}$$

or in vector form:

$$\frac{1}{2}[01\bar{1}]_{(111)} \rightarrow \frac{1}{6}[11\bar{2}]_{(111)} + \frac{1}{6}[\bar{1}2\bar{1}]_{(111)} \tag{4.7a}$$

The dislocation is fully absorbed by the upper TB instead of transmitting to the twinned grain. This absorption is also observed on the middle TB plane. Later on parts of the screw dislocation transmit across the TB and a new dislocation is formed in the twinned grain. During the propagation of this dislocation, the dissociated dislocation on the TB plane shrinks and is annihilated. Thus the whole dislocation transmits across the TB, as shown in Figure 4.7.

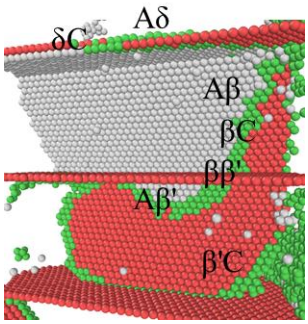

Figure 4.7 The absorption of a dislocation on the upper TB and its transmission across the middle TB at 5.25% strain.

After the transmission, the newly formed leading partial from the direct transmission interacts with the non-transmitted part of leading partial deposited on the TB to form

a Frank partial dislocation **ββ'** connecting the two stacking faults across the TB plane. This combination process can be expressed as:

$$\beta C_{(b)} - \beta' C_{(b')} \rightarrow \beta C_{(b)} + C\beta'_{(b')} \rightarrow \beta\beta' \tag{4.8}$$

or in vector form:

$$\frac{1}{6}[12\bar{1}]_{(1\bar{1}\bar{1})} - \frac{1}{18}[\bar{1}2\bar{7}]_{(5\bar{1}\bar{1})} \rightarrow \frac{2}{9}[111] \tag{4.8a}$$

with:

$$\frac{1}{18}[\bar{1}2\bar{7}]_{(5\bar{1}\bar{1})} = \frac{1}{6}[12\bar{1}]^{T}_{(1\bar{1}\bar{1})^{T}} \tag{4.8b}$$

Equation (4.8) is a variant of equation (4.1) and this interaction is energetically favourable according to Frank rule. This combination of two leading partials across the TB eliminate the need for transmission and leave a Frank partial dislocation on the TB plane, which is eliminated when trailing partials catch up, according to equation (4.2).

Extended dislocations continue to transmit the TB under further straining and suffer annihilation when they meet after crossing the periodic boundary as those dislocations are opposite in sign. These slip transfers indicate a full transmission of the shear strain across the TB plane, so the plastic strain produced by the dislocation motion is fully compatible across the TB. These interactions restore the original crystal structure, leaving the TB intact and with no dislocation debris after full transmission.

4.3.3.2 Indirect transmission of the dislocation

Dislocations may nucleate simultaneously within individual grains due to the complex columnar GB structure as shown in Figure 4.5a. These dislocations interact with each other when they meet on the TB. Figure 4.8 illustrates the detailed reactions between two leading partials in T1 and T2 grain. The two dislocations glide on coincident slip planes. The leading partial **β'C** in T2 first transmits across the TB to emit a new leading **βC** in M1 grain (Figure 4.8a), while leaving a Frank partial dislocation **ββ'** on the TB, similar reaction as equation (4.1). Within a short while, a

trailing partial dislocation **Aβ** is nucleated and quickly combines with the left Frank partial to form another trailing partial **Aβ'** across the TB (Figure 4.8b). Meanwhile, the extension of the leading partial **βC** in M1 grain is stopped by the TB, and it interacts with the leading partial **β'C** in T1 grain according to equation (4.8). Another two trailing dislocations are formed across the upper TB and the two trailing partials in M1 grain are annihilated when they meet (Figure 4.8c). It can be seen that the interaction between dislocations on coincident slip planes is just a variant of direct slip transfer, through which the full screw dislocation swipes across the whole columnar grain and the strain compatibility is fulfilled across the TB (Figure 4.8d).

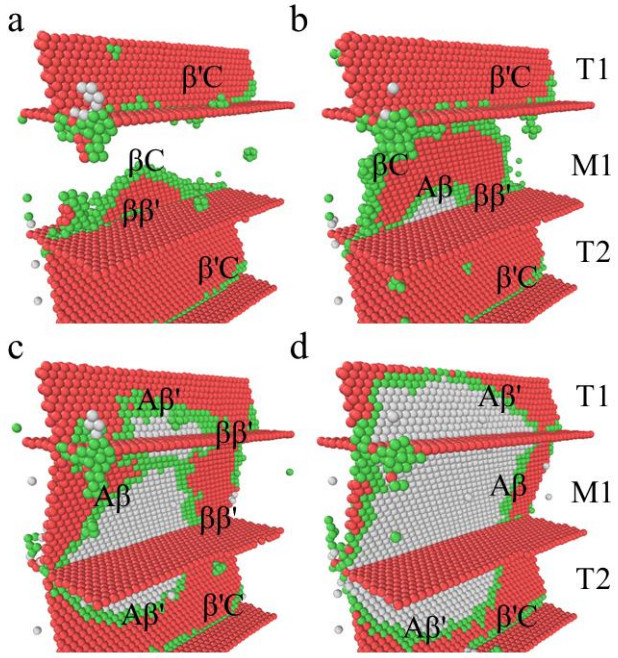

Figure 4.8. Interactions between dislocations on coincident slip planes. (a) Transmission of the leading partial across the middle TB at 3.6% strain. (b) Nucleation of the trailing partials near the middle TB and its transmission at 3.65% strain. (c) Nucleation of trailing partials near the upper TB at 3.7% strain. (d) Full transmission of the screw dislocation at 3.725% strain.

The interaction between slips on non-coincident slip planes is more complicated. Figure 4.9 demonstrates an interaction between an extended dislocation and a leading partial across the TB. The motion of the extended dislocation in T2 grain is blocked by the TB and is constricted to form a full dislocation **AC** as shown in Figure 4.9a. The leading partial **βC** deposited on the TB, restricts the full dislocation transmitting

across the TB. This full dislocation then cross-slips to the TB plane and splits into two Shockley partials **Aδ** and **δC** according to equation (4.3), (4.6) and (4.7). The partial dislocation **Aδ** interacts with the deposited leading partial **βC** to form a Hirth partial **AC/δβ** on the TB as shown in Figure 4.9b. This interaction can be expressed as:

$$A\delta_{(d)} - \beta C_{(b)} \rightarrow A\delta_{(d)} + C\beta_{(b)} \rightarrow AC/\delta\beta \tag{4.9}$$

or in vector form:

$$\frac{1}{6}[\bar{1}2\bar{1}]_{(111)} - \frac{1}{6}[12\bar{1}]_{(1\bar{1}\bar{1})} \rightarrow \frac{1}{3}[\bar{1}00] \tag{4.9a}$$

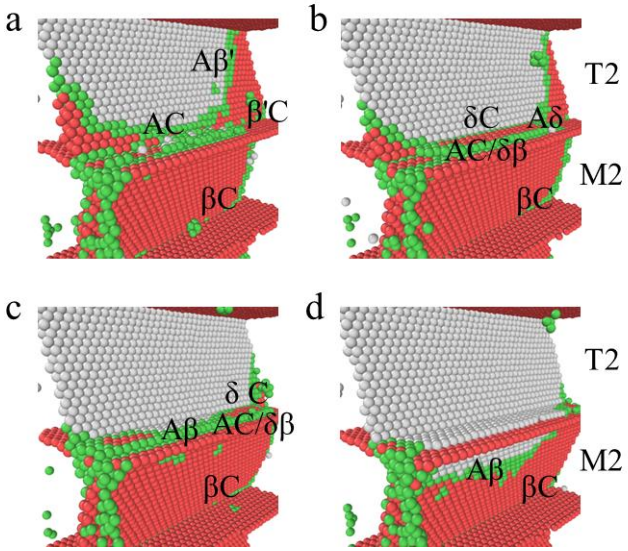

Figure 4.9. The first type of interactions between dislocations on non-coincident slip planes. (a) An extended dislocation is contracted on the TB at 3.75% strain. (b) The dislocation cross-slips to the TB plane and splits into two Shockley partial dislocations. One partial dislocation interacts with the deposited leading partial to form a Hirth partial on the TB at 3.775% strain. (c) The other partial combines with the Hirth dislocation to form a trailing partial at 3.8% strain. (d) Full transmission of the extended dislocation at 3.825% strain.

Then the other partial dislocation **δC** catches up and combined with the Hirth partial dislocation to form a trailing dislocation **Aβ** in M2 grain (Figure 4.9c). The interaction can be summarized as:

$$\delta C_{(d)} + AC/\delta\beta \rightarrow A\beta_{(b)} \tag{4.10}$$

or in vector form:

$$\frac{1}{6}[11\bar{2}]_{(111)} + \frac{1}{3}[\bar{1}00] \rightarrow \frac{1}{6}[\bar{1}1\bar{2}]_{(1\bar{1}\bar{1})} \tag{4.10a}$$

Thus the extended dislocation transmits across the TB as shown in Figure 4.9d.

Figure 4.10 illustrates another interaction involving two extended dislocations. An extended dislocation in M3 grain is absorbed by the TB and splits into two Shockley partials **Aδ** and **δC**. The Shockley partial **δC** glides on the twin plane and combines with a leading partial **β'C** in T3 grain to form a stair-rod dislocation **β'δ**; while the other dislocation **Aδ** partially transmits across the TB to emit a leading partial **β'C** in T3 grain, which leaves a Hirth dislocation **AC/δβ'** on the TB (Figure 4.10b). These dislocation processes can be summarized as:

$$\beta' C_{(b')} - \delta C_{(d)} \rightarrow \beta' C_{(b')} + C\delta_{(d)} \rightarrow \beta'\delta \tag{4.11}$$

or in vector form:

$$\frac{1}{18}[\bar{1}2\bar{7}]_{(5\bar{1}\bar{1})} - \frac{1}{6}[11\bar{2}]_{(111)} \rightarrow \frac{1}{18}[\bar{4}\bar{1}\bar{1}] \tag{4.11a}$$

with

$$\begin{gathered}\frac{1}{18}[\bar{1}2\bar{7}]_{(5\bar{1}\bar{1})} = \frac{1}{6}[12\bar{1}]^{T}_{(1\bar{1}\bar{1})^{T}} \\ \frac{1}{18}[\bar{4}\bar{1}\bar{1}] = \frac{1}{6}[011]^{T}\end{gathered} \tag{4.11b}$$

$$A\delta_{(d)} \rightarrow \beta' C_{(b')} + AC/\delta\beta' \tag{4.12}$$

or in vector form:

$$\frac{1}{6}[\bar{1}2\bar{1}]_{(111)} \rightarrow \frac{1}{18}[\bar{1}2\bar{7}]_{(5\bar{1}\bar{1})} + \frac{1}{9}[\bar{1}22] \tag{4.12a}$$

with

$$\frac{1}{18}[\bar{1}2\bar{7}]_{(5\bar{1}\bar{1})} = \frac{1}{6}[12\bar{1}]^{T}_{(1\bar{1}\bar{1})^{T}} \tag{4.12b}$$

$$\frac{1}{9}[\bar{1}22] = \frac{1}{3}[\bar{1}00]^T$$

Equation (4.12) is just a variant of equation (4.9). This interaction is energetically unfavourable and can occur due to the high stress state and the complex dislocation structure, which induce stress concentration like dislocation pile-ups. Later on, the trailing partial **Aβ'** in T3 grain catches up and interacts with the stair-rod dislocation **β'δ** to form another dislocation **Aδ** on the TB plane as shown in Figure 4.10c. This combination can be summarized as:

$$A\beta'_{(b')} + \beta'\delta \rightarrow A\delta_{(d)} \tag{4.13}$$

Or in vector form:

$$\frac{1}{18}[17\bar{2}]_{(5\bar{1}\bar{1})} + \frac{1}{18}[\bar{4}\bar{1}\bar{1}] \rightarrow \frac{1}{6}[\bar{1}2\bar{1}]_{(111)} \tag{4.13a}$$

with

$$\begin{gathered}\frac{1}{18}[17\bar{2}]_{(5\bar{1}\bar{1})} = \frac{1}{6}[\bar{1}1\bar{2}]^T_{(1\bar{1}\bar{1})^T} \\ \frac{1}{18}[\bar{4}\bar{1}\bar{1}] = \frac{1}{6}[011]^T\end{gathered} \tag{4.13b}$$

This Shockley partial **Aδ** propagates on the TB and combines with the Hirth dislocation to restore the leading dislocation **β'C** deposited on the TB. This interaction can be summarized as:

$$A\delta - AC/\delta\beta' \rightarrow \beta'C \tag{4.14}$$

Equation (4.14) is just a variant of equation (4.12). Other part of this dislocation is annihilated with the residual partial dissociated from the first absorption. It can be seen that the two extended dislocations on non-coincident slip planes suffer annihilation with the aid of the slip systems on the TB plane, after which the strain is fully compatible throughout the individual columnar grain.

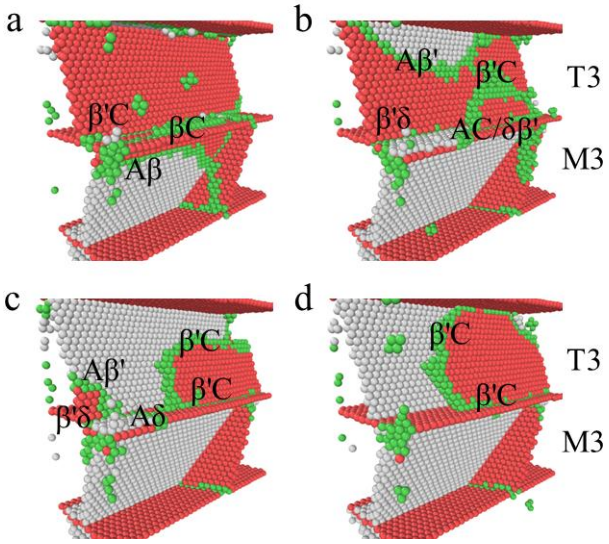

Figure 4.10. The second type of interactions between dislocations on non-coincident slip planes. (a) The motion of an extended dislocation in M3 grain is blocked by the TB at 3.9% strain. (b) The extended dislocation is absorbed by the TB and splits into two Shockley partials. One partial glides on the TB plane and combines with the leading partial in T3 grain to form a stair-rod dislocation. The other partial dislocation partially transmits across the TB to emit a leading partial in T3 grain, leaving a Hirth dislocation on the TB at 3.95% strain. (c) The trailing partial in T3 grain catches up and interacts with the stair-rod dislocation to form another partial dislocation on the TB plane. This partial combines with the Hirth dislocation to restore the leading dislocation deposited on the TB. Other part of this partial is annihilated with the partial dissociated from the first absorption at 4% strain. (d) The two extended dislocations are annihilated with the help of the slip systems on the TB plane at 4.05% strain.

4.3.4 Anomalous dislocation slip on {112} plane

Another intriguing process illustrated in Figure 4.11 involves the anomalous dislocation movement on {112} plane. To the authors' knowledge, this is the first observation of dislocation gliding on {112} plane. These dislocations are those comprising the low angle GBs. Two grains which rotates about [111] axis by 13° and 22° respectively are combined to form an asymmetric tilt GB with a misorientation angle of 9°. During minimization and annealing procedure, the dis-ordered atoms on the GBs are rearranged to form several sets of dislocation lines as shown in Figure 4.11a, which agrees with the fact that the small angle GBs consist of dislocation arrays.

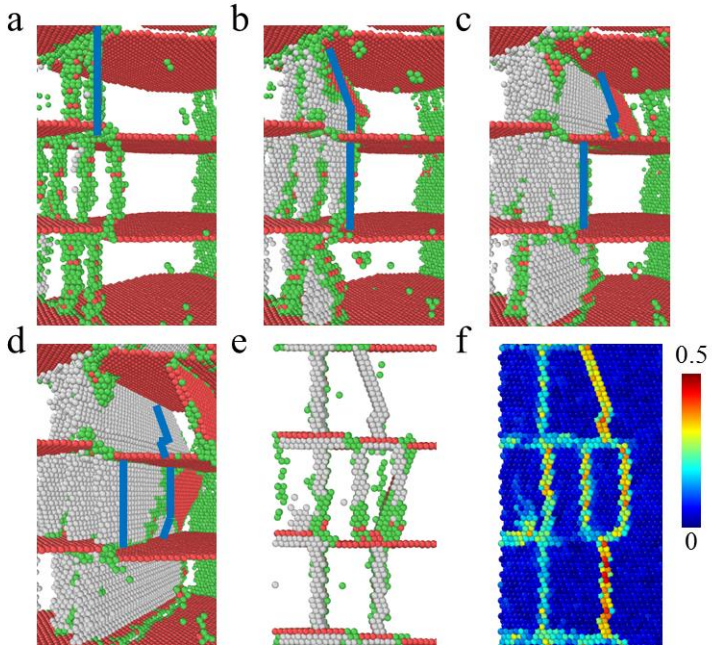

Figure 4.11. Anomalous dislocations movement on {112} slip plane. (a) Dislocation structure at 2.0% strain. (b) Propagation of dislocation on $(\bar{2}11)$ slip plane and the cross-slip to $(\bar{1}11)$ slip plane at 3.0% strain. (c-d) The cross-slip of the middle dislocation and the glide of the low dislocation on the $(\bar{2}11)$ plane at 3.2% and 3.4% strain. (e) Vertical slip traces from $[01\bar{1}]$ direction. (f) Shear strain distribution at 3.4% strain.

The Burgers vector of these dislocations is $1/2[01\bar{1}]$. The GB dislocations do not move during initial strain because a large stress is needed to drive the dislocations to propagate. At first, the dislocation lines are perpendicular to the Burger vector, so the dislocations are of a pure edge nature. The glide on $(\bar{2}11)$ plane until 3% strain leaves straight slip traces, indicated by vertical lines in Figure 4.11b. As the dislocation line evolves, parts of the dislocations become parallel to the Burger vector, turning into a pure screw dislocation. Because $(\bar{2}11)$ and $(\bar{1}11)$ slip planes intersect on $[01\bar{1}]$ direction, the screw parts of the up dislocation cross-slips to the conventional $(\bar{1}11)$ slip plane (indicated by slanted lines) while others keep moving on the $(\bar{2}11)$ plane (Figure 4.11c). Later the same cross-slip occurs to the middle dislocation (Figure 4.11d). The cross-slipped dislocation splits into two Shockley partial dislocations connected by a stacking fault. And the low dislocation keeps

moving on $(\bar{2}11)$ slip planes until being absorbed by other GBs (Figure 4.11d). The vertical slip traces from $[01\bar{1}]$ direction (Figure 4.11e) confirm the anomalous slip on $(\bar{2}11)$ plane. Moreover, the $\{112\}$ slips are composed of short composite slips on $\{111\}$ planes. The shear strain distributions also show the composite $\{111\}$ slip (Figure 4.11f). This anomalous movement of dislocation on $(\bar{2}11)$ plane is only observed during initial plastic deformation, as a result of GB dislocation motion. No dislocation is emitted on $\{112\}$ plane during later straining process.

4.3.5 Intergranular processes

In addition to these intragranular dislocation processes, the simulations also reveal abundant intergranular processes, involving the interactions between dislocations and GBs, and GB-based mechanism, including GB sliding and migration. Most of these processes were extensively investigated by experiment in coarse grained polycrystalline materials and by computer simulation in nanocrystalline metals. In the simulation cells, although the mechanical integrity of the GBs is remained, individual grains suffer considerable deformation, as reflected by the significant change of grain shape compared to their initial regular hexagonal structure. Some general GBs become thicker and rougher, while grains surrounded by the low angle GBs tend to coalescence, and some small angle GBs almost vanish after the glide of GB dislocation. Slip transmission across the small angle GB is widely observed, as indicated by the continuous dislocation structure shown in Figure 4.4. The detailed slip transmission mechanism is illustrated with the help of the displacement vector of each atom. Figure 4.12a shows at 4.5% strain a partial dislocation transmits across a low angle GB which leaves a transverse stacking fault across two neighbouring grains. Dislocations rarely transmit across general GBs because they are strong barriers to dislocation motion. Figure 4.12b illustrates the passage of a full dislocation which results in the nucleation of a leading partial in an adjacent grain at 4.5% deformation, as previously investigated in nanocrystalline aluminium by (Brandl et al., 2007). No trailing dislocation is emitted and finally the leading partial shrinks back and is absorbed by the GB. A vast number of slips transmit across the small angle GBs at 6% strain as shown in Figure 4.12c. The low angle GB has little effect on hindering dislocation motion because of the slight crystallographic

misalignment across the boundary. When a dislocation passes a low angle GB, the change of slip directions and the slip planes is very small due to the low misorientation angle.

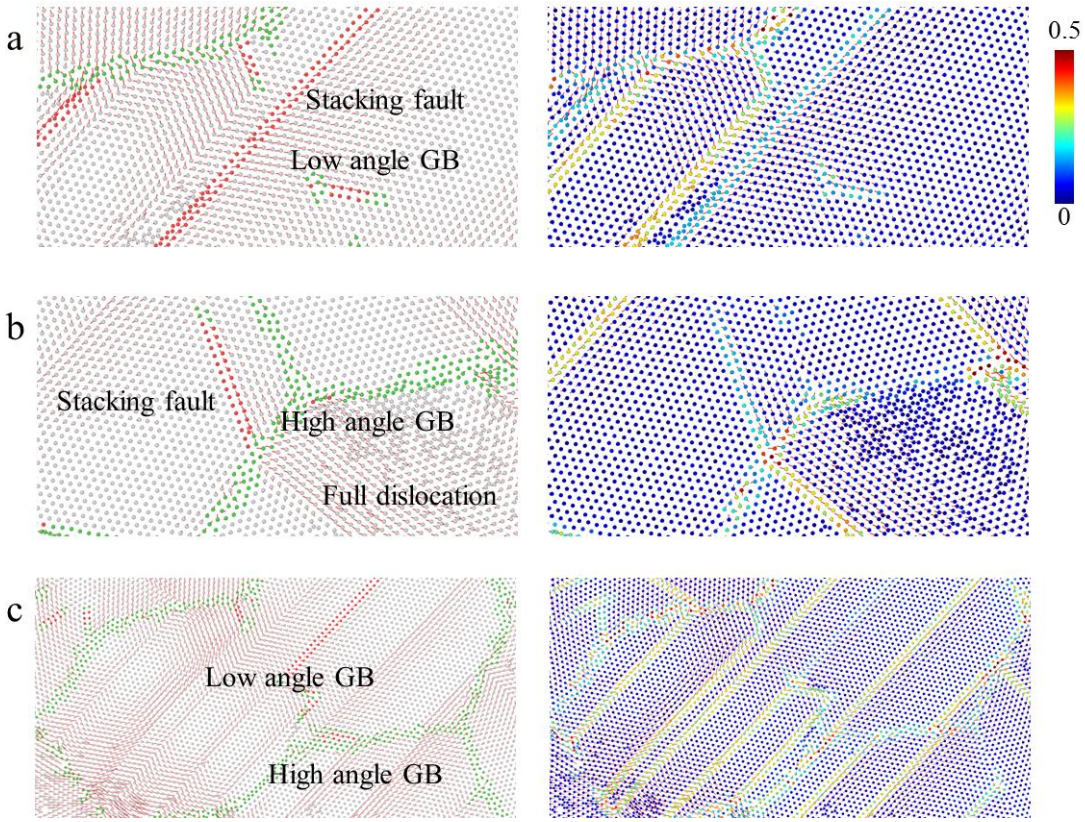

Figure 4.12. Slip transmission across the GB. Atoms are coloured according to crystalline order (left) and shear strain (right). (a) A partial dislocation passes a low angle GB at a strain of 4.5%. (b) A full dislocation transmits across the general GB and a partial dislocation is emitted at 4.5% deformation. (c) Plenty of slip transfers at 6% strain.

4.4 Discussion

MD simulations of <111> textured polycrystalline Cu with and without nanoscale twins reveal a clear strengthening effect in nanotwinned models. The tensile strength monotonically increases as the twin spacing decreases. A transition in the deformation mechanism is observed. In twin-free nanocrystalline Cu, deformation twining plays an important role in addition to conventional dislocation slip, especially during the later stages of the deformation. However, the deformation of

nanotwinned materials is mainly due to dislocation activities in the grain interior and no deformation twinning takes place.

4.4.1 Strengthening mechanisms

The presence of the nanoscale growth twins strengthens the polycrystalline material as indicated by the increased maximum stress and flow stress. The strengthening effect can be explained in two ways. First, the introduction of TBs leads to a complex columnar boundary structure where, in addition to the conventional columnar GB between the matrix grains, three more sets of GBs are generated between neighbouring columnar grains. This is more obvious for small angle GBs because the original low angle GBs is replaced by the alternative high angle and low angle GBs in nanotwinned samples. The motions of the dislocations comprising the small angle GBs are restricted as they may be pinned by the connected high angle GB. The complicated columnar boundary can absorb more elastic strain, which delays the dislocation nucleation process, and hence it strengthens the materials as illustrated by the 20% increase in the maximum stress. Second, and more importantly, TBs act as barriers to dislocation motion during the plastic flow of nanotwinned samples. The existence of the TB causes a change of crystallographic orientation between the matrix and twinned grain, which disrupts the slip systems across the TB. In contrast to the free propagation in the twin-free samples, the movement of dislocations is confined by the TB. The stress keeps on increasing even after the initial dislocation nucleation, as the stress relief is localized within individual grain. This is another reason for the increase in the maximum stress. The motion of the dislocation induces a strain incompatibility across the TB, so a higher stress is needed for the dislocation to penetrate across the TBs, which strengthens the materials. These phenomena are more pronounced in the experiment, because most of the columnar grains consist of thousands of TBs, compared to only six TBs in the simulation cells.

The tensile strength of <111> textured polycrystalline Cu monotonically increases as the twin spacing decreases. Lu et al. (Lu et al., 2009b) reported a softening phenomenon in the deformation of nanotwinned Cu as the twin spacing decreases below a critical size and explained it in terms of detwinning mechanism (Li et al., 2010b). The grains in their samples have random crystallographic orientations

without any texture. Detwinning could be a favourable deformation mechanism for some grains. When the twin spacing is small enough, corresponding to a high TB density, the propensity for detwinning is significantly increased (Wang et al., 2010) as more detwinning sites are available, thus the materials become soft. However, in the present study, the TBs are parallel to the loading axis, and do not experience any resolved shear stress, so detwinning contribute a minor part to the deformation. The majority of the twins remain even after a 30% deformation, in agreement with the behaviour of nanotwinned Cu after tensile (Morris Wang et al., 2013) or cyclic loading (Shute et al., 2011). This continuous strengthening mechanism as the twin thickness decreases is supported by available experimental work on <111> textured nanotwinned Cu (Hodge et al., 2011, Anderoglu et al., 2008a, You et al., 2011), and was reported in computer simulations (Zhou et al., 2014). This phenomenon was also reported in nanotwinned cubic boron nitride via nanoindentation experiments carried out on a specific crystallographic orientation (Tian et al., 2013). The tensile loading parallel to the TB plane suppresses detwinning mechanism that softens nanotwinned Cu with random orientations, thus the strength always increases as the TB spacing decreases under such loading condition.

4.4.2 Dislocation processes

The initial yielding is due to the motion of 30° Shockley partial dislocations, which leave plenty of stacking faults transecting the sample. As individual grains in <111> textured nanotwinned Cu are rotated about <111> axis by a random degree, the Schmid factors of 12 partial slip systems were calculated as the grain rotated over 180°. It has been found that the 30° Shockley partial dislocations always have the maximum Schmid factors, which is consistent with the simulation results that most of the dislocation processes indeed occur on these slip systems. An in situ synchrotron X-ray experiment showed initial negative deviation of lattice strain for <200> and <111> reflections in the tensile deformation of nanotwinned Cu, which indicate the incipient plastic deformation is due to 1/6<112> partial dislocation related deformation mechanism (Morris Wang et al., 2013), in agreement with the simulation results.

Slip-twin interactions play an important role in the deformation of nanotwinned materials. Throughout the simulation, the transmission of screw dislocation across the TB dominates the deformation of <111> textured nanotwinned Cu. Although slip transfer has been widely investigated in theory and experiment, the underlying dislocation interactions at atomic level has not been available for experimental exploration. MD simulations can give deeper insight into the dynamics of dislocation reactions. Two possible pathways are identified for direct transmission of the screw dislocation. The first path is initiated with the transmission of a leading partial to form a new leading partial across the TB as schematically shown in Figure 4.13a. The transmission of the leading partial is energetically unfavourable according to Frank rule. On the other hand, this energy barrier is lower than dislocation nucleation since the two leading partials have a common projection parallel to the TB as shown in Figure 4.14a, which extracts the slip systems involved in the interaction. This common projection makes dislocation transmit across the TB possible other than nucleation of a new dislocation. Moreover, the increase in elastic energy is eliminated by the nucleation of the trailing dislocation, which combines the Frank dislocation to form a new trailing partial across the TB. And the glides of these dislocations remove the stacking fault inside the grain and release the elastic energy. Deformation twinning is suppressed as the formation of deformation twins increases the system energy. The second pathway involves the transmission of an extended dislocation. This interaction was widely investigated in bicrystal models (Jin et al., 2006, Zhu et al., 2007). An extended dislocation is formed by combining a trailing partial with a leading partial. This dislocation can either transmit across the TB via successive transmission of the leading and tailing partial or be absorbed by the TB. In the absorption process, the dislocation is constricted to form a full dislocation when meeting the TB. This full dislocation is of a pure screw nature and can easily transmits across the TB, which dissociates into two partial dislocations to decrease the elastic energy, as shown in Figure 4.13b. The transmission of screw dislocation across the TB operates as the main deformation mechanism throughout the deformation. A higher twin density or lower twin spacing results in more restrictions on the dislocation motion as more transmissions are needed, thus the strength of nanotwinned materials monotonically increases as the twin spacing decreases.

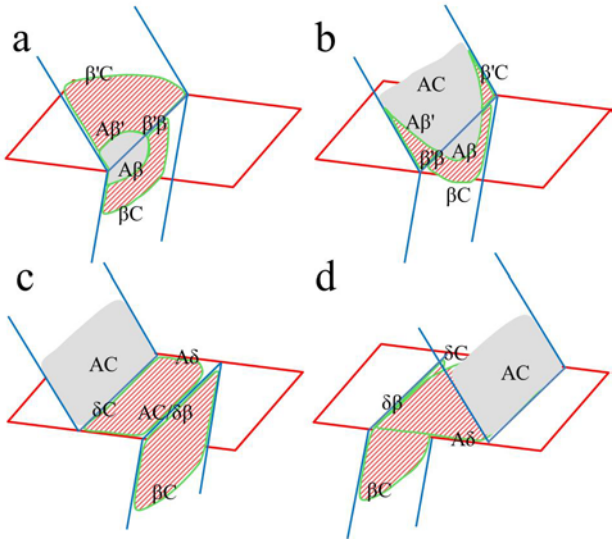

Figure 4.13. Schematic illustration of the slip transfer mechanism. (a) Direct transmission of a leading and a trailing partial dislocation across the TB. (b) Direct transmission of an extended dislocation. (c) Indirect transmission with the formation of a stair-rod dislocation. (d) Indirect transmission with the formation of a Hirth dislocation.

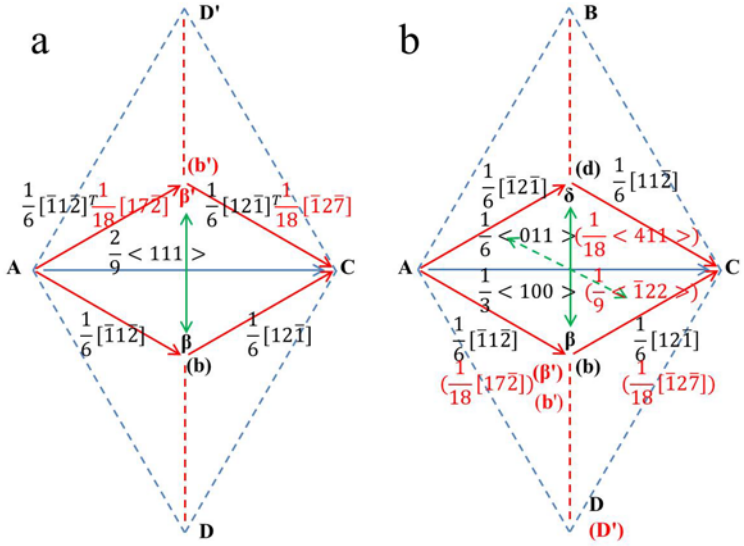

Figure 4.14. Dislocation reactions diagram in the unfolded double Thompson tetrahedron. (a) Direct slip transmission between corresponding slip planes across the TB plane. (b) Indirect slip transfer involving slip systems on TB plane. The dislocation reactions between slip planes in the matrix (black letter) and twin (red letter) are shown.

The transmitted dislocation may combine with the original dislocation to form a Frank partial dislocation on the TB while the two dislocations glide as shown in Figure 4.6. This interaction was reported to be jogged dislocations in the deformation

of nanotwinned Cu (Zhou et al., 2014). The magnitude of this Frank partial dislocation is 2/3 of the interplanar spacing of (111) plane. The partial jogs are continuously formed when two leading partials meet on the TB and are eliminated after combining with the trailing dislocations. They are intermediate products from the collective motion of corresponding dislocation across the TB plane, rather than from transmission of the leading partial (Zhou et al., 2014). The jog may be contracted to form a fourfold node connecting the four partial dislocations to decrease the elastic energy. The combination of two partial dislocations to form a partial jog on the TB plane eliminates the need for slip transfer, another confirmation that a high energy barrier is involved in slip transmission across TB.

The complicated columnar GB structure can simultaneously emit multiple dislocations within individual grains. If these dislocations are emitted on coincident slip plane, they can penetrate across the TB just like direct transmission. However, dislocations on non-coincident slip planes across the TB restrict direct transmission, because of the strain compatibility resulting from the common projection. Instead of transmission to the twinned grain, the dislocation is absorbed by the TB. Then the slip-twin interactions can be treated as dislocation reactions on intersected slip planes as shown in Figure 4.14b. Two possible pathways are identified. The first interactions involve the combination of a leading partial and a trailing partial on different slip planes, and a Hirth dislocation with a burgers vector of 1/3<100> is formed at the intersection of the planes as illustrated in Figure 4.13c. The angle between two stacking faults is 70.5°, which is an acute angle. The second pathway involves reactions between two leading partial dislocations as illustrated in Figure 4.13d. A stair-rod dislocation with a burgers vector of 1/6<011> is formed and the stacking faults intersect with an obtuse angle of 110.5°. When the other partial catches up, it will combine with the residual dislocation and emit a new Shockley partial. The whole dislocation structures, including two dislocations across the TB and the one on the TB plane, can be treated as special types of extended superjogs (Hirth and Lothe, 1982). These superjogs are formed to fulfil the strain compatibility. As dislocations are plastic strain carriers in the deformation of crystalline materials, the applied plastic strain at that stage can only sustain a single dislocation, thus direct transmission is suppressed. Other dislocations either nucleated from the GB or

transmitted across the TB, will be annihilated after the transmission. Without the dislocation transmission or the formation of the superjog, the strain compatibility is disrupted, inducing stress concentration. But the strain is fully compatible across the TB with the aid of the dislocation reactions. Moreover, only horizontal TBs are involved in our simulations, the effect of slanted TBs is ignored. Inclination of TBs leads to more dislocation activities on the TB plane (Jang et al., 2012, Morris Wang et al., 2013), because TBs experience resolved shear stress.

Continuous dislocation transmissions across the TB and interactions of dislocations within individual grains leave zigzag slip traces as indicated by dislocation structure and shear strain distribution (Figure 4.4 and Figure 4.5). These slip traces agree well with the observations by (Pan et al., 2013) in nanotwinned Cu after cyclic loading. Moreover, since the Burgers vector of the full dislocation is parallel to the TB, the extension in sample length is offset by shrinkage on the perpendicular direction within the TB plane while the sample retains its dimension on the direction perpendicular to the TB, which agrees with the experimental observations. Under tensile deformation, shear band and necking were observed from the plane view and there was almost no change in the thickness of the sample and the TB spacing (Hodge et al., 2011, You et al., 2011), despite a strong accumulation of dislocations between TBs (You et al., 2011, Shute et al., 2011, Morris Wang et al., 2013). After cyclic loading, the change in morphology was more pronounced from the cross-sectional view; while large fractions of smooth surface were preserved on the plane view (Pan et al., 2013).

The non-uniform deformation is due to the random crystallographic orientation, as indicated by the variations of the slip traces of individual grains. The polycrystalline samples can be treated as composite materials composed of both hard and soft grains similar to the model proposed in [110] textured nanotwinned Cu (Shabib and Miller, 2009). The stress-strain behaviour of nanotwinned single crystal Cu showed that the stress monotonically decreased as the loading axis rotated from <112> to <110> orientation. The calculated Schmid factors near <112> orientation are lower than those close to <110> orientation. So the orientation close to <112> orientation can be defined as the hard phase, whereas the soft phase is around <110> orientation. There

are more dislocation activities in the soft grains, as reflected by several parallel slip traces, unlike the hard grains, where fewer dislocation slips occur. This inhomogeneous deformation also leads to significant strain incompatibilities among individual columnar grains, which can, to some extent, be minified by GB-based mechanism, such as GB sliding or grain rotation, as reflected by the increase in GB thickness and change of grain shape. In addition, a large number of slip transfers across the columnar GBs is observed, especially near the small angle GBs due to the weak restriction to dislocation motion. Nanotwinned materials can be engineered by increasing the fraction of <112> hard phase to get a higher strength. This method was confirmed by the super high strength of magnetron sputtered Cu, which is only composed of <112> hard phase, like a single crystal (Anderoglu et al., 2008a).

The occurrence of dislocation gliding on {112} plane is surprising. It is well known that {111}<110> is the operative slip system in fcc materials, because the {111} plane is the most densely packed plane and the 1/2<110> is the smallest full dislocation Burgers vector. The {100}<110> slip system was observed to operate at elevated temperature in experiment (Hirth and Lothe, 1982) and was then verified through computer simulation at room temperature (Afanasyev and Sansoz, 2007, Wu et al., 2009). It is the first time to reveal the operation of {112}<110> slip system. However, the {112} slip is a result of GB dislocation movement, rather than being nucleated during the plastic deformation. These dislocations are formed by annealing the initial constructed structure because it can rearrange the dis-ordered atoms to obtain a lower energy status. Parts of dis-ordered atoms between two grains with small misorientation angle evolve to several arrays of dislocation to lower the GB energy, while others turn to discrete lines, which form low angle GBs. There are three $1/2 < 1\bar{1}0 >$ Burgers vectors on the (111) plane, and other $\{11\bar{1}\}$ slip planes intersect with the <111> textured direction hence, these dislocations reside on the $\{11\bar{2}\}$ plane perpendicular to the (111) plane. GB dislocations were also reported in nanocrystalline materials during GB relaxation (Stukowski et al., 2010). Under plastic straining, these dislocations can glide on the anomalous {112} planes due to the high resolved shear stress, reflected by the high Schmid factor on those slip systems. From a cross-sectional view, the {112} slip are actually composed of short composite slip steps on {111} planes (Figure 4.11f), in agreement with the

assumption that slip on non-{111} planes occurs by composite {111} slip (Hirth and Lothe, 1982). To examine the possibility of this anomalous slip, the generalized planar fault energy are calculated for leading, trailing, and twinning partial dislocations on the {111} slip plane, full dislocations on the {111}, {100}, {110} and {112} planes, as shown in Figure 4.15. A summary of the values of the fault energy is given in Table 4.1. The fault energy of {112}<110> is only 36% more than conventional {111}<110> slip system, and is lower than {100}<110> slip system, this indicates that {112}<110> slip system is theoretically possible. The fact that the two slip planes, {112} and {111} intersect at a single line leads to a cross-slip when the anomalous dislocation turns to a screw nature. No slip on {112} plane has been noticed during the later stages of deformation.

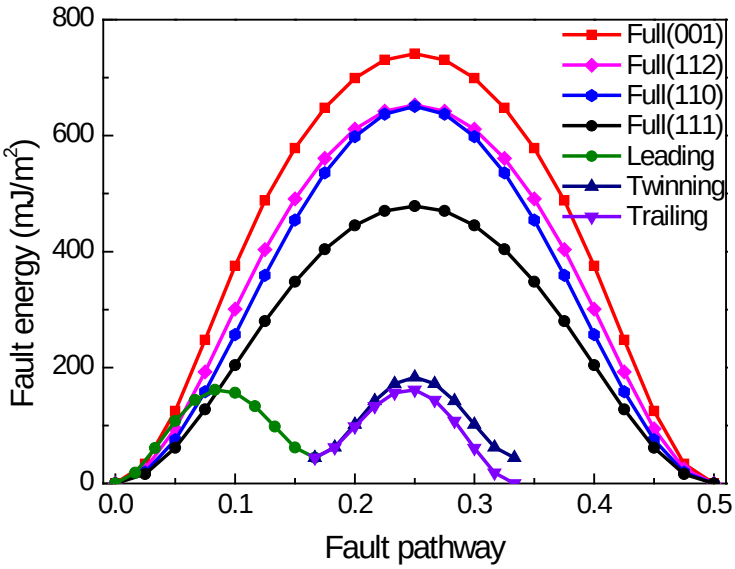

Figure 4.15. Generalized planar faults energy curves for Cu on different slip systems.

Table 4.1 The relaxed values for stacking fault energy (γ_{sf}), unstable stacking fault energy (γ_{usf}), unstable twinning fault energy (γ_{utf}) and planar fault energy (E_f) of full dislocation 1/2[1-10] on {111}, {100}, {110} and {112} slip planes.

	Displacement	**Planar fault energy E_f (mJ/m^2)**	E_f/γ_{usf}	$E_f/E_{f(111)[1\bar{1}0]}$
γ_{usf}	0.0833	161.29		
γ_{sf}	0.167	44.38		
γ_{utf}	0.25	183.43		
$(111)[1\bar{1}0]$	0.25	478.57	2.97	
$(001)[1\bar{1}0]$	0.25	741.38	4.6	1.55
$(112)[1\bar{1}0]$	0.25	652.73	4.05	1.36
$(110)[1\bar{1}0]$	0.25	650.45	4.03	1.36

4.5 Summary

MD simulations have been performed to investigate the mechanical behaviour of <111> textured polycrystalline Cu with and without nanoscale twins under tensile loading parallel to the TB. The full three-dimensional simulation cells contain a statistically large number of grains and the small angle GBs are retained. The following summary can be drawn:

1. The simulations reveal a shift in deformation mechanism from a combination of dislocation slip and deformation twinning in twin-free samples to pure dislocation activities in nanotwinned simulation cells.
2. The tensile strength of <111> textured polycrystalline Cu monotonically increases as the twin spacing decreases since the detwinning mechanism that softens nanotwinned Cu with random orientations is suppressed under parallel loading conditions. The main strengthening effect in columnar nanotwinned Cu originates from TB restricting the dislocation transmission across TB. Moreover, the presence of TBs complicates the columnar GB structure, which delays the dislocation nucleation.

3. Dislocation processes involved in the slip-twin interactions are identified at atomic level. Both the direct and indirect transmissions are observed. Two possible pathways are identified for the direct transmission. The first pathway involves the successive transmission of the leading and trailing partial dislocations by the Fleischer cross-slip model. The second pathway involves the absorption and desorption of the extended dislocation by the Friedel-Escaig cross-slip mechanism. In contrast, the indirect transmission involves the formation of special superjogs to fulfil the strain compatibility between dislocations on non-coincident slip planes.
4. Slip activities vary within individual grains due to their plastic anisotropy, which leads to an inhomogeneous deformation. Extensive slip transmissions across low angle GBs occur as they are not effective in hindering dislocation motion. Heterogeneous deformation leads to the formation of intersected slip bands on the plane view and persistent slip transfer leaves zigzag slip traces on the cross-sectional view. Most of the TBs retain their initial coherency even after a considerable deformation. Moreover, dislocation slip occurs on anomalous {112} plane and is described as composite {111} slip.

5 DEFORMATION MECHANISMS IN NANOTWINNED COPPER WITH DIFFERENT ORIENTATIONS

5.1 Introduction

Recently Jang et al. (Jang et al., 2012) investigated the influence of TB orientation on the plastic deformation of nanotwinned Cu. The Cu nanopillars contain densely spaced nanotwins and no GBs or other defects. Two distinct deformation mechanisms were observed. The plastic deformation in samples with orthogonal TBs is dominated by dislocation-TB interactions, which lead to the necking and shear bands formation; whereas detwinning governs the plastic deformation in samples with slanted TBs. You et al. (You et al., 2013) studied the plastic anisotropy in the deformation of columnar nanotwinned Cu. Three dislocation processes were identified: dislocation pile-up and transmission across the TB, threading dislocation movement confined inside neighbouring TBs and partial dislocation-mediated TB migration. The deformation mechanism transition was obtained by changing the loading orientation, but only three directions were tested. Experimental investigation of the deformation mechanism of nanotwinned materials has been limited because of the difficulty in synthesizing bulk nanotwinned materials. Moreover most of the prepared nanotwinned samples, such as nanotwinned Cu (Morris Wang et al., 2013), Pt (Idrissi et al., 2011) and stainless steels (Wei et al., 2014), are polycrystalline forms which contain a large fraction of GBs, TBs with random orientation and other defects. Thus it is difficult to identify the origins of their supreme mechanical properties.

Experimental investigation on TWIP steels revealed the evolution of twin structure during plastic deformation (Karaman et al., 2000, Gutierrez-Urrutia et al., 2010, Gutierrez-Urrutia and Raabe, 2011, Idrissi et al., 2010). Multiple twinning systems can be activated simultaneously. Until now no attempt has been made to explore the possibility for deformation twinning in nanotwinned fcc materials. It is not easy to distinguish deformation twins and growths twins after plastic deformation, as they are identical from a crystallographic view.

In this chapter, MD simulations are used to investigate the effects of TB orientation and twin spacing on the mechanical behaviour of nanotwinned Cu. The simulations

elucidate the deformation mechanisms of nanotwinned Cu as the TB varies from the horizontal direction, to the slant direction and to the vertical direction. The nature of the dislocation activity in nanotwinned Cu can be interpreted with the aid of Schmid's law. Under specific crystallographic orientation secondary twinning occurs in addition to conventional dislocation slip. The atomistic mechanisms involved in secondary twinning and dislocation-twin reactions are analysed.

5.2 Methods

Nanotwinned models with periodic conditions in all three dimensions are used to investigate the response of bulk nanotwinned materials. The nanotwinned Cu was constructed by continuous atomic displacements on adjacent (111) planes to produce a symmetric twin while keeping the matrix unchanged (Callister Jr, 2007). Atoms above one (111) plane were shifted along the $[11\bar{2}]$ direction by the magnitude of a partial dislocation $1/6[11\bar{2}]$, a process that was repeated to produce the specific twin spacing. Figure 5.1 shows the process of introducing nanoscale twins to a perfect fcc structure through an intrinsic stacking fault, an extrinsic stacking fault and finally a three-layer twin. The samples were produced with three twin thicknesses: 1.25 nm (T1.25), 2.09 nm (T2) and 3.97 nm (T4). In all constructed samples, the twin and matrix were spaced equally, indicating a uniform distribution of twin spacing.

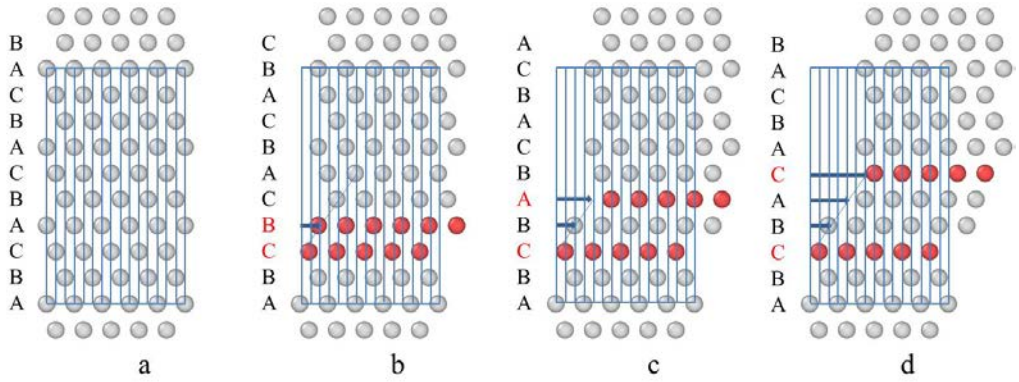

Figure 5.1 The introduction of nanoscale twins in fcc materials.

The nanotwinned model was rotated about $[1\bar{1}0]$ direction along the clockwise direction by various inclination angles (0°, 15°, 19.5°, 30°, 45°, 54.7°, 60°, 75° and 90°) to obtain the specific twin orientation. Then the rotated samples were cut to get the unit rectangular structure, with length and width varying a little to satisfy periodic boundary conditions. The unit cell was replicated in three dimensions to get near the same sample sizes. The constructed sample dimensions were around 100 nm × 50 nm × 2 nm and the total atom number was around 850,000. Figure 5.2 shows the cross sectional view of fabricated sample T4A0, T4A30, T4A60 and T4A90. The letters T and A in the sample names indicate the twin spacing and inclination angle.

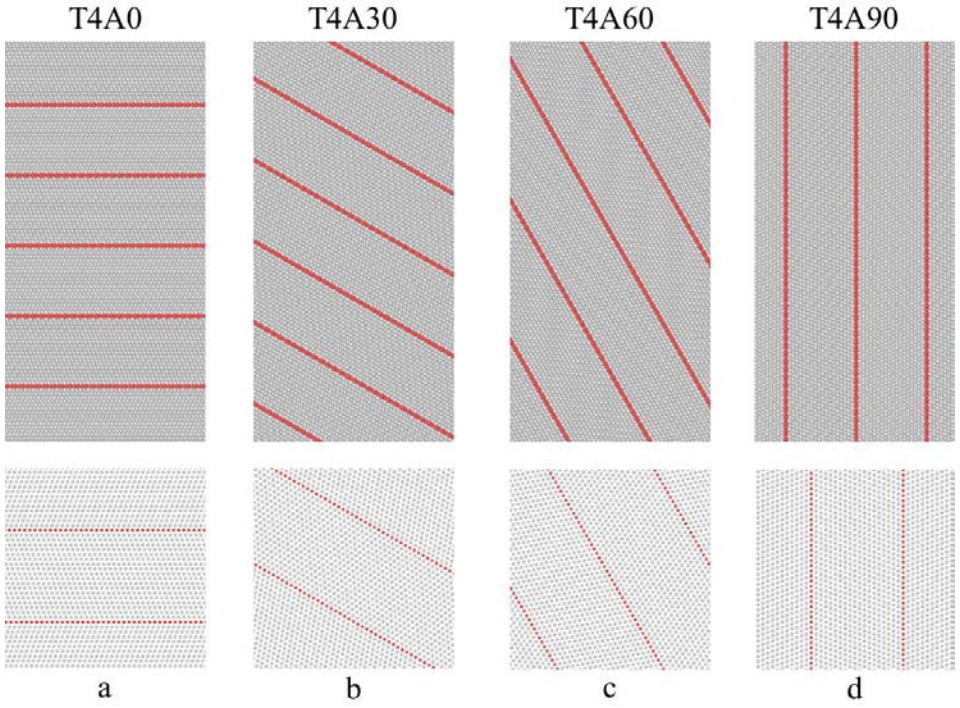

Figure 5.2 Cross sectional view of constructed nanotwinned samples with different orientation. (a) T4A0, (b) T4A30, (c) T4A60, (d) T4A90.

Figure 5.3 shows the cross-sectional view of dislocation activities along the [1-10] direction. The slip system in nanotwinned fcc materials can be divided into three groups: dislocations parallel to the TB on slip plane (d); dislocations inclined to TB at 70.5° on slip plane (c) or (c') and dislocations inclined to TB at 54.7°on other slip planes (a), (a'), (b) or (b').

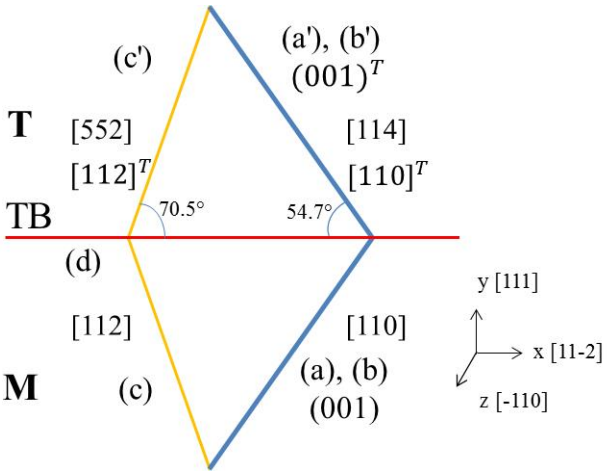

Figure 5.3 Cross-sectional view of dislocation activities along [1-10] direction. Three dislocation activities on different slip planes are identified. Dislocation activities on equivalent slip planes are indicated with the same colour.

5.3 Deformation mechanism transitions in nanotwinned copper

5.3.1 Stress-strain behaviour

Figure 5.4 shows the stress-strain behaviour of nanotwinned Cu with twin spacing of 1.25 nm, 2 nm and 4 nm and different TB orientations (A0-A90). Obviously, variations in inclination angle have a significant influence on the mechanical response of nanotwinned samples. The stress-strain responses of all the samples resemble each other. The stress increases at the initial part of deformation until it reaches a peak point followed by a dramatic drop. After the stress decreases to a lower level, a steady-state situation is reached where the stress fluctuates around a mean value.

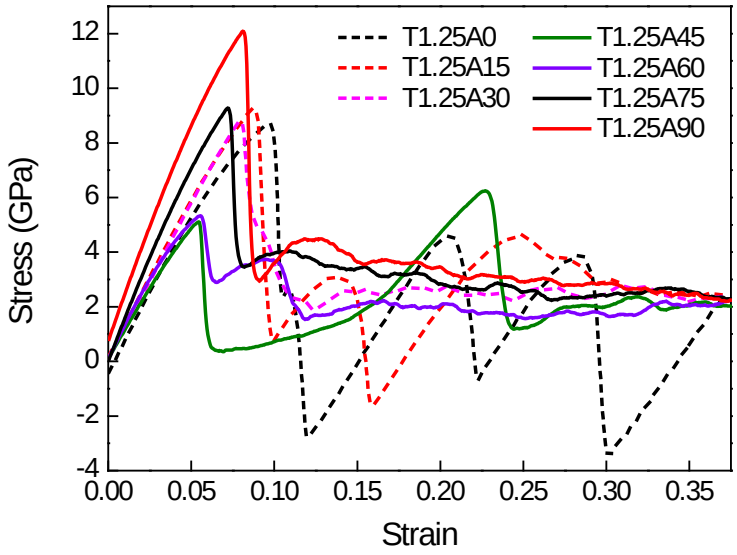
T1.25A0
T1.25A15
T1.25A30
T1.25A45
T1.25A60
T1.25A75
T1.25A90
Stress (GPa)
Strain
12
10
8
6
4
2
0
-2
-4
0.00
0.05
0.10
0.15
0.20
0.25
0.30
0.35

(a)

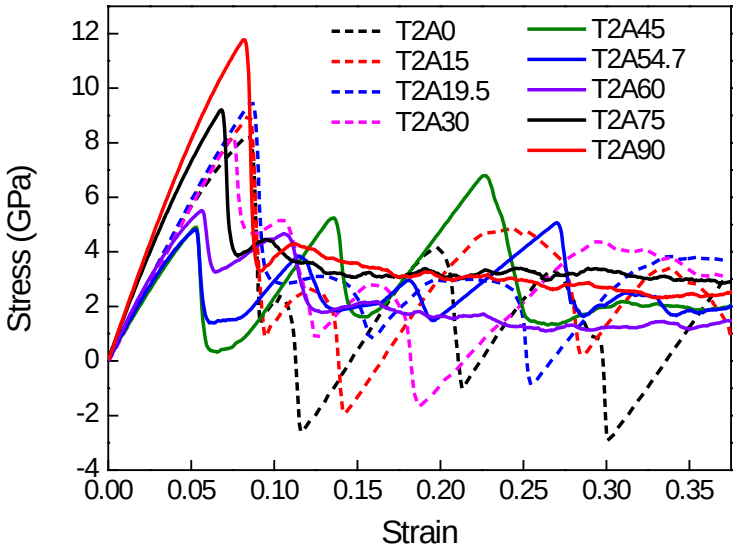
T2A0
T2A15
T2A19.5
T2A30
T2A45
T2A54.7
T2A60
T2A75
T2A90
Stress (GPa)
Strain
12
10
8
6
4
2
0
-2
-4
0.00
0.05
0.10
0.15
0.20
0.25
0.30
0.35

(b)

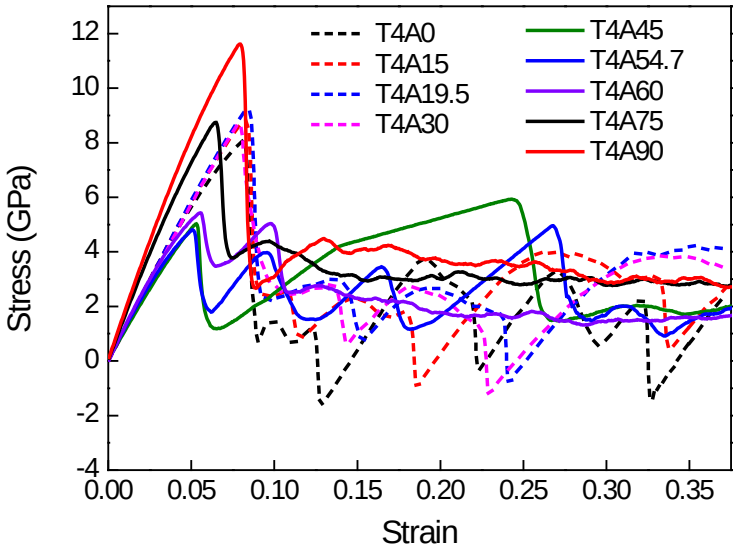

(c)

Figure 5.4 The stress-strain behaviour of nanotwinned samples with twin spacing of 1.25 nm, 2 nm and 4 nm.

It can be seen that the stress-strain curves begin to deviate from the linear elastic region at 2% strain. The slope of the linear stress-strain curve within the initial 2% deformation is defined as the Young's modulus and it is plotted as a function of inclination angle in Figure 5.5. It is clear that the Young's modulus is strongly orientation dependant. The Young's modulus first decreases slightly as the angle of inclination increases from 0° to 19.47°, and then decreases to a minimum value as the angle increases to 45°, and then rises to reach the maximum value at the perpendicular orientation. The calculated elastic modulus varies from 102.58 to 175.56 GPa, which is close to the ideal Young's modulus of pure Cu of 124 GPa (Schiøtz et al., 1999).

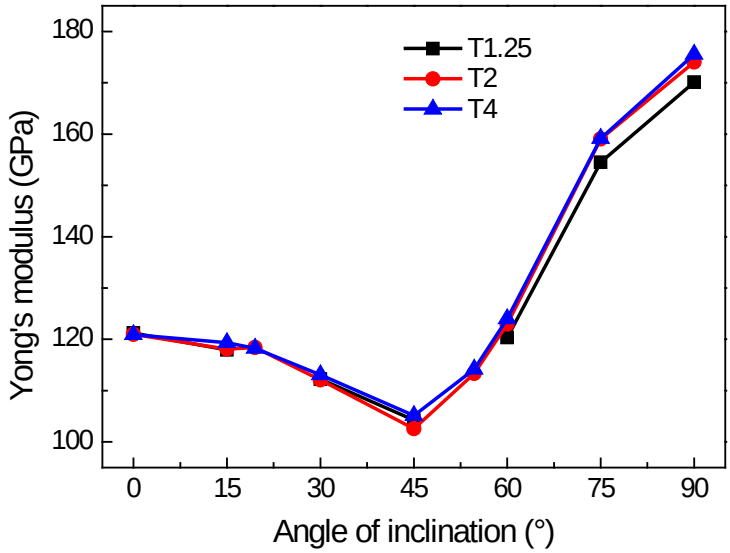

Figure 5.5 Young's modulus as a function of inclination angle.

The yield strain ε_y and yield stress σ_y (defined at the peak point in the stress-stain curve) of all samples are listed in Table 5.1. Also included in the table are the calculated maximum Schmid factors on slip planes in the matrix and twinned grain, and the critical resolved shear stress (CRSS). The Schmid factors are calculated based on 1/6<112> partial dislocations as partial dislocation activities dominate in nanocrystalline materials. CRSS is based on the yield slip system and the yield stress.

Table 5.1 The mechanical properties of nanotwinned Cu with different TB orientations and twin spacing.

Angle (°)	**Schmid factor**		**T1.25**			**T2**			**T4**		
	max	**yield**	$\boldsymbol{\varepsilon_y}$ **(%)**	$\boldsymbol{\sigma_y}$ **(GPa)**	**CRSS (GPa)**	$\boldsymbol{\varepsilon_y}$ **(%)**	$\boldsymbol{\sigma_y}$ **(GPa)**	**CRSS (GPa)**	$\boldsymbol{\varepsilon_y}$ **(%)**	$\boldsymbol{\sigma_y}$ **(GPa)**	**CRSS (GPa)**
0	0.3928	0.3928	9.7	8.71	3.42	8.45	8.24	3.24	8.1	8.07	3.17
15	0.3699	***0.3421***	8.75	9.26	3.17	8.45	8.96	3.06	8.2	8.82	3.02
19.5	0.3492	***0.3143***				8.65	9.5	2.98	8.4	9.23	2.9
30	0.433	0.433	7.95	8.79	3.81	7.5	8.21	3.55	7.85	8.7	3.77
45	0.5	0.5	5.45	5.1	2.55	5.25	4.9	2.45	5.3	5.02	2.51
54.7	0.4714	0.4714				5.2	4.81	2.27	5.05	4.81	2.27
60	0.4939	***0.433***	5.55	5.33	2.31	5.65	5.51	2.39	5.55	5.43	2.35
75	0.4666	0.4666	7.2	9.27	4.33	6.8	9.21	4.3	6.45	8.75	4.08
90	0.3143	0.3143	8.1	12.1	3.8	8.15	11.8	3.7	7.95	11.6	3.65

Figure 5.6 shows the yield stress as a function of the inclination angle. It is obvious that the yield stress strongly depends on the inclination angle. The mechanical behaviour of nanotwinned samples can be categorised into three groups according to the range of inclination angles; each group corresponds to one type of stress-stain behaviour in Figure 5.4.

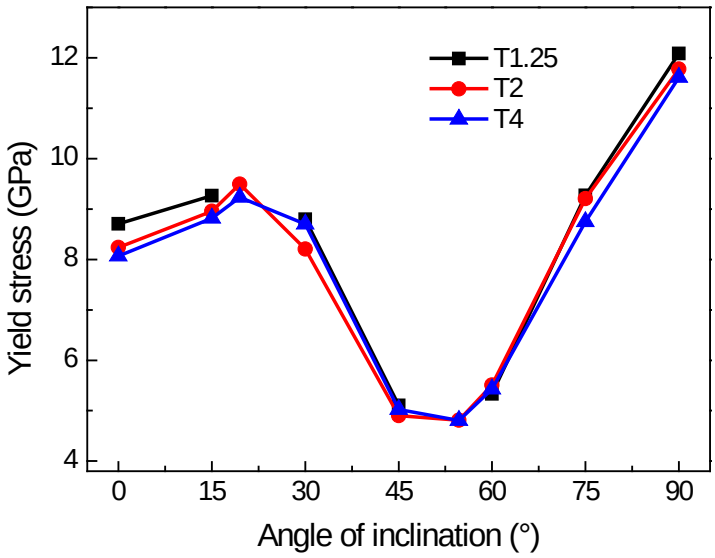

Figure 5.6 The TB orientation dependence of the yield stress with twin spacing of 1.25 nm, 2 nm and 4 nm.

(1) Small inclination angles (A0-A30). For this group, the yield stress is quite high, varying from 8.07 to 9.5 GPa. In the corresponding stress-strain curves (dash lines in Figure 5.4), the stress decreases to a negative value of -2 GPa after the yielding point and then fluctuates around zero value as it repeatedly increases and decreases.

(2) Medium inclination angles (A45-A60). For this group, the yield stress is low with an average value of 5.11 GPa. In the corresponding stress-strain curves (Figure 5.4), the stress decreases after the yielding point, and then rises to other higher values, even higher than the yield stress for some cases (T4A45).

(3) Large inclination angles (A75-A90). The yielding stress keeps increasing with increasing inclination angle and reaches the peak strength at the perpendicular orientation (A90).

The yielding stress is always dependent on the TB orientation despite varying twin spacing. Another interesting observation is the influence of twin spacing on yield stress. The yield stress increases with decreasing twin thickness at small inclination angles of less than 19.5° or large inclination angles of more than 75°, while the effect is insignificant for medium inclination angles. Moreover, the effect of twin spacing on the yield stress is small compared to TB orientation.

The variation of yield strength due to the change of the TB orientation probably results from the different underlying deformation mechanism. The main deformation mechanism for each group will be analysed in details in the following sections. Since the inclination angle exhibits the same effect on the stress for three different twin spacing, the following analysis is based on the samples with the twin spacing of 4 nm.

5.3.2 Small inclination angles (A0-A30)

Figure 5.7 shows the snapshots of simulation cells with small inclination angles at different strains. The samples yield due to the nucleation of Shockley partial dislocations, the glide of which forms parallel stacking fault networks. These stacking faults are along the [110] direction in the matrix and the corresponding $[110]^T$ direction in the twin. Dislocations on slip planes (a) and (b) or (a') and (b') have projections along [110] or $[110]^T$ direction on $(1\bar{1}0)$ plane (Figure 5.3), so the stacking faults results from the glide of partial dislocation on these slip planes. Due to the periodic boundary conditions adopted in the simulation, the partial dislocations continually glide out from the simulation cell and re-enter on the other side to form the repeated stacking faults networks. Figure 5.8 shows the shear strain distribution at 20% strain. After the dislocation propagation, zigzag slip traces are left in the samples.

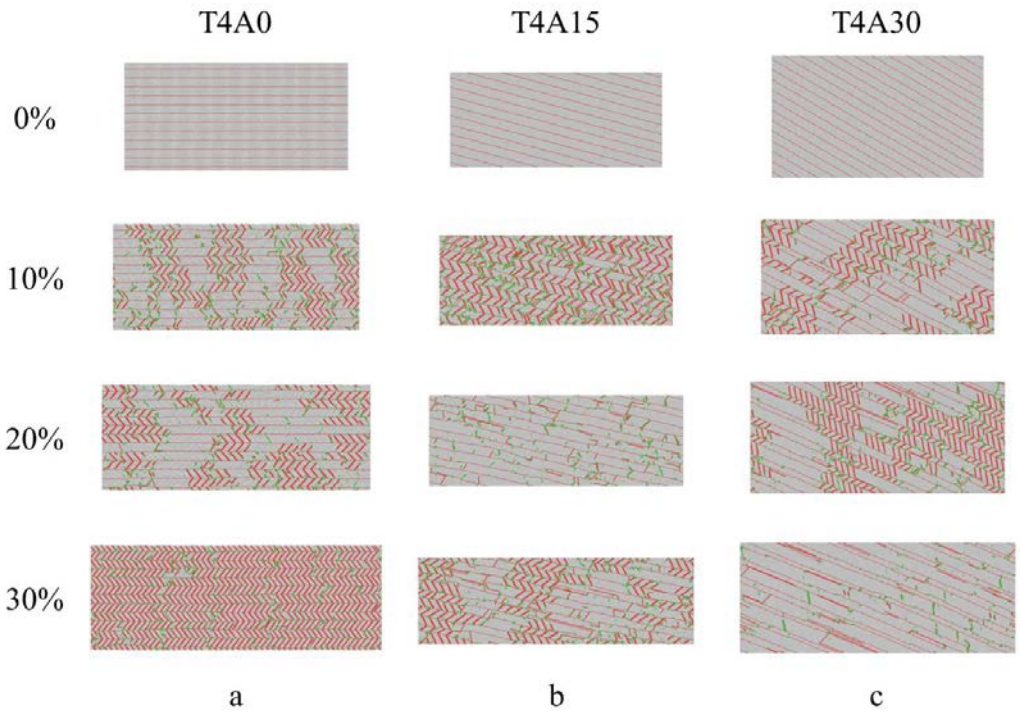

Figure 5.7 Atomic configurations of nanotwinned Cu with small inclination angles. (a) T4A0, (b) T4A15 and (c) T4A30.

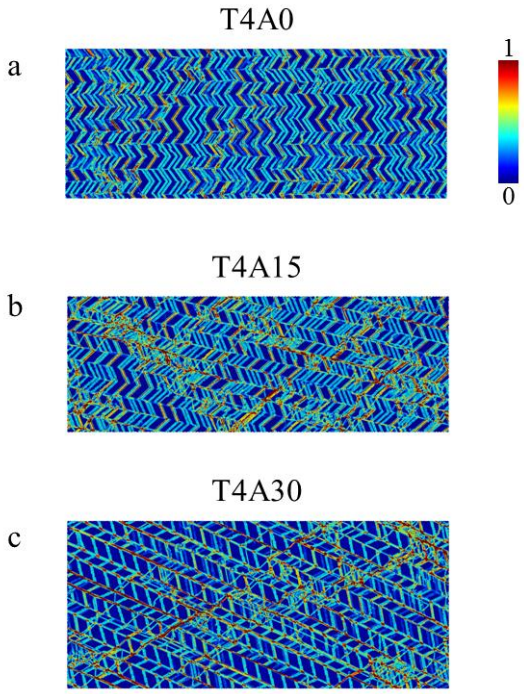

Figure 5.8 Shear strain distribution of samples with small inclination angles at 20% strain. (a) T4A0, (b) T4A15 and (c) T4A30.

It can be seen in Figure 5.7 that the TBs are hardly destroyed after a considerable deformation of 30% engineering strain, especially when the loading axis is parallel to the twin plane (T4A0). At this orientation, there is no resolved shear stress on the twin planes, thus dislocations will not glide on these planes. As the inclination angle increases, more TBs are found to lose coherency. The twin thicknesses are no longer the same, some twins grow while others shrink and more steps are formed at the TBs.

The calculated CRSS shown in Figure 5.9 is almost the same with an average of 3.12 GPa for the inclination angles from 0° to 19.5°, indicating a unique underlying deformation mechanism for this inclination angle range. When the loading direction is parallel to the twin plane (T4A0), the calculated maximum Schmid factor is 0.4082 for dislocations **AC** and **BC** for <110> full dislocations. Since partial dislocation activities dominate in nanocrystalline materials, the Schmid factors are also calculated based on <112> partial dislocations. Schmid factor for **αC** and **βC** is 0.3928 and is -0.3143 for **Bα** and **Aβ** respectively. Due to the symmetry between the twin and the matrix, the same Schmid factors for the corresponding slip systems in the twin can be obtained; this is also confirmed by results calculated from the twined slip system after coordinate transformation. As the inclination angle increases, the Schmid factors on slip planes (d) and (c') increase, and more dislocation activities on these slip planes are observed. Actually, the yielding of samples with inclination angle of 30° are due to the nucleation of twinning dislocations on the twin plane, that is why the CRSS is high for these samples.

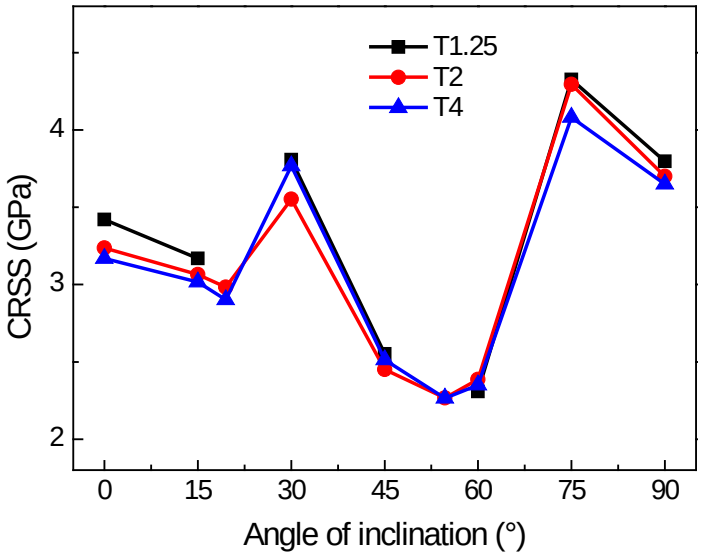

Figure 5.9 The TB orientation dependence of the CRSS with twin spacing of 1.25 nm, 2 nm and 4 nm.

At the yield point, multiple 30° Shockley partial dislocations nucleate between neighbouring TBs. These partial dislocations can multiply according to **βC→βα+αC**. Due to the small twin thickness, the propagation of the partial dislocations is blocked by the TBs. Under the high stress state, the leading partials can transmit across the TB to emit corresponding partial dislocations in the twinned grain with the help of sessile Frank dislocations on the TB according to **βC→β'C+ββ'**. This interaction occurs at high stress state and is partly in agreement with the criteria for slip transmission (Clark et al., 1992). First, the slip planes of the incoming and outgoing dislocations intersect on a common line, so the angle between them is zero. Second, the resolved shear stress acting on the emitted dislocation is very high due to the maximum Schmid factor. But the magnitude of the Burgers vector of the residual dislocation left on the TB is not small, comparable to the Shockley partial dislocation. The stacking fault networks and sessile dislocations on the twin plane cause a significant increase of the total energy. Moreover the partial dislocation cannot sustain further plastic strain.

The trailing partial dislocations then nucleate and immediately interact with the sessile Frank dislocations to emit new trailing partials across the TB according to

Aβ+ββ'→Aβ'. This interaction is energetically factorable according to Frank rule. The glide of the trailing partials eliminates the stacking faults left by the leading partials. Once the trailing dislocations nucleate, they continuously combine with the sessile dislocations on the TBs and eliminate the stacking faults to lower the total energy. The plastic strain carried by these dislocations is able to overcome the applied strain, so the sample may experience a compressive stress as observed in Figure 5.4. Similar phenomenon named strain burst occurs in nanoindentation experiments (Gouldstone et al., 2007). The transmission of the trailing dislocations eliminates the residual dislocations on the TBs, which leaves the TBs intact. The plastic deformation is dominated by slip transmission.

In addition, screw dislocations can also cross-slip to the twin plane. Both partials are absorbed by the TB to form a screw dislocation, which then dissociates into two partials, according to **βC+Aβ→AC→Aδ +δC**. There is no resolved stress on the TB, so these partials cannot move and pairs of steps are left on the TB. Little twin shrinkage or growth occurs for horizontal TB orientation.

More twinning partials propagate along the TB as the resolved shear stresses increase with increasing inclination angle. But their motion is impeded by other dislocations, which change the local twin thickness. In sample T4A30, twin growth competes with slip transmission (Figure 5.8c). A small amount of deformation twinning occurs in sample with inclination angle between 15° and 30°, and the twinning mechanism is analysed in Section 5.4.2.

5.3.3 Medium inclination angles (A45-A60)

Figure 5.10 shows atomic configuration of samples with medium inclination angles (T4A45, T4A54.7 and T4A60) at different strains. The samples yield due to the nucleation of twinning dislocations on the twin plane. Extensive TB migration occurs through the successive nucleation of twinning dislocations and their unrestricted glide along the TBs. These processes significantly change the twin spacing and finally lead to the disappearance of the TBs.

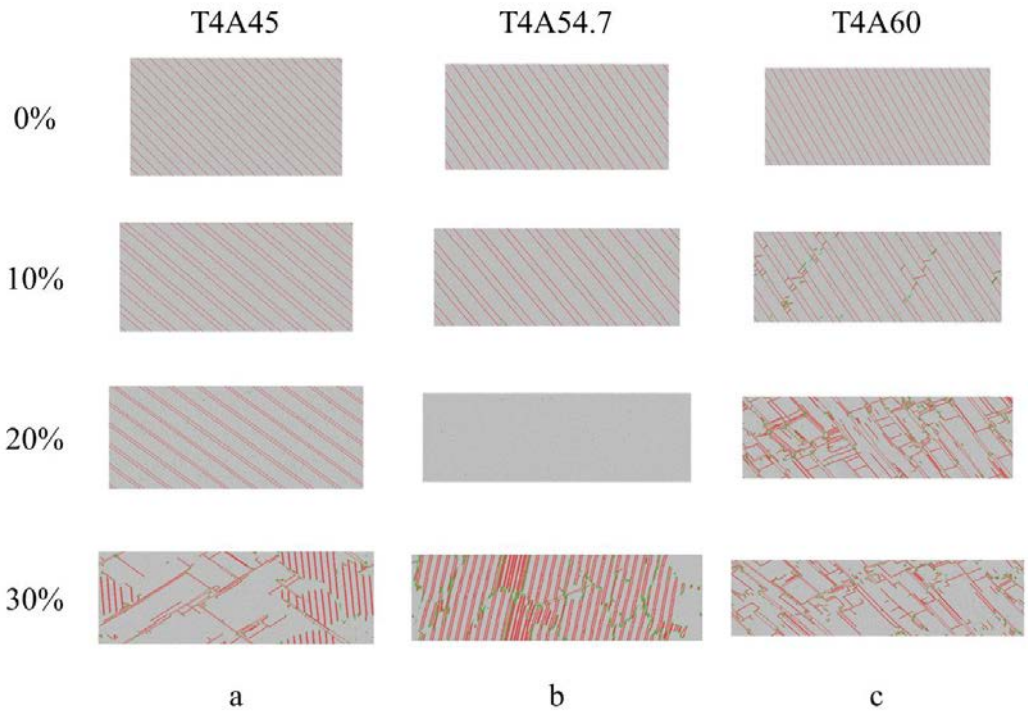

0. A B C B A C B A C A B C A B C B A C B A C A B C
1. A B C B A C B A C B C A B C A C B A C B A B C A
2. C A B A C B A C B A B C A B A C B A C B A B C A
3. C A B A C B A C B A C A B C B A C B A C B C A B
4. B C A C B A C B A C B C A C B A C B A C B C A B
5. B C A C B A C B A C B A B A C B A C B A C A B C
6. A B C B A C B A C B A C B A C B A C B A C A B C

Figure 5.10 Atomic configurations of nanotwinned Cu with medium inclination angles. (a) T4A45, (b) T4A54.7, (c) T4A60. The stacking sequences shown below the figure demonstrate the twinning process.

Figure 5.11 shows shear strain distribution of three samples (T4A45, T4A54.7 and T4A60) at 20% strain. The plastic deformation concentrates in the original matrix grains where homogeneous shear strain is observed, while the twinned grains experience no shear deformation. The disappearance of original TB results from continuous twinning of the matrix grains. After full twinning processes, the matrix grains are reoriented to the same orientation as the twinned grain.

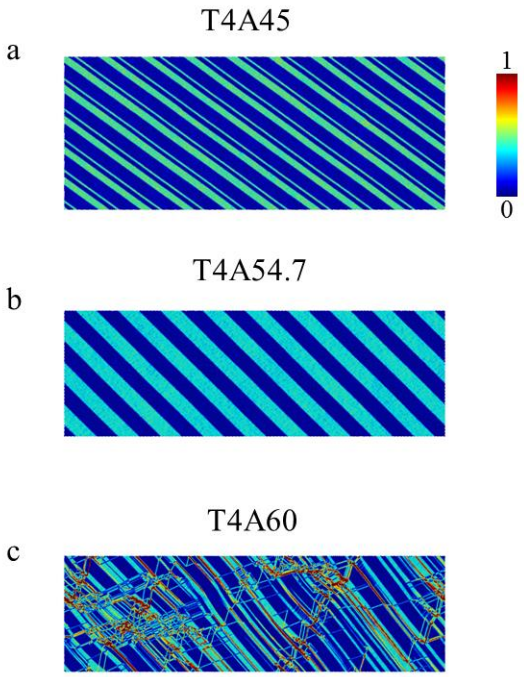

Figure 5.11 Shear strain distribution of samples with medium inclination angles at 20% strain. (a) T4A45, (b) T4A54.7, (c) T4A60.

The twinning process in nanotwinned samples resembles the well-known twinning process in nanocrystalline materials (Yamakov et al., 2002c), which involves the successive nucleation and propagation of Shockley partials on adjacent (111) slip planes. A nanotwinned model with twin thickness of six-layer atoms is chosen to demonstrate change in the stacking sequence during twinning processes. The constructed sample contains parallel nanoscale growth twins, so the stacking sequences change from normal ABCABC to twinned ABCBACBACABC. The red letters indicate TB and the twin lamella are highlighted by grey colour. During the initial tensile deformation, elastic strain is uniformly distributed along the sample length as a result of the coherency of the TBs and the twinned sequence is retained. The tensile strain has a maximum projection along the TB as reflected by the maximum Schmid factor. As the tensile stain increases, the resolved shear stress along the TB reaches a maximum of around 2.4 GPa, which is high enough to nucleate a twinning partial **δC** along the TB. The glide of the twinning partial shifts parts of the sample by the magnitude of the Burgers vector. This process consists of a slight relative movement across the TB, which leaves a shear strain gradient along

the tensile direction. The tensile strain is absorbed via TB migration, which leads to a dramatic decrease in tensile stress. But this stress cannot drop to zero or even minus value as seen in the last section, because TB migration only occurs when the resolved shear stress above a critical level. The TB migration continuously takes place as the strain increases. Adjacent TBs migrate on the opposite directions. After successive emission of multiple twinning dislocations on adjacent (111) planes, these TBs migrate towards each other. The fully twinned sample is a single crystal with the same orientation as the twinned grain.

In sample T4A60, multiple dislocations nucleate from the matrix grain at 10% strain before the sample is fully twinned, as shown in Figure 5.10c.

5.3.4 Large inclination angles (A75-A90)

Figure 5.12 shows atomic configurations of samples with large inclination angles (T4A75 and T4A90) at different strains. An obvious inhomogeneous plastic deformation occurs. Extensive dislocation processes take place. The interactions between these dislocations and the growth TBs lead to the formation of shear bands. TBs are no longer as sharp and straight as the original coherent TBs after slip-twin interactions. At 10% deformation, parts of the TBs are decorated with steps or even become curved. As the deformation continues, TBs within the shear bands are completely destroyed.

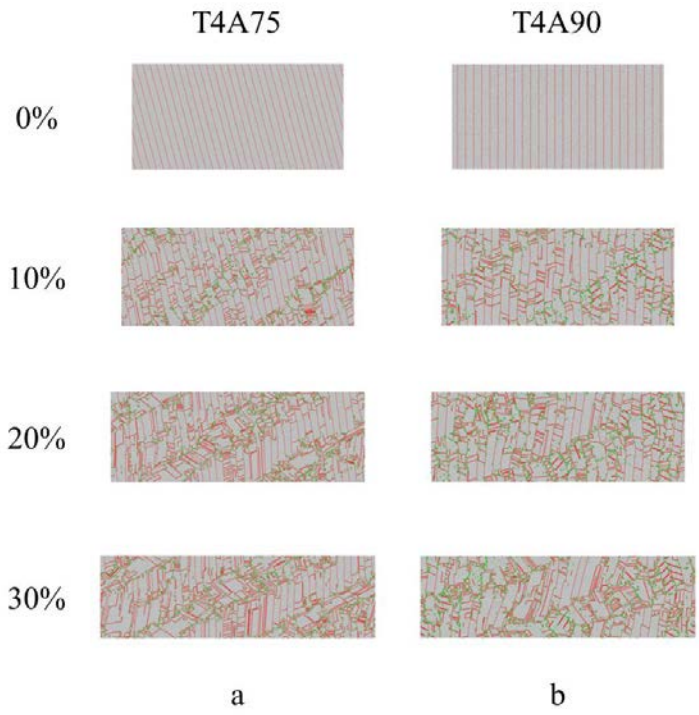

Figure 5.12 Atomic configurations of nanotwinned Cu with large inclination angles. (a) T4A75 and (b) T4A90.

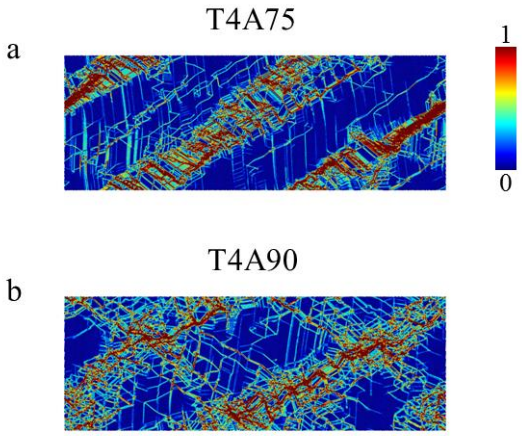

Figure 5.13 Shear strain distribution of samples with large inclination angles at 20% strain. (a) T4A75 and (b) T4A90.

The yielding of sample T4A75 is due to the nucleation of Shockley partial dislocations in the matrix grain. The glide of these dislocations leaves multiple stacking faults along [112] direction. The dislocation on slip plane (c) has a projection on $(1\bar{1}0)$ plane along [112] direction (Figure 5.3), so the partial

dislocation nucleate from this slip plane. The maximum Schmid factor is 0.4666 on slip system **γD** in the matrix grain. The motion of the partial dislocation is blocked by the TB. Then this partial transmits across the TB according to **γD→D'C(-2-21)+γC/DD'**. Dislocation **D'C** is a Lomer dislocation gliding on (-2-21) or $(001)^T$ plane and a sessile Hirth dislocation is left on the twin plane. The Lomer dislocation generated from dislocation-TB interaction was previously reported in nanotwinned Au (Afanasyev and Sansoz, 2007) and Cu (Wu et al., 2009, Wang and Huang, 2006). The occurrence of this interaction agrees well with the criteria for slip transmission (Clark et al., 1992). First, the slip planes of the incoming and outgoing dislocations intersect on a common line. Second, the Lomer dislocation experience a maximum Schmid factor of 0.4916, larger than all the other slip systems on conventional (111) planes. Third, the Burgers vector of the residual Hirth dislocation has a small magnitude. Moreover, the Burgers vector projection of the incoming and outgoing dislocations matches well on the loading direction. The leading partial **γD** in the matrix has a projection of 1.2166 angstrom and the emitted Lomer dislocation **D'C** in the twin has a projection of 1.6334 angstrom along the external strain direction.

The $(001)^T$ plane is not a normal slip plane and the Lomer dislocation can only move under high stress state until impinging with the next TB. Slip transfer occurs again to the Lomer dislocation in the twinned grain. Two Shockley partial dislocations nucleate on the matrix grain while leaving a sessile stair-rod dislocation on the TB according to **D'C→2×γD+γδ**. These two Shockley partials of the same type slip on adjacent slip planes and form an extrinsic stacking fault. As more dislocations are emitted from the grain interior or TB-mediated slip transfer, the stress state decreases significantly. The mobility of later nucleated Lomer dislocations is reduced as their motion on anomalous $(001)^T$ plane involves a higher Peierls energy barrier (Hirth and Lothe, 1982). So the Lomer dislocation may split into a triad of dislocations consisted of one stair-rod dislocation and two Shockley partials on normal {111} slip planes according to **D'C→D'γ'+γ'δ +δC**. The dissociation of Lomer dislocation into the Lomer-Cottrell locks reduces the total energy and agrees well with classic dislocation theory (Weertman and Weertman, 1992). Dislocations also nucleate on slip planes (a') and (b') in the twinned grain, resulting in a complex dislocation networks after large plastic deformation.

In sample T4A90, the TB is perpendicular to the loading direction. There is no resolved stress on the twin plane, and all other slip planes are equivalent, which indicates the slip-twin interactions observed in sample T4A75 occur to the other five slip planes. The columnar structure may restrict the activation of slip systems, but intersected shear bands are observed at 10% deformation. Furthermore, after the nucleation of a leading partial dislocation, a trailing dislocation can be emitted to form a full non-screw dislocation. This full dislocation cuts through the TB to form a Lomer dislocation according to **BD→D'C+δA**. A twinning partial is left on the TB. The twin lamella would shrink or expand by one atomic layer through the motion of the twinning partial until it is absorbed by other defects.

The continuous reactions of dislocations and TBs result in the formation of shear bands in the simulation cell. Then deformation mainly occurs within the shear bands which become the strain carriers as shown in Figure 5.13.

5.3.5 Discussion

In fcc crystals, the activation of the slip systems is determined by Schmid's law. In nanotwinned models the effect of the TB needs to be considered. The importance of TB can be understood in two ways. First, the introduction of twins is accompanied by crystallographic reorientations. New slip systems are placed in orientations that are favourable to the stress axis such that slip can take place. Second, the slip systems that are not on the twin plane are disrupted by the TB. The motion of the corresponding dislocations is restricted by the TB. On the other hand, the slip activities on the twin plane are also affected. Figure 5.14 shows the Schmid factors for the {111}<112> slip systems both in the matrix (solid lines) and twinned grain (dash lines). The three distinct dislocation processes can be explained with the relationship between the activated slip system and twin plane.

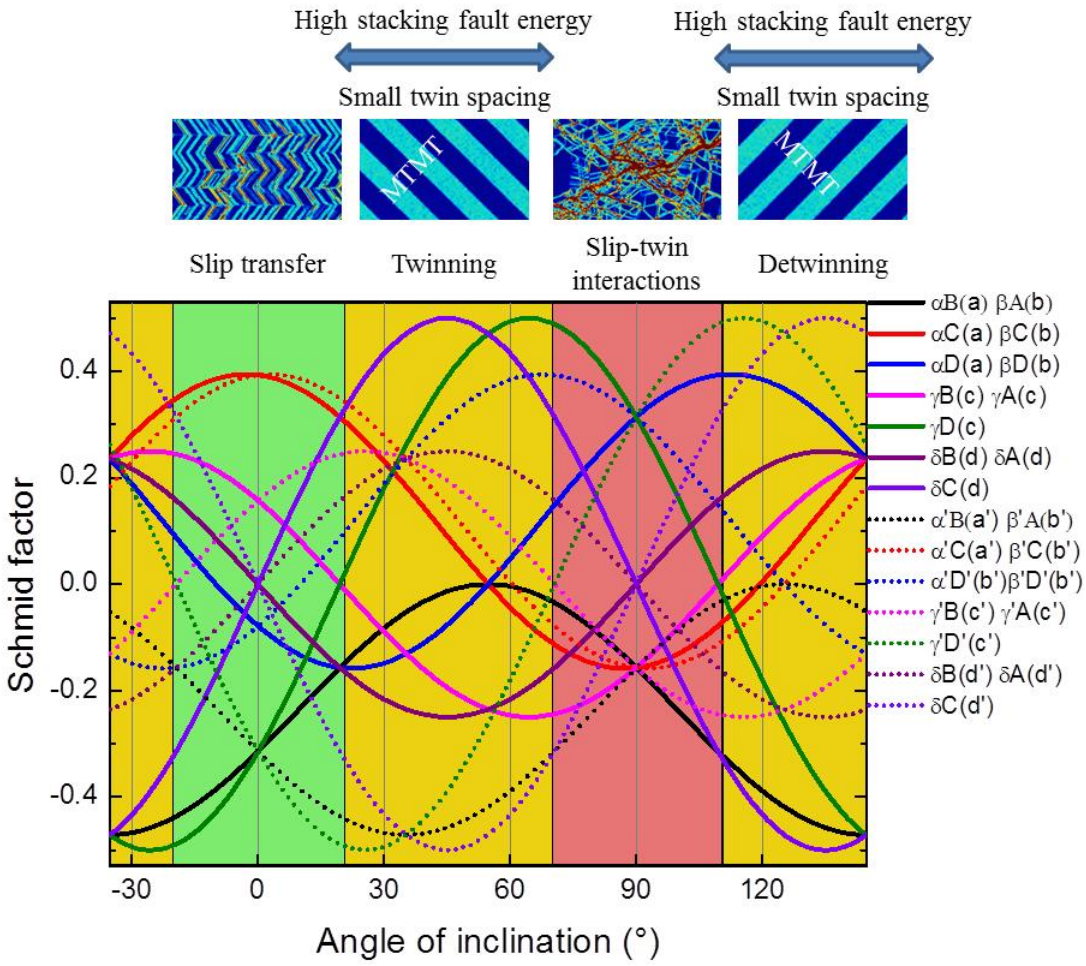

Figure 5.14 The Schmid factors for the {111}<112> slip systems both in the matrix (solid lines) and twinned grain (dash lines) as the TB is inclined to the loading direction by an angle between -35° and 145°.

When the TB is parallel or inclined by an angle less than 30° to the loading axis, two sets of 30° partial dislocations (shown by red lines) in the matrix and in the twin always have the maximum Schmid factors. Slip occurs on these slip systems and can transmit across the TB between the corresponding slip systems because of high stress state on both slip systems. Besides the corresponding 30° trailing partials (black lines) have negative Schmid factors, and the magnitude is comparable to the leading partial. But the nucleation of the trailing partials depends on the structure of the simulation cells. In nanocrystalline Cu without nanotwins, the trailing partials may not nucleate, which lead to the formation of deformation twins in <111> textured Cu as reported in Chapter 4. In nanotwinned models, the transmissions of the leading partials leave sessile Frank partial dislocations on the TBs and the glide of the

leading partials forms stacking fault networks inside the grain, which significantly increase the elastic energy. The triple intersections among the two corresponding stacking faults and the TBs become energetically unstable and trailing partials are nucleated from these intersections. The trailing dislocations interact with the residual dislocations on the TBs to emit new trailing dislocations across the TB. The glide of these trailing dislocations removes the stacking fault networks inside the grain, which further release the elastic energy. The transmission of the screw dislocation leaves no debris on the TB and the coherency of TB is retained.

The Schmid factors of the corresponding slip systems are the same on the horizontal orientation. And these values change slightly as the inclination angle changes as shown in Figure 5.14. But the yielding is initiated by dislocation processes on slip systems with the second maximum Schmid factor, specifically the matrix slip systems between 0° and 30° (T4A15 and T4A19.5), and the twin slip systems between 0° and -30°. There is some kind of non-Schmid factors effect on dislocation nucleation as slip does not occur on slip systems with the maximum Schmid factor. This can be attributed to the principle of minimum shear (Yamakov et al., 2001). The slip system with the lower Schmid factors has a larger projection along the tensile axis, which means the corresponding dislocations carry more plastic strain. The efficiency of the slip is high and the related friction work is minimal. On the other hand, deformation twinning occurs in grains with the maximum Schmid factors to compensate the shear deformation. The trailing dislocations have opposite projections along the tensile axis and the strain compatibility is fulfilled after their glides.

As the TB orientation angle increases to around 45°, a softening phenomenon occurs, which is represented by a dramatic decrease in the yield stress to around 5 GPa. TB migration via the nucleation and propagation of twinning partials along the TBs takes over the main deformation mechanism (Wang et al., 2010, Zhu and Gao, 2012, You et al., 2013). Figure 5.15 shows the generalized planar fault energy curves for stacking fault formation and TB migration. The energy barriers associated with the nucleation of a partial dislocation and a twinning dislocation can be obtained from these curves. It can be seen that the TB migration has a slight smaller energy barrier

than stacking fault formation. So the nucleation of twining partials on the TBs is energetically favourable. The substantial decrease in yield stress confirms the low energy barrier for the nucleation of a twinning partial dislocation. The average CRSS is about 2.4 GPa, much lower than other groups (Figure 5.9).

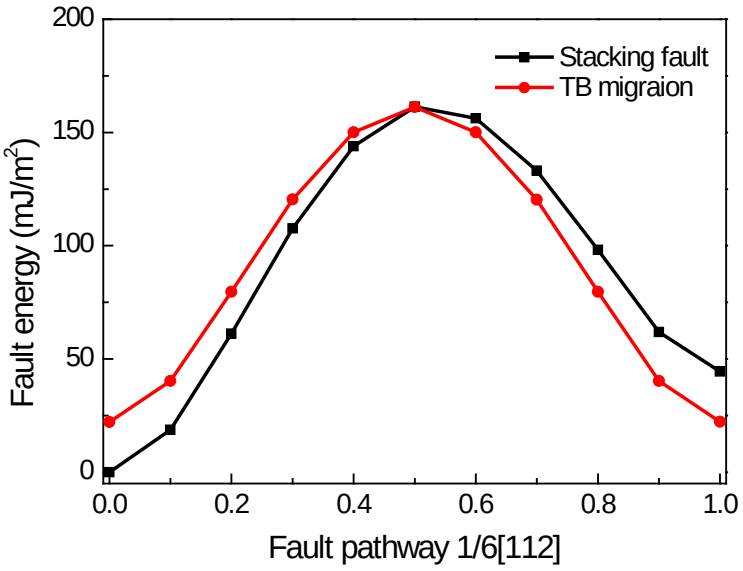

Figure 5.15 Generalized planar faults energy curves for Cu.

The continuous TB migration eventually leads to the disappearance of the original TBs. Two possible pathways are available for the elimination of the TBs. The first one is growth of the twins through continuous twinning. When the TB is inclined by an angle between 30° and 60° to the loading axis, a slip system (shown by violet lines) on the twin plane has the maximum Schmid factor. If the angle of inclination is between 30° and 60°, the maximum Schmid factor is in the matrix grain, and its activation leads to the expansion of growth twins. The second one is shrinkage of the twins through continuous detwinning. If the angle is between -30°(150°) and -60° (120°), the maximum Schmid factor is in the twinned grain, its activation results in the shrinkage of the growth twins or the growth of the matrix. The reversible twinning and detwinning processes also can be obtained by changing the loading direction.

The difference in energy barriers for stacking fault formation and TB migration is quite small. So the nucleation of partial dislocations is possible. Simulations of nanopillars with slanted TBs (A72) revealed the formation of stacking faults (Jang et al., 2012). On the other hand, the energy barriers for TB migration are much smaller than stacking fault formations for Al (Frøseth et al., 2004a) and Pd (Stukowski et al., 2010). So TB migration is energetically favoured irrespective of the TB orientations.

When the TB is orientated nearly perpendicular to the loading axis, 90° partial dislocations (shown by olive and blue lines) in the matrix and twinned grain always have the maximum Schmid factors. These dislocations can transmit across the TB to emit Lomer dislocations. Besides the 30° partial dislocations have much smaller Schmid factors, which may not be activated, thus deformation twinning occurs. The interactions between dislocation and TBs lead to complicated dislocation structures and the formation of shear bands, within which the coherency of TBs is lost.

5.4 Deformation twinning in nanotwinned copper

5.4.1 General observation

Deformation twinning occurs in samples with inclination angle in the range of 15°-30° and 75°-90°. Figure 5.16 shows three typical deformation structures (T4A19.5, T4A75 and T4A90) which contain deformation twins. In sample T4A19 (Figure 5.16a), the dislocation process is accompanied by a small amount of deformation twinning. The mechanical twins are formed in the twinned grain, while slip activities dominate in the matrix grain. These twins are only several layers of atoms thick and are embedded in the twinned grains, in contact with the growth TBs. Moreover the thin twin plates are not stable and can be eliminated during later deformation. But most of the growth TBs retain their original coherency even after a considerable deformation.

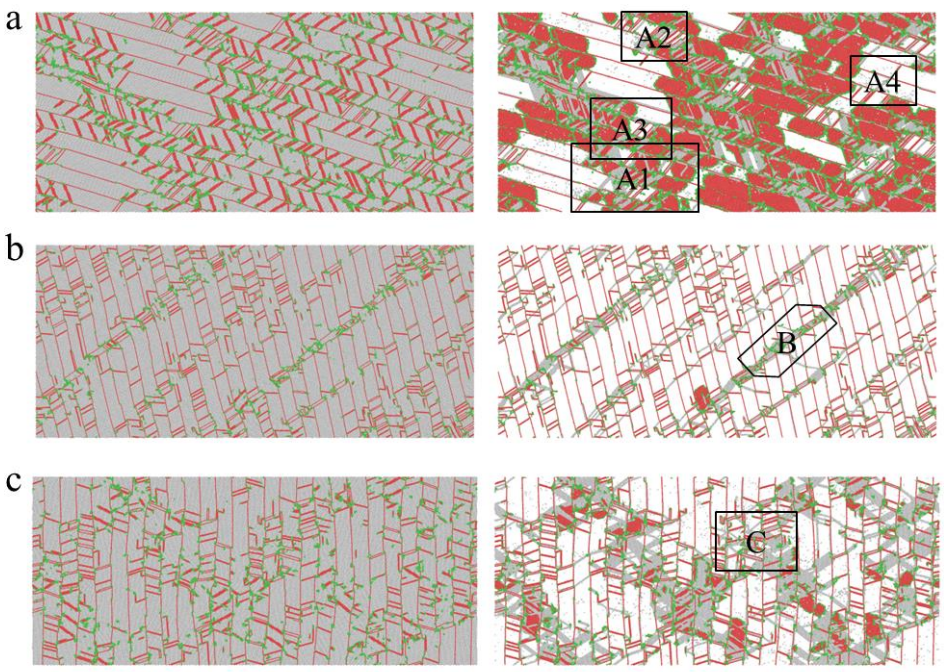

Figure 5.16 Typical deformation structures containing deformation twins. (a) T4A19.5 at 9.3% strain, (b) T4A75 at 7.5% strain (c) T4A90 at 9% strain. In the right figures, perfect fcc atoms that are not involved in the plastic deformation are eliminated for clarity.

Extensive deformation twinning takes place in the matrix grain in sample T4A75 as shown in Figure 5.16b. These twinning partials continuously transmit across the growth TBs, which leads to the formation of parallel shear bands across the sample. In sample T4A90 (Figure 5.16c), deformation twinning occurs both in the matrix and twinned grain. The interactions between dislocations and the growth TBs lead to the formation of complex dislocation networks and intersected slip bands. The mechanical twins in these two cases are more stable while the original growth twins within the shear bands are completely destroyed. The deformation kinetics that leads to the formation of deformation twins will be analysed in detail in the following sections.

5.4.2 Deformation twinning in sample T4A19.5

In sample T4A19.5, the tensile deformation was applied along the [11-1] direction. It is well known that fcc metals twin in tension along the <111> direction. But in the

present simulations of nanotwinned models, no twinning occurs in the matrix grains. In contrast, twinning takes place in the twinned grains.

To reveal the dislocation processes involved in the formation of deformation twins, a small part of the simulation cells is extracted for further analysis. Figure 5.17 shows the dislocation structure evolutions of Region A1 in Figure 5.16. The deformation twinning is initiated by homogenous nucleation of a partial dislocation **γ'B** from the twinned grain, the glide of which leaves an intrinsic stacking fault. Very quickly a second Shockley dislocation **γ'A** is emitted from the upper end of the stacking fault, which combines with the first partial to form a new Shockley partial **Dγ'**. This combination can be summarised as:

$$\gamma' A_{(c')} + \gamma' B_{(c')} \rightarrow D' \gamma'_{(c')} \tag{5.1}$$

Or in vector form:

$$\frac{1}{18}[2\bar{7}\bar{1}]_{(\bar{1}\bar{1}5)} + \frac{1}{18}[\bar{7}2\bar{1}]_{(\bar{1}\bar{1}5)} \rightarrow \frac{1}{18}\left[\bar{5}\bar{5}\bar{2}\right]_{(\bar{1}\bar{1}5)} \tag{5.1a}$$

with

$$\begin{aligned} \frac{1}{18}[2\bar{7}\bar{1}]_{(\bar{1}\bar{1}5)} &= \frac{1}{6}[2\bar{1}1]^T_{(\bar{1}\bar{1}1)^T} \\ \frac{1}{18}[\bar{7}2\bar{1}]_{(\bar{1}\bar{1}5)} &= \frac{1}{6}[\bar{1}21]^T_{(\bar{1}\bar{1}1)^T} \\ \frac{1}{18}\left[\bar{5}\bar{5}\bar{2}\right]_{(\bar{1}\bar{1}5)} &= \frac{1}{6}[112]^T_{(\bar{1}\bar{1}1)^T} \end{aligned} \tag{5.1b}$$

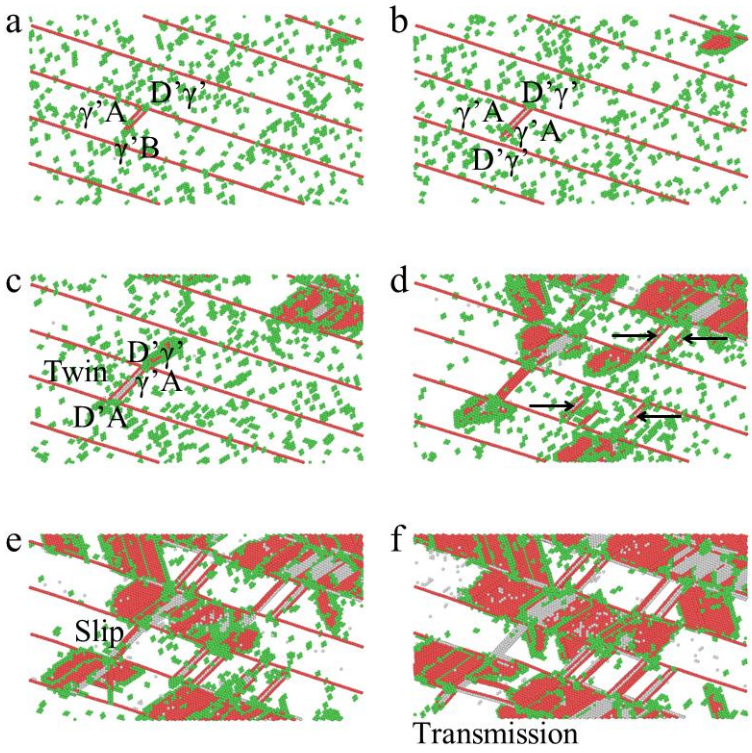

Figure 5.17 Deformation twinning in sample T4A19.5 (Region A1). (a) The nucleation of a deformation twin through the glide of a double-Shockley dislocation at 8.6% strain. (b) The nucleation of another double-Shockley partial at 8.63% strain. (c) The formation of a three-layer deformation twin at 8.7% strain. (d) Extensive deformation twins are formed at 8.78% strain. (e) Glides of trailing partials eliminate deformation twins at 8.84% strain. (f) Dislocation structure and the transmission of a Lomer dislocation at 8.94% strain.

At the lower end, these two Shockley partials form a double-Shockley dislocation **γ'A-γ'B**. Thus an extrinsic stacking fault or a one-layer deformation twin is formed after their glide as shown in Figure 5.17a.

The same multiplication also occurs in the lower end of the stacking fault (Figure 5.17b). The combination of the three Shockley dislocation forms a triple dislocation with a total burgers vector equal to **DA**. This reaction can be expressed as:

$$D'\gamma'_{(c')} + \gamma' A_{(c')} \rightarrow D' A_{(c')} \tag{5.2}$$

Or in vector form:

$$\frac{1}{18}[\bar{5}\bar{5}\bar{2}]_{(\bar{1}\bar{1}5)} + \frac{1}{18}[2\bar{7}\bar{1}]_{(\bar{1}\bar{1}5)} \rightarrow \frac{1}{6}[\bar{1}\bar{4}\bar{1}]_{(\bar{1}\bar{1}5)} \tag{5.2a}$$

with

$$\begin{aligned} \frac{1}{18}[\bar{5}\bar{5}\bar{2}]_{(\bar{1}\bar{1}5)} &= \frac{1}{6}[112]^{T}_{(\bar{1}\bar{1}1)^{T}} \\ \frac{1}{18}[2\bar{7}\bar{1}]_{(\bar{1}\bar{1}5)} &= \frac{1}{6}[2\bar{1}1]^{T}_{(\bar{1}\bar{1}1)^{T}} \\ \frac{1}{6}[\bar{1}\bar{4}\bar{1}]_{(\bar{1}\bar{1}5)} &= \frac{1}{2}[101]^{T}_{(\bar{1}\bar{1}1)^{T}} \end{aligned} \tag{5.2b}$$

After the glide of the above three dislocations, a three-layer microtwin is produced (Figure 5.17c). Later on, a large number of twin nuclei are formed in the twinned grain through the nucleation of double-Shockley partials as shown in Figure 5.17d. These microtwins can grow if other dislocations nucleate on neighbouring slip plane and combine with the twin nucleus.

The deformation twins are not stable as the trailing partial has a higher Schmid factor. The glide of a trailing partial changes the twinned fcc atoms to hcp atoms (Figure 5.17d). Further movement of another two trailing partials eliminates the deformation twins (Figure 5.17e) and restores the original fcc structure (Figure 5.17f). The tendency for the nucleation of trailing dislocation restricts the growth of the deformation twins and only thin twin plates are formed.

Figure 5.18 shows the dislocation structure evolutions of Region A2 in Figure 5.16. It can be seen that the deformation twins can grow thicker by the agglomeration of small twin nuclei (Christian and Mahajan, 1995). The first step in this twin formation is the nucleation of a partial dislocation at 8.73% strain (Figure 5.18a). Within a short while, three twin nucleuses are formed independently as indicated by the arrows in Figure 5.18b. Two of these deformation twins assemble with each other to form a six-layer twin and a stacking fault is left inside the twinned region, which will be absorbed later (Figure 5.18c). The growing deformation twin is then connected with the left two-layer twin nucleated from glide of a double-Shockley partial (Figure 5.18d). These twins can either be treated as a single twin containing a stacking fault or a pile-up of two separate twins. The formation of this deformation twin takes place

almost instantaneously within a stain of 0.1% and can give an insight into the formation of transformation twins.

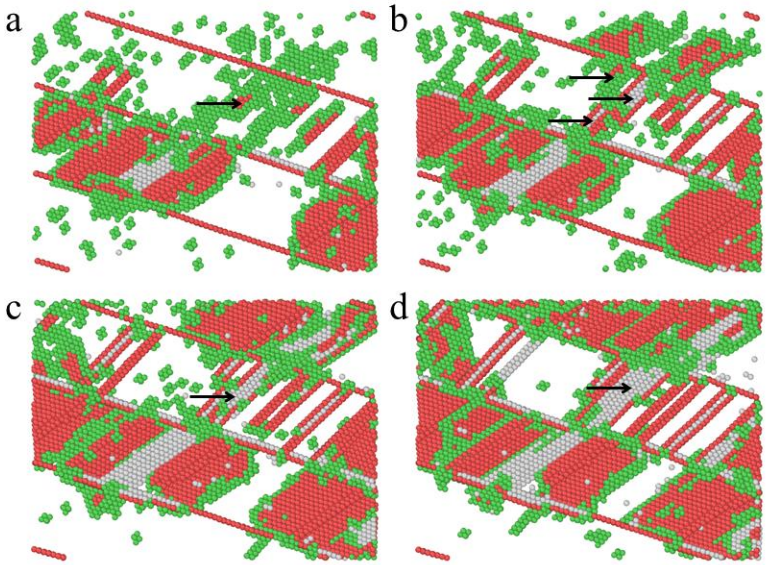

Figure 5.18 The growth of deformation twins through the agglomeration of twin nuclei (Region A2). (a) Dislocation nucleation at 8.73% strain. (b) The independent formation of three mechanical twins at 8.76% strain. (c) The overlap of two deformation twins at 8.79% strain. (d) Another agglomeration at 8.83% strain.

Figure 5.19 shows the dislocation structure evolutions of Region A3 in Figure 5.16, where the shrinkage of the original growth twins is revealed. This twin first grows by two atomic layers due to the glide of two twinning dislocations **δC** as shown in Figure 5.19a. In the twinned grain, a three-layer twin fault is connected with an intrinsic stacking fault. A Shockley partial **δA** is emitted from the deposited dislocation on the growth TB, the glide of which reduces the twin thickness by one atomic layer. Another partial dislocation **δB** is nucleated which has an equal edge component with **δA**. This dislocation climbs downwards and its slip further thins the growth twin. This twin is further decreased by two atomic layers through the nucleation and propagation of dislocation **δA** (Figure 5.19b) and **δB** (Figure 5.19c). Then a Shockley dislocation is nucleated and its glide eliminates the stacking fault within the newly formed mechanical twin (Figure 5.19d). This process can further thin the growth twin as shown in Figure 5.16a. It can be seen that the glide of dislocation of different types leads to the shrinkage of growth twins, just like the detwinning process reported above.

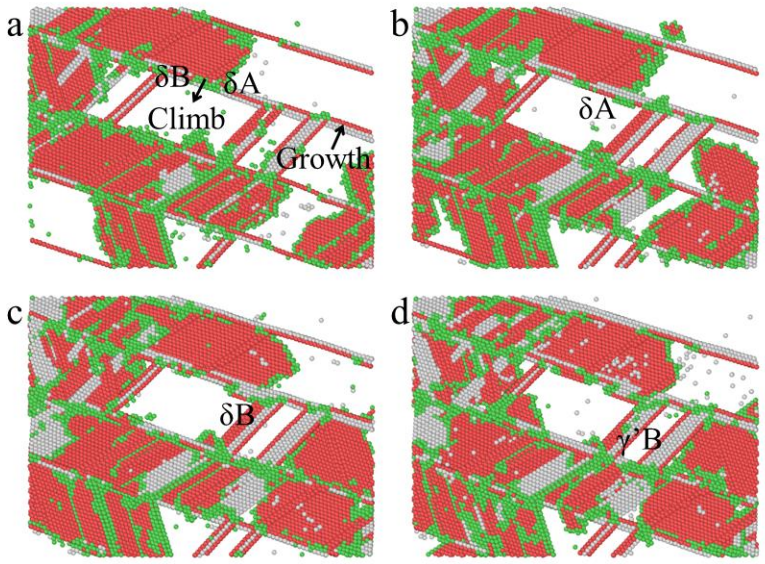

Figure 5.19 The shrinkage of original growth twins through the glide of dislocation of different types (Region A3). (a) The glide of a dislocation dissociated from the deposited dislocations reduces the twin thickness at 8.8% strain. (b) Climb of a partial dislocation, the slip of which further thins the growth twin, and the nucleation of a dislocation at 8.37% strain. (c) Further shrinkage of the growth twins at 8.94% strain. (d) Growth of a deformation twin at 8.99% strain.

The formation of deformation twins involves the successive glide of dislocations on adjacent slip planes. These dislocations are of different types so the plastic strain is halved after the overlap of dislocation cores. But the equal edge component of these dislocations produces a step of a height equal to 1/3 of the {111} interplanar spacing on the twin plane. So groups of three or more twinning dislocations can give steps with heights of larger than a unit height. The pile-up of twinning dislocations causes a high stress concentration on the original growth TBs. Accommodating slip is needed to release these stress (Christian and Mahajan, 1995).

Figure 5.20 shows the reaction between twinning dislocations and the TB of Region A4 in Figure 5.16. At first a Shockley dislocation **Dγ'** from the overlap of two twinning dislocations is deposited on the TB (Figure 5.20a). Another twinning dislocation **γ'A** is nucleated and combined with the deposited dislocation to form a full dislocation **D'A** on the TB. This dislocation transmits across the TB and a Lomer dislocation is **CD** emitted in the matrix grain, while leaving a partial dislocation **Bδ** on the TB (Figure 5.20b). This transmission process can be expressed as:

$$D'A_{(c')} \rightarrow CD_{(001)} + B\delta_{(d)} \tag{5.3}$$

Or in vector form:

$$\frac{1}{6}[\bar{1}\bar{4}\bar{1}]_{(\bar{1}\bar{1}5)} \rightarrow \frac{1}{2}[\bar{1}\bar{1}0]_{(001)} + \frac{1}{6}[2\bar{1}\bar{1}]_{(111)} \tag{5.3a}$$

with:

$$\frac{1}{6}[\bar{1}\bar{4}\bar{1}]_{(\bar{1}\bar{1}5)} = \frac{1}{2}[101]^{T}_{(\bar{1}\bar{1}1)^{T}} \tag{5.3b}$$

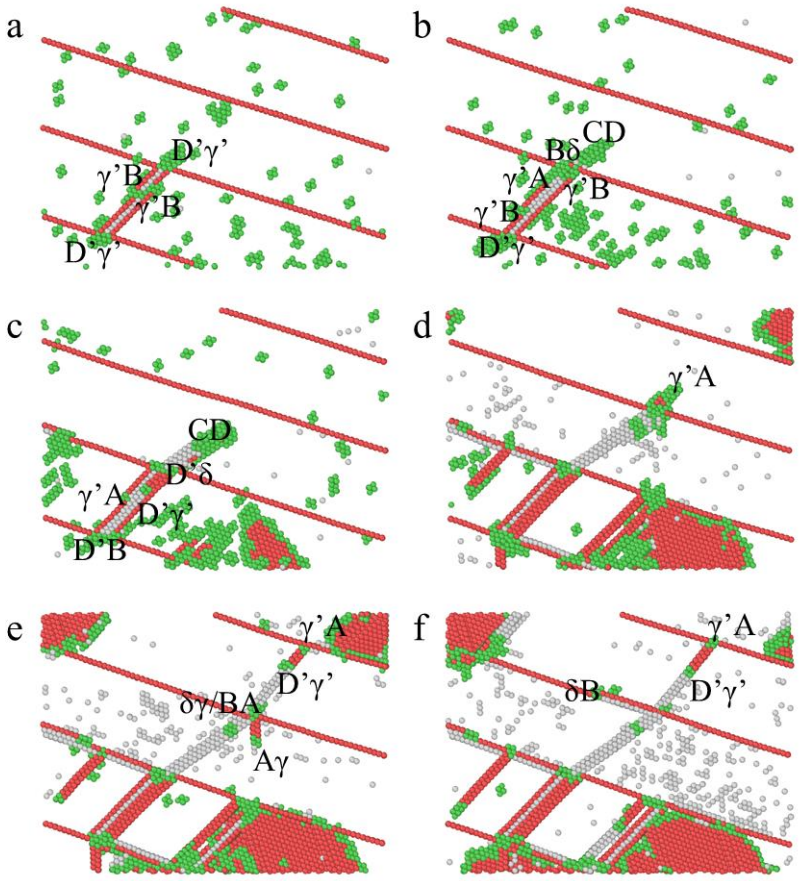

Figure 5.20 Slip-twin interactions in sample T4A19.5 (Region A4). (a) The formation of a three-layer deformation twin at 8.76% strain. (b) Nucleation of another twinning dislocation and the transmission of a full dislocation to emit a Lomer dislocation at 8.79% strain. (c) The motion of Lomer dislocation and the nucleation of a trailing dislocation at 8.83% strain. (d) The transmission of the Lomer dislocation to emit a leading partial at 8.93% strain. (e-f) The full transformation of Lomer dislocation to form an extended dislocation at 9.0% strain and at 9.22% strain.

The left dislocation **Bδ** interacts with another twinning partial **γ'B** to form a stair-rod dislocation **γ'δ** on the TB according to **γ'B+Bδ→γ'δ**. The stair-rod dislocation then

combines with a trailing partial **D'γ'** to form a Frank dislocation **D'δ** on the TB according to **γ'δ+D'γ'→D'δ** (Figure 5.20c).

The Lomer dislocation glides on anomalous (001) plane in the matrix grain. This dislocation **CD** is also a possible slip direction on slip planes (a) and (b). The screw segment of this dislocation may cross-slip to these conventional {111} slip planes and split into two Shockley partials according to **CD→Cα+αD** and **CD→Cβ+βD**. But detailed analysis reveals the stress state on the extended dislocation, with a compressive stress on the leading partial and a tensile stress on the trailing partial, restricts this dissociation (Beyerlein et al., 2014). The main motion of the Lomer dislocation occurs on {001} plane until it is blocked by the TB (Figure 5.20d). Then this Lomer dislocation transmits across the TB and a leading partial **γ'A** is emitted in the twinned grain. In a short while, a trailing partial **D'γ'** is emitted on the same slip plane, so an extended dislocation is formed in the twinned grain, which leaves a Shockley dislocation in the matrix grain and a stair-rod dislocation on the TB (Figure 5.20e). Later on, the residual dislocation is contracted to form a twinning dislocation which can freely move on the TB (Figure 5.20f). This transmission process can be summarised as:

$$CD_{(001)} \rightarrow \gamma' A_{(c')} + D'\gamma'_{(c')} + \delta B_{(d)} \tag{5.4}$$

Or in vector form:

$$\frac{1}{2}[\bar{1}\bar{1}0]_{(001)} \rightarrow \frac{1}{18}[2\bar{7}\bar{1}]_{(\bar{1}\bar{1}5)} + \frac{1}{18}\left[\bar{5}\bar{5}\bar{2}\right]_{(\bar{1}\bar{1}5)} + \frac{1}{6}[\bar{2}11]_{(111)} \tag{5.4a}$$

with

$$\begin{aligned} \frac{1}{18}[2\bar{7}\bar{1}]_{(\bar{1}\bar{1}5)} &= \frac{1}{6}[2\bar{1}1]^T_{(\bar{1}\bar{1}1)^T} \\ \frac{1}{18}\left[\bar{5}\bar{5}\bar{2}\right]_{(\bar{1}\bar{1}5)} &= \frac{1}{6}[112]^T_{(\bar{1}\bar{1}1)^T} \end{aligned} \tag{5.4b}$$

Reaction (5.4) is a reverse path of reaction (5.3).

The Lomer dislocation may transmit to neighbouring slip planes. A typical transmission involves the formation of a three-layer deformation twin as indicated in the left corner of Figure 5.17f. This process can be expressed as:

$$CD_{(001)} \rightarrow 2 \times \gamma' A_{(c')} + \gamma' B_{(c')} + \delta B_{(d)} \tag{5.5}$$

Or in vector form:

$$\frac{1}{2}[\bar{1}\bar{1}0]_{(001)} \rightarrow 2 \times \frac{1}{18}[2\bar{7}\bar{1}]_{(\bar{1}\bar{1}5)} + \frac{1}{18}[\bar{7}2\bar{1}]_{(\bar{1}\bar{1}5)} + \frac{1}{6}[\bar{2}11]_{(111)} \tag{5.5a}$$

with

$$\begin{aligned} \frac{1}{18}[2\bar{7}\bar{1}]_{(\bar{1}\bar{1}5)} &= \frac{1}{6}[2\bar{1}1]^{T}_{(\bar{1}\bar{1}1)^{T}} \\ \frac{1}{18}[\bar{7}2\bar{1}]_{(\bar{1}\bar{1}5)} &= \frac{1}{6}[\bar{1}21]^{T}_{(\bar{1}\bar{1}1)^{T}} \end{aligned} \tag{5.5b}$$

Reaction (5.5) may also derive from reaction (5.4), as dislocation **D'γ'** can dissociate according to the reverse path of equation (5.1) (Christian and Mahajan, 1995).

5.4.3 Deformation twinning in sample T4A75

Figure 5.21 reveals the nucleation of deformation twins in sample T4A75 (Region B in Figure 5.16). In this sample, the tensile deformation was applied along the [221] direction. The plastic deformation is initiated by a homogenous dislocation nucleation in the matrix grain. This dislocation **γD** has a pure edge nature and its glide creates a step with a height equal to 2/3 of the {111} interplanar spacing on the TB. Under the high stress state, this dislocation can transmit across the TB and a Lomer dislocation **D'C** is formed in the twinned grain, which leaves a Hirth dislocation **γC/DD'** on the TB (Figure 5.21a). This transmission is expressed as:

$$\gamma D_{(c)} \rightarrow D'C_{(\bar{2}\bar{2}1)} + \gamma C/DD' \tag{5.6}$$

Or in vector form:

$$\frac{1}{6}[\bar{1}\bar{1}\bar{2}]_{(\bar{1}\bar{1}1)} \rightarrow \frac{1}{6}[\bar{1}\bar{1}\bar{4}]_{(\bar{2}\bar{2}1)} + \frac{1}{3}[001] \tag{5.6a}$$

with

$$\frac{1}{6}[\bar{1}\bar{1}\bar{4}]_{(\bar{2}\bar{2}1)} = \frac{1}{2}[110]^{T}_{(001)^{T}} \tag{5.6b}$$

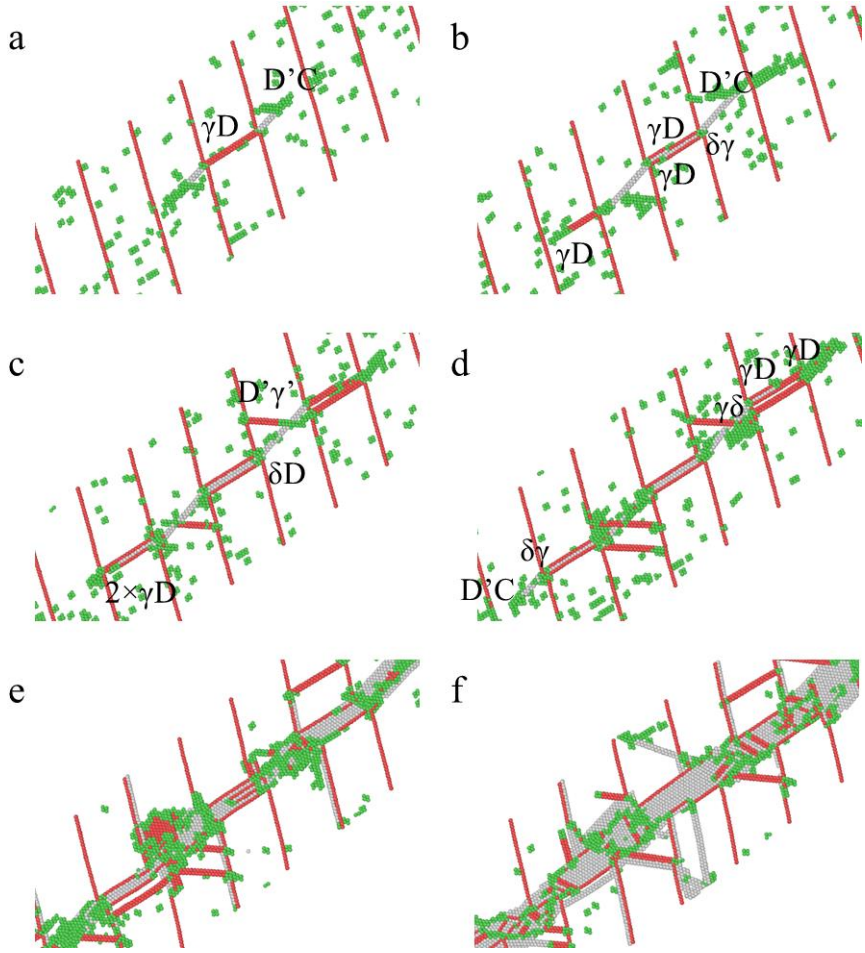

Figure 5.21 Deformation twinning and dislocation-TB interactions in sample T4A75 (Region B). (a) The transmission of a Shockley partial across the TB to Lomer dislocations in the twinned grain at 6.4% strain. (b) The emission of another two Shockley partials and their combinations with the residual dislocation on the TB and the motion of Lomer dislocations at 6.45% strain. (c) The dissociation of a Lomer dislocation at 6.5% strain. (d) The transmission of Lomer dislocations at 6.55% strain. (e) Further growth of deformation twins at 6.8% strain. (f) The formation of a shear band from complicated dislocation-TB interactions at 7.5% strain.

The motion of the Lomer dislocation produces a step with a height of a unit interplanar spacing, which cause a discrepancy between the displacements across the TB. So a second Shockley dislocation **γD** is emitted from the right intersection of the stacking fault and the TB as the plastic strain increases. This dislocation interacts with the residual Hirth dislocation to form a stair-rod dislocation **δγ** on the TB (Figure 5.21b). This combination can be expressed as:

$$\gamma C/DD' + \gamma D_{(c)} \rightarrow \delta\gamma \tag{5.7}$$

Or in vector form:

$$\frac{1}{3}[001] + \frac{1}{6}[\bar{1}\bar{1}\bar{2}]_{(\bar{1}\bar{1}1)} \rightarrow \frac{1}{6}[\bar{1}\bar{1}0] \tag{5.7a}$$

A third Shockley dislocation **γD** is emitted from the left intersection of the stacking fault and the TB, which interacts with the stair-rod dislocation to form a Frank dislocation **δD** on the TB according to **γD+ δγ → δD** (Figure 5.21c). A three-layer microtwin is formed after the glide of the twinning dislocation.

As the Lomer dislocation propagates, part of the dislocation line can dissociate into a conventional Shockley dislocation **D'γ'** and a Frank dislocation **γ'C** perpendicular to the slip plane. The Frank dislocation is annihilated after the Lomer dislocation swipes away and the Shockley dislocation is retained as shown in Figure 5.21c. This split can be expressed as:

$$D'C_{(\bar{2}\bar{2}1)} \rightarrow D'\gamma'_{(c')} + \gamma'C \tag{5.8}$$

Or in vector form:

$$\frac{1}{6}[\bar{1}\bar{1}\bar{4}]_{(\bar{2}\bar{2}1)} \rightarrow \frac{1}{18}\left[\bar{5}\bar{5}\bar{2}\right]_{(\bar{1}\bar{1}5)} + \frac{1}{9}\left[11\bar{5}\right] \tag{5.8a}$$

with

$$\begin{aligned} \frac{1}{6}[\bar{1}\bar{1}\bar{4}]_{(\bar{2}\bar{2}1)} &= \frac{1}{2}[110]^T_{(001)^T} \\ \frac{1}{18}\left[\bar{5}\bar{5}\bar{2}\right]_{(\bar{1}\bar{1}5)} &= \frac{1}{6}[112]^T_{(\bar{1}\bar{1}1)^T} \\ \frac{1}{9}\left[11\bar{5}\right] &= \frac{1}{3}[11\bar{1}]^T \end{aligned} \tag{5.8b}$$

The Lomer dislocation keeps gliding on $(001)^T$ plane until being blocked by the TB. This Lomer dislocation then transmits across the TB and two Shockley partials are emitted on neighbouring slip plane in the matrix grain while leaving a stair-rod dislocation on the TB (Figure 5.21d). This slip transfer can be summarised as:

$$D'C_{(\bar{2}\bar{2}1)} \rightarrow 2 \times \gamma D_{(c)} + \gamma\delta \tag{5.9}$$

Or in vector form:

$$\frac{1}{6}[\bar{1}\bar{1}\bar{4}]_{(\bar{2}\bar{2}1)} \rightarrow 2 \times \frac{1}{6}[\bar{1}\bar{1}\bar{2}]_{(\bar{1}\bar{1}1)} + \frac{1}{6}[110] \tag{5.9a}$$

with

$$\frac{1}{6}[\bar{1}\bar{1}\bar{4}]_{(\bar{2}\bar{2}1)} = \frac{1}{2}[110]^{T}_{(001)^{T}} \tag{5.9b}$$

Reaction (5.9) is the reverse path of reaction (5.6) and (5.7). So an extrinsic stacking fault is formed through the slip transmission.

Alternatively, this Lomer dislocation may split into two partial dislocations connected by a sessile stair-rod dislocation, forming a Cottrell-Lomer lock as shown in Figure 5.16b. The formation of this triad of dislocation agrees well with classic dislocation theory (Weertman and Weertman, 1992) and can be expressed as:

$$D'C_{(\bar{2}\bar{2}1)} \rightarrow D'\gamma'_{(c')} + \gamma'\delta + \delta C_{(d)} \tag{5.10}$$

Or in vector form:

$$\frac{1}{6}[\bar{1}\bar{1}\bar{4}]_{(\bar{2}\bar{2}1)} \rightarrow \frac{1}{18}\left[\bar{5}\bar{5}\bar{2}\right]_{(\bar{1}\bar{1}5)} + \frac{1}{18}[\bar{1}\bar{1}\bar{4}] + \frac{1}{6}[11\bar{2}]_{(111)} \tag{5.10a}$$

with

$$\begin{aligned} \frac{1}{6}[\bar{1}\bar{1}\bar{4}]_{(\bar{2}\bar{2}1)} &= \frac{1}{2}[110]^{T}_{(001)^{T}} \\ \frac{1}{18}\left[\bar{5}\bar{5}\bar{2}\right]_{(\bar{1}\bar{1}5)} &= \frac{1}{6}[112]^{T}_{(\bar{1}\bar{1}1)^{T}} \\ \frac{1}{18}[\bar{1}\bar{1}\bar{4}] &= \frac{1}{6}[110]^{T} \end{aligned} \tag{5.10b}$$

These processes can further proceed. The deformation twins grow though the continuous nucleation and propagation of the twinning dislocation on adjacent slip plane in the matrix grain (Figure 5.21e and f). In Figure 5.21e, a double-Shockley partial can be seen in the twinned matrix grains.

5.4.4 Deformation twinning in sample T4A90

Figure 5.22 shows the dislocation structure evolution in sample T4A90 (Region C in Figure 5.16). Extensive deformation twinning takes place in addition to conventional dislocation slip during the deformation. The mechanism for deformation twinning

involves the successive glide of twinning partials on adjacent slip planes. In this sample, the tensile deformation was applied along the [111] direction. Therefore the slip systems in the matrix and twinned grain are equivalent, so the plastic strain is more uniformly distributed, unlike sample T4A75, where a primary slip system in the matrix grain dominates the deformation. Deformation twins are observed in both the matrix and twinned grains. Although the stacking fault energy for Cu is low, a high density of mechanical twins leads to a significant energy increase as the twin spacing is only 4 nm, which supresses the growth of mechanical twins. The deformation twins may be eliminated by the glide of trailing partials and dislocation slip replaces deformation twinning.

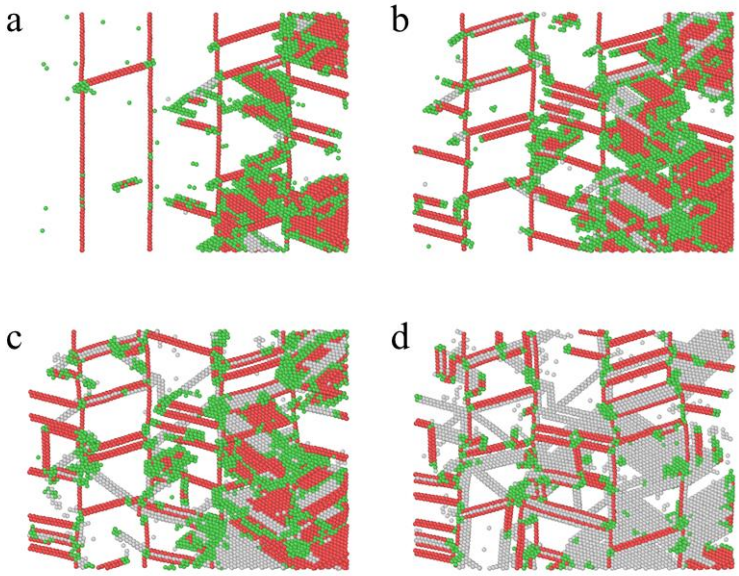

Figure 5.22 Deformation twinning and dislocation-TB interactions in sample T4A90 (Region C). (a) 8.3% strain. (b) 8.4% strain. (c) 8.5% strain. (d) 9% strain.

5.4.5 Discussion

5.4.5.1 Deformation twinning mechanisms

The existence of growth TBs causes a change in the deformation mechanism in the matrix grain in sample T4A19.5, from deformation twinning in Cu single crystal under $[11\bar{1}]$ tensile deformation to dislocation slip in nanotwinned model. The plastic deformation is dominated by the transmission of screw dislocation across the TB as previously reported in nanotwinned Cu (Morris Wang et al., 2013, You et al.,

2013, Wu et al., 2009). The yielding is initiated by the nucleation of Shockley partial dislocations **αC** and **βC** in the matrix grain with a lower Schmid factor than the corresponding slip systems **α'C** and **β'C** in the twinned grain. Dislocation nucleation cannot simply be decided by the Schmid's law. A leading partial in the matrix grain has a projection of 0.943 of its Burgers vector along the tensile axis while the projection in the twinned grain is only 0.629. So slip in the matrix grain contributes more to the plastic deformation, as dislocation is the carrier of plastic strain. The shear displacement along this slip direction produces the maximum strain, which agrees well with the principle of minimal shear (Yamakov et al., 2001).

Other activated slip systems in the twinned grain in sample T4A19.5, are **γ'A** and **γ'B** on the slip plane (c), which have a slight lower Schmid factor of 0.2444 than **βC** and **αC** of 0.3143. After the nucleation of a Shockley partial, either **γ'A** or **γ'B**, the other one would be emitted on neighbouring slip plane instead of nucleation of a trailing dislocation **Dγ'** on the same slip plane. The trailing dislocation can only be emitted after the leading partial swipe over the splitting distance of an extended dislocation due to the mutual repulsive force (Yamakov et al., 2001). On the other hand, the Shockley partials **γ'A** and **γ'B** have opposite screw components that promotes their successive nucleation. The two Shockley dislocations are attracted with each other and combined to form a double-Shockley with a net Burgers vector equal to Dγ'. The Schmid factor of this dislocation is 0.4889, the sum of the two composing dislocations, so it can easily glide. Moreover, the total work of friction during this slip process is halved.

Yamakov et al. (Yamakov et al., 2002a, Yamakov et al., 2002c) revealed that the nucleation of double-Shockley partials left behind extrinsic stacking faults in nanocrystalline Al by MD simulations. Mahajan and Chin (Mahajan and Chin, 1973a) proposed a dislocation reaction **AD+BD→Aγ+γD+Bγ+γD→3×γD**, which led to the nucleation of a three-layer twin. This mechanism required the dissociation of two coplanar dislocations. Li et al. (Li et al., 2009) revealed a similar dislocation reaction **Aγ+Bγ+γD→2×γD** that created a two-layer twin embryo under shear along **γD** direction. But later simulations under the same shear deformation, revealed that deformation twinning occurred through successive nucleation and propagation of

Shockley partials **γD** on adjacent slip planes (Daphalapurkar and Ramesh, 2012). On the other hand, shear deformation along the reverse direction of **γD** revealed another type of deformation twinning. This hard twin was developed through simultaneous and cooperative activation of **γA** and **γB** (Daphalapurkar and Ramesh, 2012), which agrees with present simulations.

The double-Shockley partial dislocation has a net Burgers vector of a single partial dislocation. In situ nanoindentation of bimetal Cu/Nb composite revealed the formation of a two-layer twin nucleus by alternative nucleation of two partial dislocations of different types (Zheng et al., 2012). Further analysis revealed the twin growth was due to motion of mixed twinning partials with zero net Burgers vectors, as evidenced by the flat interface after twinning (Zheng et al., 2013). This zero macroscopic strain twinning mechanism involving simultaneous nucleation of partials with zero net Burgers vector was also observed in nanocrystalline metals (Wu et al., 2008). But the Schmid factors of the three Shockley partials on one slip plane have a relation $m_1+m_2+m_3=0$. The three slip systems cannot be activated simultaneously under normal deformation. The activation of two slip systems on neighbouring slip planes which creates two-layer twin faults would be followed by the inverse slip system with a higher Schmid factors. Dislocation slip takes over the role of deformation from deformation twinning, which restricts the growth of deformation twin. Deformation twins are continuously nucleated and eliminated throughout the simulations, indicating their low stability.

The mechanical behaviour of nanotwinned metals under uniaxial strain perpendicular to the TB has been widely investigated. Most of the researches focus on the incipient plastic deformation and the accompanying slip-twin interactions, which contribute to the high strain rate sensitivity in nanotwinned materials. Under further staining, deformation twinning takes place through motion of twinning partials of the same type on adjacent slip planes in samples with large inclination angles.

5.4.5.2 Orientation dependence of deformation twinning

The simulations reveal that deformation twinning is strongly dependent on the crystallographic orientation in nanotwinned fcc metals. Three types of twin structure

have been identified according to the crystallographic orientation, which to some extent agrees with the twin structure evolution in TWIP steels (Karaman et al., 2000, Gutierrez-Urrutia et al., 2010, Gutierrez-Urrutia and Raabe, 2011). The specific twinning systems changes due to existence of the TB which introduces more slip systems.

In sample T4A19.5, the small amount of deformation twinning contributes little to the plastic deformation. In the twinned grains, the $[11\bar{1}]$ loading direction is close to $[22\bar{1}]$ ($[00\bar{1}]^T$), with an inclination angle of 15.8°. As the inclination angle changes from 15° to 30°, the loading direction intersects with $[00\bar{1}]^T$ direction at angles between 20° and 5°. Similarly, as the inclination angle changes from -15° to -30°, the intersecting angle between the loading direction and the $[00\bar{1}]$ direction in the matrix grains changes from 20° to 5°. In these cases, deformation twinning is expected to occur in the matrix grains. It can be seen deformation twinning occurs in grains oriented close to the <001> direction with an inclination angle between 5° and 20°. Gutierrez-Urrutia (Gutierrez-Urrutia et al., 2010, Gutierrez-Urrutia and Raabe, 2011) systematically investigated the win structure evolution in TWIP steels and distinguished three types of grains according to the twining behaviour. The grains oriented close to <001> directions within an angular range of 15° were characterized by a low deformation twinning activity (Gutierrez-Urrutia et al., 2010, Gutierrez-Urrutia and Raabe, 2011), which agree well with the present simulations (A15-A30). No twin was observed during [001] tension of Hadfield steel single crystal (Karaman et al., 2000).

In sample T4A75, the loading direction [221] is 15° inclined with the [111] orientation. Deformation twinning is only activated on one twinning slip system in the matrix grain. In the present simulations, the twinning results from one twinning system on slip plane (c) (olive dash lines in Figure 5.14). Besides, the two twinning systems on slip planes (a') and (b') are restricted, so only limited dislocations are observed. Due to the structural symmetry, similar deformation twinning is expected to occur in the twinned grain in samples with inclination angles close to 105° or -75°. But this twinning process is different from the twinning in grains oriented between <001> and <111> directions, which also contained twins along one primary twinning

system (Gutierrez-Urrutia et al., 2010, Gutierrez-Urrutia and Raabe, 2011). The primary twinning of grains close to [112] direction (A105 or A-75) in experiments may result from twinning systems on slip planes (a) and/or (b) (blue solid lines in Figure 5.14). These two slip planes have the same projection along the [110] direction on (1-10) plane (Figure 5.3), which means only one sets of parallel slip lines can be seen (Gutierrez-Urrutia et al., 2010, Gutierrez-Urrutia and Raabe, 2011). The [221] orientation of sample T4A75 was not stable and was significantly decreased during deformation in experiment (Gutierrez-Urrutia et al., 2010, Gutierrez-Urrutia and Raabe, 2011). So the twin structure was not well documented.

In sample T4A90, the loading axis is along the [111] direction. Deformation twins are formed in twinning systems on slip planes (c) and (c'). Moreover, dislocation processes are observed on slip planes (a) and (b). Experiments revealed that grains close to <111> orientations were rendered by twins on more than one twinning system (Gutierrez-Urrutia et al., 2010, Gutierrez-Urrutia and Raabe, 2011, Karaman et al., 2000). The intersected slip lines results from twinning systems on slip planes (c) and (a) and/or (b) (Figure 5.3).

5.4.5.3 Slip-twin interactions

The formation of deformation twins creates steps and induces stress concentration on the TBs. Plastic accommodation is needed to release this stress and maintain the strain compatibility across the TB. Previous analysis focused on steps with heights which are integral multiples of the unit interplanar spacing (Christian and Mahajan, 1995). In this way, the shear strain can be fully transmitted. The present simulations reveal the transmission of dislocations which creates steps of height more than 2/3 of the interplanar spacing. The transmission leads to the formation of Lomer dislocation across the growth TB and leaves a residual dislocation. The transmission agrees well with the classic slip transfer criteria. The {001} slip plane of the newly formed Lomer dislocation intersects with the $\{\bar{1}\bar{1}1\}$ slip plane on the growth TB. The Lomer dislocation experiences a high resolved shear stress, as indicated by the maximum Schmid factor. The residual dislocations left on the TB can be a Shockley partial dislocation (reaction (5.3)), a Hirth dislocation (reaction (5.6)) or a stair-rod dislocation (reaction (5.9)), all of which have small Burgers vectors. The Lomer

dislocation contributes to the strain hardening of nanotwinned metals (Afanasyev and Sansoz, 2007, Wu et al., 2009) as its slip involves a higher Peierls energy barrier (Hirth and Lothe, 1982).

5.5 Summary

MD simulations have been conducted to investigate the mechanical response of nanotwinned Cu with different orientations. The simulations reveal a dynamic transition in deformation mechanisms as the TB orientation varies from the horizontal direction, to the slant direction and to the vertical direction. The nature of the dislocation activity in nanotwinned Cu is in agreement with the Schmid's law. And the geometrical relation between the activated slip system and the twin plane determines three distinct dislocation processes. When the TB is parallel or inclined by an angle less than 30° to the loading direction, the plastic deformation is dominated by the transmission of extended screw dislocations. This transmission involves the successive transmissions of the leading and trailing dislocations and leaves the TB intact. As the angle of inclination increases slip systems on the TB plane can be activated. TB migration takes place in addition to slip transfer. When the TB is inclined by an angle between 30° and 60° with respect to the loading axis, TB migration governs the deformation. The TBs are eliminated after full twinning of the matrix grains or detwinning of the twinned grains, depending on the TB orientations, and a single crystal with the same orientation as the twinned grain or the matrix grain is formed. When the TB is inclined by an angle between 60° and 90° to the loading axis, dislocation-TB interactions becomes the dominant deformation mechanism, which leads to complicated dislocation networks and the formation of shear bands. Within the transition region, a combination of two types of slip activities takes place.

Deformation twinning plays an important role in the plastic deformation of nanotwinned Cu with specific crystallographic orientations. Deformation twins are formed by the motion of Shockley partial dislocations on contiguous {111} slip planes. Two mechanisms for the formation of deformation twins are identified based

on the arrangement of these Shockley partials. The first twin nucleation mechanism involves the formation of the double-Shockley partial, which results from the overlap of two Shockley partials of different types. This kind of twinning occurs when the TB is inclined by an angle between 15° and 30° to the loading direction. The formed mechanical twins are thin plates embedded either in the twinned grains or in the matrix grain, which are not sable and can be easily eliminated during later stages of deformation. The second twin formation mechanism results from the passage of Shockley dislocations of the same type. The twinning takes place when the TB is inclined by an angle between 75° and 90° to the loading axis. Deformation twins are well developed along one primary twinning system in samples with inclination angles close to 75°, while multiple twinning takes place both in the matrix and twinned grains in samples with inclination angles close to 90°. The interactions between dislocation and TBs promote the twin formation. The twinning dependence on the crystallographic orientation agrees well with available experimental results.

6 DEFORMATION MECHANISMS IN NANOTWINNED IRON

6.1 Introduction

Recent in situ experiment revealed deformation twinning dominates the plastic deformation in nanocrystalline W (Wang et al., 2015). TB migration became the dominant deformation mechanism after its nucleation and the reversible detwinning phenomenon was observed during unloading process (Wang et al., 2015, Li et al., 2010a). Ojha et al. (Ojha et al., 2014, Ojha and Sehitoglu, 2014) determined the TB migration stress in bcc metals and alloys and investigated the twin-twin reactions. Song et al. (Song et al., 2014) also reported that severe irradiation enhances TB migration in bcc Fe.

Previous simulations focused on the mechanical behaviour of nanotwinned fcc materials, little research has been carried out to investigate the effect of nanotwins on mechanical response of nanocrystalline bcc materials. In this chapter, MD simulations are used to investigate the effects of TB orientation and twin spacing on the mechanical behaviour of nanotwinned Fe. The simulations elucidate the deformation mechanisms of nanotwinned Fe as the TB varies from the horizontal direction, to the slant direction and to the vertical direction. The nature of the dislocation activity in nanotwinned Fe can be interpreted with the aid of Schmid's law to some extent. The plausible dislocation-twin reactions are systematically analysed.

6.2 Methods

Full three-dimensional nanotwinned samples with periodic conditions are used to simulate the response of bulk nanotwinned Fe. Similar methods were used to construct nanotwinned Fe. The slip plane changed to (112) plane and slip direction was $[\bar{1}\bar{1}1]$. Atoms above one (112) plane were shifted along the $[\bar{1}\bar{1}1]$ direction by the magnitude of a twinning partial dislocation $1/6[\bar{1}\bar{1}1]$. Figure 6.1 shows the process of introducing nanoscale twins in bcc Fe.

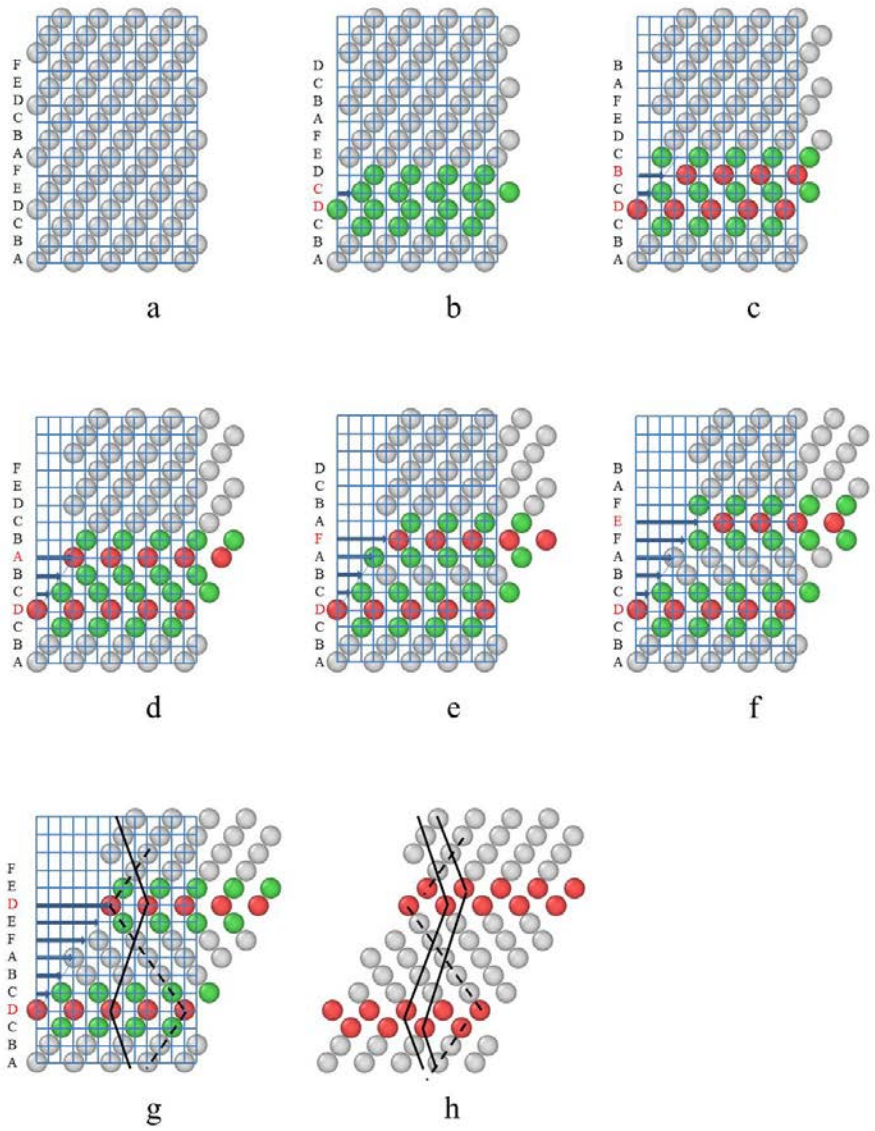

Figure 6.1 The introduction of nanoscale twins in bcc materials.

The initial TB consisted of three-layer of atoms as shown in Figure 6.1g. This structure was not stable and after energy minimization, it transformed into a two-layer structure as shown in Figure 6.1h.

The nanotwinned model with a twin spacing of 4 nm was rotated about the $[1\bar{1}0]$ direction by 0°(A0), 15.8°(A16), 30°(A30), 45°(A45), 60°(A60), 74.2°(A74) and 90°(A90) to obtain the specific twin orientation. Then the rotated samples were cut to get the unit rectangular structure, with length and width varying a little to satisfy

periodic boundary conditions. The unit cell was replicated in three dimensions to get the length around 30 nm and the sample thickness was fixed at 12.11 nm to save the computing time. Figure 6.2 shows the cross sectional view of fabricated sample T4A0, T4A30, T4A60 and T4A90.

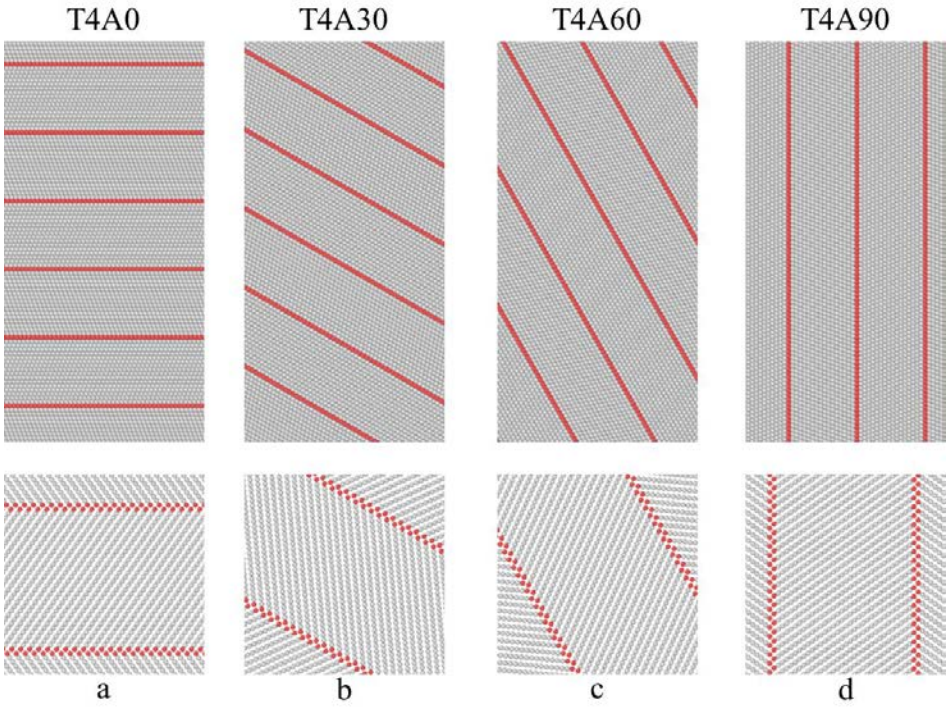

Figure 6.2 Cross sectional view of constructed nanotwinned samples with different orientations. (a) T4A0, (b) T4A30, (c) T4A60, (d) T4A90.

6.3 Results

6.3.1 Stress-strain behaviour

Figure 6.3 shows the stress-strain curves of nanotwinned Fe with a twin spacing of 4 nm (T4) and different TB orientations (A0-A90). It can be seen that TB orientations have a significant influence on the mechanical response of nanotwinned samples.

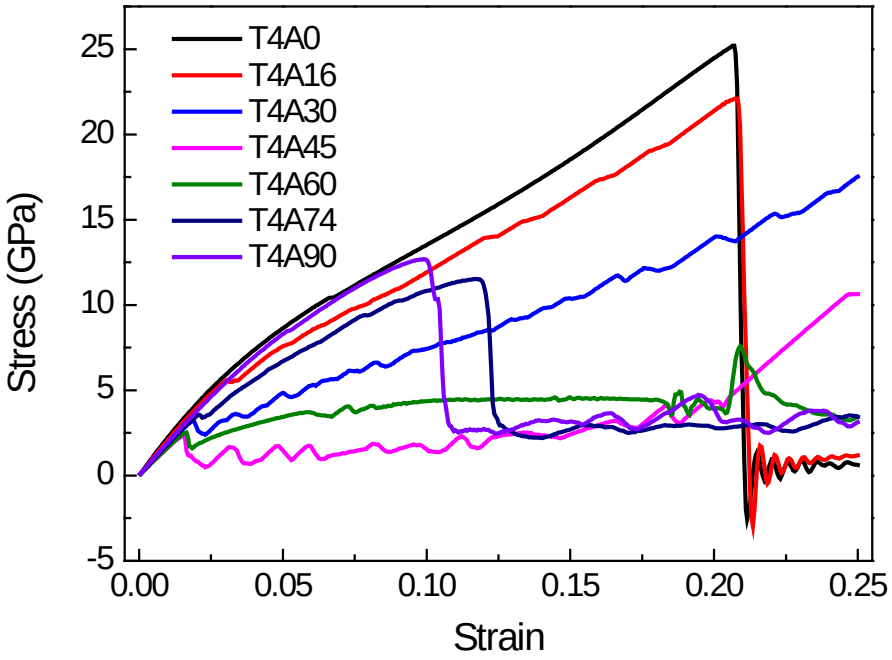

Figure 6.3 The stress-strain curves of samples with twin spacing of 4 nm.

The stress-strain responses of all the samples resemble each other at the initial part of deformation. The stress-strain curves begin to deviate from the linear elastic region at 1% strain. The Young's modulus is defined as the slope of the linear stress-strain curve within the first 1% strain and is plotted as a function of inclination angle in Figure 6.4. It can be seen that the Young's modulus first decreases dramatically as the angle of inclination increases from 0° to 45°, and then increases slightly as the angle increases to 90°. The maximum value of 223.66 GPa is found at the when the loading direction is parallel to the TB. The minimum value is 161.23 GPa 30% less than the maximum value when the TB is 45° inclined to the loading axis. The variation in Young's modulus is due to the change of the crystallographic orientation and they are close to the value of conventional Fe of 211 GPa measured in experiments.

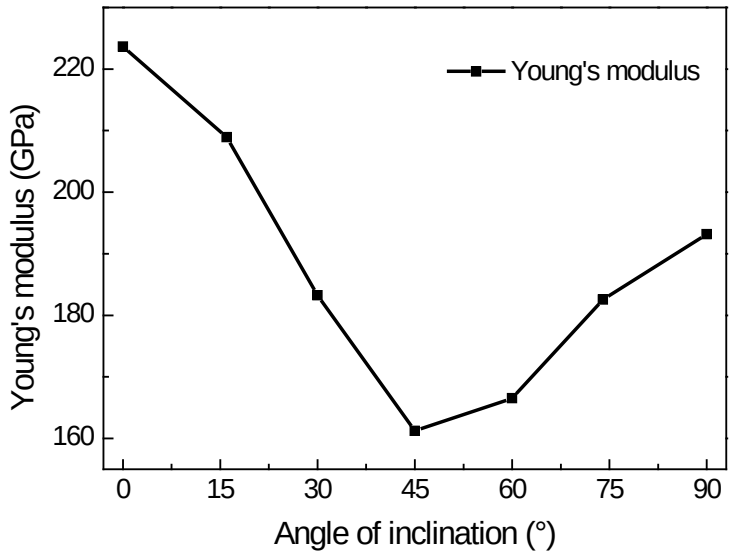

Figure 6.4 The TB orientation dependence of the Young's modulus.

The yield strain ε_y and yield stress σ_y of nanotwinned Fe with different TB orientations were extracted and shown in Table 6.1.

Table 6.1. The mechanical properties of nanotwinned Fe with different TB orientations.

Angle (°)	**Schmid factor**	$\boldsymbol{\varepsilon_y}$ **(%)**	$\boldsymbol{\sigma_y}$ **(GPa)**	**CRSS (GPa)**	**Young's modulus (GPa)**	$\boldsymbol{\varepsilon_m}$ **(%)**	$\boldsymbol{\sigma_m}$ **(GPa)**
0	0.3143	20.7	25.21	**7.92**	223.66		
16	0.2619	3.05	5.60	1.47	208.93	20.75	22.11
30	0.4330	1.9	3.21	1.39	183.25		
45	0.5	1.55	2.35	1.18	161.23		
60	0.4330	1.65	2.52	1.09	166.52		
74	0.2619	2.1	3.57	0.93	182.56	11.7	11.52
90	0.4083	9.9	12.69	**5.18**	193.16		

Figure 6.5 shows the yield stress as a function of the inclination angle. The yield stress strongly depends on the inclination angle and the samples with slanted TBs

yield at much lower stresses. The stress-strain behaviour can be divided into three groups according to the range of inclination angles:

(1) Small inclination angles (A0-A30). Sample T4A0 yields at the maximum stress of 25.2 GPa. The stress increases continuously until it reaches the peak point after which the stress decreases dramatically to around zero. Sample T4A16 yields at 5.6 GPa. From the stress-strain curves, the stress keeps increasing to the maximum stress of 22.1 GPa after the yielding point and then drops to zero. A negative stress value is detected during the stress drop. Sample T4A30 yields at 3.21 GPa. The stress keeps increasing after the yielding point and no stress drop occurs within 25% deformation.

(2) Medium inclination angles (A45-A60). In this group, the yield stress is the lowest one. Sample T4A45 yields at the minimum stress of 2.35 GPa, after the yield point the stress fluctuates around a mean value before 10% deformation. Then the stress slightly increases with the deformation and rises significantly to a much higher stress after 20% deformation. Sample T4A60 yields at 2.52 GPa and the stress increases gradually before a sharp stress jump, which is followed by a slight stress drop.

(3) Large inclination angles (A75-A90). It can be seen from the stress-train curve, after the initial yield yields at 3.57 GPa, the stress of sample T4A74 keeps increasing to a peak stress of 11.52 GPa. Then it decreases dramatically and fluctuates around 3 GPa. In sample T4A90, the yield stress is also the maximum stress. After a significant stress drop, a steady-state situation is reached where the stress fluctuates around a mean value.

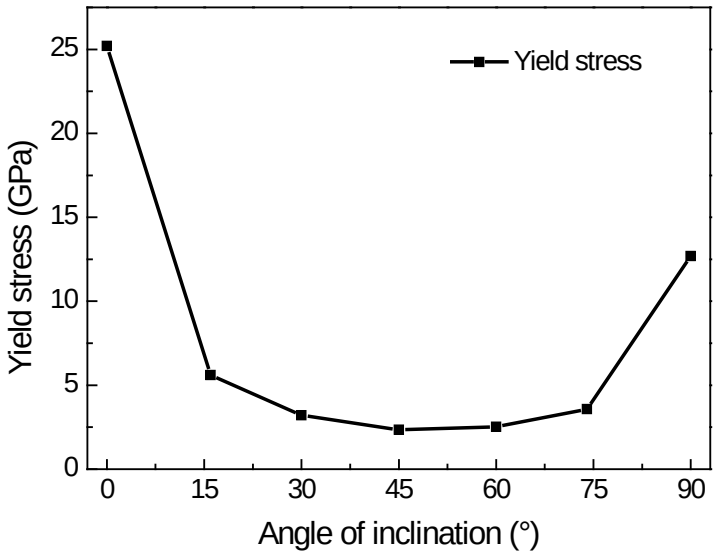

Figure 6.5 The TB orientation dependence of the yield stress.

In nanotwinned fcc samples with vertical TBs, the yield stress increases with decreasing twin spacing, as reported in Chapter 5. The effect of twin spacing on the mechanical response of nanotwinned bcc metals with vertical TBs is studied in this chapter. Figure 6.6 shows the stress-strain curves of nanotwinned Fe with different twin thicknesses, the response of single crystal is also included. A clear softening effect is observed for nanotwinned Fe. The maximum stress decreases as the twin spacing decreases, in contrast to the behaviour of nanotwinned fcc materials.

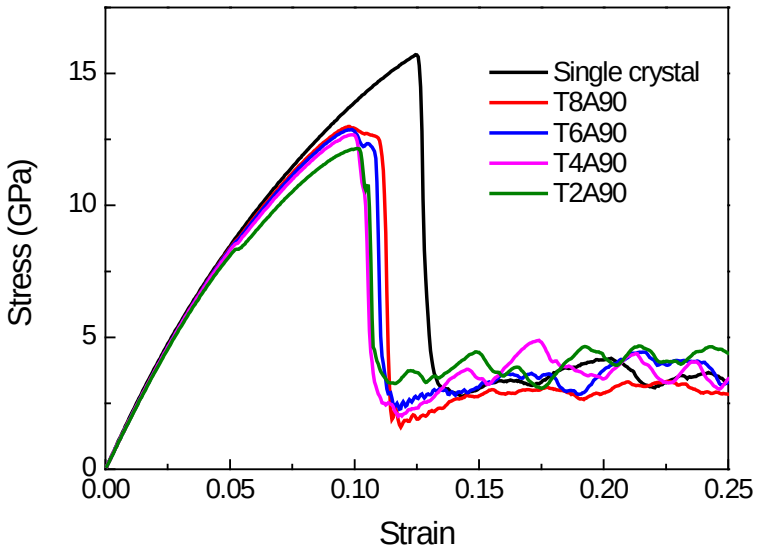

Figure 6.6 The stress-strain behaviour of nanotwinned Fe with different twin spacing.

The variation of yield strength as the TB orientation changes probably results from the different underlying deformation mechanism. The main deformation mechanism for each group will be analysed in details in next sections.

6.3.2 Small inclination angles (A0-A30)

Figure 6.7 shows the atomic configurations of nanotwinned Fe with low inclination angles (T4A0, T4A16 and T4A30) at different strains. No dislocation is nucleated until 20% deformation in nanotwinned sample with horizontal TBs (Figure 6.7a). After the maximum stress at 20.7% strain, the sample fractures in the middle within 0.2% deformation. Figure 6.8 shows the snapshots of a 10 nm thick slice cut from the top of the sample. The fracture initiates at 20.8% strain where microvoids form inside the sample. In Figure 6.8a, because the size of these microvoids is less than 5 nm, they are invisible in the 10 nm slice. As the deformation continues, these microvoids combine together and coalesce to form larger voids. The crack continues to grow by the coalescence of these microvoids (Figure 6.8b). Finally the crack propagates rapidly by shear deformation, leaving behind cup-and-cone surfaces (Figure 6.8c). Few dislocations are emitted from the crack and the crack propagates

in an almost brittle manner. The occurrence of the fracture is due to the high stress of 25.2 GPa as shown in Figure 6.3.

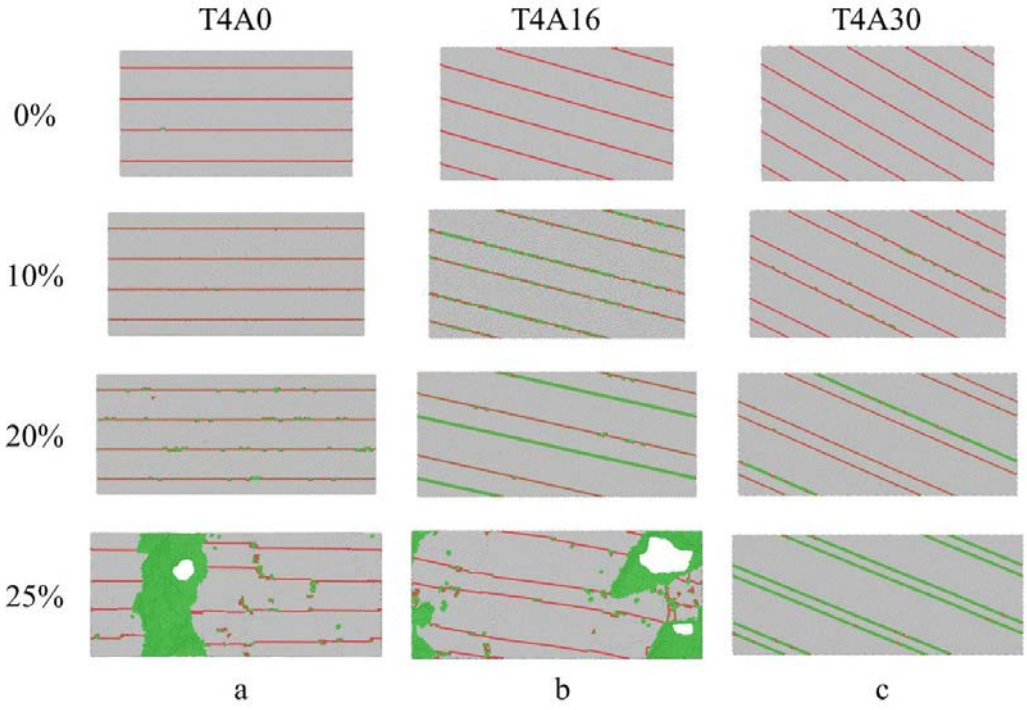

Figure 6.7 Atomic configurations of nanotwinned Fe with small inclination angles. (a) T4A0, (b) T4A16 and (c) T4A30.

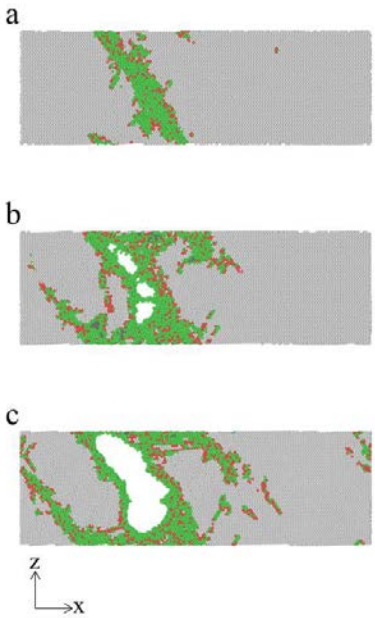

Figure 6.8 Fracture process in sample T4A0 at different strains. (a) 20.8%, (b) 20.9% and (c) 21%.

For other samples with small inclination angles (T4A16 and T4A30), the initial yielding is due to detwinning processes (to be discussed in Section 6.3.3). As the deformation continues, the nucleation of twinning dislocation is restricted, despite the increasing stress state of the samples as shown in the stress-strain curves (Figure 6.3). Figure 6.9 shows the shear strain evolution during the deformation. All samples with small inclination angles show a significant increase in shear strain at 20% strain resulting from the high stress. Sample T4A16 fractures at 20.75% strain in the same way as sample T4A0, while no fracture occur to sample T4A30 within the 25% deformation.

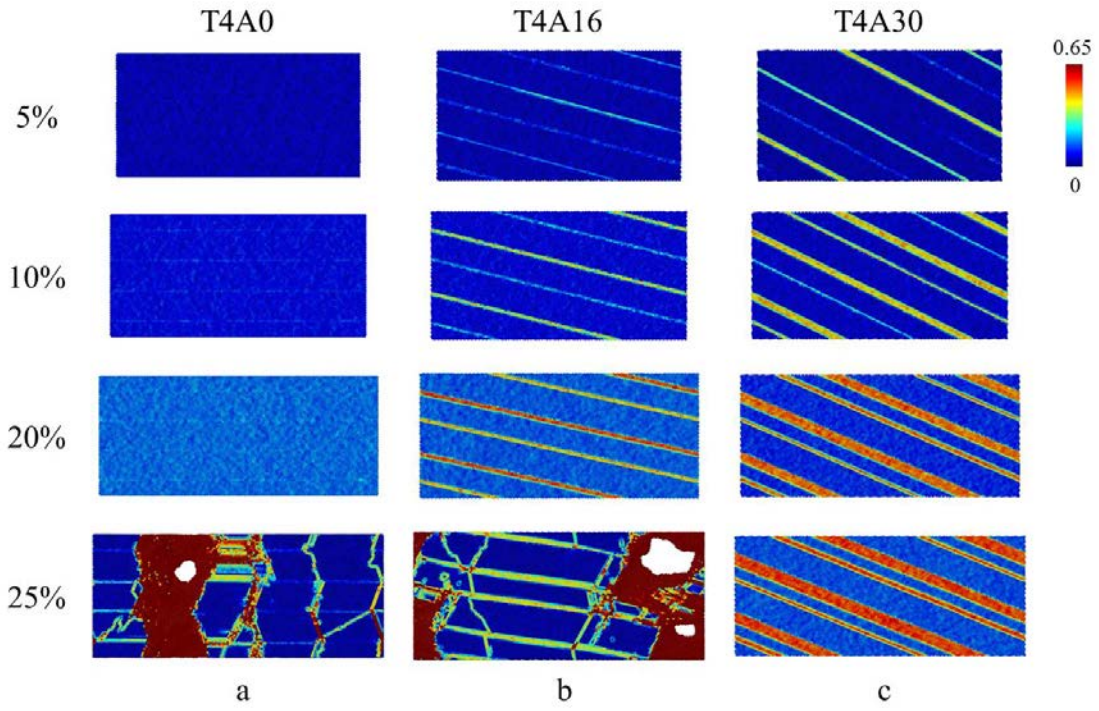

Figure 6.9 Shear strain distribution of samples with small inclination angles at different strains. (a) T4A0, (b) T4A16 and (c) T4A30.

It can be seen from the shear strain distribution in Figure 6.9, some dislocation activities take place during the deformation in addition to the fracture process. Figure 6.10 shows a typical evolution of dislocation structures in sample T4A16. In the top figures, bcc atoms that are not involved in slip activities are deleted for clarity while in the bottom figures, all bcc atoms are deleted. The Burgers vector of the dislocation is 1/2[111] in the matrix grain. The slip plane is composite {110}-{112} planes. The

propagation of this dislocation is blocked by the TB (Figure 6.10a) and it is deposited on the TB (Figure 6.10b). Then it transmits across the TB and a new dislocation is nucleated on the other side of the TB plane (Figure 6.10c). The dislocation line on the $(10\bar{1})$ plane (BC) is taken as an example and the transmission process can be summarised as:

$$d_{(BC)} \rightarrow -d'_{(BC')} - \frac{2}{3} \times c_{(\gamma D)} \tag{6.1}$$

or in vector form:

$$\frac{1}{2}[111]_{(10\bar{1})} \rightarrow -\frac{1}{6}[\bar{1}\bar{1}\bar{5}]_{(41\bar{1})} - \frac{1}{3}[\bar{1}\bar{1}1]_{(\bar{1}\bar{1}\bar{2})} \tag{6.1a}$$

with

$$\frac{1}{6}[\bar{1}\bar{1}\bar{5}]_{(41\bar{1})} = \frac{1}{2}[111]^{T}_{(10\bar{1})^{T}} \tag{6.1b}$$

The matrix slip plane intersects with the twin in the $[1\bar{3}1]$ direction. Thus the dislocation transmits into the twin and glides on the corresponding twinned slip plane. As this dislocation also propagates on the $(01\bar{1})$ plane (AC) and the $(11\bar{2})$ plane (δC), other possible transmission reactions include:

$$d_{(AC)} \rightarrow -d'_{(AC')} - \frac{2}{3} \times c_{(\gamma D)} \tag{6.1c}$$

and

$$d_{(\delta C)} \rightarrow -d'_{(\delta' C')} - \frac{2}{3} \times c_{(\gamma D)} \tag{6.1d}$$

In these situations, the matrix slip plane intersects with the twin in $[\bar{1}3\bar{1}]$ and $[1\bar{1}0]$ direction respectively. In all the three reactions, the slip in the twinned grain is on the symmetry-related plane with respect to the matrix grain. The residual dislocation $1/3[11\bar{1}]$ forms a double step on the TB. This dislocation glides along the TB and the TB migrates downwards by two atomic layers. The transmission is energetically unfavourable, but can occur under high stress as in the simulation. Moreover, the dislocation deposited on the lower TB does not transmit across the TB during later deformation, which confirms the high energy barrier in slip transmission.

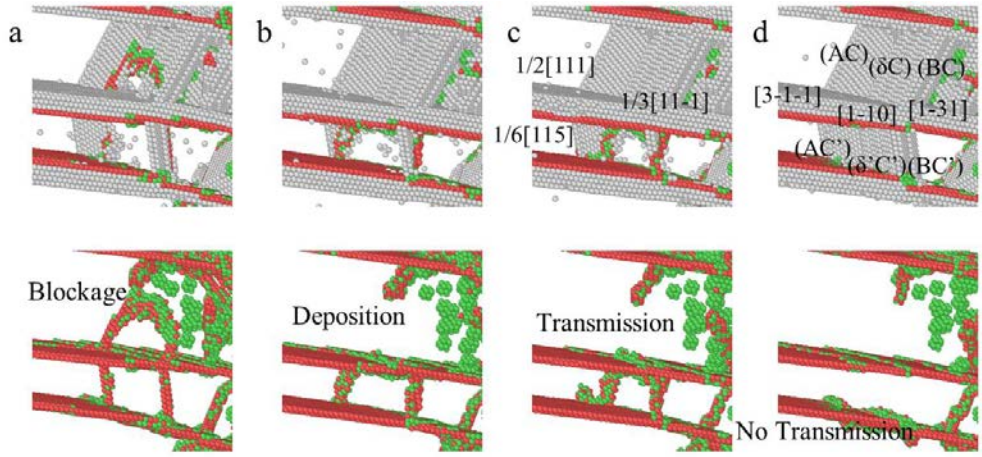

Figure 6.10 Dislocation structure in sample T4A16 during fracture processes.

6.3.3 Medium inclination angles (A45-A60)

Figure 6.11 shows atomic configuration of samples with medium inclination angles (T4A45 and T4A60) at different strains. The samples yield due to the nucleation of twinning dislocations on the twin plane. Extensive TB migration occurs through the successive nucleation of twinning dislocations and their unrestricted glide along the TBs. These processes significantly change the twin spacing and finally lead to the disappearance of the TBs.

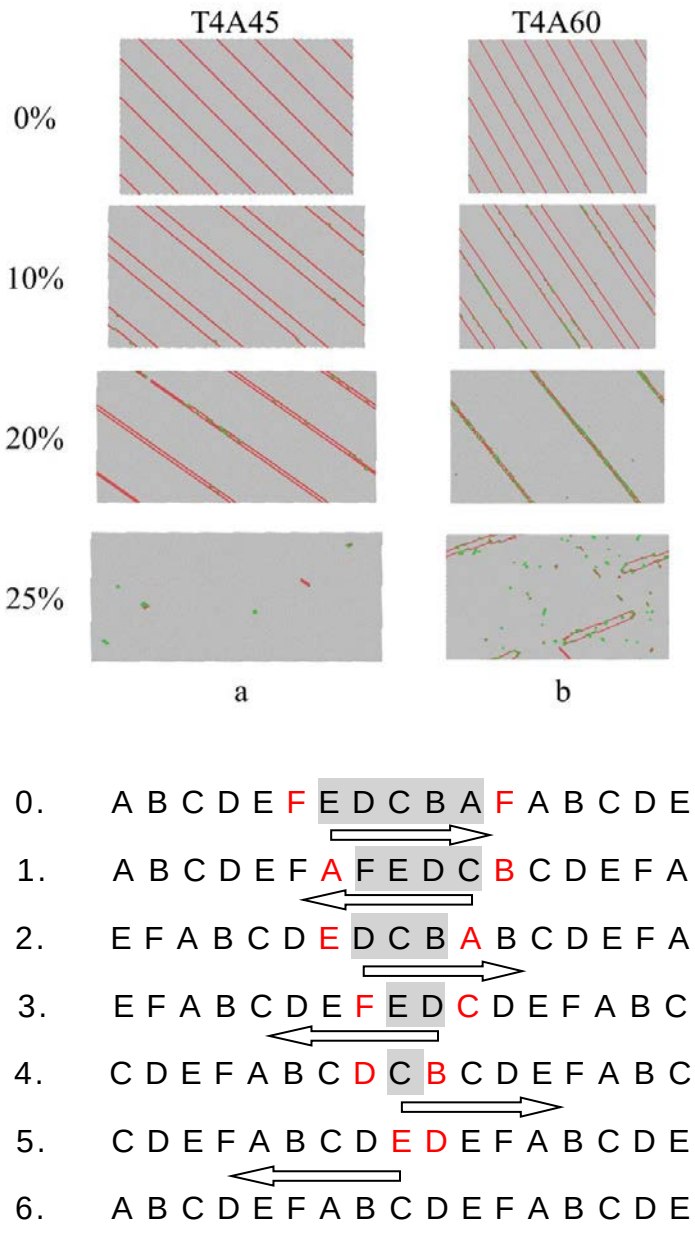

Figure 6.11 Atomic configurations of nanotwinned Fe with medium inclination angles. (a) T4A45 and (b) T4A60. The stacking sequences shown below the figure demonstrate the detwinning process.

Figure 6.12 shows shear strain distribution of the samples. The plastic deformation concentrates in the original twinned grains where homogeneous shear strain is observed, while the matrix grains experience no shear deformation. The disappearance of original TB results from continuous detwinning of the twinned grains. After full detwinning processes, the twinned grains are reoriented to the same orientation as the matrix grain.

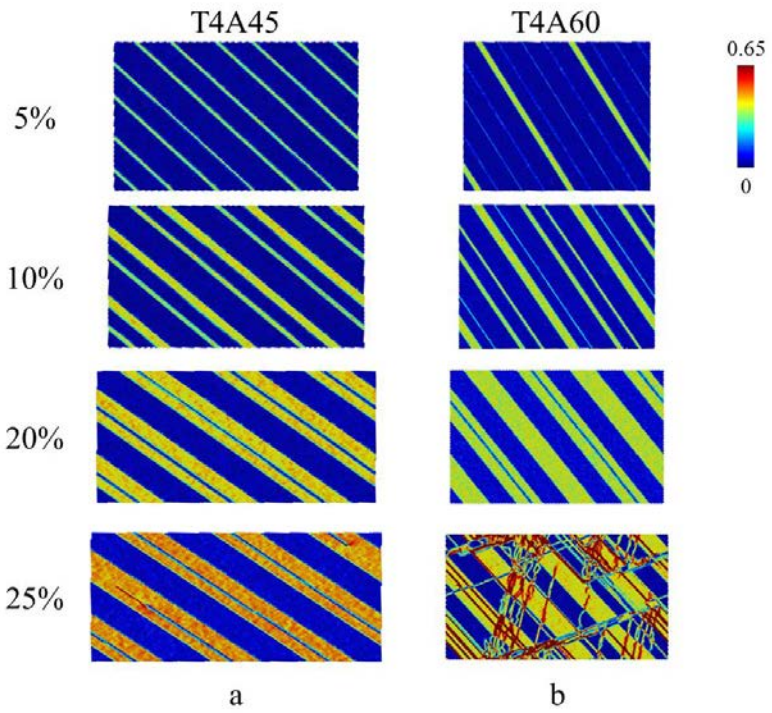

Figure 6.12 Shear strain distribution of samples with large inclination angles. (a) T4A45 and (b) T4A60.

The detwinning process is just the opposite process of the well-known deformation twinning mechanism which involves the successive nucleation and propagation of twinning dislocations 1/6<111> from adjacent (112) slip planes. A nanotwinned model with twin thickness of six-layer atoms is chosen to demonstrate change in the stacking sequence during detwinning processes. The constructed sample contains parallel nanoscale growth twins, so the stacking sequence changes from normal ABCDEFABCDEF to twinned ABCDEFEDCBAFABCDE. The red letters which denotes the atoms having the same neighbours indicate TB and the twin lamella is highlighted by grey colour. During initial deformation, elastic strain is uniformly distributed along the sample length due to the coherency of the TBs and the twinned sequence is retained. As the tensile stain increases, the resolved shear stress along the TB reached a critical value of 1.21 GPa on average, and a twinning dislocation 1/6[-1-11] is nucleated on the TB plane. The glide of the dislocation shifts the twinned part of the sample by the magnitude of the Burgers vector. This process consists of a slight relative movement across the TB, which leaves a shear strain gradient along the tensile direction. The applied strain is absorbed by TB migration, which leads to

a slight decrease in tensile stress. But this stress cannot drop to zero or even minus value. TB migration only occurs when the resolved shear stress above a critical level. From the stress-strain curves, the fluctuation of the tensile stress is observed. The TB migration continuously takes place as the strain increases. Adjacent TBs migrate in the opposite directions. After successive emission of multiple twinning dislocations on adjacent (112) planes, these TBs migrate towards each other. The fully detwinned sample becomes a single crystal with the same orientation as the matrix grain. As the deformation continues, secondary twinning occurs in sample T4A60 at 25% strain.

6.3.4 Large inclination angles (A75-A90)

Figure 6.13 shows the microstructure evolution of samples with high inclination angles during the deformation and Figure 6.14 shows the shear strain distribution. The initial yielding of sample T4A74 is due to the TB migration which changes the TB spacing and leaves shear strain behind. No slip activity is detected until 10% deformation in sample T4A90. As the deformation continues, extensive dislocation processes take place as reflected by the complicated shear strain distribution in Figure 6.14. Most of the dislocations are full dislocations, the glide of which leaves no stacking faults or TBs inside the sample (Figure 6.13). But actually a high density of dislocations has propagated across the deformed sample. And a significant amount of cross-slip has occurred during the dislocation motion. TBs with deformation debris are no longer as sharp and straight as the original coherent TBs. Parts of the TBs are decorated with steps or even become curved as shown in Figure 6.13, but no TB disappears after the deformation.

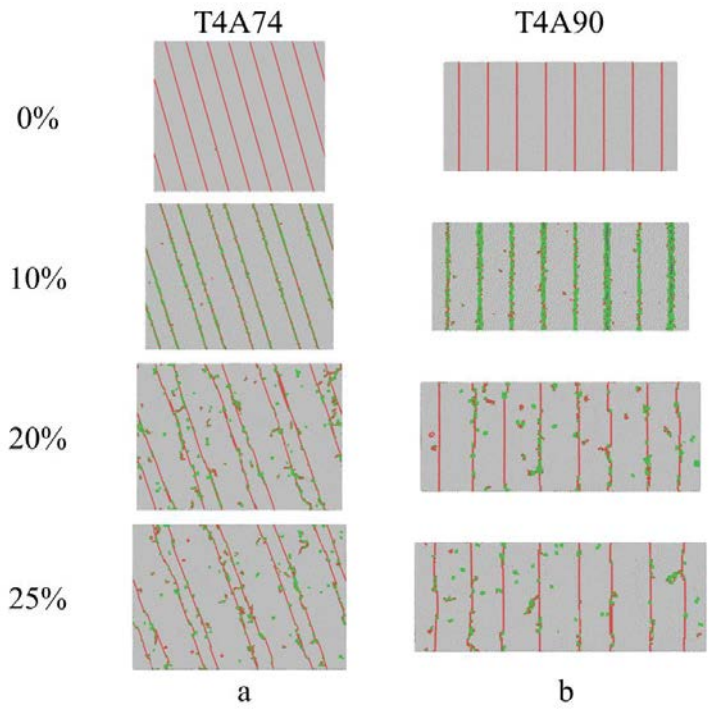

Figure 6.13 Atomic configurations of nanotwinned Fe with large inclination angles. (a) T4A75 and (b) T4A90.

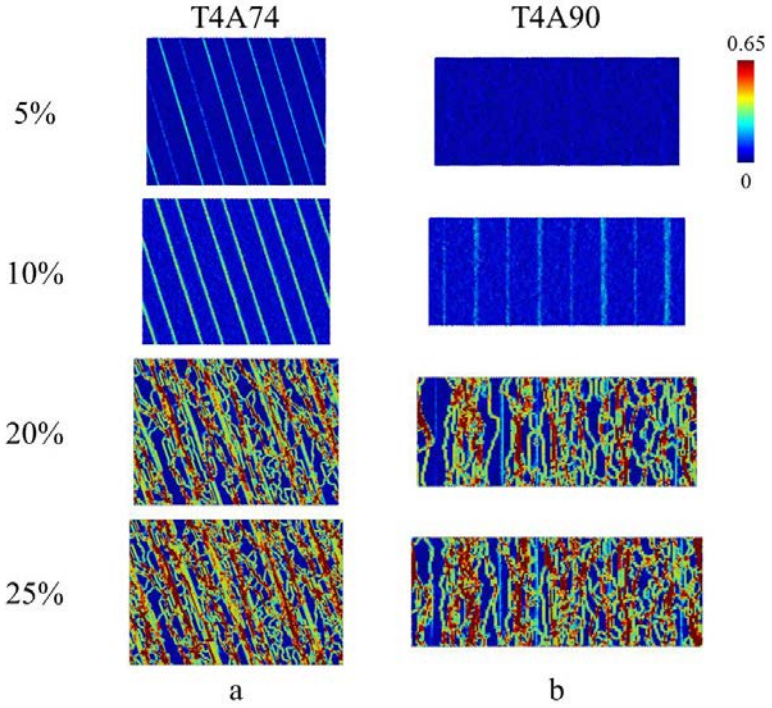

Figure 6.14 Shear strain distribution of samples with large inclination angles. (a) T4A75 and (b) T4A90.

6.3.4.1 Bcc→fcc phase transformation

Figure 6.15 shows the atomic configurations of sample T4A90. Bcc atoms that are not involved in slip activities are deleted for clarity. Figure 6.16 represents the atomic fraction during the plastic deformation. The original TBs which consist of two-layer atoms is stable within 5% deformation (Figure 6.15a). As the strain increases, the TBs thicken to a three-layer structure (Figure 6.15b) and eventually become almost five-layer atoms at the maximum stress (Figure 6.15c). Then some fcc atoms (indicated by dark grey colour in Figure 6.15d) appear from the thickened TBs. The new fcc phases grow into lenticular shape with increasing strain and account for 13.8% of the total atoms at 10.3% strain (Figure 6.15e). The transformation from bcc structure to fcc structure is accompanied by the decrease of the stress as shown in Figure 6.3. Phase transformation only occurs to parts of the TBs, while the other parts restore the structure of three-layer atoms. At 10.4% strain, multiple dislocations nucleate and propagate inside the samples (Figure 6.15f), which is accompanied by the disappearance of the fcc phases (Figure 6.15g). The dislocation processes lead to significant stress drop. After the dislocations swipe over the samples, all fcc phases disappear and the TBs restore the initial two-layer atoms structure (Figure 6.15h).

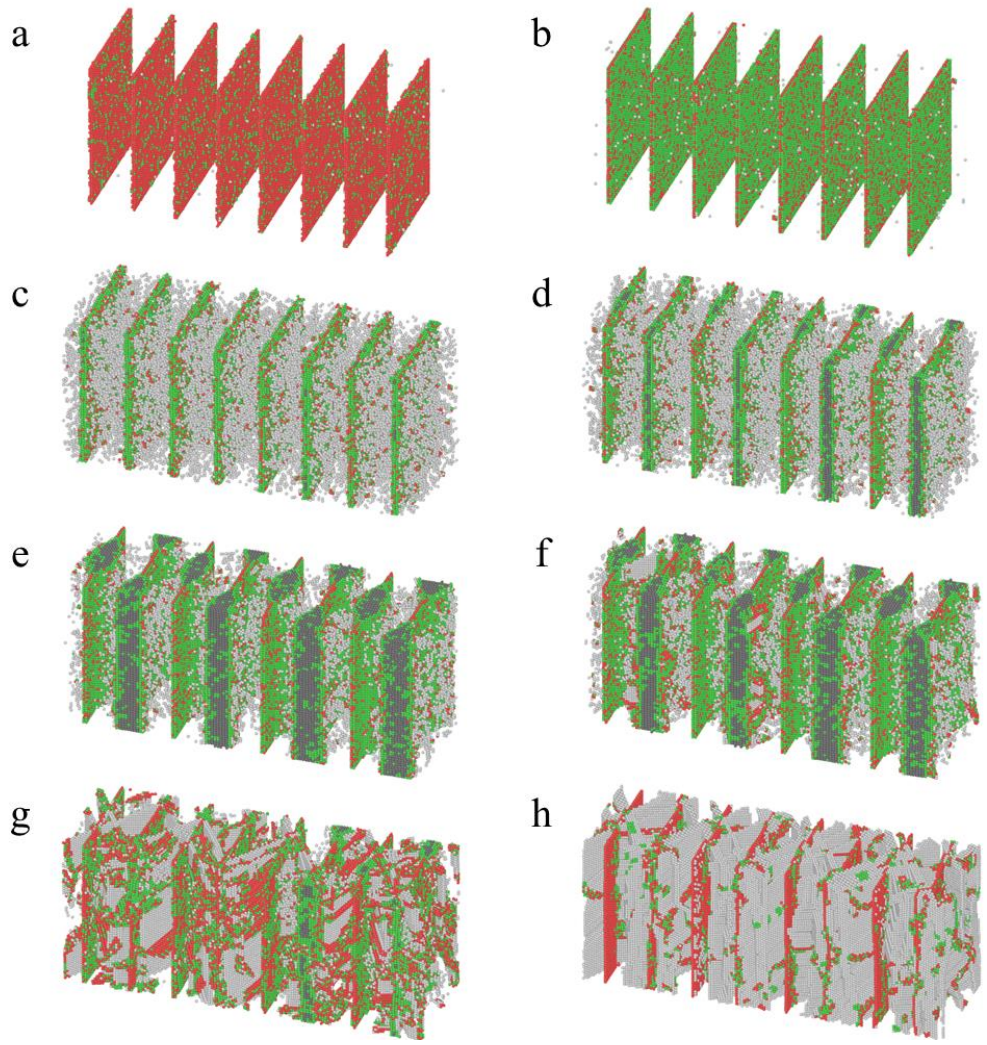

Figure 6.15 Atomic configuration of sample T4A90 at different strains. (a) 5%, (b) 6%, (c) 9.9%, (d) 10.1%, (e) 10.3%, (f) 10.4%, (g) 10.5%, (h) 11%.

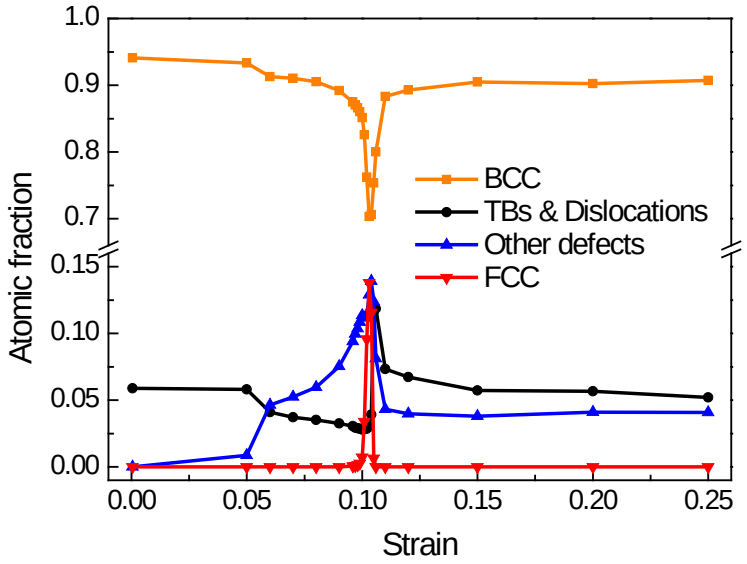

Figure 6.16 Atomic fraction evolution of sample T4A90.

6.3.4.2 Slip transmission across the TB

Another interesting observation in Figure 6.15 is the transmission of dislocations across the TBs. Figure 6.17 shows plane view of the shear strain evolution during initial yielding processes. After the dislocation nucleation from the TB, these dislocations quickly glide across the sample until impinging the TB. Then these dislocations easily transmit across the TB without any blockage. Continuous dislocation transmissions across the TB leave two series of intersected slip traces as indicated by dislocation structure (Figure 6.15h) and shear strain distribution (Figure 6.17d).

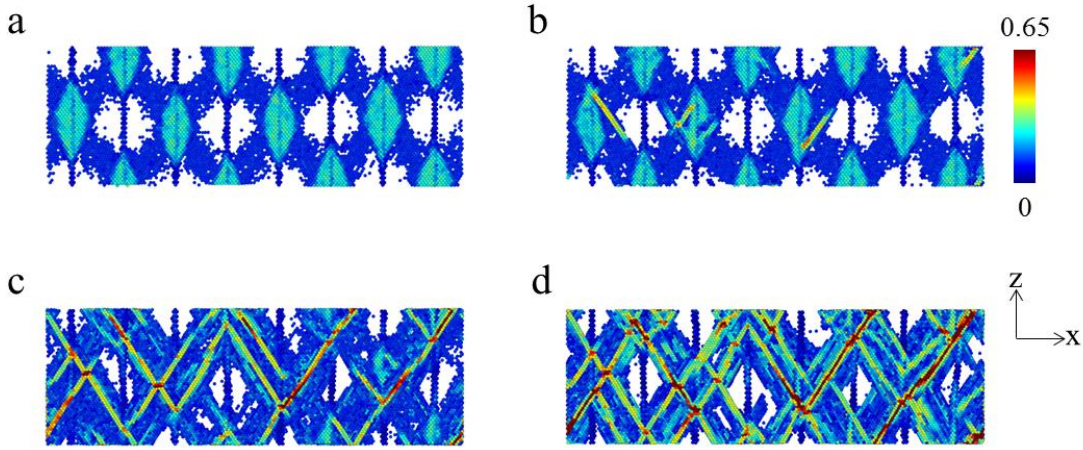

Figure 6.17 Plane view of shear strain distribution of sample T4A90 at different strains. (a) 10.3%, (b) 10.4%, (c) 10.5%, (d) 10.6%.

The transmission interaction can be summarised as:

$$a_{(DB)} \rightarrow -b'_{(D'A)} - \frac{2}{3} \times c \tag{6.2}$$

or in vector form:

$$\frac{1}{2}[\bar{1}1\bar{1}]_{(011)} \rightarrow -\frac{1}{6}[5\bar{1}1]_{(0\bar{1}\bar{1})} - \frac{1}{3}[\bar{1}\bar{1}1]_{(\bar{1}\bar{1}2)} \tag{6.2a}$$

with

$$\frac{1}{6}[5\bar{1}1]_{(0\bar{1}\bar{1})} = \frac{1}{2}[1\bar{1}\bar{1}]^{T}_{(101)^{T}} \tag{6.2b}$$

Another possible transmission is

$$b_{(DA)} \rightarrow -a'_{(D'B)} - \frac{2}{3} \times c \tag{6.2c}$$

This reaction is just a crystallographically equivalent variant of equation (6.2). In both reactions, the slip in the twinned grain is not on the symmetry-related plane with respect to the matrix grain. Instead, the slip lanes in the matrix grain and the twinned grain are parallel to each other and are intersected along the $[11\bar{1}]$ direction. The transmission is energetically unfavourable according to the Frank rule but can occur under high stress as in the simulation. On the other hand, the slip in the matrix and

the twinned grain produce almost compatible strain at the TB. The *x*, *y* and *z* axes is along the [112], $[\bar{1}\bar{1}1]$ and $[1\bar{1}0]$ directions respectively, the strain components on the three axes are computed for reaction (6.2) and listed below.

$$\varepsilon_{xx}^{M} = \frac{-2}{3\sqrt{2}} \qquad \varepsilon_{xx}^{T} = \frac{-2}{3\sqrt{2}}$$

$$\varepsilon_{yy}^{M} = \frac{-1}{3} \qquad \varepsilon_{yy}^{T} = \frac{1}{3}$$

$$\varepsilon_{zz}^{M} = \frac{-2}{\sqrt{6}} \qquad \varepsilon_{zz}^{T} = \frac{-2}{\sqrt{6}}$$

It is obvious that the strain is completely compatible along the *x* and *z* axes. This strain compatibility makes dislocation transmission across the TB easily as the energy barrier for slip transfer is lower than that for dislocation nucleation.

6.3.4.3 Secondary twinning

In addition to transmission across the TB, significant cross-slip occurs during the dislocation motion. Due to the screw nature of the dislocations in bcc materials, dislocations on <110> slip planes easily cross-slip to <112> slip planes as indicated by black arrows in Figure 6.18. These dislocations may dissociate on <112> planes according to:

$$a_{(DB)} \rightarrow 3 \times \frac{1}{3} a_{(\alpha B)} \tag{6.3}$$

or in vector form:

$$\frac{1}{2}[\bar{1}1\bar{1}]_{(011)} \rightarrow 3 \times \frac{1}{6}[\bar{1}1\bar{1}]_{(\bar{1}12)} \tag{6.3a}$$

This dissociation process results in the nucleation of deformation twins (Figure 6.18b). But the small spacing of the growth TBs restricts the growth of the twin nucleus. The high TB density indicates that a significant amount of deformation twins emerge simultaneously, which increases the elastic energy of the system. The number of atoms belonging to the TBs increases dramatically in Figure 6.16. The dissociated dislocation cannot transform to stable a twin nucleus, which either retains its configuration or propagates as a twin during further deformation (Beyerlein et al.,

2014). Instead, the dissociated dislocations which forms unstable twin embryo are contracted together, so the number of atoms belonging to the TBs decreases in Figure 6.16. As the deformation continues, dislocation slip takes over the role of deformation twinning as the main deformation mechanism (indicated by red arrows in Figure 6.18).

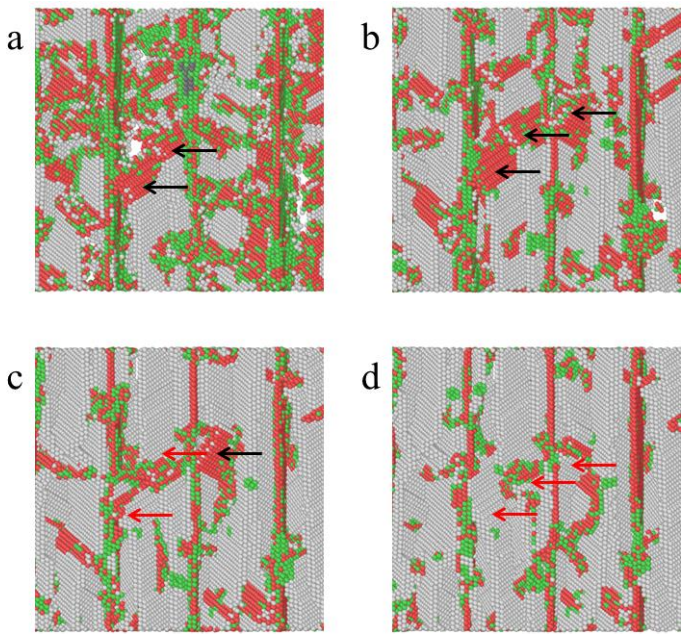

Figure 6.18 Dislocation cross-slip inside individual grains. (a) 10.5%, (b) 10.6%, (c) 10.7%, (d) 10.8%.

Figure 6.19 compares the mechanical response of nanotwinned Fe with different twin spacing. For samples with smallest twin spacing of 2 nm, slip transfer are prevalent during the plastic deformation as dislocations frequently imping on the TB. The TB has little effect on blocking dislocation transmission. The majority of dislocation motion leaves straight slip traces, which indicates little cross-slip occur during dislocation motion. As the twin thickness increases, the mean free path for dislocations increases, which increases the probability for cross-slip. In samples with twin thickness of 4 nm, extensive cross-slip occurs, which leaves complicated slip traces after deformation. In samples with twin thickness of 6 nm, dislocation cross-slip results in the formation of unstable twin nucleus, which is replaced by dislocation slip under further deformation. But in samples with twin spacing of 8 nm,

deformation twinning dominates the plastic deformation, just like Fe single crystal with the same orientation.

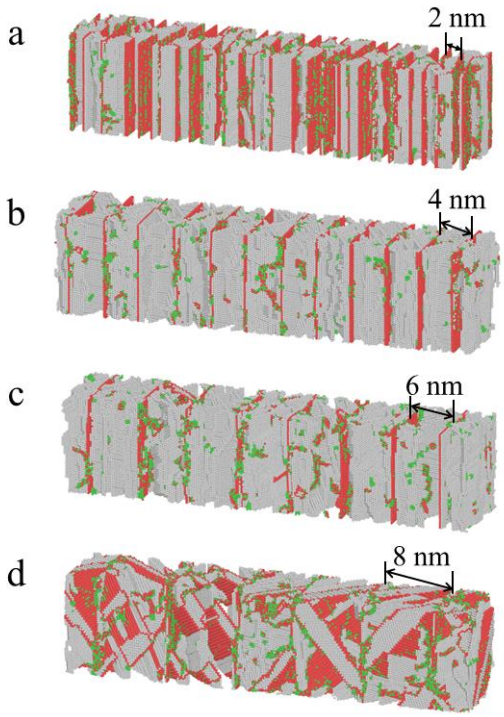

Figure 6.19 Mechanical response of nanotwinned Fe with different twin spacing. (a) 2 nm, (b) 4 nm, (c) 6 nm, (d) 8 nm.

6.4 Discussion

6.4.1 Deformation mechanism transitions in nanotwinned iron

The mechanical properties of crystalline solids depend strongly on their crystal structures. In fcc materials, the plastic deformation obeys Schmid's law. Slip begins when the resolved shear stress on a slip system reaches the CRSS which is orientation independent. In contrast, there is a strong plastic anisotropy in bcc metals. The CRSS strongly depends on the orientation of the applied stress (Duesbery and Vitek, 1998). Moreover, in nanotwinned models the effect of the TB needs to be considered. The importance of TB can be understood in two ways. First, the introduction of twins is accompanied by crystallographic reorientations. New slip systems are placed in orientations that are favourable to the stress axis such that slip

can take place. Second, the slip systems that are not on the twin plane are disrupted by the TB. The motion of the corresponding dislocations is restricted by the TB. On the other hand, the slip activities on the twin plane are also affected by the TB.

Figure 6.20 shows the Schmid factors for the {112}<111> slip and twinning systems both in the matrix (solid lines) and twinned grain (dash lines). The three distinct dislocation processes can be explained with the relationship between the activated slip system and twin plane.

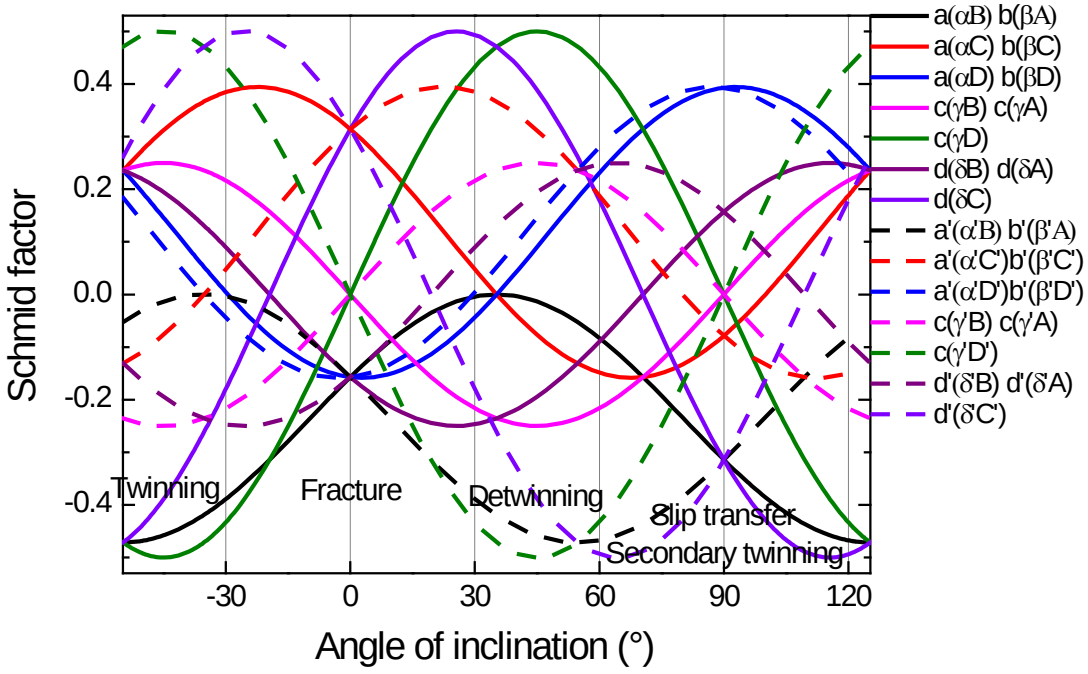

Figure 6.20 The Schmid factors for the {112}<111> twinning systems both in the matrix (solid lines) and the twin (dash lines) as the TB is inclined to the loading direction by an angle between -54.74° and 125.26°.

When the TB is parallel to the loading axis, no dislocation slip takes place within 20% deformation. The yield stress is as high as 25.2 GPa and the resolved stress on {112} slip is 7.92 GPa. It is still not clear why no dislocation nucleates under so high stress. Moreover, the sample cannot sustain any stress increase and fractures in the middle.

As the TB orientation angle increases, a softening phenomenon occurs, which is represented by a dramatic decrease in the yield stress. When the inclination angle is low (T4A16 and T4A30), the samples eventually fracture in a brittle manner as the deformation continues (Figure 6.7). When the inclination angle is high (T4A74), slip activities take over the role of the main deformation mechanism (Figure 6.13). With a medium inclination angle, TB migration via the nucleation and propagation of twinning partials along the TBs takes over the main deformation mechanism. Neither fracture nor dislocation processes occur until the samples are fully detwinned (Figure 6.11).

Figure 6.21 shows the generalized planar faults energy of Fe for a six-layer twin and a full dislocation. The energy barriers associated with the twin nucleation, TB migration and dislocation nucleation can be obtained from these curves. The unrelaxed twin formation energy is 752.56 mJ/m^2 and the dislocation nucleation energy is 796.16 mJ/m^2, but the TB migration energy is only 61.9 mJ/m^2. TB migration has a much smaller energy barrier. So the nucleation of twining partials on the TBs is energetically favourable. The substantial decrease in yield stress (Figure 6.5) confirms the low energy barrier for the nucleation of a twinning partial dislocation.

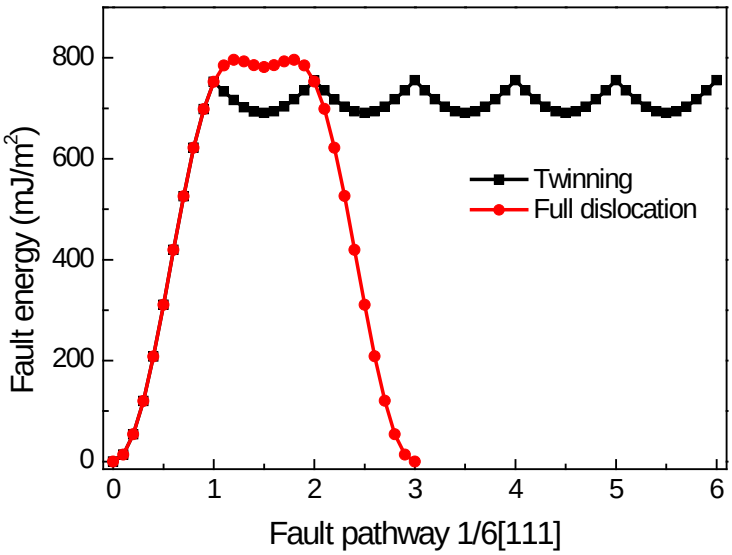

Figure 6.21 Generalized planar faults energy curves for Fe on {112}<111> twinning and slip systems.

The continuous TB migration eventually leads to the disappearance of the original TBs. Two possible pathways are available for the elimination of the TBs. The first one is shrinkage of the twins through continuous detwinning. When the TB is inclined by an angle between 0° and 90° to the loading axis, the twinning system (shown by dash olive lines in Figure 6.20) in the twinned grains has negative Schmid factors. Under tensile deformation, a twinning dislocation nucleates on slip systems with negative Schmid factors. The activation of twinning system in the twinned grains leads to the shrinkage of twins. The second one is shrinkage of the matrixes through continuous twinning. When the TB is inclined by an angle between 0° and -90° to the loading axis, the twinning system (shown by solid olive lines in Figure 6.20) in the matrix grains has negative Schmid factors. Its activation leads to the shrinkage of matrixes. The reversible twinning and detwinning processes also can be obtained by changing the loading direction (Wang et al., 2015, Li et al., 2010b).

The energy barrier for TB migration is much smaller than dislocation nucleation. In nanotwinned bcc pillars with slant TBs, TB migration is the dominant deformation mechanism irrespective of the TB orientations.

When the TB is orientated nearly perpendicular to the loading axis, extensive dislocation processes take place in the samples. Figure 6.22 shows the Schmid factors for the {110}<111> slip systems both in the matrix (solid lines) and the twin (dash lines). Two sets of slip systems (shown by blue lines) across the TB have the maximum Schmid factors. Slip transmission takes place between the corresponding dislocations.

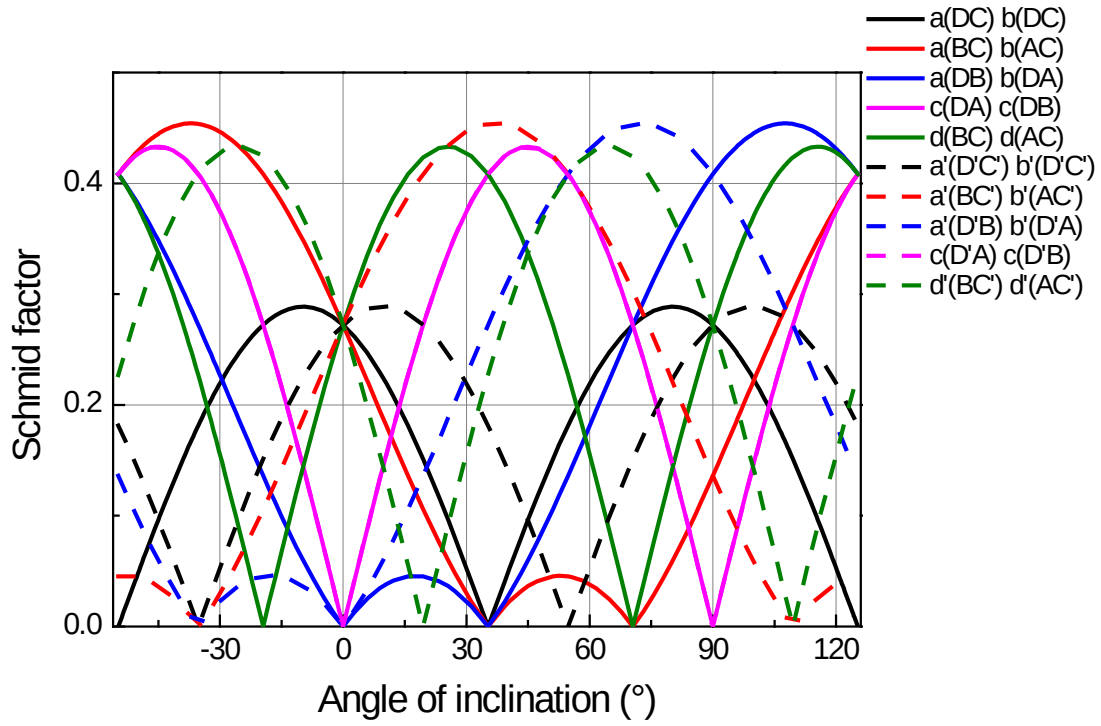

Figure 6.22 The Schmid factors for the {110}<111> slip systems both in the matrix (solid lines) and the twin (dash lines) as the TB is inclined to the loading direction by an angle between -54.74° and 125.26°.

The full dislocations on the {110} slip planes can cross-slip to the {112} slip planes which have negative Schmid factors (shown by black lines in Figure 6.20). These dislocations dissociate on the {112} slip planes, which lead to secondary twinning. This phenomenon is more obvious in samples with large twin spacing, because of the increase in the dislocation mean free path. Moreover, cross-slips have been widely observed during the dislocation motion, which lead to complicated slip traces. The TBs lose initial coherency after extensive slip-twin interactions.

6.4.2 Slip-twin interactions

Slip-twin interactions in bcc materials have been observed both experimentally and theoretically (Christian and Mahajan, 1995). But no systematic investigation on the interactions has been carried out. The plausible dislocation reactions at the TBs are systematically described in this section.

At atomic level, the slip in bcc structure is confined to the {110} and {112} planes. The slip planes includes six {110} planes and twelve {112} planes, but only four <111> slip directions exist. In nanotwinned bcc structure, two of the four slip directions are the shear direction $[\bar{1}\bar{1}1]$ and the conjugate shear direction [111]. Thus the slip activities can be divided into three groups: (1) $[\bar{1}\bar{1}1]$ slip **c** parallel to the shear direction; (2) [111] slip **d** parallel to the conjugate shear direction; (3) other slips including $[\bar{1}1\bar{1}]$ slip **a** and $[1\bar{1}\bar{1}]$ slip **b** that are not parallel to the shear direction or the conjugate shear direction.

6.4.2.1 Slip parallel to the shear direction **c** → **c'**

Consider a special case of slip across the TB when the slip is parallel to the twin interface. The dislocations impinge on the TB with a screw nature and they may cross-slip into the twinned grain without leaving a step on the interface. The transmission reaction can be summarized as:

$$c \rightarrow c' \tag{6.4}$$

or in vector form:

$$\frac{1}{2}[\bar{1}\bar{1}1] \rightarrow \frac{1}{2}[\bar{1}\bar{1}1] \tag{6.4a}$$

The dislocation with Burges vector parallel to the shear direction can glide on any of the three {110} planes (AB, DA and DB) or any of the three {112} planes (γD, γB and γA), the corresponding Burgers vector in the twin has identical indices as in the matrix. The possible slip plane in the twin is the mirror image of the matrix slip plane, and these two slip planes are crystallographically equivalent. The symmetry-related slip planes intersect in the $[11\bar{1}]$ direction. So the slip transfer conditions are fulfilled provided the shear stress on both the matrix and twin systems is adequate.

6.4.2.2 Slip parallel to the conjugate shear direction: Case I **d** → **-d'**

In all other three types of slips, the component normal to the shear plane means that a step is created on the twin interface after slip transmission. Figure 6.23 schematically illustrates the transmission of the dislocation with Burgers vector parallel to the conjugate shear direction. This dislocation can dissociate according to:

$$\frac{1}{2}[111] \rightarrow 2 \times \frac{1}{6}[112] + \frac{1}{6}[11\bar{1}]$$

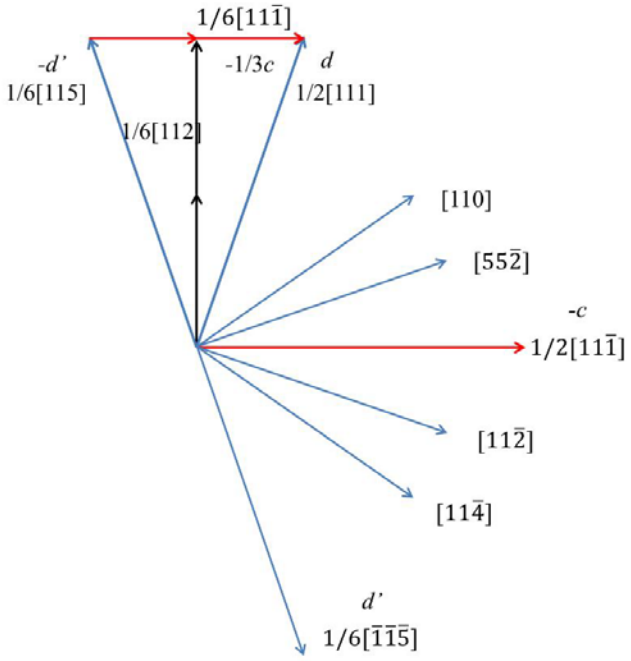

Figure 6.23 Schematic illustration of transmission of the dislocation with Burgers vector parallel to the conjugate shear direction.

The dislocation on the corresponding slip direction in the twin also has the same projection on the plane perpendicular to the shear plane, so this dislocation is nucleated from the step and the dislocation is transmitted across the TB. The transmission reaction can be summarised as:

$$d \rightarrow -d' - \frac{2}{3} \times c \tag{6.5}$$

or in vector form:

$$\frac{1}{2}[111] \rightarrow -\frac{1}{6}[\bar{1}\bar{1}5] + \frac{1}{3}[11\bar{1}] \tag{6.5a}$$

with

$$\frac{1}{6}[\bar{1}\bar{1}5] = \frac{1}{2}[111]^T \tag{6.5b}$$

The various slip planes of this dislocation intersect the shear plane in different directions. The geometrically possible slip plane in the twin is the mirror image of

the matrix slip plane, because in this case the line of the intersection of the slip plane in the matrix and the twin lies in the twin interface. If the dislocation glides on one of the three {110} slip planes, the possible reactions include:

$$d_{(AB)} \rightarrow -d^{'}_{(AB)} - \frac{2}{3} \times c_{(\gamma D)} \tag{6.5c}$$

$$d_{(BC)} \rightarrow -d^{'}_{(BC^{'})} - \frac{2}{3} \times c_{(\gamma D)} \tag{6.5d}$$

$$d_{(AC)} \rightarrow -d^{'}_{(AC^{'})} - \frac{2}{3} \times c_{(\gamma D)} \tag{6.5e}$$

The matrix slip plane intersects the twin interface in the $[11\bar{1}]$, $[1\bar{3}1]$ and $[3\bar{1}\bar{1}]$ directions respectively. If the dislocation glides on one of the three {112} slip planes, the possible reactions are:

$$d_{(\delta C)} \rightarrow -d^{'}_{(\delta' C')} - \frac{2}{3} \times c_{(\gamma D)} \tag{6.5f}$$

$$d_{(\delta A)} \rightarrow -d^{'}_{(\delta' A')} - \frac{2}{3} \times c_{(\gamma D)} \tag{6.5g}$$

$$d_{(\delta B)} \rightarrow -d^{'}_{(\delta' B')} - \frac{2}{3} \times c_{(\gamma D)} \tag{6.5h}$$

The matrix slip plane intersects the twin interface in the $[1\bar{1}0]$, $[51\bar{3}]$ and $[15\bar{3}]$ direction respectively. This reaction was reported in Section 6.3.2. Mahajan suggested that this reaction is probable because less energy is required (Mahajan, 1971, Christian and Mahajan, 1995).

6.4.2.3 Slip parallel to the conjugate shear direction: Case II **d → a'**

In addition to the transmission to the corresponding slip direction, the dislocation may transmit to the other slip direction in the twin. A typical reaction is:

$$d \rightarrow a^{'} - a - \frac{1}{3} \times c \tag{6.6}$$

or in vector form:

$$\frac{1}{2}[111] \rightarrow \frac{1}{6}[\bar{1}51] + \frac{1}{2}[1\bar{1}1] + \frac{1}{6}[11\bar{1}] \tag{6.6a}$$

with

$$\frac{1}{6}[\bar{1}51] = \frac{1}{2}[\bar{1}1\bar{1}]^T \tag{6.6b}$$

This transmission leaves a dislocation symmetric to the emitted slip in the twin on the interface. The choice of the slip planes is restricted by the geometrical conditions. In the present situation, only two sets of slip planes satisfy the boundary condition. If the transmission occurs on non-symmetric slip planes, the reaction can be written as:

$$d_{(AB)} \rightarrow a'_{(D'B)} - a_{(DB)} - \frac{1}{3} \times c_{(\gamma D)} \tag{6.6c}$$

If the transmission occurs on symmetry-related slip planes, the reaction can be written as:

$$d_{(BC)} \rightarrow a'_{(BC')} - a_{(BC)} - \frac{1}{3} \times c_{(\gamma D)} \tag{6.6d}$$

The matrix slip plane intersects the twin interface in the $[11\bar{1}]$ and $[1\bar{3}1]$ directions respectively.

The transmission of **d** → **b'** can be summarized as:

$$d \rightarrow b' - b - \frac{1}{3} \times c$$

This reaction is just a crystallographically equivalent variant of equation (6.6).

6.4.2.4 Other slips: Case I **a** → **d'**

When the slip direction is not parallel to the shear direction or the conjugate shear direction, there are three possible dislocation reactions. The first possible slip in the twin is on the conjugate slip direction, analogical to that reported in Section 6.4.2.3. The reaction can be written as:

$$a \rightarrow d' - b - \frac{1}{3} \times c \tag{6.7}$$

or in vector form:

$$\frac{1}{2}[\bar{1}1\bar{1}] \rightarrow \frac{1}{6}[\bar{1}\bar{1}\bar{5}] + \frac{1}{2}[\bar{1}11] + \frac{1}{6}[11\bar{1}] \tag{6.7a}$$

with

$$\frac{1}{6}[\bar{1}\bar{1}\bar{5}] = \frac{1}{2}[111]^T \tag{6.7b}$$

Consider the geometrical restrictions, the possible reactions include:

$$a_{(BC)} \rightarrow d'_{(BC')} - b - \frac{1}{3} \times c_{(\gamma D)} \tag{6.7c}$$

$$a_{(DB)} \rightarrow d'_{(AB)} - b - \frac{1}{3} \times c_{(\gamma D)} \tag{6.7d}$$

The matrix slip plane intersects the twin interface in the $[1\bar{3}1]$ and $[11\bar{1}]$ directions respectively.

6.4.2.5 Other slips: Case II **a** → **a'**

The second possible slip in the twin is on the corresponding slip direction in the twin. The reaction can be written as:

$$a \rightarrow a' - d - \frac{1}{3} \times c \tag{6.8}$$

or in vector form:

$$\frac{1}{2}[\bar{1}1\bar{1}] \rightarrow \frac{1}{6}[\bar{1}51] + \frac{1}{2}[\bar{1}\bar{1}\bar{1}] + \frac{1}{6}[11\bar{1}] \tag{6.8a}$$

with

$$\frac{1}{6}[\bar{1}51] = \frac{1}{2}[\bar{1}1\bar{1}]^T \tag{6.8b}$$

The geometrically possible slip plane in the twin is the mirror image of the matrix slip plane. The possible reactions for the {110} slip include:

$$a_{(DC)} \rightarrow a'_{(D'C')} - d_{(AB)} - \frac{1}{3} \times c_{(\gamma D)} \tag{6.8c}$$

$$a_{(BC)} \rightarrow a'_{(BC')} - d_{(BC)} - \frac{1}{3} \times c_{(\gamma D)} \tag{6.8d}$$

$$a_{(DB)} \rightarrow a'_{(D'B)} - d_{(AB)} - \frac{1}{3} \times c_{(\gamma D)} \tag{6.8e}$$

The matrix slip plane intersects the twin interface in the $[1\bar{1}0]$, $[1\bar{3}1]$ and $[11\bar{1}]$ directions. The possible reactions for the $\{112\}$ slip include:

$$a_{(\alpha B)} \rightarrow a'_{(\alpha' B)} - d - \frac{1}{3} \times c_{(\gamma D)} \tag{6.8f}$$

$$a_{(\alpha D)} \rightarrow a'_{(\alpha' D')} - d_{(AC)} - \frac{1}{3} \times c_{(\gamma D)} \tag{6.8g}$$

$$a_{(\alpha C)} \rightarrow a'_{(\alpha' C')} - d - \frac{1}{3} \times c_{(\gamma D)} \tag{6.8h}$$

The matrix slip plane intersects the twin interface in the $[0\bar{2}1]$, $[\bar{3}11]$ and $[3\bar{5}1]$ directions.

6.4.2.6 Other slips: Case III **a** → **-b'**

The third possible slip in the twin is on the other slip direction in the twin. The transmission is schematically illustrated in Figure 6.24.

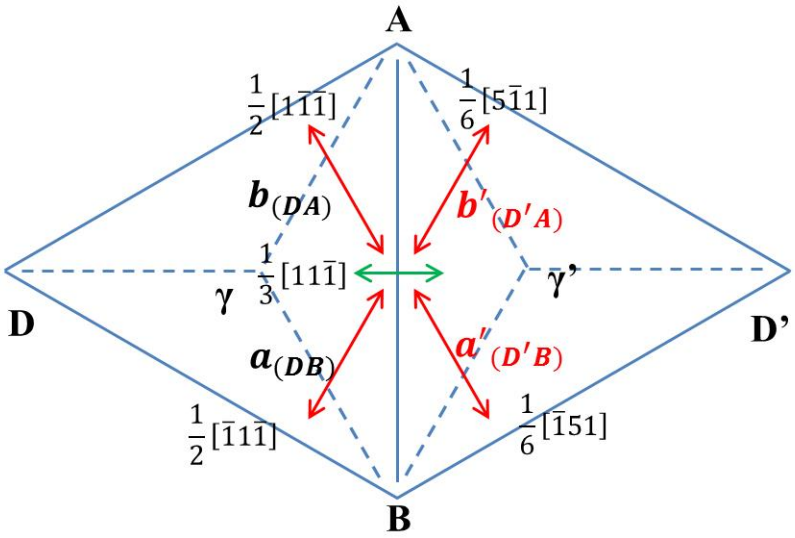

Figure 6.24 Schematic illustration of transmission between non-symmetric other dislocations.

The reaction can be written as:

$$a \rightarrow -b' - \frac{2}{3} \times c \tag{6.9}$$

or in vector form:

$$\frac{1}{2}[\bar{1}1\bar{1}] \rightarrow \frac{1}{6}[\bar{5}1\bar{1}] + \frac{1}{3}[11\bar{1}] \tag{6.9a}$$

with

$$\frac{1}{6}[5\bar{1}1] = \frac{1}{2}[1\bar{1}\bar{1}]^T \tag{6.9b}$$

Only two sets of slip planes satisfy the geometrical condition. If the transmission occurs on symmetry-related slip planes, the reaction can be written as:

$$a_{(DC)} \rightarrow -b'_{(D'C')} - \frac{2}{3} \times c_{(\gamma D)} \tag{6.9c}$$

If the transmission occurs on non-symmetric slip planes, the reaction can be written as:

$$a_{(DB)} \rightarrow -b'_{(D'A)} - \frac{2}{3} \times c_{(\gamma D)} \tag{6.9d}$$

The matrix slip plane intersects the twin interface in the $[1\bar{1}0]$ and $[11\bar{1}]$ directions. This reaction was reported in Section 6.3.4.2. The reaction of dislocation **b** with the twin interface is crystallographically equivalent to dislocation **a**.

The overall transmission reactions are listed in Table 6.2. All the dislocation reactions are energetically unfavourable according to the Frank rule. The reactions in red colour are energetically more favourable as the elastic energy increases by 4/9 of the energy of a full dislocation, while the energy increase is 10/9 of a full dislocation in other reactions. In addition, the latter reactions produce new full dislocations with the matrix slip system at the twin interface, which reduce the effective shear strain produced by the incident slip. Only reactions in bold style were observed in the simulations.

Table 6.2 Plausible dislocation reactions involved in slip transfer.

	d'	a'	b'
d	$\boldsymbol{d \rightarrow -d' - \frac{2}{3} \times c}$	$d \rightarrow a' - a - \frac{1}{3} \times c$	$d \rightarrow b' - b - \frac{1}{3} \times c$
a	$a \rightarrow d' - b - \frac{1}{3} \times c$	$a \rightarrow a' - d - \frac{1}{3} \times c$	$\boldsymbol{a \rightarrow -b' - \frac{2}{3} \times c}$
b	$b \rightarrow d' - a - \frac{1}{3} \times c$	$\boldsymbol{b \rightarrow -a' - \frac{2}{3} \times c}$	$b \rightarrow b' - d - \frac{1}{3} \times c$

6.5 Summary

MD simulations have been performed to investigate the effect of TB orientation and twin spacing on the mechanical response of nanotwinned Fe. The simulations reveal a dynamic transition in the deformation mechanism as the TB orientation changes from the horizontal direction, to the slant direction and to the vertical direction. The nature of the dislocation activity in nanotwinned Fe cannot be explained by the Schmid's law. And the geometrical relation between the activated slip system and the twin plane determines three distinct dislocation processes. When the TBs are parallel or inclined less than 30° to the loading direction, the samples eventually fracture in an almost brittle manner. As the angle of inclination increases, slip systems on the twin plane can be activated. The initial yielding is due to TB migration in samples with slanted TBs. When the TBs are inclined with angles between 45° and 60° to the loading direction, plastic deformation is dominated by TB migration. The TBs are eliminated after full detwinning of the twinned grains or full twinning of the matrix grains, depending on the TB orientations, and a single crystal with the same orientation as the matrix grain or the twinned grain is formed. When the TBs are inclined by more than 74° to the loading axis, dislocation-TB interactions are the main deformation mechanism, which leads to complicated dislocation networks. Under vertical orientations, extensive slip transmission takes place in samples with small twin spacing, while twinning occurs in addition to conventional dislocation slip in samples with large twin spacing.

7 CONCLUSIONS AND RECOMMENDATIONS

7.1 Conclusions

In this thesis, MD simulations are performed to investigate the deformation mechanisms in nanotwinned fcc and bcc materials. The following conclusions can be drawn.

The simulations of <111> textured polycrystalline Cu under tensile loading parallel to the TB reveal a shift in deformation mechanism from a combination of dislocation slip and deformation twinning in twin-free samples to pure dislocation activities in nanotwinned simulation cells. The tensile strength of <111> textured polycrystalline Cu monotonically increases as the twin spacing decreases since the detwinning mechanism that softens nanotwinned Cu with random orientations is suppressed under parallel loading conditions. The strengthening effect in columnar nanotwinned Cu originates from TB restricting the dislocation transmission across TB. Moreover, the presence of TBs complicates the columnar GB structure, which delays the dislocation nucleation. Dislocation processes involved in the slip-twin interactions are identified at atomic level. Both the direct and indirect transmissions are observed. The direct transmission involves either the successive transmission of the leading and trailing partial dislocations by the Fleischer cross-slip model or the absorption and desorption of the extended dislocation by the Friedel-Escaig cross-slip mechanism. In contrast, the indirect transmission involves the formation of special superjogs to fulfil the strain compatibility between dislocations on non-coincident slip planes. An inhomogeneous deformation occurs due to the plastic anisotropy of individual grains. Extensive slip transmissions across low angle GBs occur as they are not effective in hindering dislocation motion. Heterogeneous deformation leads to the formation of intersected slip bands on the plane view and persistent slip transfer leaves zigzag slip traces on the cross-sectional view. Most of the TBs retain their initial coherency even after a considerable deformation. Moreover, dislocation slip occurs on anomalous {112} plane and is described as composite {111} slip.

The simulations of nanotwinned Cu with different orientations reveal a dynamic transition in deformation mechanisms as the TB orientation varies from the

horizontal direction, to the slant direction and to the vertical direction. The nature of the dislocation activity in nanotwinned Cu agrees well with the Schmid's law. And the geometrical relation between the activated slip system and the twin plane determines three distinct dislocation processes. When the TB is parallel or inclined by an angle less than 30° to the loading direction, the plastic deformation is dominated by the transmission of extended screw dislocations. This transmission involves the successive transmissions of the leading and trailing dislocations and leaves the TB intact. As the angle of inclination increases slip systems on the TB plane can be activated. TB migration takes place in addition to slip transfer. When the TB is inclined by an angle between 30° and 60° with respect to the loading axis, TB migration governs the deformation. The TBs are eliminated after full twinning of the matrix grains or full detwinning of the twinned grains, depending on the TB orientations, and a single crystal with the same orientation as the twinned grain or the matrix grain is formed. When the TB is inclined by an angle between 60° and 90° to the loading axis, dislocation-TB interactions become the dominant deformation mechanism, which leads to the formation of complicated dislocation networks and shear bands. Within the transition region, a combination of two types of slip activities takes place.

Deformation twinning plays an important role in the plastic deformation of nanotwinned Cu with specific crystallographic orientations. Deformation twins are formed by the motion of Shockley partial dislocations on contiguous {111} slip planes. Two mechanisms for the formation of deformation twins are identified based on the arrangement of these Shockley partials. The first twin nucleation mechanism involves the formation of the double-Shockley partial, which results from the overlap of two Shockley partials of different types. This kind of twinning occurs when the TB is inclined by an angle between 15° and 30° to the loading direction. The formed mechanical twins are thin plates embedded either in the twinned grains or in the matrix grain, which are not sable and can be easily eliminated during later stages of deformation. The second twin formation mechanism results from the passage of Shockley dislocations of the same type. The twinning takes place when the TB is inclined by an angle between 75° and 90° to the loading axis. Deformation twins are well developed along one primary twinning system in samples with inclination

angles close to 75°, while twinning takes place along multiple twinning systems both in the matrix and twinned grains in samples with inclination angles close to 90°. The interactions between dislocation and TBs promote the twin formation. The twinning dependence on the crystallographic orientation agrees well with available experimental results.

The simulations of nanotwinned Fe reveal a dynamic transition in the deformation mechanism as the TB orientation changes from the horizontal direction, to the slant direction and to the vertical direction. The nature of the dislocation activity in nanotwinned Fe cannot be explained by the Schmid's law. And the geometrical relation between the activated slip system and the twin plane determines three distinct dislocation processes. When the TBs are parallel or inclined less than 30° to the loading direction, the samples eventually fracture in an almost brittle manner. As the angle of inclination increases, slip systems on the twin plane can be activated. The initial yielding is due to TB migration in samples with slanted TBs. When the TBs are inclined with angles between 45° and 60° to the loading direction, plastic deformation is dominated by TB migration. The TBs are eliminated after full detwinning of the twinned grains or full twinning of the matrix grains, depending on the TB orientations, and a single crystal with the same orientation as the matrix grain or the twinned grain is formed. When the TBs are inclined by more than 74° to the loading axis, dislocation-TB interactions are the main deformation mechanism, which leads to complicated dislocation networks. Under vertical orientations, extensive slip transmission takes place in samples with small twin spacing, while twinning occurs in addition to conventional dislocation slip in samples with large twin spacing.

7.2 Recommendations for future work

In spite of the considerable progresses made in the understanding of the mechanical behaviour of the nanocrystalline and nanotwinned materials, there are still a large number of intriguing directions for future work. Several areas are listed as follows.

Conventional strengthening methods introduce internal defects and boundaries to restrict dislocation motion, but the ductility is compromised. On the other hand, materials can be strengthened by engineering nanoscale coherent TBs while the ductility is retained. High density of TBs has been successfully generated in metals and alloys with low stacking fault energies, such as Cu and stainless steels. This strengthening method may also apply to other engineering materials. Nanoscale twins are easily formed in materials with low stacking fault energies. It is still a big challenge to generate dense nanoscale twins in materials with high stacking fault energies. The nanotwinned microstructure may also be realised in materials with other lattice structures such as bcc and hcp.

MD simulations reveal the deformation mechanisms in nanotwinned fcc and bcc materials. How the different types of deformation modes interact with each other to fulfil strain compatibility in polycrystalline materials and affect the mechanical properties of is not well understood.

The deformation mechanisms of nanocrystalline fcc materials have been widely studied, but the deformation mechanisms of bcc and hcp crystals are not fully understood. The twinning mechanisms in bcc and hcp materials need to be systematically studied. The interplay between dislocation slip and deformation twinning is not clear. Moreover, the effect of nanoscale twins on the mechanical behaviour of hcp materials remains unexplored.

MD simulations can only provide the qualitative insights into the deformation mechanisms due to the inherent limitation in spatial and temporal scale. The obtained simulation results need to be explained with care and verified by experiments. To overcome the inherent limitation of MD simulations, multiscale modelling by coupling MD simulations with mesoscopic or continuum methods has been developed, which provides a better understanding of plastic deformation.

REFERENCES

ABUZAID, W. Z., SANGID, M. D., CARROLL, J. D., SEHITOGLU, H. & LAMBROS, J. 2012. Slip transfer and plastic strain accumulation across grain boundaries in Hastelloy X. *Journal of the Mechanics and Physics of Solids,* 60**,** 1201-1220.

AFANASYEV, K. A. & SANSOZ, F. 2007. Strengthening in gold nanopillars with nanoscale twins. *Nano Letters,* 7**,** 2056-2062.

ALCALÁ, J., DALMAU, R., FRANKE, O., BIENER, M., BIENER, J. & HODGE, A. 2012. Planar defect nucleation and annihilation mechanisms in nanocontact plasticity of metal surfaces. *Physical Review Letters,* 109.

ANDEROGLU, O., MISRA, A., WANG, H., RONNING, F., HUNDLEY, M. F. & ZHANG, X. 2008a. Epitaxial nanotwinned Cu films with high strength and high conductivity. *Applied Physics Letters,* 93.

ANDEROGLU, O., MISRA, A., WANG, H. & ZHANG, X. 2008b. Thermal stability of sputtered Cu films with nanoscale growth twins. *Journal of Applied Physics,* 103.

BACHURIN, D. V., WEYGAND, D. & GUMBSCH, P. 2010. Dislocation-grain boundary interaction in 〈1 1 1〉 textured thin metal films. *Acta Materialia,* 58**,** 5232-5241.

BEYERLEIN, I. J., ZHANG, X. & MISRA, A. 2014. Growth twins and deformation twins in metals. *Annual Review of Materials Research.* Annual Reviews Inc.

BITZEK, E., BRANDL, C., DERLET, P. M. & VAN SWYGENHOVEN, H. 2008a. Dislocation cross-slip in nanocrystalline fcc metals. *Physical Review Letters,* 100.

BITZEK, E., DERLET, P. M., ANDERSON, P. M. & VAN SWYGENHOVEN, H. 2008b. The stress-strain response of nanocrystalline metals: A statistical analysis of atomistic simulations. *Acta Materialia,* 56**,** 4846-4857.

BRANDL, C., BITZEK, E., DERLET, P. M. & VAN SWYGENHOVEN, H. 2007. Slip transfer through a general high angle grain boundary in nanocrystalline aluminum. *Applied Physics Letters,* 91.

BUDROVIC, Z., VAN SWYGENHOVEN, H., DERLET, P. M., VAN PETEGEM, S. & SCHMITT, B. 2004. Plastic Deformation with Reversible Peak Broadening in Nanocrystalline Nickel. *Science,* 304**,** 273-276.

BUFFORD, D., BI, Z., JIA, Q. X., WANG, H. & ZHANG, X. 2012. Nanotwins and stacking faults in high-strength epitaxial Ag/Al multilayer films. *Applied Physics Letters,* 101.

BUREK, M. J. & GREER, J. R. 2010. Fabrication and microstructure control of nanoscale mechanical testing specimens via electron beam lithography and electroplating. *Nano Letters,* 10**,** 69-76.

CALLISTER JR, W. D. 2007. *Materials science and engineering : an introduction.*

CHASSAGNE, M., LEGROS, M. & RODNEY, D. 2011. Atomic-scale simulation of screw dislocation/coherent twin boundary interaction in Al, Au, Cu and Ni. *Acta Materialia,* 59**,** 1456-1463.

CHEN, C. Q., FLORANDO, J. N., KUMAR, M., RAMESH, K. T. & HEMKER, K. J. 2014. Incipient deformation twinning in dynamically sheared bcc tantalum. *Acta Materialia,* 69**,** 114-125.

CHEN, C. Q., HU, G., FLORANDO, J. N., KUMAR, M., HEMKER, K. J. & RAMESH, K. T. 2013. Interplay of dislocation slip and deformation twinning in tantalum at high strain rates. *Scripta Materialia,* 69**,** 709-712.

CHEN, J., LU, L. & LU, K. 2006. Hardness and strain rate sensitivity of nanocrystalline Cu. *Scripta Materialia,* 54**,** 1913-1918.

CHEN, M., MA, E., HEMKER, K. J., SHENG, H., WANG, Y. & CHENG, X. 2003. Deformation twinning in nanocrystalline aluminum. *Science,* 300**,** 1275-1277.

CHEN, Z., JIN, Z. & GAO, H. 2007. Repulsive force between screw dislocation and coherent twin boundary in aluminum and copper. *Phys. Rev. B,* 75.

CHOKSHI, A. H., ROSEN, A., KARCH, J. & GLEITER, H. 1989. On the validity of the hall-petch relationship in nanocrystalline materials. *Scripta Metallurgica,* 23**,** 1679-1683.

CHOOKAJORN, T., MURDOCH, H. A. & SCHUH, C. A. 2012. Design of stable nanocrystalline alloys. *Science,* 337**,** 951-954.

CHRISTIAN, J. W. & MAHAJAN, S. 1995. Deformation twinning. *Progress in Materials Science,* 39**,** 1-157.

CLARK, W. A. T., WAGONER, R. H., SHEN, Z. Y., LEE, T. C., ROBERTSON, I. M. & BIRNBAUM, H. K. 1992. On the criteria for slip transmission across interfaces in polycrystals. *Scripta Metallurgica et Materiala,* 26**,** 203-206.

COHEN, J. B. & WEERTMAN, J. 1963. A dislocation model for twinning in f.c.c. metals. *Acta Metallurgica,* 11**,** 996-998.

COLLA, M. S., WANG, B., IDRISSI, H., SCHRYVERS, D., RASKIN, J. P. & PARDOEN, T. 2012. High strength-ductility of thin nanocrystalline palladium films with nanoscale twins: On-chip testing and grain aggregate model. *Acta Materialia,* 60**,** 1795-1806.

COTTRELL, A. H. & BILBY, B. A. 1951. A mechanism for the growth of deformation twins in crystals. *Philosophical Magazine,* 42**,** 573-581.

DAO, M., LU, L., ASARO, R. J., DE HOSSON, J. T. M. & MA, E. 2007. Toward a quantitative understanding of mechanical behavior of nanocrystalline metals. *Acta Materialia,* 55**,** 4041-4065.

DAO, M., LU, L., SHEN, Y. F. & SURESH, S. 2006. Strength, strain-rate sensitivity and ductility of copper with nanoscale twins. *Acta Materialia,* 54**,** 5421-5432.

DAPHALAPURKAR, N. P. & RAMESH, K. T. 2012. Orientation dependence of the nucleation and growth of partial dislocations and possible twinning mechanisms in aluminum. *Journal of the Mechanics and Physics of Solids,* 60**,** 277-294.

DAW, M. S. & BASKES, M. I. 1983. Semiempirical, quantum mechanical calculation of hydrogen embrittlement in metals. *Physical Review Letters,* 50**,** 1285-1288.

DAW, M. S. & BASKES, M. I. 1984. Embedded-atom method: Derivation and application to impurities, surfaces, and other defects in metals. *Physical Review B,* 29**,** 6443-6453.

DAW, M. S., FOILES, S. M. & BASKES, M. I. 1993. The embedded-atom method: a review of theory and applications. *Materials Science Reports,* 9**,** 251-310.

DE KONING, M., CAI, W. & BULATOV, V. V. 2003a. Anomalous dislocation multiplication in FCC metals. *Physical Review Letters,* 91**,** 025503/1-025503/4.

DE KONING, M., KURTZ, R. J., BULATOV, V. V., HENAGER, C. H., HOAGLAND, R. G., CAI, W. & NOMURA, M. 2003b. Modeling of dislocation-grain boundary interactions in FCC metals. *Journal of Nuclear Materials,* 323**,** 281-289.

DE KONING, M., MILLER, R., BULATOV, V. V. & ABRAHAM, F. F. 2002. Modelling grain-boundary resistance in intergranular dislocation slip transmission. *Philosophical Magazine A: Physics of Condensed Matter, Structure, Defects and Mechanical Properties,* 82**,** 2511-2527.

DENG, C. & SANSOZ, F. 2009a. Enabling ultrahigh plastic flow and work hardening in twinned gold nanowires. *Nano Letters,* 9**,** 1517-1522.

DENG, C. & SANSOZ, F. 2009b. Fundamental differences in the plasticity of periodically twinned nanowires in Au, Ag, Al, Cu, Pb and Ni. *Acta Materialia,* 57**,** 6090-6101.

DENG, C. & SANSOZ, F. 2009c. Near-ideal strength in gold nanowires achieved through microstructural design. *ACS Nano,* 3**,** 3001-3008.

DERLET, P. M., HASNAOUI, A. & VAN SWYGENHOVEN, H. 2003a. Atomistic simulations as guidance to experiments. *Scripta Materialia,* 49**,** 629-635.

DERLET, P. M. & VAN SWYGENHOVEN, H. 2002. Length scale effects in the simulation of deformation properties of nanocrystalline metals. *Scripta Materialia,* 47**,** 719-724.

DERLET, P. M., VAN SWYGENHOVEN, H. & HASNAOUI, A. 2003b. Atomistic simulation of dislocation emission in nanosized grain boundaries. *Philosophical Magazine,* 83**,** 3569-3575.

DEWALD, M. & CURTIN, W. A. 2011. Multiscale modeling of dislocation/grain-boundary interactions: III. 60° dislocations impinging on Σ3, Σ9 and Σ11 tilt boundaries in Al. *Modelling and Simulation in Materials Science and Engineering,* 19.

DEWALD, M. P. & CURTIN, W. A. 2007a. Multiscale modelling of dislocation/grain-boundary interactions: I. Edge dislocations impinging on Σ11 (1 1 3) tilt boundary in Al. *Modelling and Simulation in Materials Science and Engineering,* 15**,** S193-S215.

DEWALD, M. P. & CURTIN, W. A. 2007b. Multiscale modelling of dislocation/grain boundary interactions. II. Screw dislocations impinging on tilt boundaries in Al. *Philosophical Magazine,* 87**,** 4615-4641.

DUESBERY, M. S. & VITEK, V. 1998. Plastic anisotropy in B.C.C. transition metals. *Acta Materialia,* 46**,** 1481-1492.

EZAZ, T., SANGID, M. D. & SEHITOGLU, H. 2011. Energy barriers associated with slip-twin interactions. *Philosophical Magazine,* 91**,** 1464-1488.

FINNIS, M. W. & SINCLAIR, J. E. 1984. SIMPLE EMPIRICAL N-BODY POTENTIAL FOR TRANSITION METALS. *Philosophical Magazine A: Physics of Condensed Matter, Structure, Defects and Mechanical Properties,* 50**,** 45-55.

FLEISCHER, R. L. 1959. Cross slip of extended dislocations. *Acta Metallurgica,* 7**,** 134-135.

FREDERIKSEN, S. L., JACOBSEN, K. W. & SCHIØTZ, J. 2004. Simulations of intergranular fracture in nanocrystalline molybdenum. *Acta Materialia,* 52**,** 5019-5029.

FRØSETH, A., VAN SWYGENHOVEN, H. & DERLET, P. M. 2004a. The influence of twins on the mechanical properties of nc-Al. *Acta Materialia,* 52**,** 2259-2268.

FRØSETH, A. G., DERLET, P. M. & VAN SWYGENHOVEN, H. 2004b. Dislocations emitted from nanocrystalline grain boundaries: Nucleation and splitting distance. *Acta Materialia,* 52**,** 5863-5870.

FRØSETH, A. G., DERLET, P. M. & VAN SWYGENHOVEN, H. 2004c. Grown-in twin boundaries affecting deformation mechanisms in nc-metals. *Applied Physics Letters,* 85**,** 5863-5865.

FRØSETH, A. G., DERLET, P. M. & VAN SWYGENHOVEN, H. 2005. Twinning in nanocrystalline fcc metals. *Advanced Engineering Materials,* 7**,** 16-20.

FUJITA, H. & MORI, T. 1975. A formation mechanism of mechanical twins in F.C.C. Metals. *Scripta Metallurgica,* 9**,** 631-636.

FURNISH, T. A., LOHMILLER, J., GRUBER, P. A., BARBEE JR, T. W. & HODGE, A. M. 2013. Temperature-dependent strain localization and texture evolution of highly nanotwinned Cu. *Applied Physics Letters,* 103.

GLEITER, H. 1989. Nanocrystalline materials. *Progress in Materials Science,* 33**,** 223-315.

GLEITER, H. 2000. Nanostructured materials: basic concepts and microstructure. *Acta Materialia,* 48**,** 1-29.

GOULDSTONE, A., CHOLLACOOP, N., DAO, M., LI, J., MINOR, A. M. & SHEN, Y. L. 2007. Indentation across size scales and disciplines: Recent developments in experimentation and modeling. *Acta Materialia,* 55**,** 4015-4039.

GU, P., DAO, M., ASARO, R. J. & SURESH, S. 2011. A unified mechanistic model for size-dependent deformation in nanocrystalline and nanotwinned metals. *Acta Materialia,* 59**,** 6861-6868.

GUTIERREZ-URRUTIA, I. & RAABE, D. 2011. Dislocation and twin substructure evolution during strain hardening of an Fe-22 wt.% Mn-0.6 wt.% C TWIP steel observed by electron channeling contrast imaging. *Acta Materialia,* 59**,** 6449-6462.

GUTIERREZ-URRUTIA, I., ZAEFFERER, S. & RAABE, D. 2010. The effect of grain size and grain orientation on deformation twinning in a Fe-22wt.% Mn-0.6wt.% C TWIP steel. *Materials Science and Engineering A,* 527**,** 3552-3560.

HALL, E. O. 1951. The deformation and ageing of mild steel: III Discussion of results. *Proceedings of the Physical Society. Section B,* 64**,** 747-753.

HASLAM, A. J., MOLDOVAN, D., YAMAKOV, V., WOLF, D., PHILLPOT, S. R. & GLEITER, H. 2003. Stress-enhanced grain growth in a nanocrystalline material by molecular-dynamics simulation. *Acta Materialia,* 51**,** 2097-2112.

HIGGINBOTHAM, A., SUGGIT, M. J., BRINGA, E. M., ERHART, P., HAWRELIAK, J. A., MOGNI, G., PARK, N., REMINGTON, B. A. & WARK, J. S. 2013. Molecular dynamics simulations of shock-induced deformation twinning of a body-centered-cubic metal. *Physical Review B - Condensed Matter and Materials Physics,* 88.

HIRTH, J. P. & LOTHE, J. 1982. *Theory of Dislocations.*

HODGE, A. M., FURNISH, T. A., NAVID, A. A. & BARBEE JR, T. W. 2011. Shear band formation and ductility in nanotwinned Cu. *Scripta Materialia,* 65**,** 1006-1009.

HODGE, A. M., FURNISH, T. A., SHUTE, C. J., LIAO, Y., HUANG, X., HONG, C. S., ZHU, Y. T., BARBEE JR, T. W. & WEERTMAN, J. R. 2012. Twin stability in highly nanotwinned Cu under compression, torsion and tension. *Scripta Materialia,* 66**,** 872-877.

HODGE, A. M., WANG, Y. M. & BARBEE JR, T. W. 2006. Large-scale production of nano-twinned, ultrafine-grained copper. *Materials Science and Engineering A,* 429**,** 272-276.

HODGE, A. M., WANG, Y. M. & BARBEE JR, T. W. 2008. Mechanical deformation of high-purity sputter-deposited nano-twinned copper. *Scripta Materialia,* 59**,** 163-166.

HSIAO, H. Y., LIU, C. M., LIN, H. W., LIU, T. C., LU, C. L., HUANG, Y. S., CHEN, C. & TU, K. N. 2012. Unidirectional growth of microbumps on (111)-oriented and nanotwinned copper. *Science,* 336**,** 1007-1010.

IDRISSI, H., RENARD, K., RYELANDT, L., SCHRYVERS, D. & JACQUES, P. J. 2010. On the mechanism of twin formation in Fe-Mn-C TWIP steels. *Acta Materialia,* 58**,** 2464-2476.

IDRISSI, H., WANG, B., COLLA, M. S., RASKIN, J. P., SCHRYVERS, D. & PARDOEN, T. 2011. Ultrahigh strain hardening in thin palladium films with nanoscale twins. *Advanced Materials,* 23**,** 2119-2122.

JACOBSEN, K. W., NORSKOV, J. K. & PUSKA, M. J. 1987. Interatomic interactions in the effective-medium theory. *Physical Review B,* 35**,** 7423-7442.

JANG, D., CAI, C. & GREER, J. R. 2011. Influence of homogeneous interfaces on the strength of 500 nm diameter Cu nanopillars. *Nano Letters,* 11**,** 1743-1746.

JANG, D., LI, X., GAO, H. & GREER, J. R. 2012. Deformation mechanisms in nanotwinned metal nanopillars. *Nature Nanotechnology,* 7**,** 594-601.

JIN, M., MINOR, A. M., STACH, E. A. & MORRIS JR, J. W. 2004. Direct observation of deformation-induced grain growth during the nanoindentation of ultrafine-grained Al at room temperature. *Acta Materialia,* 52**,** 5381-5387.

JIN, Z. H., GUMBSCH, P., ALBE, K., MA, E., LU, K., GLEITER, H. & HAHN, H. 2008. Interactions between non-screw lattice dislocations and coherent twin boundaries in face-centered cubic metals. *Acta Materialia,* 56**,** 1126-1135.

JIN, Z. H., GUMBSCH, P., MA, E., ALBE, K., LU, K., HAHN, H. & GLEITER, H. 2006. The interaction mechanism of screw dislocations with coherent twin boundaries in different face-centred cubic metals. *Scripta Materialia,* 54**,** 1163-1168.

KARAMAN, I., SEHITOGLU, H., GALL, K., CHUMLYAKOV, Y. I. & MAIER, H. J. 2000. Deformation of single crystal hadfield steel by twinning and slip. *Acta Materialia,* 48**,** 1345-1359.

KE, M., HACKNEY, S. A., MILLIGAN, W. W. & AIFANTIS, E. C. 1995. Observation and measurement of grain rotation and plastic strain in nanostructured metal thin films. *Nanostructured Materials,* 5**,** 689-697.

KIM, S. W., LI, X., GAO, H. & KUMAR, S. 2012. In situ observations of crack arrest and bridging by nanoscale twins in copper thin films. *Acta Materialia,* 60**,** 2959-2972.

KUMAR, K. S., SURESH, S., CHISHOLM, M. F., HORTON, J. A. & WANG, P. 2003a. Deformation of electrodeposited nanocrystalline nickel. *Acta Materialia,* 51**,** 387-405.

KUMAR, K. S., VAN SWYGENHOVEN, H. & SURESH, S. 2003b. Mechanical behavior of nanocrystalline metals and alloys. *Acta Materialia,* 51**,** 5743-5774.

LAGERLÖF, K. P. D. 1993. On deformation twinning in b.c.c. metals. *Acta Metallurgica Et Materialia,* 41**,** 2143-2151.

LAGRANGE, T., REED, B. W., WALL, M., MASON, J., BARBEE, T. & KUMAR, M. 2013. Topological view of the thermal stability of nanotwinned copper. *Applied Physics Letters,* 102.

LEE, T. C., ROBERTSON, I. M. & BIRNBAUM, H. K. 1990a. An In Situ transmission electron microscope deformation study of the slip transfer mechanisms in metals. *Metallurgical Transactions A,* 21**,** 2437-2447.

LEE, T. C., ROBERTSON, I. M. & BIRNBAUM, H. K. 1990b. TEM in situ deformation study of the interaction of lattice dislocations with grain boundaries in metals. *Philosophical Magazine A: Physics of Condensed Matter, Structure, Defects and Mechanical Properties,* 62**,** 131-153.

LI, B., CAO, B. Y., RAMESH, K. T. & MA, E. 2009. A nucleation mechanism of deformation twins in pure aluminum. *Acta Materialia,* 57**,** 4500-4507.

LI, N., WANG, J., MISRA, A., ZHANG, X., HUANG, J. Y. & HIRTH, J. P. 2011. Twinning dislocation multiplication at a coherent twin boundary. *Acta Materialia,* 59**,** 5989-5996.

LI, S., DING, X., DENG, J., LOOKMAN, T., LI, J., REN, X., SUN, J. & SAXENA, A. 2010a. Superelasticity in bcc nanowires by a reversible twinning mechanism. *Physical Review B - Condensed Matter and Materials Physics,* 82.

LI, X., WEI, Y., LU, L., LU, K. & GAO, H. 2010b. Dislocation nucleation governed softening and maximum strength in nano-twinned metals. *Nature,* 464**,** 877-880.

LIAO, X. Z., ZHAO, Y. H., SRINIVASAN, S. G., ZHU, Y. T., VALIEV, R. Z. & GUNDEROV, D. V. 2004. Deformation twinning in nanocrystalline copper at room temperature and low strain rate. *Applied Physics Letters,* 84**,** 592-594.

LIAO, X. Z., ZHOU, F., LAVERNIA, E. J., HE, D. W. & ZHU, Y. T. 2003a. Deformation twins in nanocrystalline Al. *Applied Physics Letters,* 83**,** 5062-5064.

LIAO, X. Z., ZHOU, F., LAVERNIA, E. J., SRINIVASAN, S. G., BASKES, M. I., HE, D. W. & ZHU, Y. T. 2003b. Deformation mechanism in nanocrystalline Al: Partial dislocation slip. *Applied Physics Letters,* 83**,** 632-634.

LU, K., LU, L. & SURESH, S. 2009a. Strengthening materials by engineering coherent internal boundaries at the nanoscale. *Science,* 324**,** 349-352.

LU, L., CHEN, X., HUANG, X. & LU, K. 2009b. Revealing the maximum strength in nanotwinned copper. *Science,* 323**,** 607-610.

LU, L., DAO, M., ZHU, T. & LI, J. 2009c. Size dependence of rate-controlling deformation mechanisms in nanotwinned copper. *Scripta Materialia,* 60**,** 1062-1066.

LU, L., SCHWAIGER, R., SHAN, Z. W., DAO, M., LU, K. & SURESH, S. 2005. Nano-sized twins induce high rate sensitivity of flow stress in pure copper. *Acta Materialia,* 53**,** 2169-2179.

LU, L., SHEN, Y., CHEN, X., QIAN, L. & LU, K. 2004. Ultrahigh Strength and High Electrical Conductivity in Copper. *Science,* 304**,** 422-426.

LU, L., YOU, Z. S. & LU, K. 2012. Work hardening of polycrystalline Cu with nanoscale twins. *Scripta Materialia,* 66**,** 837-842.

MA, E., WANG, Y. M., LU, Q. H., SUI, M. L., LU, L. & LU, K. 2004. Strain hardening and large tensile elongation in ultrahigh-strength nano-twinned copper. *Applied Physics Letters,* 85**,** 4932-4934.

MAHAJAN, S. 1971. Twin- slip and twin- twin interactions in Mo- 35 at.% Re alloy. *Philosophical Magazine,* 23**,** 781-794.

MAHAJAN, S. 1972. Nucleation and growth of deformation twins in Mo-35 at. % Re alloy. *Philosophical Magazine,* 26**,** 161-171.

MAHAJAN, S. 2013. Critique of mechanisms of formation of deformation, annealing and growth twins: Face-centered cubic metals and alloys. *Scripta Materialia,* 68**,** 95-99.

MAHAJAN, S. & CHIN, G. Y. 1973a. Formation of deformation twins in f.c.c. crystals. *Acta Metallurgica,* 21**,** 1353-1363.

MAHAJAN, S. & CHIN, G. Y. 1973b. Twin-slip, twin-twin and slip-twin interactions in Co-8 wt.% Fe alloy single crystals. *Acta Metallurgica,* 21**,** 173-179.

MARIAN, J., CAI, W. & BULATOV, V. V. 2004. Dynamic transitions from smooth to rough to twinning in dislocation motion. *Nature Materials,* 3**,** 158-163.

MENDELEV, M. I., HAN, S., SROLOVITZ, D. J., ACKLAND, G. J., SUN, D. Y. & ASTA, M. 2003. Development of new interatomic potentials appropriate for crystalline and liquid iron. *Philosophical Magazine,* 83**,** 3977-3994.

MEYERS, M. A., MISHRA, A. & BENSON, D. J. 2006. Mechanical properties of nanocrystalline materials. *Progress in Materials Science,* 51**,** 427-556.

MEYERS, M. A., VÖHRINGER, O. & LUBARDA, V. A. 2001. The onset of twinning in metals: A constitutive description. *Acta Materialia,* 49**,** 4025-4039.

MISHIN, Y., MEHL, M. J., PAPACONSTANTOPOULOS, D. A., VOTER, A. F. & KRESS, J. D. 2001. Structural stability and lattice defects in copper: Ab initio, tight-binding, and embedded-atom calculations. *Physical Review B,* 63**,** 224106.

MORRIS WANG, Y., SANSOZ, F., LAGRANGE, T., OTT, R. T., MARIAN, J., BARBEE, T. W. & HAMZA, A. V. 2013. Defective twin boundaries in nanotwinned metals. *Nature Materials,* 12**,** 697-702.

NIEH, T. G. & WADSWORTH, J. 1991. Hall-petch relation in nanocrystalline solids. *Scripta Metallurgica et Materiala,* 25**,** 955-958.

OGAWA, K. 1965. Edge dislocations dissociated in {112} planes and twinning mechanism of b.c.c. metals. *Philosophical Magazine,* 11**,** 217-233.

OJHA, A. & SEHITOGLU, H. 2014. Twinning stress prediction in bcc metals and alloys. *Philosophical Magazine Letters,* 94**,** 647-657.

OJHA, A., SEHITOGLU, H., PATRIARCA, L. & MAIER, H. J. 2014. Twin nucleation in Fe-based bcc alloys - Modeling and experiments. *Modelling and Simulation in Materials Science and Engineering,* 22.

PAN, Q. S. & LU, L. 2014. Strain-controlled cyclic stability and properties of Cu with highly oriented nanoscale twins. *Acta Materialia,* 81**,** 248-257.
PAN, Q. S., LU, Q. H. & LU, L. 2013. Fatigue behavior of columnar-grained Cu with preferentially oriented nanoscale twins. *Acta Materialia,* 61**,** 1383-1393.
PAN, Z., LI, Y. & WEI, Q. 2008. Tensile properties of nanocrystalline tantalum from molecular dynamics simulations. *Acta Materialia,* 56**,** 3470-3480.
PETCH, N. J. 1953. The cleavage strength of polycrystals. *J. Iron Steel Inst.,* 174**,** 25-28.
PLIMPTON, S. 1995. Fast parallel algorithms for short-range molecular dynamics. *Journal of Computational Physics,* 117**,** 1-19.
PLIMPTON, S. J. & THOMPSON, A. P. 2012. Computational aspects of many-body potentials. *MRS Bulletin,* 37**,** 513-521.
PRIESTNER, R. & LESLIE, W. C. 1965. Nucleation of deformation twins at slip plane intersections in B.C.C. metals. *Philosophical Magazine,* 11**,** 895-916.
PÜSCHL, W. 2002. Models for dislocation cross-slip in close-packed crystal structures: A critical review. *Progress in Materials Science,* 47**,** 415-461.
QIN, E. W., LU, L., TAO, N. R. & LU, K. 2009a. Enhanced fracture toughness of bulk nanocrystalline Cu with embedded nanoscale twins. *Scripta Materialia,* 60**,** 539-542.
QIN, E. W., LU, L., TAO, N. R., TAN, J. & LU, K. 2009b. Enhanced fracture toughness and strength in bulk nanocrystalline Cu with nanoscale twin bundles. *Acta Materialia,* 57**,** 6215-6225.
REMINGTON, T. P., RUESTES, C. J., BRINGA, E. M., REMINGTON, B. A., LU, C. H., KAD, B. & MEYERS, M. A. 2014. Plastic deformation in nanoindentation of tantalum: A new mechanism for prismatic loop formation. *Acta Materialia,* 78**,** 378-393.
RICE, J. R. 1992. Dislocation nucleation from a crack tip: An analysis based on the Peierls concept. *Journal of the Mechanics and Physics of Solids,* 40**,** 239-271.
SANGID, M. D., EZAZ, T., SEHITOGLU, H. & ROBERTSON, I. M. 2011. Energy of slip transmission and nucleation at grain boundaries. *Acta Materialia,* 59**,** 283-296.
SCHIOØTZ, J. & JACOBSEN, K. W. 2003. A maximum in the strength of nanocrystalline copper. *Science,* 301**,** 1357-1359.
SCHIØTZ, J., DI TOLLA, F. D. & JACOBSEN, K. W. 1998. Softening of nanocrystalline metals at very small grain sizes. *Nature,* 391**,** 561-563.
SCHIØTZ, J., VEGGE, T., DI TOLLA, F. D. & JACOBSEN, K. W. 1999. Atomic-scale simulations of the mechanical deformation of nanocrystalline metals. *Physical Review B - Condensed Matter and Materials Physics,* 60**,** 11971-11983.
SHABIB, I. & MILLER, R. E. 2009. Deformation characteristics and stress-strain response of nanotwinned copper via molecular dynamics simulation. *Acta Materialia,* 57**,** 4364-4373.
SHAN, Z., STACH, E. A., WIEZOREK, J. M. K., KNAPP, J. A., FOLLSTAEDT, D. M. & MAO, S. X. 2004. Grain boundary-mediated plasticity in nanocrystalline nickel. *Science,* 305**,** 654-657.
SHEN, Z., WAGONER, R. H. & CLARK, W. A. T. 1986. Dislocation pile-up and grain boundary interactions in 304 stainless steel. *Scripta Metallurgica,* 20**,** 921-926.

SHEN, Z., WAGONER, R. H. & CLARK, W. A. T. 1988. Dislocation and grain boundary interactions in metals. *Acta Metallurgica,* 36**,** 3231-3242.

SHUTE, C. J., MYERS, B. D., XIE, S., BARBEE JR, T. W., HODGE, A. M. & WEERTMAN, J. R. 2009. Microstructural stability during cyclic loading of multilayer copper/copper samples with nanoscale twinning. *Scripta Materialia,* 60**,** 1073-1077.

SHUTE, C. J., MYERS, B. D., XIE, S., LI, S. Y., BARBEE JR, T. W., HODGE, A. M. & WEERTMAN, J. R. 2011. Detwinning, damage and crack initiation during cyclic loading of Cu samples containing aligned nanotwins. *Acta Materialia,* 59**,** 4569-4577.

SINGH, A., TANG, L., DAO, M., LU, L. & SURESH, S. 2011. Fracture toughness and fatigue crack growth characteristics of nanotwinned copper. *Acta Materialia,* 59**,** 2437-2446.

SINNOTT, S. B. & BRENNER, D. W. 2012. Three decades of many-body potentials in materials research. *MRS Bulletin,* 37**,** 469-473.

SLEESWYK, A. W. 1963. ½<111> screw dislocations and the nucleation of {112}<111> twins in the b.c.c. lattice. *Philosophical Magazine,* 8**,** 1467-1486.

SONG, D., XUE, J., LI, X., DUAN, H. & JIN, Z. 2014. Irradiation-enhanced twin boundary migration in BCC Fe. *Philosophical Magazine Letters,* 94**,** 361-369.

SPEAROT, D. E., JACOB, K. I. & MCDOWELL, D. L. 2005. Nucleation of dislocations from [0 0 1] bicrystal interfaces in aluminum. *Acta Materialia,* 53**,** 3579-3589.

SPEAROT, D. E., JACOB, K. I. & MCDOWELL, D. L. 2007a. Dislocation nucleation from bicrystal interfaces with dissociated structure. *International Journal of Plasticity,* 23**,** 143-160.

SPEAROT, D. E., TSCHOPP, M. A., JACOB, K. I. & MCDOWELL, D. L. 2007b. Tensile strength of ⟨1 0 0⟩ and ⟨1 1 0⟩ tilt bicrystal copper interfaces. *Acta Materialia,* 55**,** 705-714.

STEINMETZ, D. R., JÄPEL, T., WIETBROCK, B., EISENLOHR, P., GUTIERREZ-URRUTIA, I., SAEED-AKBARI, A., HICKEL, T., ROTERS, F. & RAABE, D. 2013. Revealing the strain-hardening behavior of twinning-induced plasticity steels: Theory, simulations, experiments. *Acta Materialia,* 61**,** 494-510.

STUKOWSKI, A. 2010. Visualization and analysis of atomistic simulation data with OVITO-the Open Visualization Tool. *Modelling and Simulation in Materials Science and Engineering,* 18.

STUKOWSKI, A. & ALBE, K. 2010. Extracting dislocations and non-dislocation crystal defects from atomistic simulation data. *Modelling and Simulation in Materials Science and Engineering,* 18.

STUKOWSKI, A., ALBE, K. & FARKAS, D. 2010. Nanotwinned fcc metals: Strengthening versus softening mechanisms. *Physical Review B - Condensed Matter and Materials Physics,* 82.

SUTTON, A. P. & BALLUFFI, R. W. 1995. *Interfaces in Crystalline Materials*.

TIAN, Y., XU, B., YU, D., MA, Y., WANG, Y., JIANG, Y., HU, W., TANG, C., GAO, Y., LUO, K., ZHAO, Z., WANG, L. M., WEN, B., HE, J. & LIU, Z. 2013. Ultrahard nanotwinned cubic boron nitride. *Nature,* 493**,** 385-388.

TSCHOPP, M. A. & MCDOWELL, D. L. 2008. Grain boundary dislocation sources in nanocrystalline copper. *Scripta Materialia,* 58**,** 299-302.
TUCKER, G. J. & FOILES, S. M. 2015. Quantifying the influence of twin boundaries on the deformation of nanocrystalline copper using atomistic simulations. *International Journal of Plasticity,* 65**,** 191-205.
VAN SWYGENHOVEN, H. & CARO, A. 1997. Plastic behavior of nanophase Ni: A molecular dynamics computer simulation. *Applied Physics Letters,* 71**,** 1652-1654.
VAN SWYGENHOVEN, H. & CARO, A. 1998. Plastic behavior of nanophase metals studied by molecular dynamics. *Physical Review B - Condensed Matter and Materials Physics,* 58**,** 11246-11251.
VAN SWYGENHOVEN, H. & DERLET, P. M. 2001. Grain-boundary sliding in nanocrystalline fcc metals. *Physical Review B - Condensed Matter and Materials Physics,* 64**,** 2241051-2241059.
VAN SWYGENHOVEN, H. & DERLET, P. M. 2008. Chapter 81 - Atomistic Simulations of Dislocations in FCC Metallic Nanocrystalline Materials. *In:* HIRTH, J. P. (ed.) *Dislocations in Solids.* Elsevier.
VAN SWYGENHOVEN, H., DERLET, P. M. & FRØSETH, A. G. 2004. Stacking fault energies and slip in nanocrystalline metals. *Nature Materials,* 3**,** 399-403.
VAN SWYGENHOVEN, H., DERLET, P. M. & FRØSETH, A. G. 2006. Nucleation and propagation of dislocations in nanocrystalline fcc metals. *Acta Materialia,* 54**,** 1975-1983.
VAN SWYGENHOVEN, H., DERLET, P. M. & HASNAOUI, A. 2002. Atomic mechanism for dislocation emission from nanosized grain boundaries. *Physical Review B - Condensed Matter and Materials Physics,* 66**,** 241011-241018.
VAN SWYGENHOVEN, H., FARKAS, D. & CARO, A. 2000. Grain-boundary structures in polycrystalline metals at the nanoscale. *Physical Review B - Condensed Matter and Materials Physics,* 62**,** 831-838.
VAN SWYGENHOVEN, H., SPACZER, M. & CARO, A. 1999a. Microscopic description of plasticity in computer generated metallic nanophase samples: A comparison between Cu and Ni. *Acta Materialia,* 47**,** 3117-3126.
VAN SWYGENHOVEN, H., SPACZER, M., CARO, A. & FARKAS, D. 1999b. Competing plastic deformation mechanisms in nanophase metals. *Physical Review B - Condensed Matter and Materials Physics,* 60**,** 22-25.
VAN SWYGENHOVEN, H. & WEERTMAN, J. R. 2006. Deformation in nanocrystalline metals. *Materials Today,* 9**,** 24-31.
VENABLES, J. A. 1961. Deformation twinning in face-centred cubic metals. *Philosophical Magazine,* 6**,** 379-396.
VO, N. Q., AVERBACK, R. S., BELLON, P., ODUNUGA, S. & CARO, A. 2008. Quantitative description of plastic deformation in nanocrystalline Cu: Dislocation glide versus grain boundary sliding. *Physical Review B - Condensed Matter and Materials Physics,* 77.
WANG, B., IDRISSI, H., GALCERAN, M., COLLA, M. S., TURNER, S., HUI, S., RASKIN, J. P., PARDOEN, T., GODET, S. & SCHRYVERS, D. 2012a. Advanced TEM investigation of the plasticity mechanisms in nanocrystalline

freestanding palladium films with nanoscale twins. *International Journal of Plasticity,* 37**,** 140-156.
WANG, B., IDRISSI, H., SHI, H., COLLA, M. S., MICHOTTE, S., RASKIN, J. P., PARDOEN, T. & SCHRYVERS, D. 2012b. Texture-dependent twin formation in nanocrystalline thin Pd films. *Scripta Materialia,* 66**,** 866-871.
WANG, J. & HUANG, H. 2006. Novel deformation mechanism of twinned nanowires. *Applied Physics Letters,* 88**,** 203112.
WANG, J., LI, N., ANDEROGLU, O., ZHANG, X., MISRA, A., HUANG, J. Y. & HIRTH, J. P. 2010. Detwinning mechanisms for growth twins in face-centered cubic metals. *Acta Materialia,* 58**,** 2262-2270.
WANG, J., SANSOZ, F., HUANG, J., LIU, Y., SUN, S., ZHANG, Z. & MAO, S. X. 2013. Near-ideal theoretical strength in gold nanowires containing angstrom scale twins. *Nature Communications,* 4.
WANG, J., ZENG, Z., WEINBERGER, C. R., ZHANG, Z., ZHU, T. & MAO, S. X. 2015. In situ atomic-scale observation of twinning-dominated deformation in nanoscale body-centred cubic tungsten. *Nature Materials,* 14**,** 594-600.
WANG, Y. B., LI, B. Q., SUI, M. L. & MAO, S. X. 2008. Deformation-induced grain rotation and growth in nanocrystalline Ni. *Applied Physics Letters,* 92.
WANG, Y. M., HODGE, A. M., BIENER, J., HAMZA, A. V., BARNES, D. E., LIU, K. & NIEH, T. G. 2005. Deformation twinning during nanoindentation of nanocrystalline Ta. *Applied Physics Letters,* 86**,** 1-3.
WEERTMAN, J. & WEERTMAN, J. R. 1992. *Elementary Dislocation Theory*.
WEI, Y., LI, Y., ZHU, L., LIU, Y., LEI, X., WANG, G., WU, Y., MI, Z., LIU, J., WANG, H. & GAO, H. 2014. Evading the strength-ductility trade-off dilemma in steel through gradient hierarchical nanotwins. *Nature Communications,* 5.
WOLF, D., YAMAKOV, V., PHILLPOT, S. R., MUKHERJEE, A. & GLEITER, H. 2005. Deformation of nanocrystalline materials by molecular-dynamics simulation: Relationship to experiments? *Acta Materialia,* 53**,** 1-40.
WU, X. L., LIAO, X. Z., SRINIVASAN, S. G., ZHOU, F., LAVERNIA, E. J., VALIEV, R. Z. & ZHU, Y. T. 2008. New Deformation Twinning Mechanism Generates Zero Macroscopic Strain in Nanocrystalline Metals. *Physical Review Letters,* 100**,** 095701.
WU, Z. X., ZHANG, Y. W. & SROLOVITZ, D. J. 2009. Dislocation-twin interaction mechanisms for ultrahigh strength and ductility in nanotwinned metals. *Acta Materialia,* 57**,** 4508-4518.
WU, Z. X., ZHANG, Y. W. & SROLOVITZ, D. J. 2011. Deformation mechanisms, length scales and optimizing the mechanical properties of nanotwinned metals. *Acta Materialia,* 59**,** 6890-6900.
YAMAKOV, V., WOLF, D., PHILLPOT, S. R. & GLEITER, H. 2002a. Deformation twinning in nanocrystalline Al by molecular-dynamics simulation. *Acta Materialia,* 50**,** 5005-5020.
YAMAKOV, V., WOLF, D., PHILLPOT, S. R. & GLEITER, H. 2002b. Grain-boundary diffusion creep in nanocrystalline palladium by molecular-dynamics simulation. *Acta Materialia,* 50**,** 61-73.
YAMAKOV, V., WOLF, D., PHILLPOT, S. R. & GLEITER, H. 2003a. Dislocation-dislocation and dislocation-twin reactions in nanocrystalline Al by molecular dynamics simulation. *Acta Materialia,* 51**,** 4135-4147.

YAMAKOV, V., WOLF, D., PHILLPOT, S. R., MUKHERJEE, A. K. & GLEITER, H. 2002c. Dislocation processes in the deformation of nanocrystalline aluminium by molecular-dynamics simulation. *Nature Materials,* 1**,** 45-48.

YAMAKOV, V., WOLF, D., PHILLPOT, S. R., MUKHERJEE, A. K. & GLEITER, H. 2003b. Deformation mechanism crossover and mechanical behaviour in nanocrystalline materials. *Philosophical Magazine Letters,* 83**,** 385-393.

YAMAKOV, V., WOLF, D., PHILLPOT, S. R., MUKHERJEE, A. K. & GLEITER, H. 2004. Deformation-mechanism map for nanocrystalline metals by molecular-dynamics simulation. *Nature Materials,* 3**,** 43-47.

YAMAKOV, V., WOLF, D., SALAZAR, M., PHILLPOT, S. R. & GLEITER, H. 2001. Length-scale effects in the nucleation of extended dislocations in nanocrystalline Al by molecular-dynamics simulation. *Acta Materialia,* 49**,** 2713-2722.

YE, J. C., WANG, Y. M., BARBEE JR, T. W. & HAMZA, A. V. 2012. Orientation-dependent hardness and strain rate sensitivity in nanotwin copper. *Applied Physics Letters,* 100.

YIP, S. 1998. The strongest size. *Nature,* 391**,** 532-533.

YOU, Z., LI, X., GUI, L., LU, Q., ZHU, T., GAO, H. & LU, L. 2013. Plastic anisotropy and associated deformation mechanisms in nanotwinned metals. *Acta Materialia,* 61**,** 217-227.

YOU, Z. S., LU, L. & LU, K. 2011. Tensile behavior of columnar grained Cu with preferentially oriented nanoscale twins. *Acta Materialia,* 59**,** 6927-6937.

YU, Q., QI, L., CHEN, K., MISHRA, R. K., LI, J. & MINOR, A. M. 2012. The Nanostructured Origin of Deformation Twinning. *Nano Letters,* 12**,** 887-892.

ZHANG, K., WEERTMAN, J. R. & EASTMAN, J. A. 2004a. The influence of time, temperature, and grain size on indentation creep in high-purity nanocrystalline and ultrafine grain copper. *Applied Physics Letters,* 85**,** 5197-5199.

ZHANG, K., WEERTMAN, J. R. & EASTMAN, J. A. 2005. Rapid stress-driven grain coarsening in nanocrystalline Cu at ambient and cryogenic temperatures. *Applied Physics Letters,* 87.

ZHANG, R. F., WANG, J., BEYERLEIN, I. J. & GERMANN, T. C. 2011. Twinning in bcc metals under shock loading: A challenge to empirical potentials. *Philosophical Magazine Letters,* 91**,** 731-740.

ZHANG, X. & MISRA, A. 2012. Superior thermal stability of coherent twin boundaries in nanotwinned metals. *Scripta Materialia,* 66**,** 860-865.

ZHANG, X., MISRA, A., WANG, H., NASTASI, M., EMBURY, J. D., MITCHELL, T. E., HOAGLAND, R. G. & HIRTH, J. P. 2004b. Nanoscale-twinning-induced strengthening in austenitic stainless steel thin films. *Applied Physics Letters,* 84**,** 1096-1098.

ZHANG, X., MISRA, A., WANG, H., SHEN, T. D., NASTASI, M., MITCHELL, T. E., HIRTH, J. P., HOAGLAND, R. G. & EMBURY, J. D. 2004c. Enhanced hardening in Cu/330 stainless steel multilayers by nanoscale twinning. *Acta Materialia,* 52**,** 995-1002.

ZHANG, X., WANG, H., CHEN, X. H., LU, L., LU, K., HOAGLAND, R. G. & MISRA, A. 2006. High-strength sputter-deposited Cu foils with preferred orientation of nanoscale growth twins. *Applied Physics Letters,* 88.

ZHANG, Y., MILLETT, P. C., TONKS, M. & BINER, B. 2012a. Deformation-twin-induced grain boundary failure. *Scripta Materialia,* 66**,** 117-120.

ZHANG, Y., MILLETT, P. C., TONKS, M. & BINER, S. B. 2012b. Deformation twins in nanocrystalline body-centered cubic Mo as predicted by molecular dynamics simulations. *Acta Materialia,* 60**,** 6421-6428.

ZHENG, S., BEYERLEIN, I. J., CARPENTER, J. S., KANG, K., WANG, J., HAN, W. & MARA, N. A. 2013. High-strength and thermally stable bulk nanolayered composites due to twin-induced interfaces. *Nature Communications,* 4.

ZHENG, S. J., BEYERLEIN, I. J., WANG, J., CARPENTER, J. S., HAN, W. Z. & MARA, N. A. 2012. Deformation twinning mechanisms from bimetal interfaces as revealed by in situ straining in the TEM. *Acta Materialia,* 60**,** 5858-5866.

ZHENG, Y. G., LU, J., ZHANG, H. W. & CHEN, Z. 2009. Strengthening and toughening by interface-mediated slip transfer reaction in nanotwinned copper. *Scripta Materialia,* 60**,** 508-511.

ZHOU, H., LI, X., QU, S., YANG, W. & GAO, H. 2014. A Jogged Dislocation Governed Strengthening Mechanism in Nanotwinned Metals. *Nano Letters,* 14**,** 5075-5080.

ZHU, L., RUAN, H., LI, X., DAO, M., GAO, H. & LU, J. 2011a. Modeling grain size dependent optimal twin spacing for achieving ultimate high strength and related high ductility in nanotwinned metals. *Acta Materialia,* 59**,** 5544-5557.

ZHU, T. & GAO, H. 2012. Plastic deformation mechanism in nanotwinned metals: An insight from molecular dynamics and mechanistic modeling. *Scripta Materialia,* 66**,** 843-848.

ZHU, T., LI, J., SAMANTA, A., KIM, H. G. & SURESH, S. 2007. Interfacial plasticity governs strain rate sensitivity and ductility in nanostructured metals. *Proceedings of the National Academy of Sciences of the United States of America,* 104**,** 3031-3036.

ZHU, Y. T., LIAO, X. Z. & WU, X. L. 2012. Deformation twinning in nanocrystalline materials. *Progress in Materials Science,* 57**,** 1-62.

ZHU, Y. T., WU, X. L., LIAO, X. Z., NARAYAN, J., KECSKÉS, L. J. & MATHAUDHU, S. N. 2011b. Dislocation-twin interactions in nanocrystalline fcc metals. *Acta Materialia,* 59**,** 812-821.

ZIMMERMAN, J. A., GAO, H. & ABRAHAM, F. F. 2000. Generalized stacking fault energies for embedded atom FCC metals. *Modelling and Simulation in Materials Science and Engineering,* 8**,** 103-116.